

CONSTRUCTION OF LATE CRETACEOUS, MID-CRUSTAL
SHEETED PLUTONS FROM THE EASTERN TRANSVERSE RANGES,
SOUTHERN CALIFORNIA

Kenneth Lee Brown

Submitted to the faculty of the University of Graduate School
in partial fulfillment of the requirements
for the degree
Master of Science
in the Department of Earth Sciences
Indiana University

November 2008

Accepted by the Faculty of Indiana University, in partial
fulfillment of the requirements for the degree of Master of Science

Kathy Licht, Ph.D., Chair

Master's Thesis
Committee

R. Jeffrey Swope, Ph.D.

Lin Li, Ph.D.

To my Father and Mother

To see a world in a grain of sand
and heaven in a wild flower
To hold infinity in the palm of your hand
and eternity in an hour
- *William Blake*

ACKNOWLEDGEMENTS

Above all, I would like to thank my graduate committee for helping me find a way forward when the path was not clear. Their continued advice, guidance, and encouragement made this research possible. Dr. Kathy Licht was always supportive, readily available, and patient, even when things seemed overwhelming. Dr. Jeffrey Swope was always positive and energetic, providing support at every stage of the project. Dr. Lin Li was always a great source of support, guidance, and knowledge. Collectively, this committee helped me learn a lot about science, research, and a little about myself. I could not have defined a stronger committee; I am very grateful for all of their contributions.

Although Dr. Scott Paterson (University of Southern California) was not formally on my committee, I considered him a member and a valuable source of guidance and knowledge. I would also like to thank Dr. Paterson for his many thoughtful reviews, discussions, and the use of his unpublished data to further support this work. A special thanks also goes to Dr. Andrew P. Barth and Dr. Joseph Wooden for sharing their samples, their unpublished mapping, and for allowing me to work with them in the field. I greatly respect Dr. Paterson, Dr. Barth, and Dr. Wooden for their knowledge and their contributions to science. Without their generosity and knowledge, I would not have been successful in pulling all of the parts of this research together.

I am also very grateful for all the support and patience of my family. Although I nearly lost my father during my graduate studies, I am glad he stuck around to see how it turned out. A special thanks also goes to my fiancée, Tammy McPeck, for all of her love, patience, and understanding. To my younger sister, Grace, I am grateful for your

curiosity. Without it, I would not have learned to imagine and explore all the avenues of this research.

This research was partially funded by grants awarded to Dr. Andrew P. Barth from the U.S. National Geographic Society and the National Park Service. Additional funding was awarded to me and provided by the IUPUI Department of Geology, the Geological Society of America, and the IUPUI School of Science Graduate Student Organization.

ABSTRACT

Kenneth Lee Brown

CONSTRUCTION OF LATE CRETACEOUS, MID-CRUSTAL SHEETED PLUTONS FROM THE EASTERN TRANSVERSE RANGES, SOUTHERN CALIFORNIA

Differential exhumation within the eastern Transverse Ranges of southern California has revealed a tilted crustal section that provides a unique view into the architecture of the Mesozoic arc. At the base of this crustal section is a group of well-exposed sheeted plutons. Well-developed, gentle to moderately dipping magmatic and solid-state fabrics within these plutons are regionally consistent, margin-parallel, discordant to internal sheeting and layering, and are generally parallel to equivalent host rock structures and fabrics. In some plutons, magmatic foliations define regional fold structures, thus recording regional contraction during chamber construction. Collectively, field mapping and fabric analyses within these sheeted plutons show that the observed fabric patterns are better explained by regional deformation rather than internal magma chamber processes. This interpretation is in direct contrast to previous mapping in the region.

The host rocks also record complex processes during sheeted pluton emplacement. Deflection of host rock foliations and structures into parallelism with pluton contacts suggest that downward ductile flow played a role in making space for these plutons. However, evidence of regional faulting and shearing is not observed, suggesting that they did not play a significant role.

Although there is considerable microstructural variability within each pluton, the observed microstructures are generally consistent with a transition from magmatic to submagmatic/ high-temperature solid-state deformation. Magmatic microstructures are

defined by euhedral to subhedral plagioclase, hornblende, and biotite that do not show significant internal crystal-plastic deformation. Evidence for high-temperature solid-state deformation includes high-temperature grain boundary migration in quartz, plagioclase, potassium feldspar, and hornblende; chessboard extinction in quartz; and ductile bending in plagioclase and hornblende. Microstructural observations also indicate that mafic and intermediate compositions record stronger magmatic fabrics than felsic compositions.

Based on the structural and microstructural observations presented in this study, I interpret that these sheeted plutons were emplaced into an active continental arc setting that was undergoing regional contraction. The strong magmatic fabrics and high-temperature solid-state overprinting is likely a consequence of regional deformation during crystallization. The weak fabrics within upper crustal plutons relative to the strong fabrics within the mid-crustal plutons suggest that deformation was largely localized to the more compositionally heterogeneous mid-crustal portions of the arc structure.

Kathy Licht, Ph.D., Committee Chair

TABLE OF CONTENTS

LIST OF TABLES.....	xi
LIST OF FIGURES.....	xii
INTRODUCTION.....	1
GEOLOGIC SETTING.....	5
Tectonic Setting.....	5
Geologic Setting of Study Area.....	7
Geology of the Little San Bernardino Mountains.....	8
METHODS.....	9
Sample Collection and Fabric Mapping.....	9
Petrographic Methods.....	10
RESULTS.....	12
MACROSCOPIC RESULTS.....	12
Geologic Overview of Keys View Quadrangle.....	12
Bighorn Sheeted Complex.....	13
Petrology.....	13
Macroscopic Fabrics and Structures.....	14
Blue Cut Granodiorite Pluton.....	17
Petrology.....	17
Macroscopic Fabrics and Structures.....	18
Quail Mountain Sheeted Complex.....	20
Petrology.....	20
Macroscopic Fabrics and Structures.....	22

Stubbe Spring Granite Pluton.....	24
Petrology.....	24
Macroscopic Fabrics and Structures.....	25
Palms Granite Pluton.....	26
Petrology.....	26
Macroscopic Fabrics and Structures.....	27
Proterozoic Framework Rocks.....	29
Petrology.....	29
Macroscopic Fabrics and Structures.....	30
MICROSTRUCTURAL RESULTS.....	34
Overview of Microstructural Criteria.....	34
Quartz Microstructures.....	35
Plagioclase Microstructures.....	37
Potassium Feldspar Microstructures.....	40
Biotite Microstructures.....	41
Hornblende and Sphene Microstructures.....	44
DISCUSSION AND INTERPRETATIONS.....	47
Microstructural Interpretations and Discussion.....	47
Macroscopic Interpretations and Discussion.....	52
CONCLUSION.....	58
TABLES.....	60
FIGURES.....	78
APPENDICES.....	133

REFERENCES.....	149
CURRICULUM VITAE	

LIST OF TABLES

Table 1. Table of macroscopic criteria.....	60
Table 2. Table of microstructural criteria.....	61
Table 3. Table of hand specimen fabric data.....	62
Table 4. Table of hand specimen mineralogy data	65
Table 5. Table of quartz microstructures.....	68
Table 6. Table of plagioclase microstructures.....	70
Table 7. Table of potassium feldspar microstructures.....	72
Table 8. Table of biotite microstructures.....	74
Table 9. Table of hornblende and sphene microstructures.....	76

LIST OF FIGURES

Figure 1. Regional map of the western U.S.....	78
Figure 2. Four tectonic configurations of continental margins modified from Dickinson (1981).....	79
Figure 3. Cartoon of the two modes of subduction.....	80
Figure 4. Map of California showing the simplified physiographic terrains.....	81
Figure 5. Simplified geologic map of the Eastern Transverse Range.....	82
Figure 6. Geologic map of the Keys View 7.5 minute quadrangle.....	83
Figure 7. Method for collecting samples and systematic evaluation of fabrics.....	85
Figure 8. Method for transposing structural information for petrographic analysis.....	86
Figure 9. Field photographs of Bighorn Sheeted Complex (BSC).....	87
Figure 10. Geologic map of the Keys View quadrangle showing the distribution of fabric types and intensities.....	88
Figure 11. Outcrop photographs of Bighorn sheeted complex (BSC) magmatic structures and fabrics.....	90
Figure 12. Summary of BSC fabrics.....	94
Figure 13. Field and outcrop photographs of Blue Cut granodiorite pluton.....	95
Figure 14. Map of Blue Cut granodiorite foliations.....	96
Figure 15. Map of Blue Cut granodiorite lineations.....	97
Figure 16. Field and outcrop photographs of Quail Mountain sheeted complex	98
Figure 17. Map of Quail Mountain sheeted complex (QMSC) foliations.....	102
Figure 18. Field and outcrop photographs of Stubbe Spring granite pluton (SS).....	103
Figure 19. Map of Stubbe Spring granite foliations.....	104

Figure 20. Map of Stubbe Spring granite lineations.....	105
Figure 21. Field photographs of Palms granite pluton.....	106
Figure 22. Outcrop photographs of the Palms granite.....	107
Figure 23. Map of Palms granite fabric.....	108
Figure 24. Summary of framework rock fabrics.....	111
Figure 25. Photomicrographs of quartz microstructures.....	112
Figure 26. Photomicrographs of plagioclase microstructures.....	115
Figure 27. Photomicrographs of potassium feldspar microstructures.....	122
Figure 28. Photomicrographs of biotite microstructures.....	125
Figure 29. Photomicrographs of hornblende microstructures.....	129
Figure 30. Photomicrographs of sphene microstructures.....	131
Figure 31. Thermal constraints using chessboard extinction.....	132

INTRODUCTION

Most orogens contain a protracted history of plutonism and deformation. Such records are difficult to fully unravel because the history is complex and/or incomplete and our understanding of the record is limited by the temporal and spatial resolutions of the analytical techniques we employ. Nevertheless, detailed geochronology and microstructural analyses allow us to see past some of these complexities, giving us a better understanding of the processes of crustal assembly and evolution. One direct approach to understanding this assembly and evolution is through the evaluation of fabrics and structures within plutons that have formed successively over a period that spans the evolution of an orogenic event. Because the ‘life’ of a single pluton is short (<1 My, Paterson and Tobisch, 1992; >10 My, Glazner et al., 2004) relative to the ‘life’ of an orogenic event (e.g. Laramide Orogeny 80-45 Ma), plutons are likely to record a ‘snapshot’ of the ambient physiochemical conditions present during their emplacement and cooling (Schofield and D’Lemos, 1998). Presuming that overprinting and metamorphism do not completely destroy this record, the evaluation of fabrics and structures developed within successively emplaced plutons can, therefore, be used to build a time-transgressive record of a long-lived orogenic event (Schofield and D’Lemos, 1998; Tribe and D’Lemos, 1996; Paterson and Tobisch, 1988; Miller and Paterson, 1994). Collectively, detailed geochronologic data and fabric observations for a time-transgressive sequence of plutons should therefore enable the reconstruction of time, temperature, and deformation (Ttd) conditions at the time of pluton emplacement within an actively deforming arc (Schofield and D’Lemos, 1998). This study uses such an approach to evaluate the

construction and subsequent deformation of a well-exposed, mid-crustal sheeted plutonic complex in southern California.

Within the North American Cordillera, sheeted plutons have been recognized throughout many of the Cretaceous and Paleogene magmatic arcs (Ingram and Hutton, 1994; Manduca et al., 1993; Miller and Paterson, 2001). Although sheeted intrusive complexes are becoming increasingly controversial in understanding large-scale plutonism throughout the crust, relatively few sheeted complexes have been described in detail compared to their more elliptical pluton counterparts (in map view). Detailed studies of sheeted complexes include: (1) the ‘Great Tonalite Sill’ in the Coastal Plutonic complex (Ingram and Hutton, 1994), (2) the Skagit Gneiss complex in the Cascades crystalline core of Washington (Paterson and Miller, 1998; Miller and Paterson, 2001), (3) the sheeted complexes along the western margin of the Idaho batholith (Manduca et al., 1993), (4) the sheeted complex within the central Peninsular Ranges batholith (Schmidt et al., 2002), and (5) the Bighorn Sheeted complex in the eastern Transverse Ranges of southern California (Barth et al., 2004) (Figure 1).

Previous studies have interpreted these sheeted complexes as: (1) the “plumbing” system of upper crustal magmatic systems (Paterson and Miller, 1998), (2) magmatism along preexisting faults or shear zones (Ingram and Hutton, 1994), and (3) magmatism along fundamental boundaries between accreted crustal fragments (Manduca et al., 1993). Despite varying interpretations, these sheeted complexes have several notable features in common, which include: (1) location within the central core of orogens, (2) compositional heterogeneity at different scales, (3) long-lived, sheet-like emplacement

geometries, and (4) variable deformation in the magmatic and solid-state, indicating the presence of a long-lived deviatoric stress.

In the eastern Transverse Ranges (ETR) of southern California, a 10x70 km zone of sheeted plutons has been recognized at the base of a tilted crustal section (Barth et al., 2004). Preliminary mapping of the tilted ETR crustal-section (Paterson et al., 2006) shows that upper crustal plutonism (0-15 km) is characterized by comparatively homogeneous discordant plutons that overlie heterogeneous mid-crustal sheeted plutons (15-20 km). Whereas the upper crust records a relatively brief interval of plutonism (ca. 79-75 Ma), the mid-crust records a history of plutonism that spans 83 ± 2 Ma to 74 ± 2 Ma (Wooden et al., 1994, 2001; Barth et al., 2004; Paterson et al., 2006). These ages also show that many of the mid-crustal plutons are synchronous with upper crustal plutons, indicating that both sheeted and discordant plutons were constructed and maintained at discrete crustal levels over an extended period of arc evolution. Compared to the weak magmatic fabrics that characterize the upper crustal plutons, the mid-crustal sheeted plutons show well-developed, gently to moderately dipping fabrics that are predominantly magmatic in character (Brown et al., 2006). Solid-state overprinting is widespread, but is generally concentrated in the younger, more felsic sheets (Brown et al., 2006). Additionally, the synchronous construction and maintenance of different pluton geometries at discrete crustal levels suggests the presence of a long-lived deviatoric stress within the mid-crustal levels of the tilted section.

This study evaluates the magmatic and solid-state fabrics within ETR sheeted plutons to better understand the long-lived deviatoric stresses within the tilted crustal section throughout its construction and evolution. More specifically, this study will use detailed

fabric observations from these sheeted plutons to reconstruct the temperature and deformation conditions at the time of pluton emplacement within the actively deforming continental arc of southern California in Late Cretaceous time.

GEOLOGIC SETTING

Tectonic Setting

The western margin of North America has experienced numerous physiographic changes throughout the course of geologic history (Ingersoll, 1997). Dickinson (1981) outlines four fundamental tectonic configurations that illustrate these physiographic changes: Atlantic-type, Japanese-type, Andean-type, and Californian-type (Figure 2). Of direct relevance to this study is the Andean-type tectonic configuration (Dickinson, 1981). During the middle Triassic, subduction was initiated along the western margin of North America, forming an Andean-type arc-trench system that consumed oceanic lithosphere to the west (Ingersoll, 1997; Dickinson, 1981, 2004). This Andean-type arc-trench system not only contributed both plutonic and volcanic materials, but also brought about punctuated deformation that lasted throughout the Mesozoic (Ingersoll, 1997; Dickinson, 1981, 2004; Livaccari, 1991).

The principal record of this arc-trench system's magmatic history is a discontinuous alignment of deeply eroded Mesozoic plutons and batholiths that extend the full length of the Cordilleran orogen (Dickinson, 2004). Within southern California, magmatism was punctuated, forming three distinct pulses that lasted throughout the Mesozoic (Barth et al., 2004). Arc magmatism began in the Triassic with the emplacement of intrusions between 250-207 Ma (Barth et al., 2004). After a magmatic lull (about 40 My), magmatism was initiated again, producing Jurassic intrusions emplaced between 165 and 143 Ma (Barth et al., 2004). Following a second magmatic lull (about 45 My), magmatism was initiated ca. 95 Ma, reaching its peak between 82-72 Ma (Barth et al., 2004).

Deformation along the western margin of the U.S. during the Cretaceous has been attributed to two primary orogenic events: the Sevier and the Laramide orogenies (Armstrong, 1968). The Sevier orogeny (ca. 120-80 Ma) is characterized by the development of thin-skinned folding and thrusting (contraction) inland from the ancient continental margin within the modern-day states of Utah, Nevada, Idaho, and Wyoming (Livaccari, 1991; Heller et al., 1986; Armstrong, 1968). The orogenic structures created by the Sevier orogeny are distinctly different in age and represent a drastically different style of crustal deformation and tectonic regime than that of the younger Laramide orogeny (Armstrong, 1968) (Figure 3). By ca. 80 Ma, the locus of deformation along the western margin had shifted further inland, forming thick-skinned, basement-cored uplifts that extended as far east as the modern-day states of Colorado and Wyoming (Livaccari, 1991; Dumitru et al., 1991; Dickinson and Snyder, 1978; Maxson and Tikoff, 1996). This change in deformation style is referred to as the Laramide orogeny (80-45 Ma) (Livaccari, 1991; Dumitru et al., 1991; Dickinson and Snyder, 1978). The shift from thin-skinned (Sevier-style) to thick-skinned (Laramide-style) deformation has been attributed to the change in the angle of subduction (steep to shallow) and the rapid westward movements of the North American plate (Dickinson and Snyder, 1978; Maxson and Tikoff, 1996; Barth and Schneiderman, 1996) (Figure 3). In addition to crustal buckling and basement-cored uplifts, the Laramide orogeny is attributed to the cessation of arc magmatism (Paleogene magmatic lull) (Dickinson and Snyder, 1978).

Geologic Setting of Study Area

Located within San Bernardino and Riverside counties in southern California, the eastern Transverse Ranges (ETR) is the farthest eastern extent of a large chain of northwest-southeast trending mountain belts that are nearly perpendicular to the north-south physiographic grain of California (Powell, 1981) (Figure 4). Collectively, the ETR consists of a series of smaller ranges: the Little San Bernardino, Pinto, Hexie, Cottonwood, and Eagle Mountains (see Powell, 1981; Barth et al., 2004). These ranges are structurally controlled and bounded by the San Andreas Fault (SAF) to the west and several east-west trending, sinistral faults: (starting north and moving south) the Pinto Mountain Fault (PM), the Blue Cut Fault (BC), and the Chiriaco fault (CF), respectively (Powell, 1981; Carter et al., 1987; Crowell, 1992) (Figure 5).

Recent aluminum-in-hornblende barometry of Mesozoic plutonic rocks throughout the ETR indicates that the ETR constitutes a tilted crustal section through the Mesozoic arc of southern California to paleodepths ca. 22 km (Barth et al., 2004; Needy et al., 2006). Barth et al. (2004) argued that differential Laramide uplift generated greater exhumation along the western portions of the ETR, exposing the deeper levels of the Mesozoic orogen. However, relatively little uplift occurred along the eastern portion of the ETR (Barth et al., 2004).

Whereas the shallow, eastern and central parts of the ETR are dominated by comparatively homogeneous Mesozoic plutons that intrude Proterozoic basement and Mesozoic cover rocks, the deeper, western exposures are dominated by heterogeneous sheeted complexes of broadly Mesozoic age (Barth et al., 2004; Brown et al., 2006; Palmer et al., 2006; Wooden et al., 1994, 2001) (Figure 5). These mid-crustal sheeted

pluton exposures are the focus of the present study and can be found within the Keys View quadrangle (Figure 6).

Geology of the Little San Bernardino Mountains

Along the western margin of the ETR, the relatively homogeneous plutons and Proterozoic framework rocks that characterize the upper levels of the crustal section give way abruptly to expose more elongate plutons with evidence of internal sheeting and a heterogeneous zone of sheeted plutons in the Little San Bernardino Mountains (LSBM). The rocks exposed here were originally mapped as Precambrian(?) gneissic rocks, which was later interpreted as a broad Mesozoic gneissic complex with pervasive brittle deformation (Powell, 1981, 1993). These rocks were originally assigned to the western plutonic belt of the broad Mesozoic plutonic arc of southern California and were originally described as being either: (1) biotite-hornblende bearing quartz diorite, tonalite, and granodiorites that are intensely foliated and locally mylonitic or (2) gneissic quartz diorite and tonalite (Powell, 1993). Powell (1981) also described these exposures as being part of a zone of complexly brecciated and cataclasized Mesozoic rocks. Although recent mapping (Paterson et al., 2006; this study) agrees with the compositional heterogeneity described by Powell (1981, 1993), it is emphasized here that igneous textures and magmatic fabrics are widespread and are well preserved at the outcrop scale.

METHODS

Sample Collection and Fabric Mapping

This research uses three suites of samples collected by Dr. Joe Wooden (Stanford), Dr. Andrew P. Barth (IUPUI), and Kenneth Brown (IUPUI). All samples within each suite were located using a handheld GPS receiver. The JW suite (1998 to 2001) was collected by Dr. Joe Wooden for reconnaissance geochronology and geochemistry. Although each sample in the JW suite was uniquely located using a GPS receiver, the orientation of the JW samples with respect to the outcrop was not collected. Therefore, there is limited structural information associated with this suite.

Guided by previous mapping at the 1:24,000 scale (Paterson et al., 2006), the other two suites were collected by Dr. Andrew Barth (03 and 04 samples) and Kenneth Brown (all other samples) to capture the compositional heterogeneity of exposed sheeted plutons (two-mica, granites to quartz diorite) within the Bighorn sheeted complex (BSC). Because the BSC contains >100 sheeted plutons within the study area, samples were primarily collected from the volumetrically dominant sheets. Fresh samples were collected from well-exposed outcrops attached to the lithosphere. This approach allows the collector to link observations about the collected sample back to the outcrop, placing the sample into the regional context of the study area (Figure 7). At each outcrop, the dominant fabric elements were identified and recorded using standard structural geology techniques: strike/dip of foliation and trend/plunge of lineation. At outcrops where samples were collected, the structural information was transposed on its corresponding sample for later petrographic analysis (Figure 8). Samples were given a sample number, a mark or symbol that designated the top of the sample, and the transposed structural

information. A majority of the outcrop measurements used in this study were collected and provided by Dr. Scott Paterson (University of Southern California). Additional outcrop measurements were provided by Dr. Andrew P. Barth (IUPUI).

The type and intensity of developed fabrics were also recorded at each outcrop. A list of criteria used to define the fabric type is presented in Table 1. Fabric type was categorized as magmatic (M), solid-state (S), or a combination of both (MS or SM; the first letter denotes the stronger of the two fabrics). The intensity was defined by the following semi-quantitative scale: 1 = no observed fabric, 2 = weak fabric, and 3 = strong fabric. This semi-quantitative scale is similar to the scale used by Dr. Scott Paterson and his students. The scale used by Dr. Scott Paterson is defined by the following semi-quantitative scale: 1 = no observed fabric, 2 = weak fabric, very difficult to measure, 3 = strong crystal alignment, some layering, 4 = very strong mineral alignment, throughgoing layering (mylonite if subsolidus), and 5 = intense alignment and layering (ultramylonite if subsolidus) (see Figure 8 in Miller and Paterson, 2001). The scale used in this study, however, does not use the intensities >3 from Dr. Paterson's scale, as these values are typically reserved for mylonitized and ultramylonitized rocks deformed in the solid-state (Paterson, personal communication).

Petrographic Methods

Thin sections for each sample were made primarily to (1) evaluate the primary structures observed at the outcrop scale, (2) evaluate the microstructures and textures of each fabric-forming phase, and (3) estimate temperature conditions of deformation. Because the LSBM was originally described as a gneissic complex that is locally

mylonitic, all thin sections were created from samples that were cut parallel to any lineation and perpendicular to any foliation (Figure 8). This is the best orientation to determine the sense of shear (kinematics) in a sheared or mylonitized rock (Simpson, 1985; Passchier and Trouw, 2006). The modal mineralogy, grain size, and dominant fabric-forming phases were determined for each thin section using a standard binocular petrographic microscope with a 2.5x magnification (Leitz Laborlux 11 POL S polarizing microscope).

Thin section description is essential because some of the samples are too fine-grained to determine which minerals are forming the observed fabric at the outcrop scale. Description of both the outcrop and thin section scale was used to document relationships between primary structures observed at the outcrop scale and the phases defining that structure. After these preliminary observations were made, each phase was evaluated for characteristic microstructures used to estimate the temperature of deformation and classify the fabric type (Table 2). Discussions with Dr. Ron Vernon, Dr. Jeffrey Swope, Dr. Scott Patterson, Dr. Basil Tikoff, and Dr. Jan Tullis helped identify many of these characteristic microstructures and textures.

Finally, after each thin section's characteristic microstructures are evaluated, the thin section, and therefore the sample, is assigned a dominant fabric type: magmatic (M), magmatic/solid-state (MS), solid-state/magmatic (SM), and solid-state (S). Samples that are dominated by magmatic microstructures but show some solid-state overprinting were assigned a magmatic/solid-state (MS) fabric type. Alternatively, samples dominated by solid-state microstructures with some remaining magmatic microstructures were assigned a solid-state/ magmatic (SM) fabric type.

RESULTS

Presenting my hand specimen macrostructure results (Tables 3 and 4) and microstructure results (Tables 5-9) in a regional context is essential to understanding the significance of the observed fabrics. This necessitates including regional field data provided by Dr. Andrew Barth and Dr. Scott Paterson. Therefore, the reader should bear in mind that results of my study are those observations referring to the macro- and microstructures detailed in Tables 3-9. An additional contribution of my work is the compilation and synthesis of field observations from Dr. Andrew Barth and Dr. Scott Paterson into regional maps (see Appendices for details and credit).

MACROSCOPIC RESULTS

Geologic Overview of Keys View Quadrangle

The geologic units within the Keys View quadrangle (Figure 6) can be divided into three broad categories: sheeted plutons, discordant plutons, and older framework rocks. Of particular importance to this study are the two general types of plutons: roughly elliptical plutons (in map view) that discordantly cut the host framework rocks and their pre-existing structures; and gently dipping sheeted plutons that are generally concordant to structures in the host framework rocks. In the following sections, the similarities and differences of these three broad categories are emphasized through a systematic description of the macroscopic fabrics and structures developed within each rock unit.

Bighorn Sheeted Complex

Petrology

Within the Keys View quadrangle, the Bighorn sheeted complex (BSC) is composed of 100's of individual sheets, ranging in age, composition, texture, and thickness (meter to decimeter thick) (Figure 9A and B). Recent geochronology yielded a wide distribution of U-Pb zircon ages, spanning from ca. 83 ± 2 Ma to 74 ± 2 Ma (Barth et al., 2004; Paterson et al., 2006). The sheeted plutons exhibit a broad compositional spectrum, but are volumetrically dominated by tonalite, granodiorite, and two-mica, garnet granite intrusions (photo inserts in Figure 9A) (Table 3). Additional compositions present are hornblendite (cumulates?), quartz diorite, and porphyritic granite. Grain size is also highly variable, ranging from aplitic to pegmatitic. Although the intrusive relationships are complicated, the relative emplacement sequence is from mafic to felsic, as mafic sheets are generally intruded by more felsic sheets.

Tonalite and granodiorite sheets are volumetrically the most significant bodies within the BSC. Whereas the tonalite sheets are generally fine-grained (average 1-4 mm), the granodiorite sheets generally display a larger range of grain sizes (average 1-8 mm) (Table 3). The dominant tonalite phases include plagioclase, biotite, hornblende, quartz, sphene, and minor amounts of potassium feldspar. The typical granodiorite composition includes quartz, plagioclase, potassium feldspar, biotite, sphene, and hornblende. Although hornblende is present in both compositions, it is not as ubiquitous as biotite. No tonalite or granodiorite sheet has been observed that contains only hornblende; biotite is always present in these intermediate compositions even in small amounts.

Additionally, euhedral epidote and allanite crystals are present within some of the tonalite and granodiorite sheets.

Although tonalite and granodiorite dominate the BSC, more felsic granite compositions are also present. These granite sheets also range widely in composition and texture. Compositionally, these granites range from peraluminous (two-mica, garnet granites) to metaluminous (biotite granites) (Brown et al., 2006, 2007; Palmer et al., 2006; Wiegand et al., 2007). The mineral assemblage for an average granitic sheet includes quartz, plagioclase, potassium feldspar, and biotite. Additional minerals present include sphene, muscovite, and garnet. With respect to texture, the granitic sheets have a wider range of grain sizes than the tonalitic and granodioritic sheets, and range from aplitic (<1 mm) to pegmatitic (>10 mm) (Table 3).

Macroscopic Fabrics and Structures

The best-developed macroscopic fabrics and structures within the BSC are magmatic (Figure 10A). Although solid-state structures and fabrics exist, they are not as pervasive. Internal structures include a range of magmatic fabrics and textures (foliations, lineations, magmatic folds, layering, and schlieren), widespread inclusions (enclaves, xenoliths, and rafts), and a complex array of cross-cutting dikes and apophyses (Figure 11A-K).

Whereas exposed sheets north of the Blue Cut fault and its associated faults have a consistent northeast dip, the sheets south of the Blue Cut fault have a more consistent southwest dip. Therefore, the BSC has been divided into two domains (Figure 12, Domain I and II), to reflect the two opposing geometries. This study will only focus on the sheeted plutons exposed in Domain I, as rotation and translation of fabrics may have

occurred because of displacement along the Blue Cut fault. The relationship between Domains I and II are uncertain at this time. Nevertheless, because this different geometry may be an important feature in other quadrangles, it is important to note that the foliations within these two domains define a large antiformal fold with a hinge line that trends approximately northwest; Domain I dips northeast and Domain II dips southwest, defining the limbs of the antiformal fold structure.

Within Domain I of the BSC, the exposed sheets have a pervasive northwest-southeast magmatic foliation that dips gently northeast towards and beneath the larger discordant plutons that characterize the upper crustal portions of the ETR ($n = 30$) (Figure 12; Appendix A). The dip is relatively gentle to moderate ($15\text{-}45^\circ$) in the northwest portion (along the Stubbe Spring granite contact) and becomes steeper to the southeast ($46\text{-}85^\circ$) (along the Blue Cut granodiorite contact). Measured solid-state foliations share the same orientation, but are far less abundant than the magmatic foliations ($n = 12$) (Figure 12; Appendix A).

The magmatic foliations within the tonalitic and granodioritic sheets are defined by: (1) an increase in modal biotite and hornblende, forming mats/clots of igneous grains (Figure 11C); (2) the orientation of highly-elongate, mafic inclusions and enclaves (Figure 11C); (3) the formation of laterally continuous, compositional layers (Figure 11E); or (4) a combination of the above. Similarly, the magmatic foliations within the granitic sheets are also defined by the same type of structures, but are usually accompanied by the alignment of euhedral, feldspar phenocrysts (Figure 11F and G) and schlieren layering (Figure 11A and B). In all compositions, these magmatic foliations are generally parallel to sheet contacts. This overall geometry is parallel to foliations

observed within the surrounding Stubbe Spring granite, the Blue Cut granodiorite, and the host framework rocks (Figure 12). At the outcrop scale, however, foliations are more variable and, in some places, have orientations that cut internal sheeting and sheet contacts. Additionally, the highest fabric intensities are generally found along the eastern contact of the BSC; weaker fabrics are generally found within the central portions of the BSC (Figure 10B).

Although there are relatively few observed lineations within Domain I ($n_{\text{total}} = 7$; Figure 12; Appendix A), a comparison of lineation type reveals that both magmatic and solid-state lineations share similar orientations (trend southeast/ northwest with moderate southeast plunges) (Figure 12). These lineations have shallow pitches to the dominant northwest-southeast magmatic foliation. Lineations observed within tonalitic and granodioritic compositions are typically defined by aligned hornblende, plagioclase, and elongate mats/clots of biotite; lineations within granitic sheets are defined by aligned feldspars.

In addition to magmatic fabrics and textures, the BSC also displays a wide array of inclusions. These inclusions include mafic enclaves (magma globules), xenoliths (rotated blocks), and rafts (nonrotated blocks) of surrounding framework rocks. Mafic enclaves appear to be the most abundant inclusion type, ranging in size from 1 cm to >2 m (Figure 11C-E) and exhibiting predominantly elongate, flattened shapes in three dimensions. In general, these mafic enclaves are more mafic than their surrounding hosts, containing as much as 75% hornblende and 15% biotite. With respect to texture, these enclaves are fine-grained (1-4 mm). Interestingly, many of these inclusions are aligned parallel to the host rock fabric (Figure 11C) and contain internal magmatic fabrics that are parallel/

subparallel to the magmatic fabrics in the host granitoid (Figure 11D and E). Also present are xenoliths (rotated blocks) and rafts (nonrotated blocks) of orthogneiss and paragneiss (Proterozoic?) (Figure 11I).

The northeast dipping foliation is extensively cut by well-preserved aplitic and pegmatitic dikes, which often do not contain internal fabrics or show significant solid-state deformation. However, where internal fabrics are present, they are generally magmatic. Although there are many types of dikes within the BSC, most of them range in thickness from <1 cm to 3 m and are generally granitic in composition (Figure 11C, H, J, and K). Some of the dikes have been folded, displaying a range of geometries, wavelengths, and interlimb angles. A few dikes, particularly those which cut more mafic compositions, display boudinage and generate significant deflections (shearing?) in the host fabric (Figure 11J and K).

Blue Cut Granodiorite Pluton

Petrology

The Blue Cut granodiorite (BC) (82.1 ± 1.8 Ma; Barth et al., 2004; Paterson et al., 2006) is an elongate pluton (aspect ratio of ~3:1) (Figure 6) that contains evidence of internal sheeting, defined by subtle compositional and textural differences. Although coarse and fine-grained sheets have been observed, the pluton is predominantly a medium-grained, biotite-hornblende granodiorite that is locally seriate to porphyritic (Table 4). The dominant phases for all the internal sheets observed for this study include plagioclase, hornblende, biotite, quartz, sphene, and alkali feldspars. At the outcrop scale, hornblende, biotite, and sphene are ubiquitous in all of the exposed sheets, ranging

in size from 1-6 mm (Figure 13A-D). These mafic minerals, with the exception of sphene, often form mats/clots that define the observed foliations and lineations (Figure 13B-D). Sphene grains, on the other hand, often display perfect monoclinic crystal faces and are more homogeneously dispersed. Alkali feldspar phenocrysts are also variable in size ranging from 1-20 mm. Additionally, allanite and epidote are also present within many of the sheets.

Macroscopic Fabrics and Structures

The contact along the eastern margin of the BC is predominantly a steep dipping contact that discordantly cuts the metamorphic foliations within the framework rocks of the Lost Horse Mountains to the northeast (Barth, personal communication) (Figure 14). This contact also contains several sharp bends where the fabrics in the gneisses of the Lost Horse Mountains become parallel to the fabric within the granodiorite, forming local zones of parallelism (Figure 14). Within the pluton interior and along its margin, xenoliths (rotated host rock) and rafts (nonrotated host rock) of framework rocks are present and vary in size (Paterson, personal communication). Some of the larger, more impressive inclusions (rafts or stopped blocks?) can be seen in the southwest portion of the pluton (Figure 14).

Similar to the Bighorn sheeted complex (BSC), the best-developed macroscopic fabrics and structures within in the BC are magmatic (Figure 10A; Figure 13A-D). Relative to the BSC, the BC contains less solid-state deformation. This subsolidus deformation is found locally along the western and southwestern portions of the pluton where the granodiorite is intruded by a variety of igneous bodies similar in composition

to those exposed in the BSC and the Stubbe Spring pluton (Figure 10A). The location of these subsolidus fabrics also correspond to the locations of the large inclusions discussed above.

The BC is dominated by a weak magmatic fabric that varies spatially with respect to intensity (Figure 10A and B). In the northwest portion, the pluton contains a consistent weak magmatic fabric, as observed in both hand-specimen and outcrop. Within the central portion, the magmatic intensity becomes locally very strong (Figure 10B). Along its eastern contact, there are a few locations where the intensity increases to a 3 on the semi-quantitative scale, which is consistent with an increase in fabric intensity within the central portion of the pluton. Along its western contact, however, there does not appear to be a significant increase in fabric intensity.

The magmatic foliations within the BC are defined by: (1) an increase in the modal concentration of biotite, hornblende, and sphene and (2) mats/clots of these primary mafic phases (Figure 13B and C). Whereas the magmatic foliations along the western and central portions of the pluton have a northwest-southeast strike and gentle northeast dip, the foliations along the eastern contact have a northwest-southeast strike and southwest dip (Figure 14). The dip angle along the eastern margin is typically gentle, but increases locally along the contact. This increase in dip angle is associated with an increase in fabric intensity (compare Figure 10B and 14). Regionally, these well-developed magmatic foliations define a rather open synformal fold pattern that strikes roughly northwest-southeast (Figure 14), extending nearly the full length of the pluton and paralleling its margins. Interestingly, the most intense magmatic fabrics are found near this fold pattern (compare Figure 10B and 14). Additionally, the measured solid-

state foliations within the pluton have the same orientation as the magmatic foliations of the western and central portions (northwest-southeast strike and northeast dip) (Figure 14; Appendix B).

The lineations within the pluton are less abundant and less consistent in orientation than the magmatic foliations (Figure 15). Overall, the lineations within the BC are predominantly magmatic; solid-state lineations are present but found only within the central portion of the pluton (Figure 15; Appendix B). In the western and southwestern portions of the pluton, the magmatic lineations generally trend northeast, showing a wide range of plunge angles (3-55°) (Figure 15). These lineations are nearly perpendicular to the strike of the magmatic foliations within this portion of the pluton (compare Figures 14 and 15). However, along the eastern contact, the magmatic lineations trend northwest-southeast, paralleling the pluton margin and the hinge line of the synformal fold pattern. These lineations are subparallel to the strike of the magmatic foliation along the eastern contact of the pluton (compare Figures 14 and 15).

Quail Mountain Sheeted Complex

Petrology

In many ways, the Quail Mountain sheeted complex (QMSC) is very similar to the Bighorn sheeted complex (BSC). More specifically, the sheeted plutons within both complexes are heterogeneous with respect to composition, texture, and thickness (meter to decimeter thick) (Figure 16A-K). Compositionally, the QMSC exhibits a broad compositional spectrum volumetrically dominated by granodioritic, tonalitic, and granitic intrusions (photo inserts of Figure 16A). Based on reconnaissance field investigations,

however, the QMSC appears to have more intermediate and felsic sheets than the BSC. Grain size is also variable, ranging from fine-grained to pegmatitic. Recent geochronology of a granodiorite from this sheeted complex yielded a U-Pb zircon ages of 81.1 ± 1.2 Ma (Barth et al., 2004; Paterson et al., 2006). The relative emplacement sequence in the QMSC is from mafic to felsic, as mafic sheets are generally intruded by felsic sheets. This is consistent with that observed for the BSC.

Based on field observations, granodiorite sheets are volumetrically the most significant bodies within the QMSC, displaying a range of compositions and textures (Figure 16C, D, F, H, and I). The average granodiorite composition includes quartz, plagioclase, potassium feldspar, biotite, hornblende, and sphene. The granodiorite sheets are equally diverse with respect to texture, ranging from fine-grained, biotite granodiorite (1-2 mm) to coarse-grained, hornblende-biotite granodiorite (5-10 mm) (Table 3).

Although granodiorite sheets dominate the QMSC, more felsic and more mafic compositions are also present. Compositionally, the granitic sheets range from two-mica, garnet granites to biotite granites. The mineral assemblage for an average granitic sheet includes quartz, potassium feldspar, plagioclase, and biotite. Additional minerals present include sphene, muscovite, and garnet. With respect to texture, the granitic sheets have a wider range of grain sizes than the tonalitic and granodioritic sheets, and range from aplitic (<1 mm) to pegmatitic (>10 mm) (Figure 16E). The tonalitic sheets, however, are more homogeneous with respect to composition and texture than the granitic and granodioritic sheets. The typical mineral assemblage for an average tonalite sheet includes plagioclase, biotite, hornblende, quartz, and minor amounts of alkali feldspar.

The tonalitic sheets are generally fine-grained (1-2 mm) (photo insert in Figure 16A; Table 3).

Macroscopic Fabrics and Structures

The best-developed macroscopic fabrics and structures within in the QMSC are magmatic (Figure 10A; Figure 16A-K). Similar to the BSC, these well-preserved internal structures include a range of magmatic fabrics and textures (foliations, lineations, magmatic folds, layering, and schlieren), widespread inclusions (enclaves and xenoliths), and a complex array of cross-cutting dikes.

The QMSC is dominated by a pervasive northwest-southeast magmatic foliation that dips moderately northeast beneath the larger discordant plutons ($n = 35$) (Figure 17; Appendix C). A comparison of both magmatic and solid-state foliations shows that both types share this northwest-southeast orientation. There are, however, some southwest dipping foliations present. These southwest dipping foliations, though few, have similar orientations for both magmatic and solid-state foliations (Figure 17). The significance of these southwest dipping foliations is uncertain at this time.

The magmatic foliations within the volumetrically dominant granodioritic sheets are defined by: (1) an increase in modal biotite and hornblende, forming mats/clots of igneous grains (Figure 16D) and/ or (2) the orientation of highly-elongate, mafic inclusions and enclaves (Figure 16F). Similarly, the magmatic foliations within the granitic and tonalitic sheets are also defined by the same type of structures (Figure 16E and G), but are usually accompanied by the alignment of euhedral, feldspar phenocrysts and schlieren layering in the granitic compositions.

Although foliations are widespread, lineations are also present within the QMSC. However, at this time, the number and distribution of these fabric measurements are insufficient to evaluate their role in this sheeted complex. Where present, the lineations within the tonalitic and granodioritic sheets are typically defined by aligned hornblende and mats/clots of biotite (Figure 16H); within the granitic bodies, the lineations are defined by aligned feldspars.

Similar to the BSC, the magmatic foliations within the QMSC are generally parallel to sheet contacts. These foliations also become more variable and, in some places, cut internal sheeting. Along the southwestern contact, the magmatic foliations are generally parallel to foliations within the Stubbe Spring granite and the host framework rocks (Figure 17). Towards the northeastern contact, however, the foliations often cut the internal fabrics of the host rocks. Interestingly, within the Quail Mountain and Juniper Flats area, the magmatic foliations become parallel to the host framework rocks immediately to the west, striking approximately northeast-southwest and dipping moderately to the southeast (Figure 17). Further to the north in the Johnny Lang Canyon area, the foliations exhibit a very consistent northwest-southeast strike and northeast dip, which is similar to the rest of the QMSC to the southeast (Figure 17). The orientations in this northern area are parallel to the hinges of the kilometer-scale folds observed within the framework rocks to the east (see framework rock macroscopic fabrics and structures). Based on the measurements used in this study, there does not appear to be any spatial relationships with respect to fabric type or intensity within this sheeted complex (Figure 10A and B).

In addition to magmatic fabrics and textures, the QMSC also displays a wide array of inclusions. These inclusions include mafic enclaves (magma globules) and xenoliths (rotated blocks) of surrounding framework rocks. Similar to the BSC, mafic enclaves appear to be the most abundant inclusion type, ranging in size from 1 cm to >1 m (Figure 16F,G, I, J, and K) and exhibiting predominantly elongate, flattened shapes in three dimensions. With respect to texture, these enclaves are generally fine-grained (1-4 mm). Many of these inclusions are aligned parallel to the host rock fabric and contain internal magmatic fabrics that are parallel/ subparallel to the magmatic fabrics in the host granitoid (Figure 16F, G, I, J, and K).

Similar to the BSC, the northeast dipping foliation in the QMSC is extensively cut by well-preserved aplitic and pegmatitic dikes, which often do not contain internal fabrics or show significant solid-state deformation. These cross-cutting dikes range in thickness from <1 cm to 3 m and are generally granitic in composition (Figure 16I and K). Some of the dikes have been folded with the host granitoid, displaying a range of geometries, wavelengths, and interlimb angles (Figure 16K).

Stubbe Spring Granite Pluton

Petrology

Similar to the Blue Cut granodiorite, the Stubbe Spring granite (SS) (76 ± 4 Ma; Barth et al., 2004; Paterson et al., 2006) is an elongate pluton (aspect ratio of ~10:1) (Figure 6) that contains evidence of internal sheeting, defined by subtle compositional and textural differences. Although coarser and finer-grained sheets have been observed, the pluton is predominantly a medium-grained, biotite granite that is locally seriate to

porphyritic (Table 4). Additional compositions present include two-mica, garnet granite and biotite granodiorite. The dominant phases for all the internal sheets observed for this study include quartz, potassium feldspar, plagioclase, and biotite. Additional minerals present include muscovite, garnet, and sphene. With respect to texture, the exposed sheets display a wide range of grain sizes, ranging from fine-grained (1-2 mm) to coarse-grained (5-7 mm) (Table 3).

Macroscopic Fabrics and Structures

Relative to all the other sheeted plutons previously described, the SS granite pluton contains the most solid-state overprinting (Figure 10A). This overprinting is typically defined by ribbon-shaped aggregates of quartz, biotite, and muscovite that anastomose stronger euhedral to subhedral alkali feldspar grains. At the outcrop and hand-specimen scale, this overprinting is relatively weak, rarely forming a penetrative fabric. Spatially, this subsolidus overprinting is widespread, spanning the entire length of the pluton (Figure 10A).

Despite the widespread occurrence of subsolidus overprinting, magmatic foliations are the dominant fabrics within the pluton (Appendix D). These magmatic foliations are defined by (1) an increase in modal biotite, forming mats/clots of igneous grains (Figure 18B-D); (2) the formation of laterally continuous, compositional layers (Figure 18C and D); (3) schlieren layering; and (4) the alignment of euhedral to subhedral, feldspar phenocrysts. These magmatic foliations are generally parallel to sheet contacts. This overall geometry is parallel to foliations observed within all the surrounding igneous and metamorphic bodies (Figure 19). At the outcrop scale, however, foliations are variable

and, in some places, have orientations that cut internal sheeting and sheet contacts (northwest corner of map in Figure 19). Additionally, the highest magmatic fabric intensities are generally found within the central portions of the pluton; weaker fabrics are generally found along the margin.

Although there are relatively few observed lineations within this pluton ($n_{\text{total}} = 9$; Figure 20; Appendix D), a comparison of lineation type reveals that both magmatic and solid-state lineations share similar east-west trending orientations with moderate to steep plunge angles (Figure 12). Both types of lineations have steep pitches to the dominant northwest-southeast magmatic foliation. Despite the limited spatial distribution of lineation measurements, it appears that the southeast portion is dominated by magmatic lineations, whereas the eastern contact contains more solid-state lineations. However, more measurements are needed to evaluate the current lineation distributions.

Palms Granite Pluton

Petrology

Although domains containing garnet and muscovite occur locally, the Late Cretaceous (77.2 ± 0.6 Ma, Barth et al., 2004; Paterson et al., 2006) Palms granite is predominantly an equigranular (locally seriate), medium to coarse-grained, biotite granite. At the outcrop scale, potassium feldspar, quartz, and plagioclase are ubiquitous, ranging in size from 4-7 mm. Biotite ranges in size from 3-5 mm and is homogeneously dispersed throughout the body with the exception of where weak fabrics are formed.

Macroscopic Fabrics and Structures

The Palms granite is the dominant discordant pluton in the Keys View quadrangle, where approximately 5 by 8 km is exposed in map view (Figure 6). Along the eastern margin of the pluton, the intrusive contact is predominantly a steep, northeast to east dipping contact that cuts the metamorphic layering and dominant foliations within the surrounding framework rocks (Figure 21A and B). Although the contact is predominantly discordant, locations have been observed where the fabrics within the older framework rocks become subparallel, forming a relatively concordant contact (see Domain I in Figure 24). Within the pluton interior and along its margin, xenoliths (rotated host rock) and rafts (non-rotated host rock) of framework rocks are observed and vary in size from >10 cm to >10 m (Figure 22A).

The macroscopic fabrics within the pluton are dominated by weak magmatic fabrics, ranging from 1 to 2 on the semi-quantitative scale (Figure 10A and B; Appendix E). Because fabrics are only observed locally, the fabrics do not appear to change intensities from the pluton interior to its margins. These weak fabrics, where observed, are defined by an increase in the modal concentration of biotite, forming schlieren layering and weak foliations (Figure 22B and D). Isolated elongate, mafic enclaves are also present and help define the weak fabric. The weakly-defined biotite schlieren and foliations are also occasionally accompanied by aligned feldspars. No pervasive mineral lineations were observed within this pluton. Additionally, quartz grains tend to form equigranular pools rather than elongate quartz ribbons. Distinctly ribbon-shaped quartz aggregates have not been observed at the outcrop scale.

The fabric orientations within the pluton are variable, but are dominated by magmatic foliations (Figure 23A). These foliations have been divided spatially into two areas (northwest and southeast) because of differences in their orientations. These two areas are separated by a blue dotted line in Figure 23A-C. Interestingly, the line that separates these two areas also corresponds to a boundary that can not only be seen from satellite imagery, but also within the field (blue dotted line in Figure 23B and C). At this time, the origin and significance of this boundary is uncertain, however, because of the differences in geometry across this boundary, a structural origin is plausible.

Within the northwestern portion of the pluton (JLC area) (north of the boundary), the foliations are subhorizontal to gently dipping ($n = 9$) (average dip = 22°) (Figure 23A). At this time, no measurements have been recorded with dip angles $>45^\circ$. Along the western contact, these foliations are margin-parallel, appearing to wrap around the host framework rocks. Immediately to the east of this western contact, the fabrics cut the margin-parallel foliations and are oriented approximately east-west. Towards the southeast (below the boundary), the foliations are more variable ($n = 27$) (Figure 23A). Although shallow to moderately dipping foliations have been observed in this area ($11-40^\circ$, average dip = 22° , $n = 11$), an equal proportion of the foliations have steeper dip angles ($35-89^\circ$, average dip = 45° , $n = 16$). Interestingly, the foliations within this southwest portion also have a more consistent northwest-southeast strike and northeast dip than the northwestern portion of the pluton (Figure 23A). Additionally, the foliations along the southeastern contact are nearly parallel to the margin of the pluton, displaying a range of dip angles.

Proterozoic Framework Rocks

Petrology

Based on reconnaissance field work, the four types of older framework rocks within the study area include amphibolite, biotite gneiss, granitic gneiss, and muscovite gneiss (Figure 6). Although four types are present, this study will focus only on the biotite gneiss unit and its structures, as these gneisses are volumetrically the most significant rocks with the study area. These biotite gneisses are Proterozoic in age (Barth, personal communication).

The dominant gneiss within the Lost Horse Mountains (Domains II and III; Figure 24) is a medium to coarse-grained, compositionally layered, biotite gneiss that contains quartz, plagioclase, potassium feldspar, biotite, muscovite, sillimanite, and minor andalusite. Garnet has also been observed, but only locally along the Palms pluton and Blue Cut granodiorite contacts, forming what appears to be a weak thermal aureole. Alternatively, in the Johnny Lang Canyon (JLC) area (Domain I) to the northwest, these gneisses are mineralogically different, where they contain ubiquitous quartz, biotite, plagioclase, garnet, sillimanite, cordierite, and minor orthopyroxene. Interestingly, no muscovite or andalusite has been observed in these western rocks, indicating the presence of an isograd defined by a regional change in modal mineralogy. The change in mineralogy between the two areas is consistent with granulite facies assemblages to the west and amphibolite facies to the east.

Macroscopic Fabrics and Structures

The foliations within both the Johnny Lang Canyon area and the Lost Horse Mountains are generally defined by (1) gneissic layering of nearly parallel to anastomosing monomineralic bands and (2) the preferred planar orientations of platy minerals (biotite to the west; biotite and muscovite to the east). Migmatites and complex migmatitic folding are also present. The lineations are generally defined by (1) biotite streak lineations and (2) rods of quartz and alkali feldspar aggregates.

Although the exposed biotite gneisses are compositionally similar, they have been divided into three domains based on the orientations of their structures and fabrics (Figure 24). The following sections are a broad description of the dominant fabric patterns and structures observed within these three domains.

Domain I: Western Gneisses

Within the northwestern portion of Domain I, the fabrics within the gneisses are truncated by the moderately east dipping Quail Mountain sheeted complex to the west. Along this western contact, the foliations dip steeply to the west, exhibiting a range of dip angles (50-80°). Within a kilometer of the western contact, the foliations dip towards the east and become progressively shallower towards the eastern contact (Figure 24). Closer to the eastern contact, however, the foliations change dip direction once again, forming a moderately west dipping foliation, which progressively becomes steeper as the eastern contact is approached (Figure 24). The eastern contact is formed by the intrusion of the Palms granite (Figure 6, cross-section A-A'). Regionally, these fabrics define an antiformal/synformal, kilometer-scale fold pattern that has a hinge line that trends

approximately north to slightly northwest. These folds are asymmetrical, open folds with interlimb angles of approximately 120-140 degrees. Further to the south of this area (Quail Mountain/ Juniper Flats – QM/JF), the foliations define a single synformal pattern with a similarly trending hinge line and interlimb angle. At this time, it is uncertain whether this synformal fold pattern is a continuation of the synformal fold to the north or whether other folds are present in the area.

Along the boundary between Domains I and III (center of the map in Figure 24), the gneisses have similar orientations to the gneisses exposed farther north in the JLC area (Figure 24). Immediately west of the Domain I and Domain III boundary, the foliations retain a consistent northwest-southeast strike and southwest dip. This orientation is again truncated by exposures of the QMSC to the west and southwest. However, moving further southwest towards the Stubbe Spring granite (SS) and the Blue Cut granodiorite (BC), the foliation becomes parallel to the pluton contacts, striking northwest-southeast and dipping moderately towards the northeast. This orientation is concordant to the foliations observed within the SS, BC, and the BSC. Interestingly, northwest of the Blue Cut granodiorite contact, the orientations of the gneisses appear to rotate into parallelism with the Stubbe Spring granite pluton.

Although lineations are an important part of understanding the structural history within these framework rocks, the number of measured lineations and their distribution are not sufficient within Domain I to make any conclusions.

Domain II: Eastern Gneisses of the Northern Lost Horse Mountains

The orientations of gneisses within Domain II are strikingly different from those found within the other two domains. Within this domain, the foliations have a fairly consistent northeast-southwest strike and southeast dip, which is generally parallel to the Palms granite contact (Figure 24). Along this contact in the Ryan Mountain area (RM Area in Figure 24), the foliations are rather steep and progressively become shallower towards the southeast, indicating the presence of a structural aureole. The lineations within this domain also have a very consistent northeast trend, which is parallel to subparallel to the strike of the foliations.

Domain III: Eastern Gneisses of the Southern Lost Horse Mountains

As previously mentioned, the gneisses exposed within this domain (southern Lost Horse Mountains) are considerably different in orientation from those in the northern portion of this mountain range (Domain II). Along the western margin, the foliations within the gneisses generally strike northwest-southeast and dip moderately to the southwest. These foliations are obliquely truncated by the Blue Cut granodiorite contact. However, as mentioned previously in the Blue Cut results, local zones of parallelism do exist. Additionally, the foliations along this western contact are moderately to steeply dipping, exhibiting a range of dip angles ($46\text{-}82^\circ$). Within a kilometer of the western contact, the foliations dip towards the east (Figure 24). Closer to the eastern contact, however, the foliations change dip direction once again, forming a moderately west dipping foliation, which progressively becomes steeper, particularly along the contact with the discordant Squaw Tank pluton (Figure 24; also see Figure 14), again, indicating

the presence of a structural aureole. Regionally, these foliations define an antiformal/synformal, kilometer-scale fold pattern that has a hinge line that trends approximately northwest. Compared to the antiformal/synformal patterns of Domain I, the folds observed within this domain are generally tighter, exhibiting interlimb angles of 90-110 degrees. Interestingly, the fold patterns recorded within this domain are also comparable in orientation to the magmatic fold observed within the Blue Cut granodiorite. Towards the northern portion of this domain, the foliations dip steeply towards the Palms granite.

The lineations within this domain are better mapped and provide a clearer structural history of these rocks. The lineations along the Blue Cut granodiorite contact are subparallel to the strike of the foliations and the hinge lines of the antiformal and synformal folds (see Figure 15). This northwest trending orientation is consistent for much of this domain. However, as the Palms granite contact is approached (to the northwest), these lineations change orientations abruptly, shifting towards the southwest (Figure 15; Figure 20). This shift in orientation appears to be deflected around the eastern and northern contacts of the Blue Cut granodiorite and the southwestern contact of the Palms granite (Figure 15; Figure 20).

MICROSTRUCTURAL RESULTS

Overview of Microstructural Criteria

In the following sections, the terms magmatic, high-temperature solid-state, moderate temperature solid-state, and low-temperature solid-state are used to categorize the observed microstructures in order to estimate the temperatures of deformation. Therefore, to avoid ambiguity, each of these terms has been defined below.

Magmatic microstructures are defined as all the microstructures, textures, and preferred orientations of primary, igneous minerals (fabrics) that were formed in the presence of a melt without sufficient grain-to-grain interactions to form internal deformation. This definition corresponds to the magmatic flow fabrics of Paterson et al. (1989, 1998), the pre-full crystallization fabrics of Ingram and Hutton (1994), and the pre- rheological critical melt percentage fabrics (pre-RCMP) of Tribe and D'Lemos (1996).

High, moderate, and low-temperature solid-state microstructures, on the other hand, are restricted to absolute temperature ranges under which each microstructure is most commonly observed in naturally deformed rocks. These temperature ranges are discussed in Passchier and Trouw (2006) and are classified here as high ($>500^{\circ}\text{C}$), moderate ($500\text{--}400^{\circ}\text{C}$), and low ($<400^{\circ}\text{C}$). These temperature ranges broadly correspond to granulite - low amphibolite, low amphibolite - mid-greenschist, and mid-greenschist - low greenschist, respectively (Tribe and D'Lemos, 1996; Simpson, 1985). By definition, solid-state microstructures are all of those microstructures that are formed in the absence of a melt phase (Passchier and Trouw, 2006). However, because it is well-documented that some high-temperature solid-state microstructures ($>500^{\circ}\text{C}$) can be formed in the

presence of a melt (hypersolidus) (Means and Park, 1994; Park and Means, 1996; Rushmer, 1995), it is necessary to combine high-temperature solid-state microstructures with the submagmatic microstructures of Paterson et al., (1989; 1998). Unless unequivocal evidence was observed that would permit their discrimination, both high-temperature solid-state and submagmatic microstructures were classified together as high-temperature solid-state microstructures. Moderate and low-temperature solid-state microstructures are defined as all the microstructures, textures, and fabrics formed within the previously specified temperature ranges (discussed above) in the absence of a melt phase (melt-absent deformation).

Quartz Microstructures

The volumetrically dominant tonalite and granodiorite compositions show a range of quartz microstructures that are consistent with magmatic to high-temperature solid-state deformation conditions (Table 5). Quartz microstructures observed within tonalitic and granodioritic rocks interpreted to be magmatic include: (1) roughly spherical pools of strain-free grains; (2) inclusions of strain-free grains within other primary, igneous minerals (plagioclase, potassium feldspar, and hornblende); and (3) minor undulose extinction (Figure 25A and G). Within the fine-grained, tonalitic compositions, quartz is found primarily as small, interstitial grains. In the coarser-grained compositions, however, quartz is still found interstitially, but is much larger and is commonly observed molding other primary, igneous minerals (Figure 25B).

Although magmatic microstructures are present in the tonalitic and granodioritic samples, high-temperature solid-state overprinting is widespread and is variable from

sample to sample (Table 5). In samples with little observed deformed, primary, quartz grains record evidence of grain-boundary migration (GBM), showing a range of sutured, amoeboid shapes and sizes (Figure 25C and D). Although GBM is present, the grains retain a “pooled” appearance; rarely do they form more elongate grain shapes indicative of moderate to low-temperature solid-state deformation. Internally, these grains often show evidence of chessboard extinction, indicating that both basal and prism-slip was operating during deformation (Figure 25B and I). In the samples with greater subsolidus deformation, moderate temperature microstructures are present and are characterized by single, elongate grains and aggregates of ribbon-shaped quartz. However, these moderate temperature solid-state deformation microstructures are not pervasive, occurring only in a few of the tonalitic and granodioritic samples (Table 5).

Granitic compositions also contain well-preserved magmatic, quartz microstructures that range from anhedral pools with minor undulose extinction to strain-free grains within other primary, igneous minerals (Figure 25F). In the weakly deformed granite samples, quartz typically forms roughly spherical pools that record evidence of GBM (Figure 25E and F). Internally, these grains also show evidence of subgrain formation, undulose extinction, and chessboard extinction (Figure 25E, F, and H). In the more strongly deformed samples, GBM is widespread, particularly in the coarser-grained samples. Within the finer-grained samples, both spherical pools of quartz with evidence of GBM and more elongate, ribbon-shaped grains are present (Figure 25J). Some of these fine-grained ribbons are composed completely of recrystallized, strain-free, polygonal quartz. Although these aggregates are often visible at the outcrop scale, they rarely form a penetrative subsolidus fabric.

Compared to the more mafic compositions, solid-state overprinting of moderate temperature quartz microstructures is proportionally more abundant in the granitic compositions (Table 5). This relationship is consistent for all of the exposed igneous bodies at this level in the crust (Blue Cut granodiorite, Stubbe Spring granite, and Quail Mountain sheeted complex) (Table 5).

Plagioclase Microstructures

Plagioclase microstructures interpreted to be magmatic are also well-preserved within all of the BSC compositions (Table 6). In the weakly deformed tonalite and granodiorite compositions, magmatic microstructures include: (1) euhedral to subhedral, tabular grains that show little intracrystalline strain; (2) compositional zoning; (3) growth twins that have blocky, stepped terminations; and (4) synneusis (Figure 25A, B and E; Figure 26A-H). Tiling and/or the alignment of euhedral to subhedral plagioclase grains that do not show significant internal deformation are also present in many of the fine-grained tonalite samples (Figure 26C, G, and H). This microstructure is considered diagnostic of magmatic conditions (Paterson et al., 1989; Passchier and Trouw, 2006; Vernon, 2004).

Within the granitic compositions, well-preserved magmatic microstructures are less abundant, but are still equally represented (Figure 25E and J; Figure 26D and F). For instance, despite evidence of minor GBM, compositional zoning and growth twins are still recognizable.

Similar to observed quartz microstructures, plagioclase grains also record a range of microstructures interpreted to reflect high-temperature subsolidus conditions. In the weakly deformed tonalitic and granodioritic samples, plagioclase deformation is mostly

restricted to local bending, deformation twins, and minor GBM between impinging feldspar phenocrysts (plagioclase/plagioclase and plagioclase/potassium feldspar); granitic samples also display these high-temperature microstructures (Figure 26B, C, F J, L, and N). However, within the more strongly deformed tonalitic, granodioritic, and granitic samples, GBM is more conspicuous, displaying sutured, amoeboid crystals (Figure 26I and K). These sutured plagioclase grain-boundaries are shared with hornblende, potassium feldspar, quartz, and other plagioclase grains. Additionally, some of the larger plagioclase grains show incipient recrystallization along their grain-boundaries, forming intergranular aggregates of polygonal grains (Figure 26I, L, and N). The recrystallized plagioclase grains often exhibit the greatest range of sizes and shapes, making them easier to identify (Figure 26N). These intergranular aggregates also occur preferentially along plagioclase/plagioclase and plagioclase/potassium feldspar boundaries. Although these aggregates are more common in the strongly deformed granitic samples, they are also present within the strongly deformed mafic compositions as well, where they occur locally along impinging feldspar and feldspar/hornblende grains.

Myrmekite is also present in nearly all of the collected samples, where it commonly occurs along plagioclase/potassium feldspar boundaries (Table 6). Although a submagmatic (e.g. Hibbard, 1987) and a high-temperature solid-state origin (e.g. Simpson and Wintsch, 1989) have been proposed for its development, this study treats myrmekite as a high-temperature solid-state microstructure because there is not unequivocal evidence that would favor a distinction (see Overview of Microstructural Criteria). Nevertheless, within the weakly deformed samples, myrmekite exhibits mostly

primary features such as delicate, fanning lamellae with roughly straight grain-boundaries (Figure 26L). In the more strongly deformed samples, however, myrmekite is recrystallized with quartz, plagioclase, potassium feldspar, and biotite along grain-boundaries (Figure 26N); primary features are also present within the same sample, but are less common.

In addition to magmatic and high-temperature solid-state microstructures, many of the collected samples contain plagioclase microstructures that have been interpreted to be submagmatic. For instance, some of the plagioclase grains appear to have indented and removed material from their neighboring plagioclase grains. The removal of material is evident by the truncation of compositional zoning along irregular grain-boundaries (e.g. Vernon et al., 2004) (Figure 26O and P). Vernon (2004) and Rosenberg (2001) have argued that this textural relationship is evidence for contact melting between juxtaposed plagioclase grains in granitoids deformed in the submagmatic state.

In some of the tonalitic and granodioritic samples, plagioclase grains also show evidence of intragranular fractures that strongly resemble the submagmatic microfractures described by Bouchez et al. (1992) (Figure 26Q-S). In these weakly deformed tonalite and granodiorite samples, wedge-shaped fractures that transect single plagioclase grains are present. The minerals filling these fractures are typically quartz and potassium feldspar that are optically continuous with quartz and feldspar outside of the fracture. However, because hydrothermal alteration and deposition of quartz cannot be excluded, a solid-state origin cannot be eliminated.

Moderate temperature solid-state deformation in plagioclase is restricted to granitic compositions and is characterized by local undulose extinction and the development of

kink bands (Table 6). Although moderate-temperature microstructures are present, only a few examples were observed. Furthermore, low-temperature hydrothermal alteration is conspicuous within all the compositions, both weakly and strongly deformed (Figure 25A and J; Figure 26D, O, and P). These low-temperature features are characterized by alteration: seritization (formation of sericite) and saussuritization (formation of epidote minerals).

Potassium Feldspar Microstructures

Potassium feldspar (K-spar) is found within all of the sampled granitic, granodioritic, and tonalitic compositions (Table 4) (Figure 27A-I). In the more mafic compositions, K-spar commonly forms interstitial grains, but larger phenocrysts are also ubiquitous (Figure 26P and Q; Figure 27G and I). Within the granitic compositions, however, K-spar forms larger phenocrysts that are molded by quartz and biotite (Figure 25D; Figure 27F). In the weakly deformed samples, K-spar microstructures interpreted to be magmatic include: (1) euhedral to subhedral grains that show little intracrystalline strain; (2) weak compositional zoning that contains strain-free quartz, biotite, and plagioclase inclusions; and (3) growth twins (Figure 25G; Figure 27A and B). These magmatic microstructures are equally represented within all the weakly deformed samples, but are generally more conspicuous in the more mafic compositions.

High-temperature solid-state microstructures within K-spar are proportionally more abundant than magmatic microstructures within all the sampled compositions (Table 7). Evidence for these high-temperature microstructures is indicated by conspicuous GBM, displaying sutured, amoeboid crystals (Figure 27C, D, E, and I). These sutured grain-

boundaries are commonly shared with quartz, plagioclase, and other K-spar grains. Larger grains also show incipient recrystallization along grain-boundaries, forming intergranular aggregates of polygonal grains (Figure 27G). These intergranular aggregates occur preferentially along K-spar/ K-spar and plagioclase/K-spar boundaries. Although these aggregates are more abundant in the strongly deformed granitic samples, they have also been observed within the more mafic compositions as well. Additionally, large, isolated phenocrysts of K-spar that are completely surrounded by recrystallized aggregates of quartz, biotite, K-spar, and plagioclase are present in the strongly deformed granitic samples, giving the sample a protomylonitic-like texture (Figure 27H). This texture has only been observed in the strongly deformed granite compositions. Additional high-temperature solid-state microstructures include 1) microcline twinning and 2) myrmekite (Figure 27F).

Biotite Microstructures

Biotite shows the greatest diversity of microstructures within any sample, displaying both primary, magmatic features and variable amounts of subsolidus deformation. This is generally true for all of the sampled compositions where biotite is present. In granitic, granodioritic, and tonalitic compositions where subsolidus deformation is minimal, biotite microstructures interpreted to be magmatic include: (1) discrete, euhedral grains that do not record significant internal deformation; (2) smooth 001 crystal faces; and (3) euhedral inclusions within other primary, igneous minerals (Figure 26G, O, and P; Figure 27A and F; Figure 28A and B). These magmatic microstructures are equally represented

within all the weakly deformed samples, but are generally more conspicuous in the more mafic compositions (Table 8).

In all of the compositions that show minimal subsolidus deformation, biotite generally forms discrete interstitial grains and clusters (clots/mats) of grains (Figure 28A-E). Observed subsolidus deformation within single grains includes minor slip along cleavage-controlled planes, forming irregular, ragged crystals (Figure 28A and B). Stronger subsolidus deformation defined by kinking is rare, suggesting that strain was predominantly accommodated along cleavage planes (e.g. Vernon et al., 2004). Where kinking in biotite (or muscovite) is observed, the grains are generally trapped between impinging feldspar and hornblende crystals (Figure 28C). Additionally, when strain cannot be accommodated by cleavage-controlled slip or kinking, some of the original, magmatic grains show evidence of intragranular fracturing normal to the 001 crystal face (Figure 28B). Subsolidus deformation subsequent to fracture formation was minimal, as slightly misoriented grains formed by these intragranular fractures do not show further deformation.

Individual grains found within biotite clusters also show minimal subsolidus deformation defined by ragged crystal faces (Figure 28D and E). More significant subsolidus deformation within biotite clusters is indicated by curved and overlapping grains, local kinking, and incipient intragranular fractures with ragged terminations (e.g. Vernon et al., 2004) (Figure 28D, E, I, and J). These subsolidus deformation features are generally found within clusters impinged between strong minerals (Figure 28D). Additionally, these clusters of strain-free grains commonly anastomose plagioclase and

potassium feldspar grains, forming folia within these weakly deformed samples (Figure 28D, E, I, and J).

The incipient stages of biotite folia development within weakly deformed samples are indicated by primary grains that have been locally cleaved and squeezed between impinging strong minerals (feldspar and hornblende) (Figure 28C, F, G, H). Along these strong mineral boundaries, cleaved biotite fragments are locally recrystallized into fine-grained aggregates (Figure 28C, F, G, and H). However, both strain-free clusters (previously discussed) and aggregates of recrystallized grains are present in these weakly deformed samples, forming the folia observed in the hand-specimens (Figure 28K). In the tonalitic and granodioritic samples, these biotite folia are accompanied by laths of euhedral to subhedral hornblende, plagioclase, and sphene.

In more strongly deformed samples, recrystallization of biotite grains is evident by the formation of strain-free, single grains and clusters that display smooth 001 faces parallel to the main foliation (Figure 26K). Recrystallization is also evident by the formation of fine-grained aggregates of biotite that anastomose strong minerals (Figure 28L and M). Dynamic recrystallization of biotite is present in all compositions, both weakly and strongly deformed.

Moderate temperature solid-state deformation in biotite is not restricted to any particular rock composition. This moderate temperature deformation is primarily characterized by the local development of kink bands. Although moderate-temperature microstructures are present, they are not as pervasive as the high-temperature microstructures (Table 8). Furthermore, low-temperature retrogression of biotite to chlorite is present within all the compositions, both weakly and strongly deformed. This

retrogression is typically minor; rarely does retrogression of biotite to chlorite completely convert the entire biotite grain.

Hornblende and Sphene Microstructures

Hornblende is ubiquitous in many of the tonalitic and granodioritic compositions, where it displays a range of microstructures interpreted to reflect magmatic and high-temperature solid-state conditions (Table 4). Hornblende microstructures interpreted to reflect magmatic conditions include: (1) euhedral laths and prismatic grains and (2) euhedral inclusions within other primary, igneous grains. These magmatic microstructures are widespread in the weakly deformed samples (Figure 29A and B).

In the more strongly deformed samples, hornblende grains not only record evidence of magmatic microstructures, but also record evidence of subsolidus overprinting. For instance, some of the preferentially aligned, euhedral grains contain evidence of fractures along cleavage-controlled planes, forming misoriented fragments (Figure 29C). These misoriented fragments commonly form the incipient stages of folia development. Similar to the cleavage-controlled slip in biotite, the cleavage-controlled fractures observed in hornblende typically forms splintered grain terminations. Additionally, some of the hornblende grains form lozenge-shaped crystals that have ‘tails’ formed by fragments from these cleavage-controlled planes (Figure 29C and D). Predominantly brittle behavior in hornblende suggests temperatures <700°C (Passchier and Trouw, 2006).

With greater subsolidus deformation, hornblende becomes recrystallized by grain-boundary migration (GBM), forming sutured, amoeboid crystal shapes (Figure 29F). Recrystallization of hornblende by GBM is consistent with high-temperature solid-state

conditions ($>700^{\circ}\text{C}$) (Passchier and Trouw, 2006). These sutured grain-boundaries are commonly shared with quartz, plagioclase, K-spar grains, other hornblende grains, and clusters of biotite. Additionally, some hornblende grains show evidence of ductile bending (Figure 29G).

Similar to hornblende, sphene is also common in many of the tonalitic and granodioritic compositions, where it displays a range of magmatic and solid-state microstructures (Table 4). Microstructures interpreted to reflect magmatic conditions include: (1) euhedral to subhedral grains that show little internal deformation and (2) inclusions within other primary, igneous grains. In samples that show only minor subsolidus deformation, magmatic microstructures are conspicuous. Sphene is commonly euhedral and is aligned parallel to the dominant fabric (Figure 30A). Interestingly, some of these euhedral grains also contain evidence of twinning (deformation twinning?) (Figure 30B). Although the significance of this twinning is uncertain at this time, the orientation of these crystallographically controlled twins is commonly subparallel to the dominant foliation, suggesting that twinning may be related to fabric-forming processes.

Intragranular fractures are also present in sphene. In one particular example, the sphene grain contains an intragranular fracture that strongly resembles the submagmatic fractures in plagioclase (Figure 30C). Because the sphene grain contains euhedral crystal faces, contains inclusions of other primary, igneous minerals, and is subparallel to many of the euhedral plagioclase laths, a magmatic origin is favored. In this particular example, quartz is filling the fracture. Collectively, these observations support a

submagmatic origin. However, because quartz is filling the fracture, a solid-state origin can not be excluded.

Sphene also displays a range of microstructures interpreted to reflect predominantly brittle, solid-state conditions. However, at this time, the estimated thermal conditions for their formation are not available. Therefore, the following will only contain a description of the observed microstructures with no reference to thermal conditions under which they might form.

In the more strongly deformed samples, sphene is rarely euhedral, forming more anhedral grains and grain fragments. These grains are commonly found distributed along fine-grained biotite folia in granitic compositions and within the intergranular aggregates of tonalitic and granodioritic compositions (between impinging strong minerals). In all the observed compositions, these sphene fragments contribute to the development of foliations.

DISCUSSION AND INTERPRETATIONS

Rocks exposed within the Little San Bernardino Mountains (LSBM) were originally mapped as Precambrian gneissic rocks, and later interpreted as a broad Mesozoic gneissic complex with pervasive brittle deformation (Powell, 1981, 1993). Although there is little disagreement with the compositional heterogeneity and structural complexity described within these early studies, the macroscopic and microstructural observations presented here support an alternative interpretation that the LSBM is composed of Late Cretaceous sheeted plutons that are dominated by magmatic fabrics and microstructures formed largely by regional deformation. In the following sections, I present a synthesis of microstructural and macroscopic observations that support this alternative interpretation.

Microstructural Interpretation and Discussion

The microstructural observations made in this study place constraints on the thermal conditions present during fabric formation which could not be determined at the outcrop scale. Although the sheeted plutons within the LSBM show considerable microstructural variability, the observed microstructures are generally consistent with a transition from magmatic to submagmatic/high-temperature solid-state deformation. This is in direct contrast to the pervasive brittle deformation characterized by Powell (1981, 1993). The following is a discussion of some relevant microstructures that support this new interpretation.

Although a majority of the collected samples contain magmatic quartz microstructures, quartz also exhibits solid-state microstructures that have been constrained to temperatures $>500^{\circ}\text{C}$. This interpretation is supported by the ubiquitous

presence of high-temperature grain-boundary migration and chessboard extinction in quartz within a majority of the collected samples (Figure 25A-E, H-I; Figure 27D and E; Table 5). Whereas high-temperature grain-boundary migration within quartz indicates that recovery was concurrent with plastic deformation at high-temperatures ($>500^{\circ}\text{C}$), chessboard extinction indicates higher temperatures of deformation ($>700^{\circ}\text{C}$) (Passchier and Trouw, 2006; Vernon, 2004; Tullis, 2000). At 2-8 Kb of confining pressure, the granodiorite and tonalite solidus range from approximately 650 to 750°C , shifting to lower temperatures with higher confining pressure (Whitney, 1975). This temperature range is consistent with solidus temperatures determined by Needy et al. (2006) (669 - 786°C) for plutons examined in this study. Given 4-6Kb of confining pressure (Needy et al., 2006) for these plutons, the presence of chessboard extinction in quartz suggests that solid-state deformation was largely above or approached the granite and tonalite solidus (Figure 31).

Although a submagmatic (e.g. Hibbard, 1987) and a high-temperature solid-state origin (e.g. Simpson and Wintsch, 1989) has been proposed for the development of myrmekite, it is classified here as a high-temperature solid-state microstructure in plagioclase and potassium feldspar. Regardless of its origin, myrmekite within many of the weakly deformed samples typically forms delicate, fanning lamellae with straight grain boundaries (Figure 26L and M). This observation suggests that major solid-state deformation following myrmekite growth is unlikely because these delicate structures would be destroyed (Albertz et al., 2005). In the more strongly deformed granitic samples, however, myrmekite is extensively recrystallized within intergranular aggregates of quartz, feldspars, and biotite (Figure 26N; Figure 27G). Because these

intergranular aggregates contain recrystallized feldspars, a high-temperature solid-state origin is still favored ($>500^{\circ}\text{C}$) (Passchier and Trouw, 2006; Gapais 1989; Simpson, 1985).

In addition to the more common magmatic and high-temperature solid-state microstructures observed in plagioclase (summarized in Table 6), many of the collected samples contain plagioclase microstructures that have been interpreted to be submagmatic. For instance, some of the plagioclase grains appear to have indented and removed material from their neighboring plagioclase grains (Figure 26D; Figure 26O and P). The removal of material is evident by the truncation of compositional zoning along irregular grain boundaries (e.g. Vernon et al., 2004). Based on the experimental work of Park and Means (1996), recent studies (Vernon, 2004; Rosenberg, 2001) have argued that this is evidence for submagmatic contact melting.

Additionally, plagioclase grains also show evidence of intragranular fractures that strongly resemble the submagmatic microfractures described by Bouchez et al. (1992) (Figure 26Q-S). When the minerals filling these fractures are 1) compositionally consistent with minerals that would crystallize from a residual melt (quartz, sodic plagioclase, potassium feldspar) and 2) optically continuous with groundmass grains, a submagmatic interpretation may be inferred (Bouchez et al., 1992; Vernon et al., 2004). In the weakly deformed tonalite and granodiorite samples, wedge-shaped fractures that transect single plagioclase grains are present. The minerals filling these fractures are typically quartz and potassium feldspar that are optically continuous with quartz and feldspar outside of the fracture. Therefore, these observations favor a submagmatic

origin. However, as mentioned previously, hydrothermal alteration and deposition of quartz cannot be excluded, which implies that a solid-state origin cannot be eliminated.

As indicated by the microstructural results, the varying amounts of superimposed solid-state deformation present within these plutons are predominantly restricted to high temperatures ($>500^{\circ}\text{C}$). Microstructural evidence supporting that interpretation includes: the presence of chessboard extinction in quartz (Passchier and Trouw, 2006); high-temperature grain boundary migration in quartz, plagioclase, potassium feldspar, and occasionally hornblende (Passchier and Trouw, 2006; Vernon, 2004; Gapais, 1989; Simpson 1985); and the formation of myrmekite (Vernon, 2004).

The microstructural observations presented here also indicate that mafic rocks generally contain more magmatic microstructures than felsic rocks (Table 5-9). Tribe and D'Lemos (1996) observed this pattern within a quartz diorite complex in the Channel Islands, U.K. They argued that partitioning of deformation, and hence fabric development, are likely to be influenced strongly by magma composition. They also argued that leucogranites will be more susceptible to solid-state deformation because of the greater abundance of easily deformed phases. Similar arguments were made by Bouchez et al. (1992) regarding intragranular fractures in plagioclase. They argued that such fractures are better preserved in mafic rocks than felsic rocks because mafic magmas crystallize over a larger range of temperatures than felsic magmas. Therefore, it is likely that as crystals form in a felsic magma, competition for space between grains will destroy early-formed fabrics and magmatic microstructures.

There are a number of possible alternatives that may explain why mafic rocks in the LSBM contain more magmatic microstructures than felsic rocks. For instance, based on

the preliminary $^{40}\text{Ar}/^{39}\text{Ar}$ biotite thermochronology presented by Needy et al. (2007), regional cooling through the biotite closure temperature (ca. 350°C) was achieved by 70 Ma for plutons in this area. This 70 Ma age is consistent with the incipient stages of the Laramide orogeny at this latitude (Grove et al., 2003). Given the solidus temperatures for granite and tonalite (650–750°C) relative to the biotite closure temperature (ca. 350°C), this would suggest that magmas emplaced into this arc system towards the end of the 83-74 My span would be cooled more rapidly (ca. 75-100°C/ 1 Ma for magmas emplaced at 74 Ma) than magma emplaced towards the beginning (ca. 23-30°C/ 1 Ma for magmas emplaced during 83 Ma). Given the general sequence of emplacement from mafic to felsic observed in these sheeted plutons (see BSC and QMSC sections), it is likely that the late-stage felsic magmas would have been emplaced into a colder arc system, thus having a greater effect on their ability to preserve magmatic microstructures. This may explain why older, intermediate plutons like the Blue Cut granodiorite (82.1 ± 1.8 Ma) contain stronger magmatic fabrics than the younger, granitic Stubbe Spring pluton (76 ± 4 Ma), which contains more solid-state deformation.

Within individual plutons, fabric development is highly variable such that some areas display significant solid-state overprinting. However, taken as a whole, the microstructural observations for the plutons of the LSBM are more consistent with a continuum from magmatic to high-temperature solid-state deformation (Table 5-9). Therefore, I envision that the formation of the strong fabrics within these plutons initiated while the magma was still crystallizing, presumably within the 20-40% melt fraction range (Paterson et al., 1998). These fabrics continued to develop as the magma cooled towards its solidus temperature. After complete solidification, the pluton continued to

deform in the solid-state realm. Based on microstructural observations presented here, this solid-state deformation continued down to temperatures as low as 500°C.

Macroscopic Interpretation and Discussion

Magmatic fabrics preserved in plutons have been interpreted to represent a variety of features. For instance, they have been used to infer the shapes of plutons at depth as well as magma surges and chamber ballooning (Paterson et al., 1998 and references therein). Based on the work of Paterson et al. (1998), however, there is little evidence indicating that fabrics in plutons are reliable indicators of any of these previously mentioned processes. Instead, magmatic fabrics are generally believed to be formed during the last increment of strain by 1) magmatic flow caused by internal chamber processes or 2) by regional deformation acting on a crystallizing magma chamber (Paterson et al., 1998). As a way to distinguish between these two processes, Paterson et al. (1998) emphasized the degree of structural continuity between fabrics within plutons and their host rocks. They argue that if fabric patterns within the pluton are completely discontinuous to those observed in the host rock, the degree of coupling is low (decoupled system), and the fabric patterns are likely the result of internal magma chamber processes (Paterson et al., 1998). Alternatively, if pluton fabrics and structures are continuous with the host rock, the degree of coupling is high (coupled system), and the fabric patterns are likely the result of regional deformation during cooling and crystallization. Therefore, careful evaluation of fabrics within the pluton and their host rocks will provide valuable information about the mechanical coupling between the pluton and its host as well as likely fabric-forming processes.

The macroscopic observations presented in this study suggest that the fabric patterns recorded within the LSBM sheeted plutons were formed during regional deformation rather than internal magma chamber processes. Here, regional deformation refers to an active far-field stress that could potentially deform a crystallizing magma chamber. Therefore, I envision that a regional-scale stress was present in southern California during the cooling and crystallization of the plutons examined in this study. At this time, the cause of this regional-scale deformation is uncertain, as I do not have enough evidence to distinguish whether the deformation was formed by changes in large-scale tectonic regimes (Sevier to Laramide style tectonics) or by local stresses caused by pluton emplacement. Nevertheless, if the magma is above its solidus while regional deformation is occurring, then the recorded fabrics will be magmatic fabrics rather than solid-state fabrics. If, on the other hand, the plutons are below their solidus during this regional deformation, I would expect only solid-state fabrics. Therefore, I envision that magmatic fabrics within the LSBM sheeted plutons were formed by regional deformation acting on a crystallizing magma chamber. After each pluton reached its solidus, the primary magmatic fabrics were overprinted by high-temperature solid-state fabrics. This high-temperature overprinting was formed by a persistent regional stress acting on the newly solidified pluton. This scenario and interpretation is consistent with the microstructural observations and is further supported by the following macroscopic observations.

(1) Foliations are observed within all of the sheeted plutons emplaced during the 83-74 Ma interval (Figure 12, 14, 17, and 19) and are regionally consistent. These observations suggest that the fabric-forming process exceeded the cooling history of a single pluton. Although internal magma chamber processes could also generate

consistent chamber-wide foliations, it is unlikely that such internal processes would consistently operate for the duration of plutonism recorded in the LSBM. Additionally, foliations within the BSC become steeper along strike, presumably reflecting the heterogeneity of a far-field stress (i.e. intensity of regional shortening across the arc) (Miller and Paterson, 2001) (Figure 12).

(2) Although the magmatic fabrics have predominantly margin-parallel orientations, some fabrics are discordant to pluton contacts, internal layering, and sheeting. This observation suggests that fabric development postdates magma ascent, emplacement, and the formation of internal sheeting. According to Miller and Paterson (2001), the discordance of magmatic fabrics to contacts and internal sheeting demonstrates that a small viscosity contrast likely existed between the pluton and the host rock during the formation of magmatic structures and fabrics. This small viscosity contrast is only possible when the magma is crystal-rich and near its solidus, suggesting that magmatic structures and fabrics were formed late in the crystallization history (Miller and Paterson, 2001). This observation would not favor large-scale magma chamber processes such as convection, as this process would require low crystal contents to operate.

(3) Sheeted plutons contain both magmatic and solid-state fabrics. More specifically, magmatic and solid-state foliations have similar orientations within individual plutons, suggesting that fabric development initiated under magmatic conditions and continued below the solidus (Figure 12, 14, 17, and 19). This observation favors regional deformation rather than internal chamber processes, as fabric formation formed by internal magma chamber processes would cease upon reaching the solidus.

(4) Fabrics and structures (foliations, lineations, and folds) within some sheeted plutons are commonly parallel to equivalent host rock structures. For instance, the Blue Cut granodiorite contains both magmatic and solid-state fabrics that define a synformal fold that is nearly parallel to the antiformal and synformal folds observed within the gneisses of the Lost Horse Mountains (Figure 14, 19, and 24). This observation provides several pieces of information. First, the large-scale folding recorded by these fabrics suggest that regional contraction was concurrent with cooling and fabric formation in the Blue Cut pluton at 83 Ma. The antiformal pattern observed within the Bighorn Sheeted Complex may also be related to this regional contraction, as the orientation is similar to the synformal structure within the Blue Cut pluton. Second, the similarities in folding between the Blue Cut pluton and its host suggest a strongly coupled system as emphasized by Paterson et al. (1998).

The magmatic structures and fabrics preserved within the LSBM sheeted plutons largely provide information about regional deformation. Because the host rocks were also interpreted to be involved in this deformation, the preserved fabrics and structures within these rocks can provide additional information about the space-making processes for the emplacement of these plutons. More specifically, there are several pieces of evidence that suggest that space for these plutons were made by ductile flow and stoping.

(1) The fabrics within the host rocks often become steeper along pluton contacts, suggesting that host rock displacement was accommodated by vertical, ductile flow. For instance, within the Johnny Lang Canyon area (see Figure 17) the gneisses generally become steeper towards the eastern and western contacts. The gneisses within the Lost Horse Mountains also become steeper along the contacts with the Blue Cut granodiorite

pluton, the Palms granite pluton, and the Squaw Tank pluton (i.e. Domain II and III in Figure 24). Additionally, stretching lineations within the gneisses of the Lost Horse Mountains have steep pitches relative to the strike of the foliations (directly down-dip). The lineations also appear to be deflected around the younger plutons. Both of these observations suggest that host rock displacement was accommodated by vertical and lateral, ductile flow (see Figure 14, 15 and 20).

(2) The mineral assemblages within the host rocks are consistent with amphibolite to granulite facies mineral assemblages, which is consistent with a thermal regime suitable for ductile flow.

(3) Because all of the plutons contain evidence of host rock inclusions (rafts, xenoliths, and stoped blocks), stoping was a viable space-making process at this level in the crust.

Emplacement of magmas along faults or shear zones has also been proposed for similar sheeted complexes (Ingram and Hutton, 1994; Manduca et al., 1993). At this time, faulting does not appear to have been a space-making mechanism in this system because no evidence exists to suggest that plutons were emplaced along or within a major fault zone. Evidence to support such a mechanism would likely be found towards the ends (sheet tips) or margins of these sheeted plutons, as these locations would likely contain the highest differential stresses. However, the possibility remains plausible, as Powell (1981) proposed that the Triassic Red Cloud Thrust fault would extend through the LSBM as far north as the San Bernardino Mountains. Further work is needed to test this hypothesis. Additionally, it has also been suggested by Powell (1981, 1993) that this region is a Laramide shear zone. Based on the presented macroscopic and

microstructural observations, this contention is not supported, as I have observed only minor shearing in the field. The thin sections used in this study were prepared in such a way to evaluate this idea. However, I have not observed significant shear-related kinematics at either the outcrop or microstructural level to support this contention.

CONCLUSION

The scale of the exposed tilted section suggests that the geometric and compositional features described here are fundamental features of the Cordilleran arc, where it was constructed on thick Paleoproterozoic crust. Based on the microstructural observations presented in this study, the dominant fabrics within these Late Cretaceous plutons are predominantly magmatic. These magmatic fabrics are largely overprinted by solid-state deformation that is restricted by microstructural observations to temperatures as low as 500°C. I also conclude that mafic compositions have stronger magmatic fabrics and structures than felsic compositions. This may largely be explained by the compositional differences (see discussion above) as well as rapid cooling within the arc system leading into the Laramide orogeny. As previously indicated, by 70 Ma (onset of Laramide orogeny at this latitude) these mid-crustal plutons were passing through the biotite closure temperature (ca. 350°C). Given the general emplacement sequence of mafic to felsic, this would suggest that late-stage felsic magmas were emplaced into a colder arc system than early-emplaced, mafic magmas. This may account for the intense magmatic fabrics within the older, mafic and intermediate compositions relative to the more widespread solid-state deformation within the younger, felsic compositions. However, more geochronology is needed to evaluate this hypothesis.

Based on a compilation of structural observations from Dr. Andrew Barth and Dr. Scott Paterson, I interpret that these sheeted plutons were emplaced into an active continental arc setting that was undergoing regional contraction. The macroscopic observations suggest a strongly coupled pluton/host rock system. Therefore, the preserved fabrics are likely produced by regional deformation rather than internal magma

chamber processes. The strong magmatic fabrics and high-temperature solid-state overprinting is likely a consequence of regional deformation during crystallization. The weak fabrics within upper crustal plutons relative to the strong fabrics within the mid-crustal plutons suggest that deformation was largely localized to the mid-crustal portions of the arc structure. Finally, the macroscopic observations also suggest that space was made for these plutons by vertical and lateral ductile flow and stoping of host rocks. This conclusion is consistent with the geochemical and isotopic work of Palmer et al. (2006). Their work showed that assimilation of host rock was minimal (~10%) in the production of the plutons examined in this study. At this time, there is no significant evidence to support that these plutons were emplaced along major crustal-scale faults or within an actively deforming shear zone.

Table 1. Criteria used to identify magmatic and solid-state macroscopic structures

Magmatic		Solid-State	
1	Preferred grain shape orientation of euhedral, igneous minerals ¹	10	Preferred grain shape orientation of anhedral minerals ¹
2	Imbrication (tiling) of euhedral, igneous minerals ¹	11	Ribbon-shaped aggregates of recrystallized quartz and biotite ^{1,3}
3	No preferred orientation of quartz grains or aggregates (forming pools)	12	Boudinage of strong minerals, enclaves, and inclusions ^{1,3}
4	Visible zoning in euhedral feldspar phenocrysts ⁴	13	Foliations commonly pass through inclusions, enclaves, and xenoliths ¹
5	Poikilitic texture in potassium feldspars ⁴	14	Formation of folia defined by recrystallized minerals (biotite and muscovite) ¹
6	Preferred alignment of elongate microgranitoid enclaves ¹	15	Porphycroclasts with strain shadows ³
7	Planar to slightly curved schlieren layering ²	16	Fine-grained foliations anastomosing around porphyroclasts ^{1,3}
8	Deflection of fabrics and schlieren around xenoliths ¹	17	Monomineralic bands ^{1,3}
9	Folding of foliations where all phases are igneous minerals ¹	18	Mylonitic shear zones and S-C fabrics ¹

References: 1 = Paterson et al., 1989, 1998; 2 = Zak et al., 2007; 3 = Passchier and Trouw, 2006; 4 = this study

Table 2. Microstructural criteria for the identification of magmatic and solid-state fabrics and textures

Mineral	Magmatic	Solid-State		
		Submagmatic/ High Temperature (>500°C)	Moderate Temperature (500- 400°C)	Low Temperature (<400°C)
Quartz	Spherical pools of strain-free grains ¹	Dislocation creep - GBM (>500°C) ^{2,3}	Dislocation creep - SGR (>400°C) ^{2,3}	Dislocation creep - BLG (<400°C) ^{2,3}
	Inclusions in other igneous grains ¹	Chessboard extinction, undulose extinction ^{2,3}	Elongate grains ^{1,2}	Dissolution creep microstructures ²
	Minor undulose extinction ¹	Lobate or amoeboid grains ^{2,3}		Brittle fractures ²
Plagioclase	Euhedral to subhedral laths ¹	Dislocation creep - GBM (>850°C) ^{2,4,5}	Dislocation creep - BLG (>450°C) ^{2,5}	Brittle fractures ¹
	Oscillatory Zoning ¹	Dislocation creep - SGR (>600°C) ^{2,4,5}	Undulose extinction ^{2,5}	Dissolution creep microstructures ¹
	Growth twins parallel to long axis ¹	Tapering deformation twins and ductile bending ^{2,5}	Kink Bands ^{2,5}	Relict porphyroclasts with subgrains ¹
	Synneusis ¹	Myrmekite ^{2,3,4,5}		Altered to clays, micas, and epidote ¹
K-feldspar	Euhedral to Subhedral ¹	Dislocation creep - GBM (>850°C) ^{2,4,5}	Dislocation creep - BLG (>450°C) ^{2,5}	Brittle fractures ¹
	Oscillatory Zoning ¹	Dislocation creep - SGR (>600°C) ^{2,4,5}	Flame perthite ^{2,5}	Dissolution creep microstructures ¹
	Growth twins ¹	Tapering deformation twins and ductile bending ^{2,5}	Kink Bands ^{2,5}	Relict porphyroclasts with subgrains ¹
	Synneusis ¹	Myrmekite ^{2,4,5}		Altered to clays, micas, and epidote ¹
Biotite	Euhedral ¹	Dislocation creep - (undulose extinction) ²	Kinking ^{1,6}	Dissolution creep microstructures ¹
	Smooth 001 crystal faces ¹	Slip along 001 face (forming irregular 001 faces) ¹	Fracturing ^{1,6}	Recrystallize to chlorite ¹
	Euhedral inclusions in other grains ¹	Recrystallization with 001 planes parallel to foliation ⁶		
Hornblende	Euhedral to subhedral ¹	Anhedral polygonal to lath-shaped grains ¹	Brittle fractures ²	
	Lath-shaped to stubby ¹	Dislocation Creep - GBM (>700°C) ²		

1 = Paterson et al. (1998); 2 = Passchier and Trouw (2006); 3 = Vernon (2004); 4 = Gapais (1989); 5 = Gerald and Stünitz (1989); 6 = Simpson (1985)

Table 3. Table of hand specimen fabric data

Sample	Rock Unit	IUGS Rock Name	Fabric Type	Magnetic Intensity	Magnetic Criteria										Solid-State Criteria										Grain Size Range
					1	2	3	4	5	6	7	8	9	10	11	12	13	14	15	16	17	18			
04-549	BSC	granite	MS	2	*		*	*	*	*	*	*	*	*	*	*	*	*	*	*	*	*		1-3 mm	
04-550	BSC	granite	M	3	*	*	*	*	*	*	*	*	*	*	*	*	*	*	*	*	*	*	*	1-4 mm	
04-554	BSC	granite	M	3	*	*	*	*	*	*	*	*	*	*	*	*	*	*	*	*	*	*	*	1-4 mm	
04-562	BSC	granite	M	1	*		*	*	*	*	*	*	*	*	*	*	*	*	*	*	*	*	*	1-6 mm	
04-567	BSC	granite	M	1	*		*	*	*	*	*	*	*	*	*	*	*	*	*	*	*	*	*	1-12 mm	
JW 92-193	BSC	granite	M	1			*	*	*	*	*	*	*	*	*	*	*	*	*	*	*	*	*	1-8 mm	
JW 92-196	BSC	granite	M	1			*	*	*	*	*	*	*	*	*	*	*	*	*	*	*	*	*	1-10 mm	
JW 93-217	BSC	granite	M	1			*	*	*	*	*	*	*	*	*	*	*	*	*	*	*	*	*	1-10 mm	
JW 95-257	BSC	granite	MS	3	*	*	*	*	*	*	*	*	*	*	*	*	*	*	*	*	*	*	*	1-12 mm	
JW 95-258	BSC	granite	MS	3	*	*	*	*	*	*	*	*	*	*	*	*	*	*	*	*	*	*	*	1-12 mm	
JW 95-262	BSC	granite	MS	2	*		*	*	*	*	*	*	*	*	*	*	*	*	*	*	*	*	*	1-4 mm	
071KB	BSC	granite	M	1	*		*	*	*	*	*	*	*	*	*	*	*	*	*	*	*	*	*	1-8 mm	
JW 92-197	BSC	granite (dike)	M	1			*	*	*	*	*	*	*	*	*	*	*	*	*	*	*	*	*	1-3 mm	
JW95-261	BSC	granite (dike)	MS	1	*		*	*	*	*	*	*	*	*	*	*	*	*	*	*	*	*	*	1-4 mm	
JW 95-263	BSC	granite (dike)	MS	1			*	*	*	*	*	*	*	*	*	*	*	*	*	*	*	*	*	1-2 mm	
04-563	BSC	granodiorite	M	2	*	*	*	*	*	*	*	*	*	*	*	*	*	*	*	*	*	*	*	1-8 mm	
04-564	BSC	granodiorite	M	3	*	*	*	*	*	*	*	*	*	*	*	*	*	*	*	*	*	*	*	1-7 mm	
04-566	BSC	granodiorite	M	1			*	*	*	*	*	*	*	*	*	*	*	*	*	*	*	*	*	1-18 mm	
04-568	BSC	granodiorite	M	1			*	*	*	*	*	*	*	*	*	*	*	*	*	*	*	*	*	1-15 mm	
04-553	BSC	granodiorite	MS	3	*	*	*	*	*	*	*	*	*	*	*	*	*	*	*	*	*	*	*	1-4 mm	
04-565	BSC	granodiorite	M	1	*	*	*	*	*	*	*	*	*	*	*	*	*	*	*	*	*	*	*	1-7 mm	
JW 92-194	BSC	granodiorite	M	2	*	*	*	*	*	*	*	*	*	*	*	*	*	*	*	*	*	*	*	1-6 mm	
JW 92-195	BSC	granodiorite	M	2	*	*	*	*	*	*	*	*	*	*	*	*	*	*	*	*	*	*	*	1-8 mm	
JW 92-198	BSC	granodiorite	M	3	*	*	*	*	*	*	*	*	*	*	*	*	*	*	*	*	*	*	*	1-5 mm	
JW 92-199	BSC	granodiorite	M	2	*	*	*	*	*	*	*	*	*	*	*	*	*	*	*	*	*	*	*	1-7 mm	
JW 93-215	BSC	granodiorite	M	2	*	*	*	*	*	*	*	*	*	*	*	*	*	*	*	*	*	*	*	1-7 mm	
JW 93-216	BSC	granodiorite	MS	3	*	*	*	*	*	*	*	*	*	*	*	*	*	*	*	*	*	*	*	1-6 mm	
JW 95-259	BSC	granodiorite	SM	1			*	*	*	*	*	*	*	*	*	*	*	*	*	*	*	*	*	1-5 mm	
077KB	BSC	granodiorite	M	1			*	*	*	*	*	*	*	*	*	*	*	*	*	*	*	*	*	1-10 mm	
0711KB	BSC	granodiorite	M	2	*	*	*	*	*	*	*	*	*	*	*	*	*	*	*	*	*	*	*	1-5 mm	
0713KB	BSC	granodiorite	M	2	*	*	*	*	*	*	*	*	*	*	*	*	*	*	*	*	*	*	*	1-6 mm	
0714KB	BSC	granodiorite	M	2	*	*	*	*	*	*	*	*	*	*	*	*	*	*	*	*	*	*	*	1-5 mm	
04-548	BSC	tonalite	M	3	*	*	*	*	*	*	*	*	*	*	*	*	*	*	*	*	*	*	*	1-4 mm	

Table 3. (continued) Table of hand specimen fabric data

Sample	Rock Unit	IUGS Rock Name	Fabric Type	Magmatic Intensity	Magmatic Criteria										Solid-State Criteria										Grain Size	
					1	2	3	4	5	6	7	8	9	10	11	12	13	14	15	16	17	18	Range			
JW 95-256	BSC	tonalite	M	2	*	*	*	*	*	*	*	*	*	*	*	*	*	*	*	*	*	*	*	1-7 mm		
JW 95-264	BSC	tonalite	M	3	*	*	*	*	*	*	*	*	*	*	*	*	*	*	*	*	*	*	*	1-5 mm		
072KB	BSC	tonalite	M	3	*	*	*	*	*	*	*	*	*	*	*	*	*	*	*	*	*	*	*	1-3 mm		
073KB	BSC	tonalite	M	2	*	*	*	*	*	*	*	*	*	*	*	*	*	*	*	*	*	*	*	1-3 mm		
074KB	BSC	tonalite	M	3	*	*	*	*	*	*	*	*	*	*	*	*	*	*	*	*	*	*	*	1-2 mm		
076KB	BSC	tonalite	MS	3	*	*	*	*	*	*	*	*	*	*	*	*	*	*	*	*	*	*	*	1-3 mm		
0710KB	BSC	tonalite	M	2	*	*	*	*	*	*	*	*	*	*	*	*	*	*	*	*	*	*	*	1-8 mm		
0712KB	BSC	tonalite	M	3	*	*	*	*	*	*	*	*	*	*	*	*	*	*	*	*	*	*	*	1-5 mm		
JW 95-260	BSC	diorite	M	3	*	*	*	*	*	*	*	*	*	*	*	*	*	*	*	*	*	*	*	1-6 mm		
075KB	BSC	hornblende	M	1	*	*	*	*	*	*	*	*	*	*	*	*	*	*	*	*	*	*	*	1-6 mm		
04-523	BC	granodiorite	M	3	*	*	*	*	*	*	*	*	*	*	*	*	*	*	*	*	*	*	*	1-4 mm		
04-524	BC	granodiorite	M	2	*	*	*	*	*	*	*	*	*	*	*	*	*	*	*	*	*	*	*	1-3 mm		
04-525	BC	granodiorite	M	3	*	*	*	*	*	*	*	*	*	*	*	*	*	*	*	*	*	*	*	1-6 mm		
04-526	BC	granodiorite	M	2	*	*	*	*	*	*	*	*	*	*	*	*	*	*	*	*	*	*	*	1-4 mm		
04-527	BC	granodiorite	M	2	*	*	*	*	*	*	*	*	*	*	*	*	*	*	*	*	*	*	*	1-4 mm		
JW 00-340	BC	granodiorite	M	3	*	*	*	*	*	*	*	*	*	*	*	*	*	*	*	*	*	*	*	1-6 mm		
04-536	QMSC	alkali granite	MS	1	*	*	*	*	*	*	*	*	*	*	*	*	*	*	*	*	*	*	*	1-2 mm		
04-522	QMSC	granite	MS	1	*	*	*	*	*	*	*	*	*	*	*	*	*	*	*	*	*	*	*	1-2 mm		
04-532	QMSC	granite	MS	2	*	*	*	*	*	*	*	*	*	*	*	*	*	*	*	*	*	*	*	1-6 mm		
04-518	QMSC	granodiorite	M	2	*	*	*	*	*	*	*	*	*	*	*	*	*	*	*	*	*	*	*	1-10 mm		
04-520	QMSC	granodiorite	M	2	*	*	*	*	*	*	*	*	*	*	*	*	*	*	*	*	*	*	*	1-7 mm		
04-530	QMSC	granodiorite	M	2	*	*	*	*	*	*	*	*	*	*	*	*	*	*	*	*	*	*	*	1-4 mm		
04-531	QMSC	granodiorite	MS	2	*	*	*	*	*	*	*	*	*	*	*	*	*	*	*	*	*	*	*	1-7 mm		
04-534	QMSC	granodiorite	M	2	*	*	*	*	*	*	*	*	*	*	*	*	*	*	*	*	*	*	*	1-6 mm		
04-537	QMSC	granodiorite	M	2	*	*	*	*	*	*	*	*	*	*	*	*	*	*	*	*	*	*	*	1-7 mm		
QMSC-1	QMSC	granodiorite	M	2	*	*	*	*	*	*	*	*	*	*	*	*	*	*	*	*	*	*	*	1-8 mm		
QMSC-3	QMSC	granodiorite	M	2	*	*	*	*	*	*	*	*	*	*	*	*	*	*	*	*	*	*	*	1-6 mm		
QMSC-4	QMSC	granodiorite	M	2	*	*	*	*	*	*	*	*	*	*	*	*	*	*	*	*	*	*	*	1-5 mm		
QMSC-5	QMSC	granodiorite	MS	2	*	*	*	*	*	*	*	*	*	*	*	*	*	*	*	*	*	*	*	1-3 mm		
QMSC-10	QMSC	granodiorite	MS	2	*	*	*	*	*	*	*	*	*	*	*	*	*	*	*	*	*	*	*	1-2 mm		
04-521	QMSC	tonalite	M	2	*	*	*	*	*	*	*	*	*	*	*	*	*	*	*	*	*	*	*	1-2 mm		
04-535	QMSC	tonalite	M	3	*	*	*	*	*	*	*	*	*	*	*	*	*	*	*	*	*	*	*	1-2 mm		
QMSC-2	QMSC	tonalite	MS	3	*	*	*	*	*	*	*	*	*	*	*	*	*	*	*	*	*	*	*	1-2 mm		

Table 3. (continued) Table of hand specimen fabric data

Sample	Rock Unit	IUGS Rock Name	Fabric Type	Magmatic Intensity	Magmatic Criteria										Solid-State Criteria										Grain Size Range
					Magma (Cumulus) Crystallization										Solid-State Crystallization										
					1	2	3	4	5	6	7	8	9	10	11	12	13	14	15	16	17	18			
04-533	SS	granite	MS	1		*	*	*	*	*					*								1-3 mm		
04-541	SS	granite	MS	1			*	*	*	*					*								1-2 mm		
04-544	SS	granite	M	2	*		*	*	*	*													1-2 mm		
04-545	SS	granite	M	1	*		*	*	*	*													1-4 mm		
04-551	SS	granite	M	2	*		*	*	*	*											*		1-4 mm		
04-556	SS	granite	MS	1			*	*	*	*					*						*		1-4 mm		
04-557	SS	granite	MS	1			*	*	*	*					*						*		1-3 mm		
04-558	SS	granite	M	1			*	*	*	*													1-2 mm		
04-546	SS	granodiorite	M	3	*		*	*	*	*													1-7 mm		
03-501	Kp	granite	M	2	*		*	*	*	*													1-8 mm		
03-515	Kp	granite	M	1			*	*	*	*													1-8 mm		
04-561	Kp	granite	M	1			*	*	*	*													1-6 mm		
JW 93-221	Kp	granite	M	1			*	*	*	*													1-6 mm		
JW 93-223	Kp	granite	M	1			*	*	*	*													1-8 mm		
JW 93-224	Kp	granite	M	1			*	*	*	*													1-6 mm		
JW 93-222	Kp	granite	M	1	*		*	*	*	*													1-5 mm		
03-506	Kst	granodiorite	M	1			*	*	*	*													1-6 mm		
04-528	Kst	granite	M	1			*	*	*	*													1-8 mm		
JW92-178	Kwt	granite	MS	1			*	*	*	*					*								1-15 mm		
JW92-179	Kwt	granite	M	1			*	*	*	*													1-5 mm		
JW92-176	Kwt	granodiorite	M	2	*		*	*	*	*													1-15 mm		
JW92-190	-	granite	MS	1			*	*	*	*					*				*				1-4 mm		
JW 92-191	-	granite	M	1	*		*	*	*	*													1-5 mm		
JW 92-192	-	alkali granite	M	1			*	*	*	*													1-10 mm		
JW 93-218	-	granite	M	1			*	*	*	*													1-8 mm		
JW 93-219	-	granodiorite	M	1	*		*	*	*	*													1-6 mm		

Table 4. Table of hand specimen mineralogy data

Sample	Rock Unit	IUGS Rock Name	Primary Phases										Accessory Phases				Secondary Phases	
			Quartz	Plag	K-spar	Musc	Biotite	Hbl	Sphene	Garnet	Allanite	Zircon	Opakes	Epidote	Chlorite			
			*	*	*	*	*	*	*	*	*	*	*	*	*	*		
04-549	BSC	granite	*	*	*	*	*							*		*		
04-550	BSC	granite	*	*			*							*		*		
04-554	BSC	granite	*	*	*		*							*		*		
04-562	BSC	granite	*	*	*		*							*		*		
04-567	BSC	granite	*	*	*		*							*		*		
JW 92-193	BSC	granite	*	*	*	*	*							*		*		
JW 92-196	BSC	granite	*	*	*		*							*		*		
JW 93-217	BSC	granite	*	*	*		*							*		*		
JW 95-258	BSC	granite	*	*	*		*							*		*		
JW 95-262	BSC	granite	*	*	*		*							*		*		
071KB	BSC	granite	*	*	*		*							*		*		
JW 92-197	BSC	granite (dike)	*	*	*		*							*		*		
JW 95-263	BSC	granite (dike)	*	*	*	*	*							*		*		
04-563	BSC	granodiorite	*	*	*		*							*		*		
04-564	BSC	granodiorite	*	*	*		*							*		*		
04-566	BSC	granodiorite	*	*	*		*							*		*		
04-568	BSC	granodiorite	*	*	*		*		*					*		*		
04-553	BSC	granodiorite	*	*	*		*		*					*		*		
04-565	BSC	granodiorite	*	*	*		*		*					*		*		
JW 92-194	BSC	granodiorite	*	*	*		*		*					*		*		
JW 92-195	BSC	granodiorite	*	*	*		*		*					*		*		
JW 92-198	BSC	granodiorite	*	*	*		*		*					*		*		
JW 92-199	BSC	granodiorite	*	*	*		*		*					*		*		
JW 93-215	BSC	granodiorite	*	*	*		*		*					*		*		
JW 93-216	BSC	granodiorite	*	*	*		*		*					*		*		
077KB	BSC	granodiorite	*	*	*		*		*					*		*		
0713KB	BSC	granodiorite	*	*	*		*		*					*		*		
04-548	BSC	tonalite	*	*	*		*		*					*		*		
JW 95-256	BSC	tonalite	*	*	*		*		*					*		*		
JW 95-264	BSC	tonalite	*	*	*		*		*					*		*		
072KB	BSC	tonalite	*	*	*		*		*					*		*		
074KB	BSC	tonalite	*	*	*		*		*					*		*		
076KB	BSC	tonalite	*	*	*		*		*					*		*		
0710KB	BSC	tonalite	*	*	*		*		*					*		*		
JW 95-260	BSC	diorite	*	*	*		*		*					*		*		
075KB	BSC	hornblendite	*	*	*		*		*					*		*		

Table 4. (continued) Table of hand specimen mineralogy data

Sample	Rock Unit	IUGS Rock Name	Primary Phases					Accessory Phases				Secondary Phases		
			Quartz	Plag	K-spar	Musc	Biotite	Hbl	Sphene	Garnet	Allanite	Zircon	Opagues	Epidote
04-523	BC	granodiorite	*	*	*		*	*				*	*	*
04-524	BC	granodiorite	*	*	*		*	*				*	*	*
04-525	BC	granodiorite	*	*	*		*	*		*		*	*	*
04-526	BC	granodiorite	*	*	*		*	*				*	*	*
04-527	BC	granodiorite	*	*	*		*	*				*	*	*
04-536	QMSC	alkali granite	*	*	*	*						*	*	*
04-522	QMSC	granite	*	*	*				*			*	*	
04-532	QMSC	granite	*	*	*					*		*	*	*
04-518	QMSC	granodiorite	*	*	*		*	*		*		*	*	*
04-520	QMSC	granodiorite	*	*	*		*	*				*	*	*
04-530	QMSC	granodiorite	*	*	*	*						*	*	*
04-531	QMSC	granodiorite	*	*	*		*	*				*	*	*
04-534	QMSC	granodiorite	*	*	*		*	*		*		*	*	*
04-537	QMSC	granodiorite	*	*	*		*	*				*	*	*
04-521	QMSC	tonalite	*	*	*		*	*				*	*	*
04-535	QMSC	tonalite	*	*	*		*	*				*	*	*
04-533	SS	granite	*	*	*		*	*		*		*	*	*
04-541	SS	granite	*	*	*	*	*	*	*			*	*	
04-544	SS	granite	*	*	*		*	*				*	*	
04-545	SS	granite	*	*	*		*	*				*	*	
04-551	SS	granite	*	*	*		*	*		*		*	*	
04-556	SS	granite	*	*	*	*	*	*	*			*	*	
04-557	SS	granite	*	*	*	*	*	*				*	*	
04-558	SS	granite	*	*	*	*	*	*	*			*	*	
04-546	SS	granodiorite	*	*	*	*	*	*	*	*		*	*	*
03-501	Kp	granite	*	*	*	*	*	*		*		*	*	*
03-515	Kp	granite	*	*	*	*	*	*		*		*	*	*
04-528	Kp	granite	*	*	*	*	*	*		*		*	*	*
04-561	Kp	granite	*	*	*	*	*	*		*		*	*	*
JW 93-221	Kp	granite	*	*	*	*	*	*		*		*	*	*
JW 93-222	Kp	granodiorite	*	*	*	*	*	*	*	*		*	*	*
JW 93-223	Kp	granite	*	*	*	*	*	*		*		*	*	*
JW 93-224	Kp	granite	*	*	*	*	*	*		*		*	*	*
03-506	Kst	granite	*	*	*	*	*	*		*		*	*	*
JW92-178	Kwt	granite	*	*	*	*	*	*		*		*	*	*
JW92-179	Kwt	granite	*	*	*	*	*	*		*		*	*	*
JW92-176	Kwt	granodiorite	*	*	*	*	*	*		*		*	*	*

Table 4. (continued) Table of hand specimen mineralogy data

Sample	Rock Unit	IUGS Rock Name	Primary Phases										Accessory Phases				Secondary Phases	
			Quartz	Plag	K-spar	Musc	Biotite	Hbl	Sphene	Garnet	Allanite	Zircon	Opaques	Epidote	Chlorite			
JW92-190	-	granite	*	*	*	*	*	*				*	*		*			
JW 92-191	-	granite	*	*	*	*	*	*				*	*		*			
JW 92-192	-	alkali granite	*	*	*	*	*	*		*		*	*		*			
JW 93-218	-	granite	*	*	*	*	*	*		*		*	*		*			
JW 93-219	-	granodiorite	*	*	*	*	*	*		*		*	*	*	*			

Table 5. Table of quartz microstructures

Sample	Rock Unit	IUGS Rock Name	Quartz (Magmatic)			Quartz - SS > 500°C			Submagmatic (SS - 500-400°C)			Quartz (SS < 400°C)		
			1 2 3			1 2 3			1 2 3			1 2 3		
			1	2	3	1	2	3	1	2	3	1	2	3
04-549	BSC	granite	*	*	*	*	*	*	*	*	*	*	*	*
04-550	BSC	granite	*		*	*	*	*						
04-554	BSC	granite			*	*	*	*					*	
04-562	BSC	granite	*	*	*	*	*	*						
04-567	BSC	granite	*	*	*	*	*	*						
JW 92-193	BSC	granite	*	*	*	*	*	*						
JW 92-196	BSC	granite	*	*	*	*	*	*						
JW 93-217	BSC	granite	*	*	*	*	*	*	*	*	*			
JW 95-258	BSC	granite	*	*	*	*	*	*				*	*	*
JW 95-262	BSC	granite	*	*	*	*	*	*				*	*	*
071KB	BSC	granite	*	*	*	*	*	*				*		
JW 95-263	BSC	granite (dike)	*	*	*	*	*	*				*		
04-564	BSC	granodiorite	*	*	*	*	*	*						
04-566	BSC	granodiorite	*	*	*	*	*	*		*	*			
04-568	BSC	granodiorite	*	*	*	*	*	*		*	*		*	*
04-553	BSC	granodiorite	*	*	*	*	*	*		*	*		*	*
04-565	BSC	granodiorite	*	*	*	*	*	*		*	*			
JW 92-195	BSC	granodiorite	*	*	*	*	*	*		*	*			
JW 92-198	BSC	granodiorite	*	*	*	*	*	*		*	*			
JW 92-199	BSC	granodiorite	*	*	*	*	*	*		*	*			
JW 93-215	BSC	granodiorite	*	*	*	*	*	*		*	*			
JW 93-216	BSC	granodiorite	*	*	*	*	*	*		*	*		*	*
077KB	BSC	granodiorite	*	*	*	*	*	*		*	*			
0713KB	BSC	granodiorite	*	*	*	*	*	*		*	*			
04-548	BSC	tonalite	*	*	*	*	*	*		*	*		*	*
JW 95-256	BSC	tonalite	*	*	*	*	*	*		*	*			
JW 95-264	BSC	tonalite	*	*	*	*	*	*		*	*			
072KB	BSC	tonalite	*	*	*	*	*	*		*	*			
074KB	BSC	tonalite	*	*	*	*	*	*		*	*		*	*
076KB	BSC	tonalite	*	*	*	*	*	*		*	*		*	*
0710KB	BSC	tonalite	*	*	*	*	*	*		*	*		*	*
075KB	BSC	hornblende	*	*	*	*	*	*		*	*		*	*

Table 5. (continued) Table of quartz microstructures

Sample	Rock Unit	IUGS Rock Name	Quartz (Magmatic)			Quartz (Submagmatic - SS >500°C)			Quartz (SS - 500-400°C)			Quartz (SS <400°C)		
			1	2	3	1	2	3	1	2	3	1	2	3
04-523	BC	granodiorite	*	*	*	*	*	*	*	*	*			
04-524	BC	granodiorite	*	*	*	*	*	*						
04-525	BC	granodiorite	*	*	*	*	*	*					*	
04-526	BC	granodiorite	*	*	*	*	*	*						
04-527	BC	granodiorite	*	*	*	*	*	*						
04-536	QMSC	alkali granite	*		*	*	*	*	*	*	*			
04-522	QMSC	granite				*							*	
04-532	QMSC	granite	*	*	*	*	*	*	*	*	*		*	
04-518	QMSC	granodiorite	*	*	*	*	*	*	*	*	*			
04-520	QMSC	granodiorite	*	*	*	*	*	*	*	*	*			
04-530	QMSC	granodiorite	*	*	*	*	*	*	*	*	*			
04-531	QMSC	granodiorite	*	*	*	*	*	*	*	*	*			
04-534	QMSC	granodiorite	*	*	*	*	*	*	*	*	*		*	
04-537	QMSC	granodiorite	*	*	*	*	*	*	*	*	*			
04-521	QMSC	tonalite	*	*	*	*	*	*						
04-535	QMSC	tonalite	*	*	*	*	*	*						
04-533	SS	granite	*	*	*	*	*	*	*	*	*		*	
04-541	SS	granite	*	*	*	*	*	*	*	*	*		*	
04-544	SS	granite	*	*	*	*	*	*	*	*	*		*	
04-545	SS	granite	*	*	*	*	*	*	*	*	*		*	
04-551	SS	granite	*	*	*	*	*	*	*	*	*		*	
04-556	SS	granite	*	*	*	*	*	*	*	*	*		*	
04-557	SS	granite	*	*	*	*	*	*	*	*	*		*	
04-558	SS	granite	*	*	*	*	*	*	*	*	*		*	
04-546	SS	granodiorite	*	*	*	*	*	*	*	*	*		*	
03-501	Kp	granite	*	*	*	*	*	*	*	*	*		*	
03-506	Kp	granite	*	*	*	*	*	*	*	*	*		*	
03-515	Kp	granite	*	*	*	*	*	*	*	*	*		*	
04-561	Kp	granite	*	*	*	*	*	*	*	*	*		*	
04-528	Kst	granite	*	*	*	*	*	*	*	*	*		*	

Table 6. Table of plagioclase microstructures

Sample	Rock Unit	IUGS Rock Name	Plagioclase (Magmatic)				Plagioclase (Submagmatic - SS >500°C)				Plagioclase (SS - 500-400°C)				Plagioclase (SS <400°C)			
			1	2	3	4	1	2	3	4	1	2	3	4	1	2	3	4
			1	2	3	4	1	2	3	4	1	2	3	4	1	2	3	4
04-549	BSC	granite	*				*		*	*								*
04-550	BSC	granite	*	*			*		*	*		*						*
04-554	BSC	granite					*		*	*								*
04-562	BSC	granite	*	*	*	*			*	*								*
04-567	BSC	granite		*	*				*	*								*
JW 92-193	BSC	granite	*	*	*	*	*		*	*								*
JW 92-196	BSC	granite					*		*	*								*
JW 93-217	BSC	granite					*		*	*								*
JW 95-258	BSC	granite					*		*	*								*
JW 95-262	BSC	granite		*	*	*	*		*	*		*						*
071KB	BSC	granite	*	*	*	*	*		*	*		*						*
JW 95-263	BSC	granite (dike)		*	*	*	*		*	*		*						*
04-564	BSC	granodiorite		*	*	*	*		*	*		*						*
04-566	BSC	granodiorite		*	*	*	*		*	*		*						*
04-568	BSC	granodiorite		*	*	*	*		*	*		*						*
04-553	BSC	granodiorite			*	*	*		*	*		*						*
04-565	BSC	granodiorite	*	*	*	*	*		*	*		*						*
JW 92-195	BSC	granodiorite		*	*	*	*		*	*		*						*
JW 92-198	BSC	granodiorite		*	*	*	*		*	*		*						*
JW 92-199	BSC	granodiorite		*	*	*	*		*	*		*						*
JW 93-215	BSC	granodiorite			*	*	*		*	*		*						*
JW 93-216	BSC	granodiorite					*		*	*		*						*
077KB	BSC	granodiorite	*	*	*	*	*		*	*		*						*
0713KB	BSC	granodiorite		*	*	*	*		*	*		*						*
04-548	BSC	tonalite			*	*	*		*	*		*						*
JW 95-256	BSC	tonalite			*	*	*		*	*		*						*
JW 95-264	BSC	tonalite	*	*	*	*	*		*	*		*						*
072KB	BSC	tonalite	*	*	*	*	*		*	*		*						*
074KB	BSC	tonalite	*	*	*	*	*		*	*		*						*
076KB	BSC	tonalite	*	*	*	*	*		*	*		*						*
0710KB	BSC	tonalite	*	*	*	*	*		*	*		*						*
075KB	BSC	hornblende		*	*	*	*		*	*		*						*

Table 6. (continued) Table of plagioclase microstructures

Sample	Rock Unit	IUGS Rock Name	Plagioclase (Magmatic)				Plagioclase (Submagmatic - SS >500°C)				Plagioclase (SS - 500-400°C)				Plagioclase (SS <400°C)			
			1	2	3	4	1	2	3	4	1	2	3	4	1	2	3	4
			1	2	3	4	1	2	3	4	1	2	3	4	1	2	3	4
04-523	BC	granodiorite	*	*	*	*	*		*	*				*				*
04-524	BC	granodiorite	*	*	*	*	*		*	*				*				*
04-525	BC	granodiorite	*	*	*	*	*		*	*				*				*
04-526	BC	granodiorite	*	*	*	*	*		*	*				*				*
04-527	BC	granodiorite	*	*	*	*	*		*	*				*				*
04-536	QMSC	alkali granite					*		*	*				*				*
04-522	QMSC	granite					*		*	*				*				*
04-532	QMSC	granite		*	*	*	*		*	*				*				*
04-518	QMSC	granodiorite	*	*	*	*	*		*	*				*				*
04-520	QMSC	granodiorite	*	*	*	*	*		*	*				*				*
04-530	QMSC	granodiorite	*	*	*	*	*		*	*				*				*
04-531	QMSC	granodiorite	*	*	*	*	*		*	*				*				*
04-534	QMSC	granodiorite	*	*	*	*	*		*	*				*				*
04-537	QMSC	granodiorite	*	*	*	*	*		*	*				*				*
04-521	QMSC	tonalite	*	*	*	*	*		*	*				*				*
04-535	QMSC	tonalite	*	*	*	*	*		*	*				*				*
04-533	SS	granite		*	*	*	*		*	*				*				*
04-541	SS	granite		*	*	*	*		*	*				*				*
04-544	SS	granite		*	*	*	*		*	*				*				*
04-545	SS	granite		*	*	*	*		*	*				*				*
04-551	SS	granite		*	*	*	*		*	*				*				*
04-556	SS	granite		*	*	*	*		*	*				*				*
04-557	SS	granite		*	*	*	*		*	*				*				*
04-558	SS	granite		*	*	*	*		*	*				*				*
04-546	SS	granodiorite	*	*	*	*	*		*	*				*				*
03-501	Kp	granite	*	*	*	*	*		*	*				*				*
03-515	Kp	granite	*	*	*	*	*		*	*				*				*
04-561	Kp	granite	*	*	*	*	*		*	*				*				*
03-506	Kst	granite	*	*	*	*	*		*	*				*				*
04-528	Kst	granite	*	*	*	*	*		*	*				*				*

Table 7. Table of potassium feldspar (K-spar) microstructures

Sample	Rock Unit	IUGS Rock Name	K-Spar (Magmatic)				K-Spar (Submagmatic - SS >500°C)				K-Spar (SS - 500-400°C)				K-Spar (SS <400°C)			
			1	2	3	4	1	2	3	4	1	2	3	4	1	2	3	4
			1	2	3	4	1	2	3	4	1	2	3	4	1	2	3	4
04-549	BSC	granite					*			*				*				*
04-550	BSC	granite					*			*				*				*
04-554	BSC	granite					*			*				*				*
04-562	BSC	granite					*			*				*				*
04-567	BSC	granite					*			*				*				*
JW 92-193	BSC	granite					*			*				*				*
JW 92-196	BSC	granite					*			*				*				*
JW 93-217	BSC	granite					*			*				*				*
JW 95-258	BSC	granite					*			*				*				*
JW 95-262	BSC	granite					*			*				*				*
071KB	BSC	granite	*				*			*				*				*
JW 95-263	BSC	granite (dike)					*			*				*				*
04-564	BSC	granodiorite					*			*				*				*
04-566	BSC	granodiorite					*			*				*				*
04-568	BSC	granodiorite					*			*				*				*
04-553	BSC	granodiorite					*			*				*				*
04-565	BSC	granodiorite					*			*				*				*
JW 92-195	BSC	granodiorite					*			*				*				*
JW 92-198	BSC	granodiorite					*			*				*				*
JW 92-199	BSC	granodiorite					*			*				*				*
JW 93-215	BSC	granodiorite					*			*				*				*
JW 93-216	BSC	granodiorite					*			*				*				*
077KB	BSC	granodiorite	*				*			*				*				*
0713KB	BSC	granodiorite					*			*				*				*
04-548	BSC	tonalite					*			*				*				*
JW 95-256	BSC	tonalite					*			*				*				*
JW 95-264	BSC	tonalite	*				*			*				*				*
072KB	BSC	tonalite	*				*			*				*				*
074KB	BSC	tonalite					*			*				*				*
076KB	BSC	tonalite					*			*				*				*
0710KB	BSC	tonalite					*			*				*				*
075KB	BSC	hornblende					*			*				*				*

Table 7. (continued) Table of potassium feldspar (K-spar) microstructures

Sample	Rock Unit	IUGS Rock Name	K-Spar (Magmatic)				K-Spar (Submagmatic - SS >500°C)				K-Spar (SS - 500-400°C)				K-Spar (SS <400°C)			
			1	2	3	4	1	2	3	4	1	2	3	4	1	2	3	4
04-523	BC	granodiorite					*			*								*
04-524	BC	granodiorite					*			*								
04-525	BC	granodiorite					*			*								
04-526	BC	granodiorite					*			*								*
04-527	BC	granodiorite					*			*								*
04-536	QMSC	alkali granite					*	*		*								*
04-522	QMSC	granite					*	*		*								*
04-532	QMSC	granite		*			*			*								*
04-518	QMSC	granodiorite					*			*								*
04-520	QMSC	granodiorite					*			*								*
04-530	QMSC	granodiorite	*				*			*								*
04-531	QMSC	granodiorite		*			*			*								*
04-534	QMSC	granodiorite		*		*	*			*								*
04-537	QMSC	granodiorite					*			*								*
04-521	QMSC	tonalite																
04-535	QMSC	tonalite	*				*											*
04-533	SS	granite		*			*			*								*
04-541	SS	granite					*	*		*								*
04-544	SS	granite		*			*			*								*
04-545	SS	granite					*			*								*
04-551	SS	granite					*			*								*
04-556	SS	granite		*			*			*			*					*
04-557	SS	granite					*			*			*					*
04-558	SS	granite					*			*			*					*
04-546	SS	granodiorite		*			*			*			*					*
03-501	Kp	granite		*		*	*			*			*					*
03-515	Kp	granite					*			*			*					*
04-561	Kp	granite					*			*			*					*
03-506	Kst	granite					*			*			*					*
04-528	Kst	granite	*				*			*			*					*

Table 8. Table of biotite microstructures

Sample	Rock Unit	IUGS Rock Name	Biotite (Magmatic)			Biotite (Submagmatic - SS >500°C)			Biotite (SS - 500-400°C)			Biotite (SS <400°C)	
			1	2	3	1	2	3	1	2	1	1	2
04-549	BSC	granite		*	*		*	*				*	*
04-550	BSC	granite		*			*	*				*	*
04-554	BSC	granite		*	*		*	*				*	*
04-562	BSC	granite	*	*	*		*	*				*	*
04-567	BSC	granite	*	*	*		*	*				*	*
JW 92-193	BSC	granite		*	*		*	*				*	*
JW 92-196	BSC	granite			*		*	*				*	*
JW 93-217	BSC	granite						*				*	*
JW 95-258	BSC	granite	*	*	*		*	*				*	*
JW 95-262	BSC	granite	*	*	*		*	*				*	*
071KB	BSC	granite	*	*	*		*	*				*	*
JW 95-263	BSC	granite (dike)					*	*			*	*	*
04-564	BSC	granodiorite	*	*	*		*	*			*	*	*
04-566	BSC	granodiorite	*	*	*		*	*			*	*	*
04-568	BSC	granodiorite			*		*	*				*	*
04-553	BSC	granodiorite	*	*	*		*	*				*	*
04-565	BSC	granodiorite	*	*	*		*	*				*	*
JW 92-195	BSC	granodiorite	*	*	*		*	*			*	*	*
JW 92-198	BSC	granodiorite	*	*	*		*	*			*	*	*
JW 92-199	BSC	granodiorite	*	*	*		*	*			*	*	*
JW 93-215	BSC	granodiorite	*	*	*		*	*			*	*	*
JW 93-216	BSC	granodiorite	*	*	*		*	*			*	*	*
077KB	BSC	granodiorite	*	*	*		*	*				*	*
0713KB	BSC	granodiorite	*	*	*		*	*				*	*
04-548	BSC	tonalite		*	*		*	*				*	*
JW 95-256	BSC	tonalite		*	*		*	*				*	*
JW 95-264	BSC	tonalite	*	*	*		*	*				*	*
072KB	BSC	tonalite	*	*	*		*	*				*	*
074KB	BSC	tonalite	*	*	*		*	*				*	*
076KB	BSC	tonalite	*	*	*		*	*				*	*
0710KB	BSC	tonalite	*	*	*		*	*				*	*
075KB	BSC	hornblendite	*	*	*		*	*				*	*

Table 8. (continued) Table of biotite microstructures

Sample	Rock Unit	IUGS Rock Name	Biotite (Migmatic)						Biotite (Submagmatic - SS >500°C)						Biotite (SS - 500-400°C)						Biotite (SS <400°C)					
			1			2			3			1			2			1			2			1		
			1	2	3	1	2	3	1	2	3	1	2	3	1	2	3	1	2	3	1	2	1	2	1	2
04-523	BC	granodiorite	*	*	*	*	*	*	*	*	*	*	*	*	*	*	*	*	*	*	*	*	*	*	*	*
04-524	BC	granodiorite	*	*	*	*	*	*	*	*	*	*	*	*	*	*	*	*	*	*	*	*	*	*	*	*
04-525	BC	granodiorite	*	*	*	*	*	*	*	*	*	*	*	*	*	*	*	*	*	*	*	*	*	*	*	*
04-526	BC	granodiorite	*	*	*	*	*	*	*	*	*	*	*	*	*	*	*	*	*	*	*	*	*	*	*	*
04-527	BC	granodiorite	*	*	*	*	*	*	*	*	*	*	*	*	*	*	*	*	*	*	*	*	*	*	*	*
04-536	QMSC	alkali granite																								
04-522	QMSC	granite																								
04-532	QMSC	granite	*	*	*	*	*	*	*	*	*	*	*	*	*	*	*	*	*	*	*	*	*	*	*	*
04-518	QMSC	granodiorite	*	*	*	*	*	*	*	*	*	*	*	*	*	*	*	*	*	*	*	*	*	*	*	*
04-520	QMSC	granodiorite	*	*	*	*	*	*	*	*	*	*	*	*	*	*	*	*	*	*	*	*	*	*	*	*
04-530	QMSC	granodiorite	*	*	*	*	*	*	*	*	*	*	*	*	*	*	*	*	*	*	*	*	*	*	*	*
04-531	QMSC	granodiorite	*	*	*	*	*	*	*	*	*	*	*	*	*	*	*	*	*	*	*	*	*	*	*	*
04-534	QMSC	granodiorite	*	*	*	*	*	*	*	*	*	*	*	*	*	*	*	*	*	*	*	*	*	*	*	*
04-537	QMSC	granodiorite	*	*	*	*	*	*	*	*	*	*	*	*	*	*	*	*	*	*	*	*	*	*	*	*
04-521	QMSC	tonalite	*	*	*	*	*	*	*	*	*	*	*	*	*	*	*	*	*	*	*	*	*	*	*	*
04-535	QMSC	tonalite	*	*	*	*	*	*	*	*	*	*	*	*	*	*	*	*	*	*	*	*	*	*	*	*
04-533	SS	granite	*	*	*	*	*	*	*	*	*	*	*	*	*	*	*	*	*	*	*	*	*	*	*	*
04-541	SS	granite	*	*	*	*	*	*	*	*	*	*	*	*	*	*	*	*	*	*	*	*	*	*	*	*
04-544	SS	granite	*	*	*	*	*	*	*	*	*	*	*	*	*	*	*	*	*	*	*	*	*	*	*	*
04-545	SS	granite	*	*	*	*	*	*	*	*	*	*	*	*	*	*	*	*	*	*	*	*	*	*	*	*
04-551	SS	granite	*	*	*	*	*	*	*	*	*	*	*	*	*	*	*	*	*	*	*	*	*	*	*	*
04-556	SS	granite	*	*	*	*	*	*	*	*	*	*	*	*	*	*	*	*	*	*	*	*	*	*	*	*
04-557	SS	granite	*	*	*	*	*	*	*	*	*	*	*	*	*	*	*	*	*	*	*	*	*	*	*	*
04-558	SS	granite	*	*	*	*	*	*	*	*	*	*	*	*	*	*	*	*	*	*	*	*	*	*	*	*
04-546	SS	granodiorite	*	*	*	*	*	*	*	*	*	*	*	*	*	*	*	*	*	*	*	*	*	*	*	*
03-501	Kp	granite	*	*	*	*	*	*	*	*	*	*	*	*	*	*	*	*	*	*	*	*	*	*	*	*
03-515	Kp	granite	*	*	*	*	*	*	*	*	*	*	*	*	*	*	*	*	*	*	*	*	*	*	*	*
04-561	Kp	granite	*	*	*	*	*	*	*	*	*	*	*	*	*	*	*	*	*	*	*	*	*	*	*	*
03-506	Kst	granite	*	*	*	*	*	*	*	*	*	*	*	*	*	*	*	*	*	*	*	*	*	*	*	*
04-528	Kst	granite	*	*	*	*	*	*	*	*	*	*	*	*	*	*	*	*	*	*	*	*	*	*	*	*

Table 9. Table of hornblende and sphene microstructures

Sample	Rock Unit	IUGS Rock Name	Hornblende				Sphene			
			1	2	3	4	1	2	3	4
04-549	BSC	granite								
04-550	BSC	granite								
04-554	BSC	granite								
04-562	BSC	granite								
04-567	BSC	granite								
JW 92-193	BSC	granite								
JW 92-196	BSC	granite								
JW 93-217	BSC	granite								
JW 95-258	BSC	granite								
JW 95-262	BSC	granite								
071KB	BSC	granite								
JW 95-263	BSC	granite (dike)								
04-564	BSC	granodiorite								
04-566	BSC	granodiorite								
04-568	BSC	granodiorite					*		*	
04-553	BSC	granodiorite		*	*	*	*	*	*	*
04-565	BSC	granodiorite	*	*			*	*		*
JW 92-195	BSC	granodiorite	*	*	*	*	*		*	*
JW 92-198	BSC	granodiorite			*	*	*			*
JW 92-199	BSC	granodiorite		*	*	*	*	*		*
JW 93-215	BSC	granodiorite								
JW 93-216	BSC	granodiorite								
077KB	BSC	granodiorite	*	*	*	*	*			*
0713KB	BSC	granodiorite								
04-548	BSC	tonalite		*	*	*		*	*	*
JW 95-256	BSC	tonalite			*	*			*	*
JW 95-264	BSC	tonalite		*	*	*			*	*
072KB	BSC	tonalite		*		*	*		*	*
074KB	BSC	tonalite			*	*			*	*
076KB	BSC	tonalite					*			*
0710KB	BSC	tonalite	*	*			*			*
075KB	BSC	hornblendite	*	*			*			*

Table 9. (continued) Table of hornblende and sphene microstructures

Sample	Rock Unit	IUGS Rock Name	Hornblende				Sphene			
			1	2	3	4	1	2	3	4
04-523	BC	granodiorite	*			*	*			*
04-524	BC	granodiorite								*
04-525	BC	granodiorite					*			*
04-526	BC	granodiorite					*			*
04-527	BC	granodiorite					*			*
04-536	QMSC	alkali granite								
04-522	QMSC	granite								
04-532	QMSC	granite								
04-518	QMSC	granodiorite	*	*		*	*			*
04-520	QMSC	granodiorite	*	*		*	*	*		*
04-530	QMSC	granodiorite								
04-531	QMSC	granodiorite		*	*	*			*	*
04-534	QMSC	granodiorite	*	*	*	*	*	*	*	
04-537	QMSC	granodiorite	*		*	*	*		*	*
04-521	QMSC	tonalite	*	*			*			*
04-535	QMSC	tonalite	*	*					*	
04-533	SS	granite								
04-541	SS	granite								
04-544	SS	granite								
04-545	SS	granite								
04-551	SS	granite								
04-556	SS	granite								
04-557	SS	granite								
04-558	SS	granite								
04-546	SS	granodiorite	*		*	*	*		*	*
03-501	Kp	granite								
03-515	Kp	granite								
04-561	Kp	granite								
03-506	Kst	granite	*	*			*			
04-528	Kst	granite								

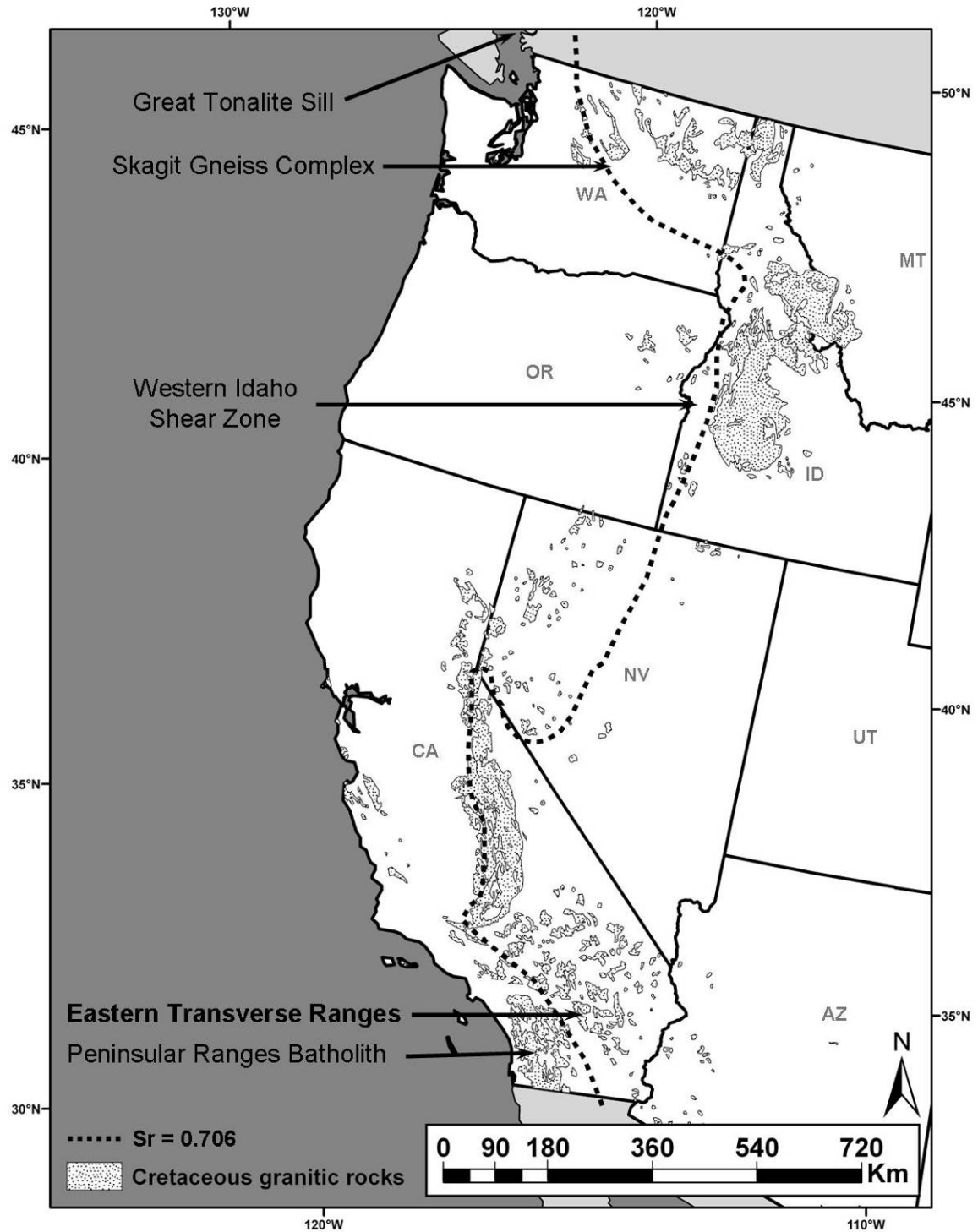


Figure 1. Regional map of the western U.S. showing the distribution of sheeted complexes within the North American Cretaceous-Paleogene magmatic arc (after Anderson, 1990). Approximate location of the Sr 0.706 line (dotted line) after Kistler (1990) and Miller et al. (1990).

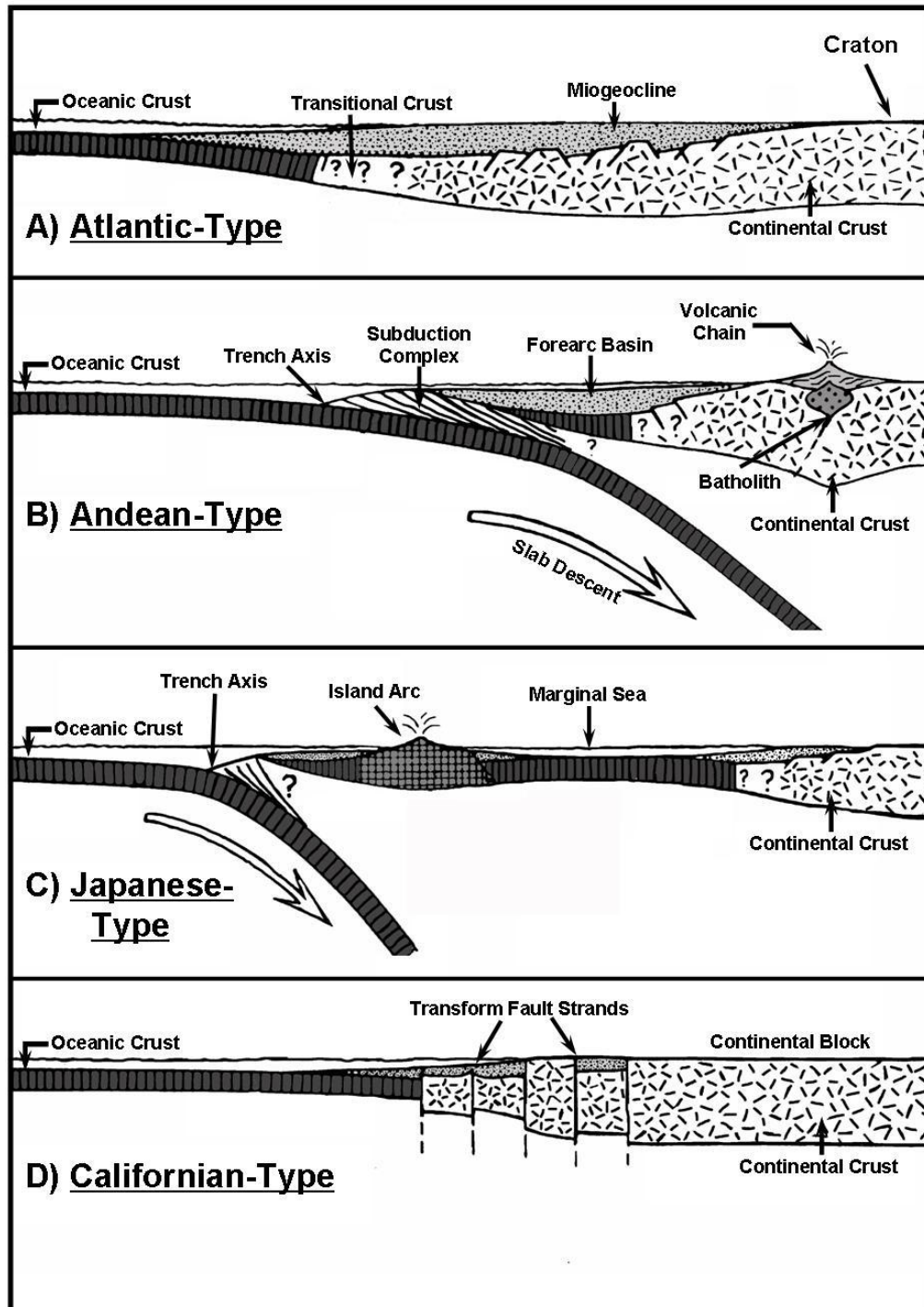


Figure 2. Four tectonic configurations of continental margins modified from Dickinson (1981): (A) Atlantic-type, (B) Andean-type, (C) Japanese-type, and (D) Californian-type. The Andean-type configuration was the dominant tectonic configuration throughout the Mesozoic.

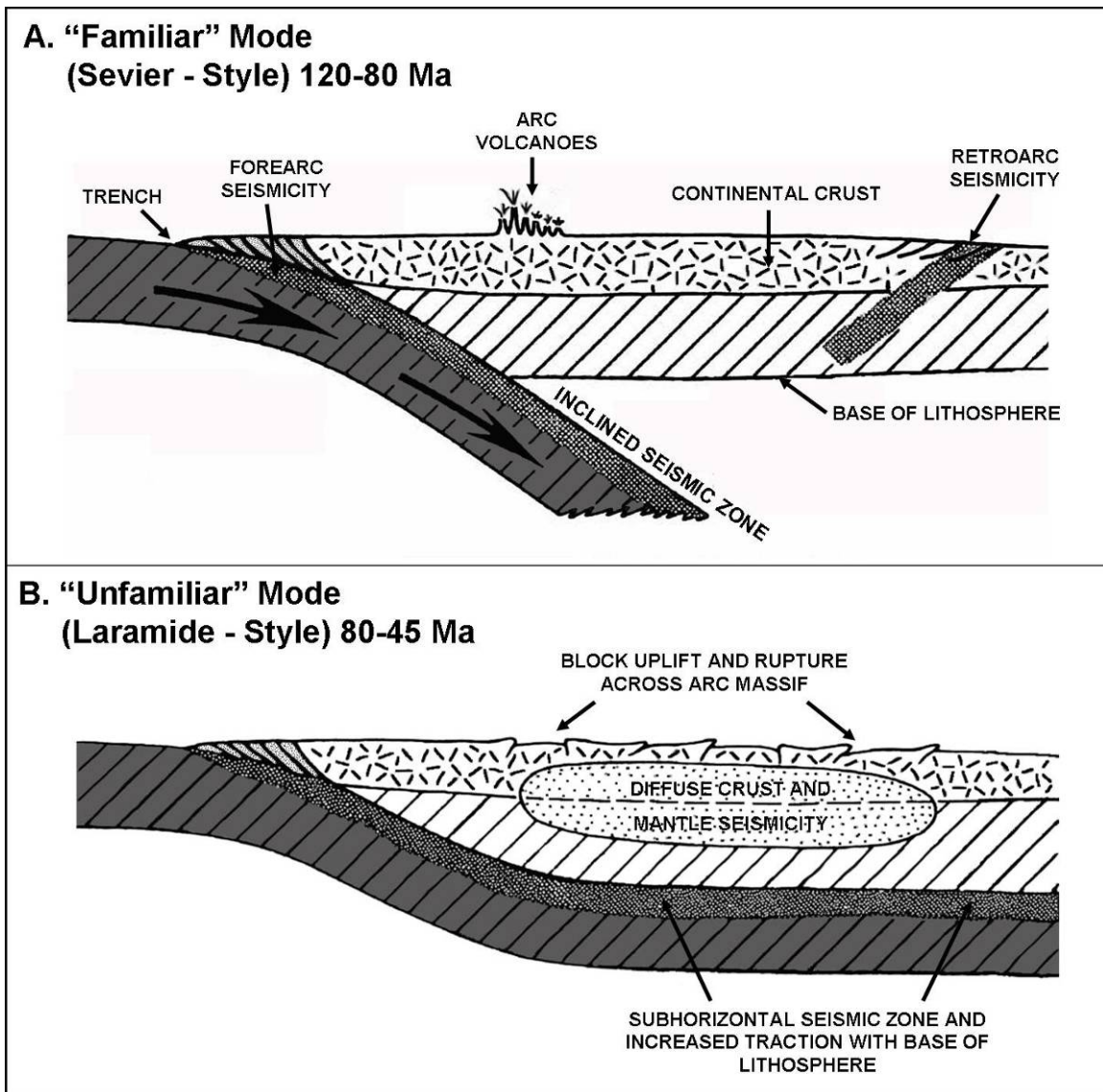


Figure 3. Cartoon of the two modes of subduction: (A) familiar mode (Sevier-style) and (B) unfamiliar mode (Laramide-style) (after Dickinson and Snyder, 1978; Barazangi and Isacks, 1976). The familiar mode is characterized by slab descent into the asthenosphere at a steep angle, whereas the unfamiliar mode is characterized by slab descent into the asthenosphere at a shallow angle, generating friction with the overriding plate of continental lithosphere and suppressing arc magmatism.

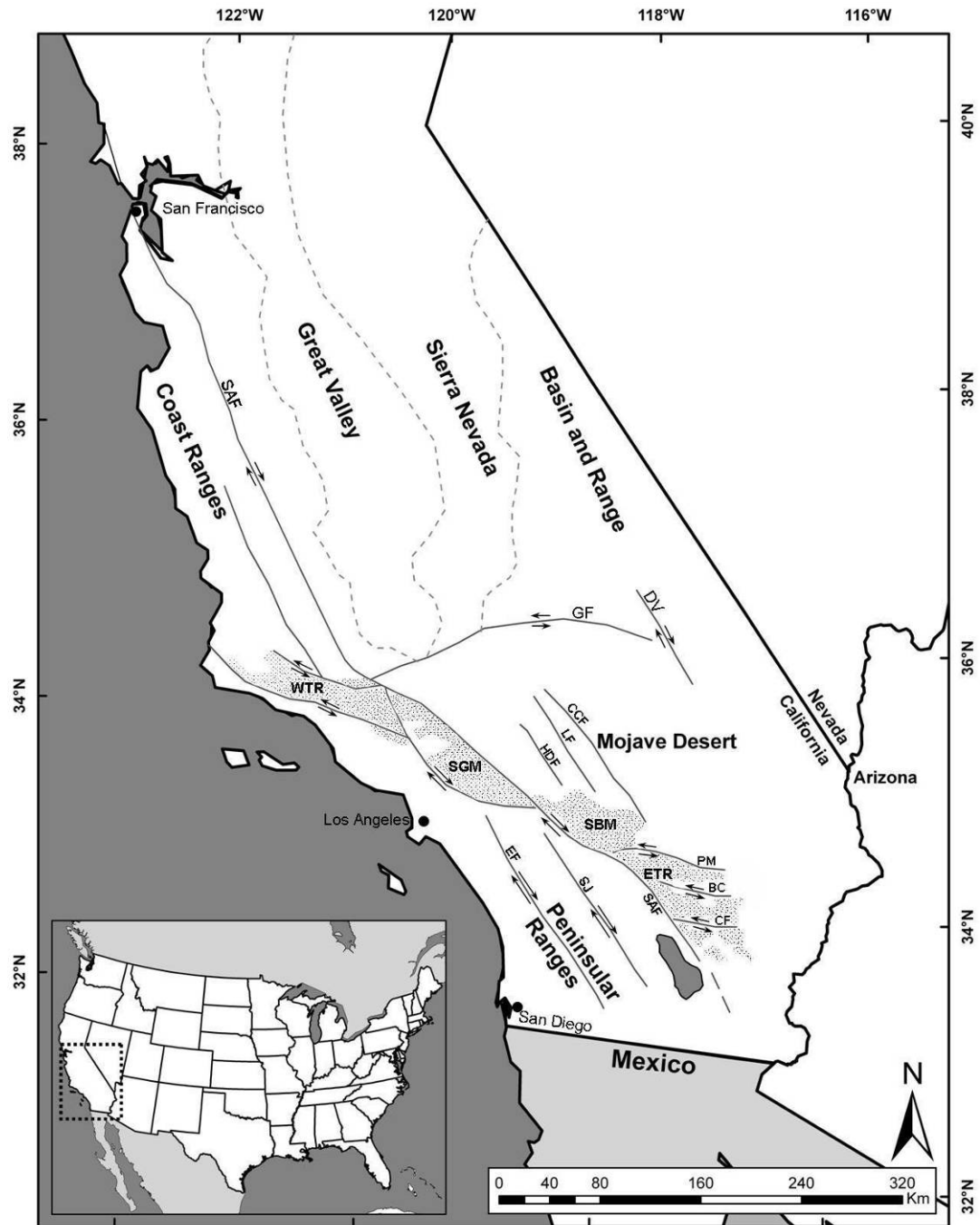


Figure 4. Map of California showing the simplified physiographic terrains (after Law et al., 2001). The northwest-southeast trending Transverse Ranges (stippled pattern) are nearly perpendicular to the north-south physiographic grain of California. Blue Cut fault = BC; Calico fault = CCF; Chiriaco fault = CF; Death Valley fault zone = DV; Elsinor fault = EF; eastern Transverse Ranges = ETR; Garlock fault = GF; Helendale fault = HDF; Lenwood fault = LF; Pinto Mountain fault = PM; San Andreas fault = SAF; San Bernardino Mountains = SBM; San Gabriel Mountains = SGM; San Jacinto fault = SJ; and western Transverse Ranges = WTR.

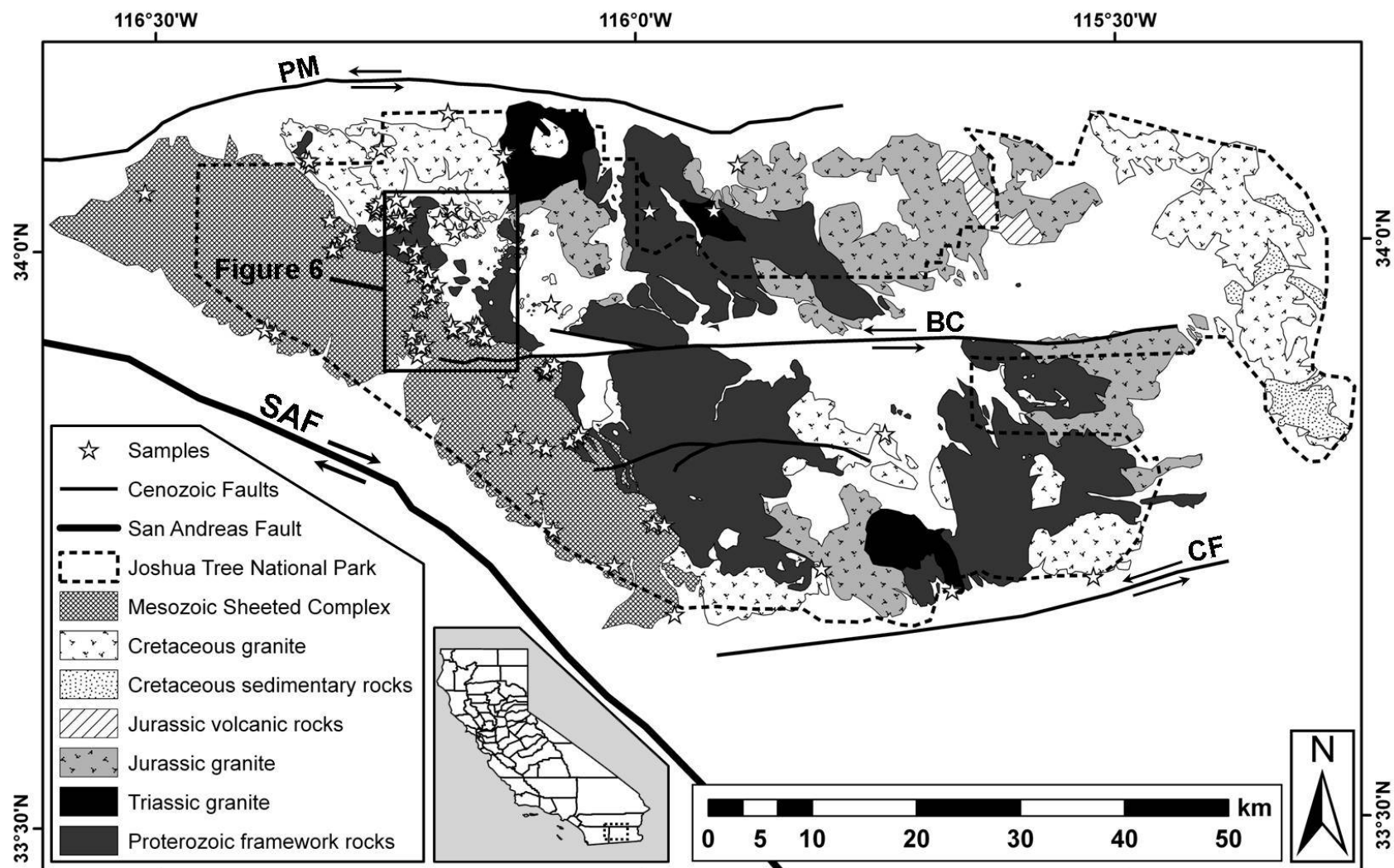


Figure 5. Simplified geologic map of the ETR (after Barth et al., 2004). Blue Cut fault = BC; Chiriaco fault = CF; Pinto Mountain fault = PM; San Andreas fault = SAF

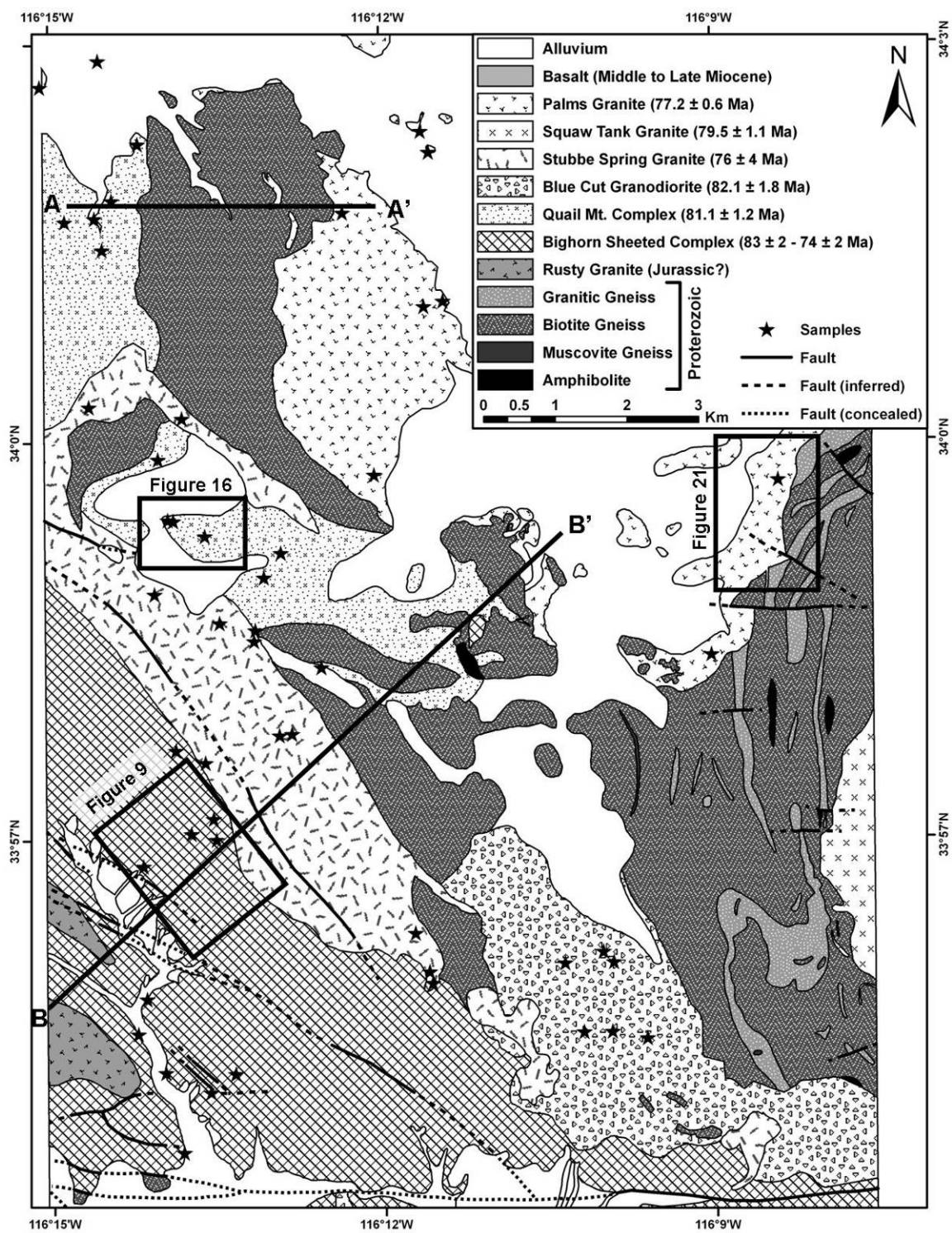


Figure 6. Geologic map of the Keys View 7.5 minute quadrangle (after Paterson et al., 2006).

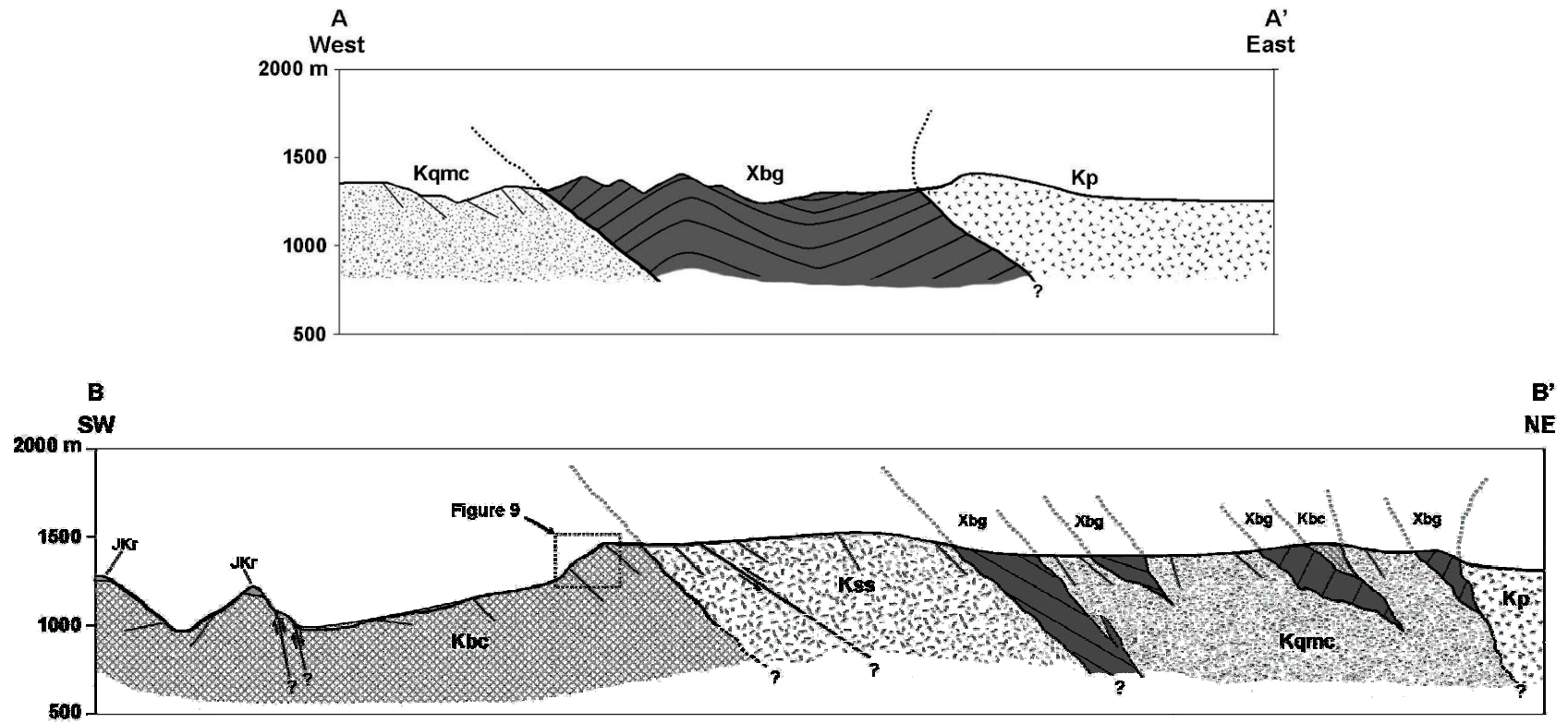


Figure 6. (continued) Generalized cross sections through the Keys View quadrangle. Lines within units represent the traces of foliations. JKr = Rusty granite; Kbc = Bighorn Sheeted Complex; Kp = Palms granite; Kqmc = Quail Mountain Complex; Kss = Stubbe Spring granite; and Xbg = Proterozoic biotite gneiss. Cross section B-B' modified from Paterson et al. (2006).

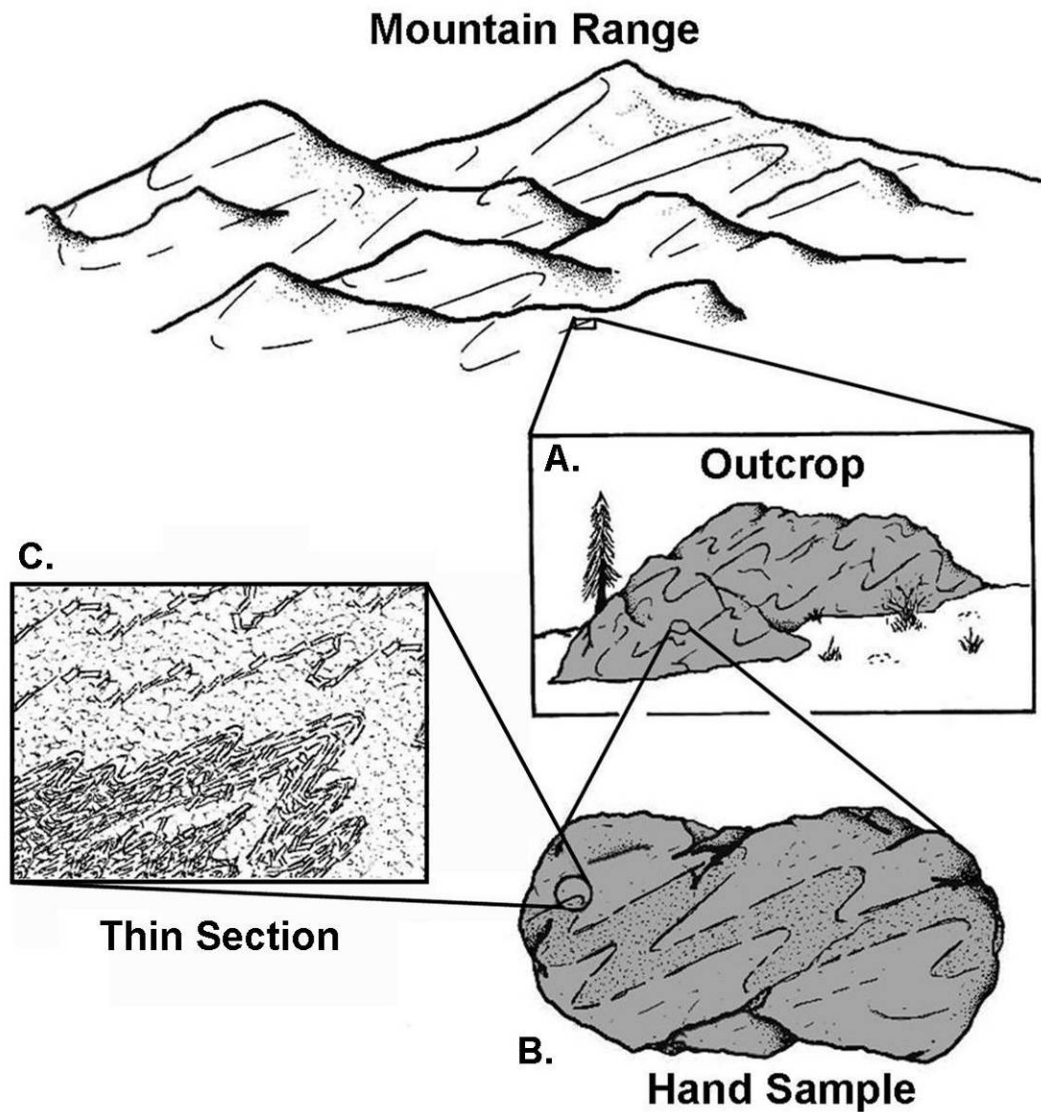


Figure 7. Method for collecting samples and systematic evaluation of fabrics (after Best, 1982). (A) Fresh, oriented samples were collected from well-exposed outcrops attached to the lithosphere. (B) Fabrics are evaluated at the hand sample scale and made into thin sections. (C) Observations made at the thin section scale can then be related back to the regional geologic framework of the study area if thin section and sample are properly oriented.

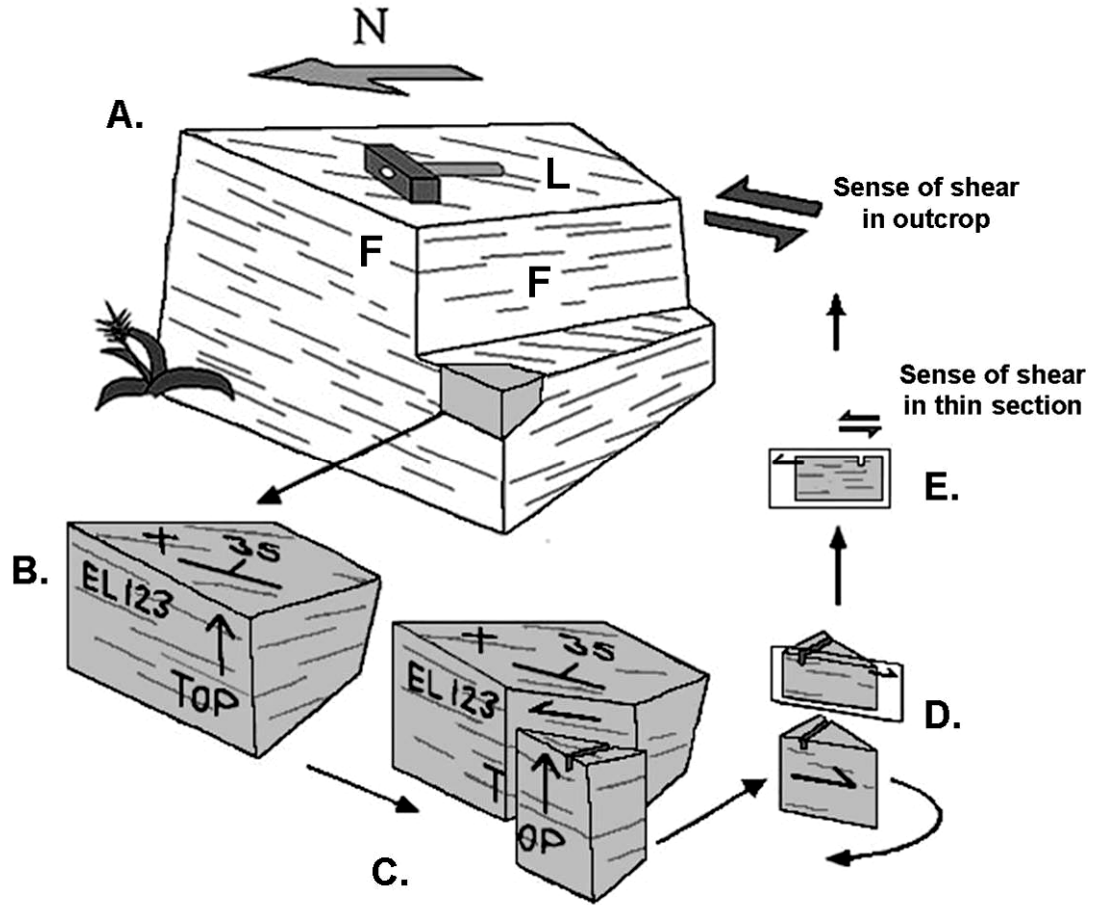


Figure 8. Method for transposing structural information for petrographic analysis (after Passchier and Trouw, 2006). (A) Exposed outcrop and location of oriented sample (grey box). F = foliation; L = lineation. (B) Structural information recorded at the outcrop is transposed onto the collected hand specimen. Transposed information includes: sample number (EL 123), structural orientation (here 160/35), and a mark to designate the top (cross). (C) Hand specimen is cut parallel to lineation and perpendicular to foliation. A small notch is cut into the top of the chip to signify the top of the specimen. A single-barbed arrow is placed on both the chip and the hand specimen to signify the sense of shear in the outcrop. (D) The rock chip (with structural information) is glued to a glass slide, which contains the single-barbed arrow and sample information. (E) Final thin section with the same orientation as the original outcrop.

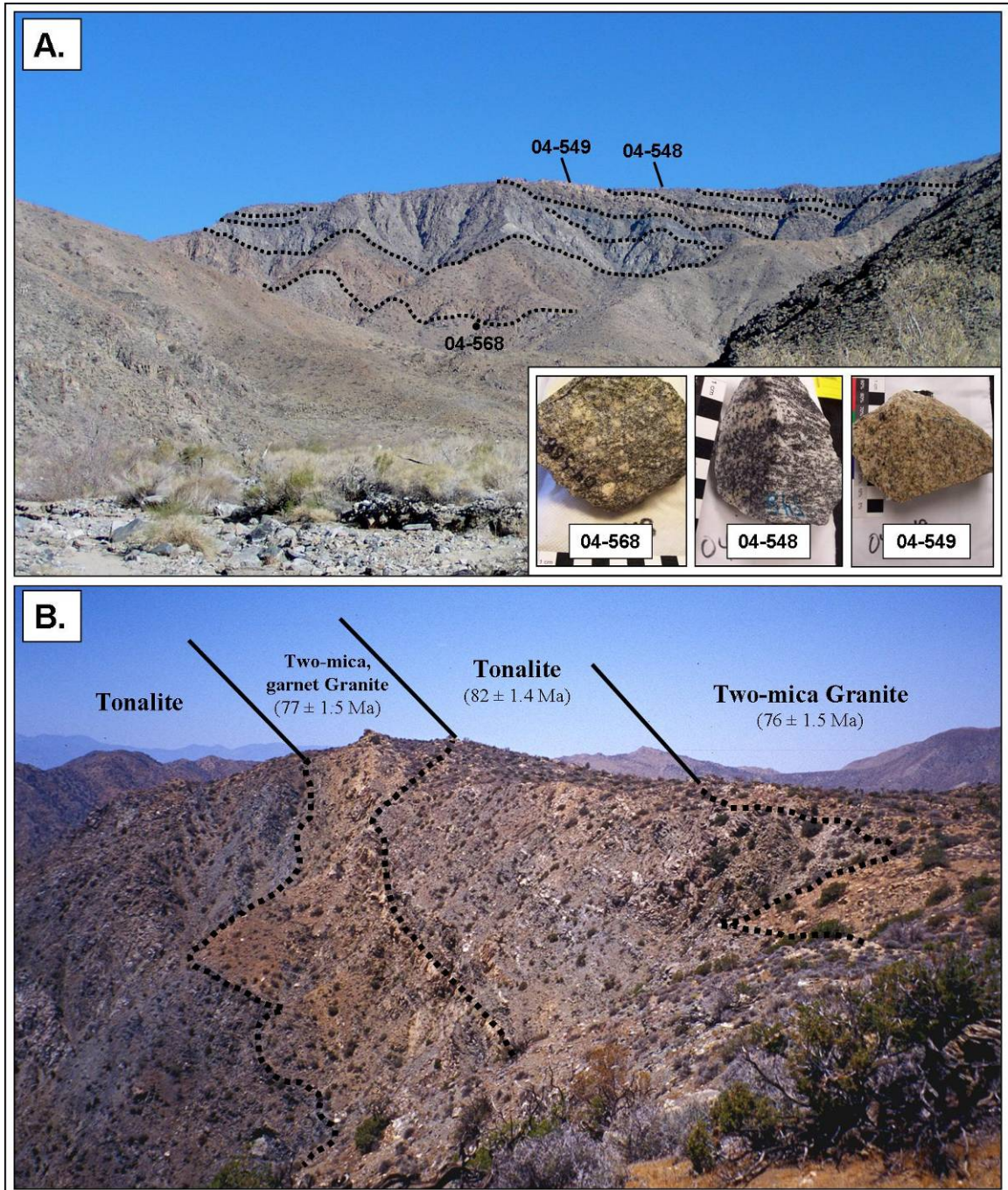


Figure 9. Field photographs of Bighorn Sheeted Complex (BSC). (A) View looking approximately north towards sheeted complex showing well-exposed magmatic sheets (dotted lines). Location marked 04-549 is a two-mica, garnet granite; 04-548 is a strongly foliated and lineated tonalite; 04-568 is a porphyritic granodiorite (see photograph inserts). (B) View looking along upper portion of ridge in photo A (facing approximately NW). U-Pb zircon ages are from Wooden et al. (1994, 2001), Barth et al. (2004), and Paterson et al. (2006).

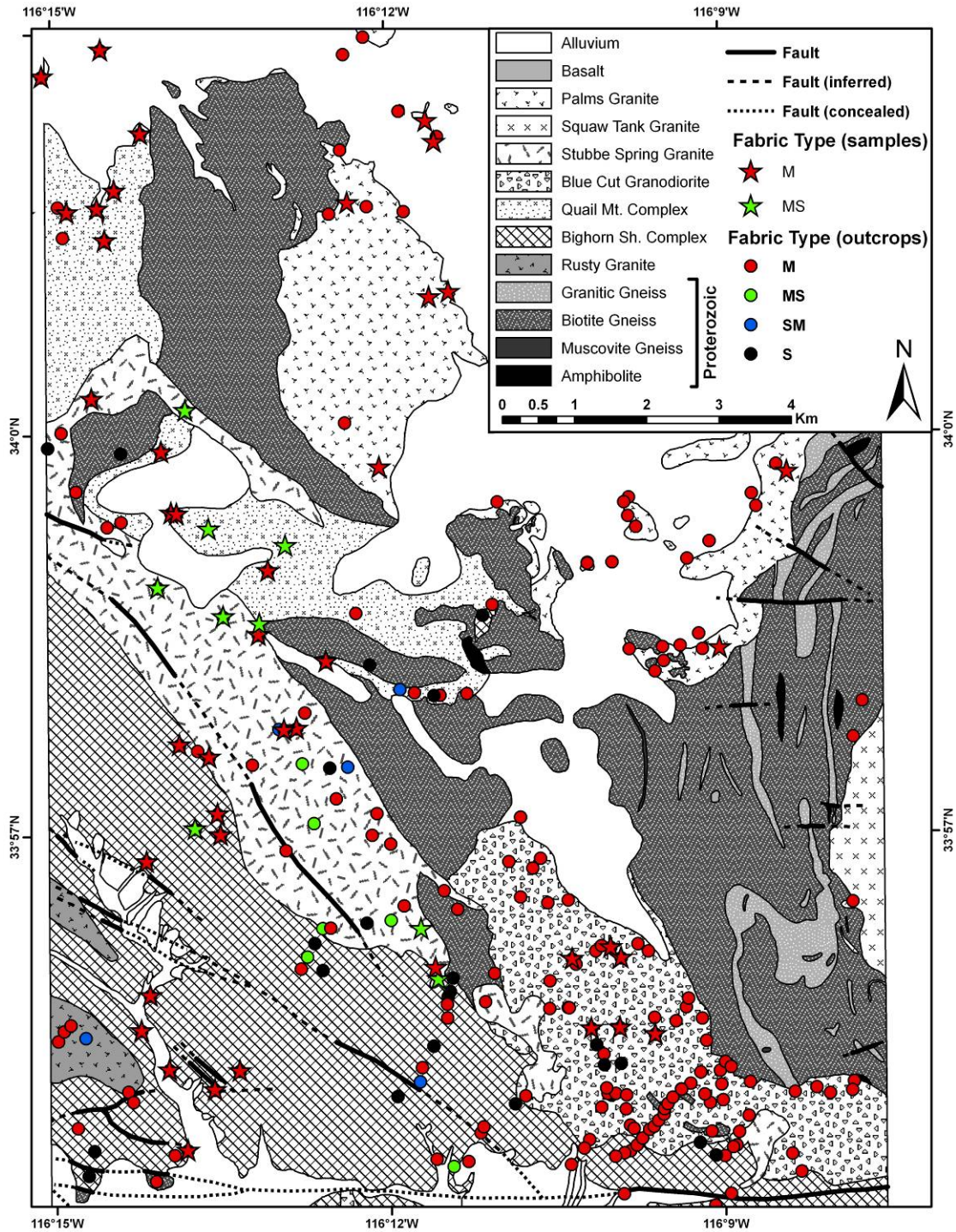


Figure 10A. Geologic map of the Keys View quadrangle (after Paterson et al., 2006) showing the distribution of fabric types within igneous bodies (both discordant and sheeted plutons): M = magmatic; MS = magmatic/solid-state; SM = solid-state/magmatic; and S = solid-state. Circles represent locations of outcrop measurements (Paterson, unpublished data; Barth, unpublished data; this study) and stars represent sample locations (this study).

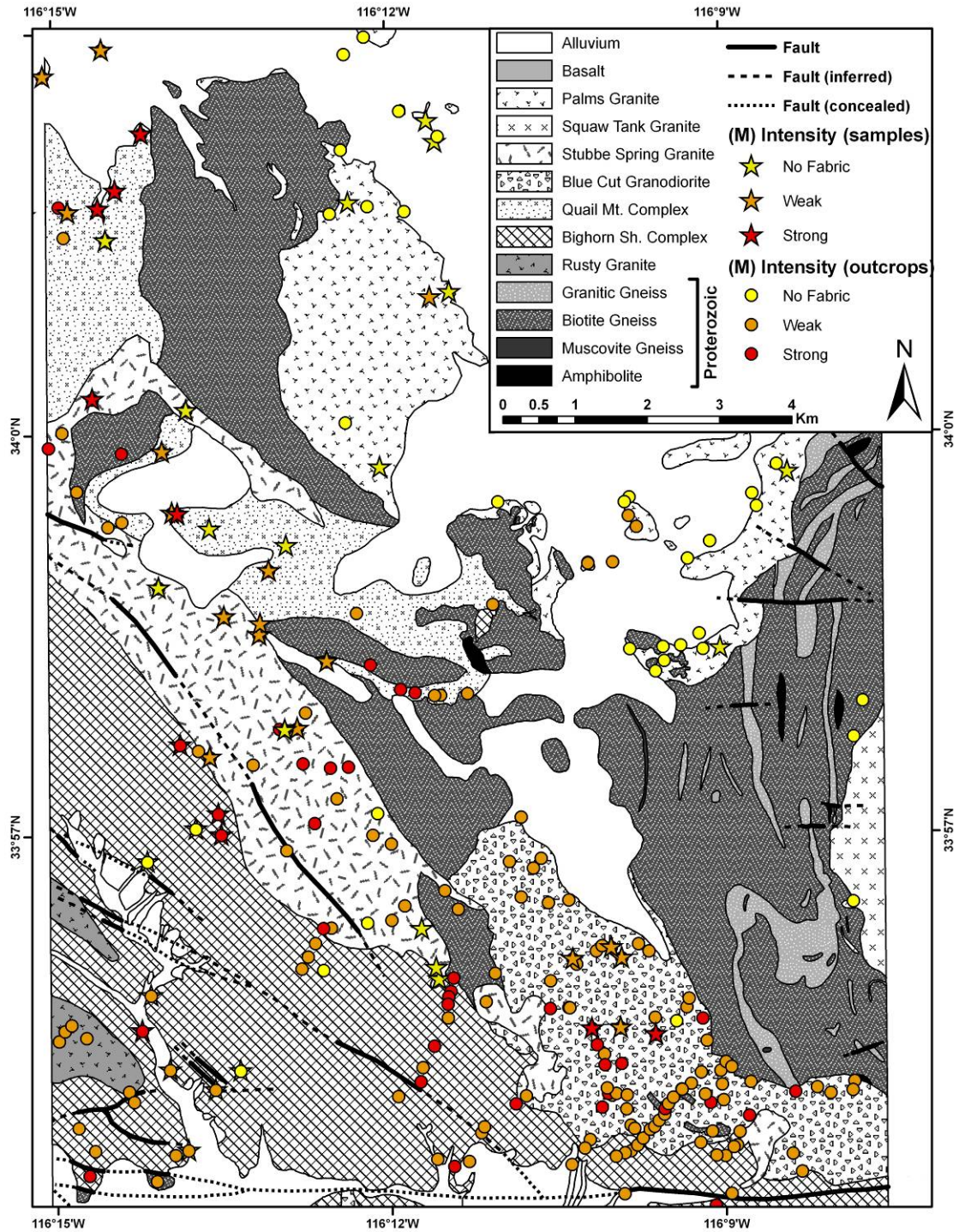


Figure 10B. Geologic map of the Keys View quadrangle (after Paterson et al., 2006) showing the distribution of magmatic fabric intensities within igneous bodies (both discordant and sheeted plutons): No fabric (yellow) = 1; weak fabric (orange) = 2; strong fabric (red) = 3. Circles represent locations of outcrop measurements (Paterson, unpublished data; Barth, unpublished data; this study) and stars represent sample locations (this study).

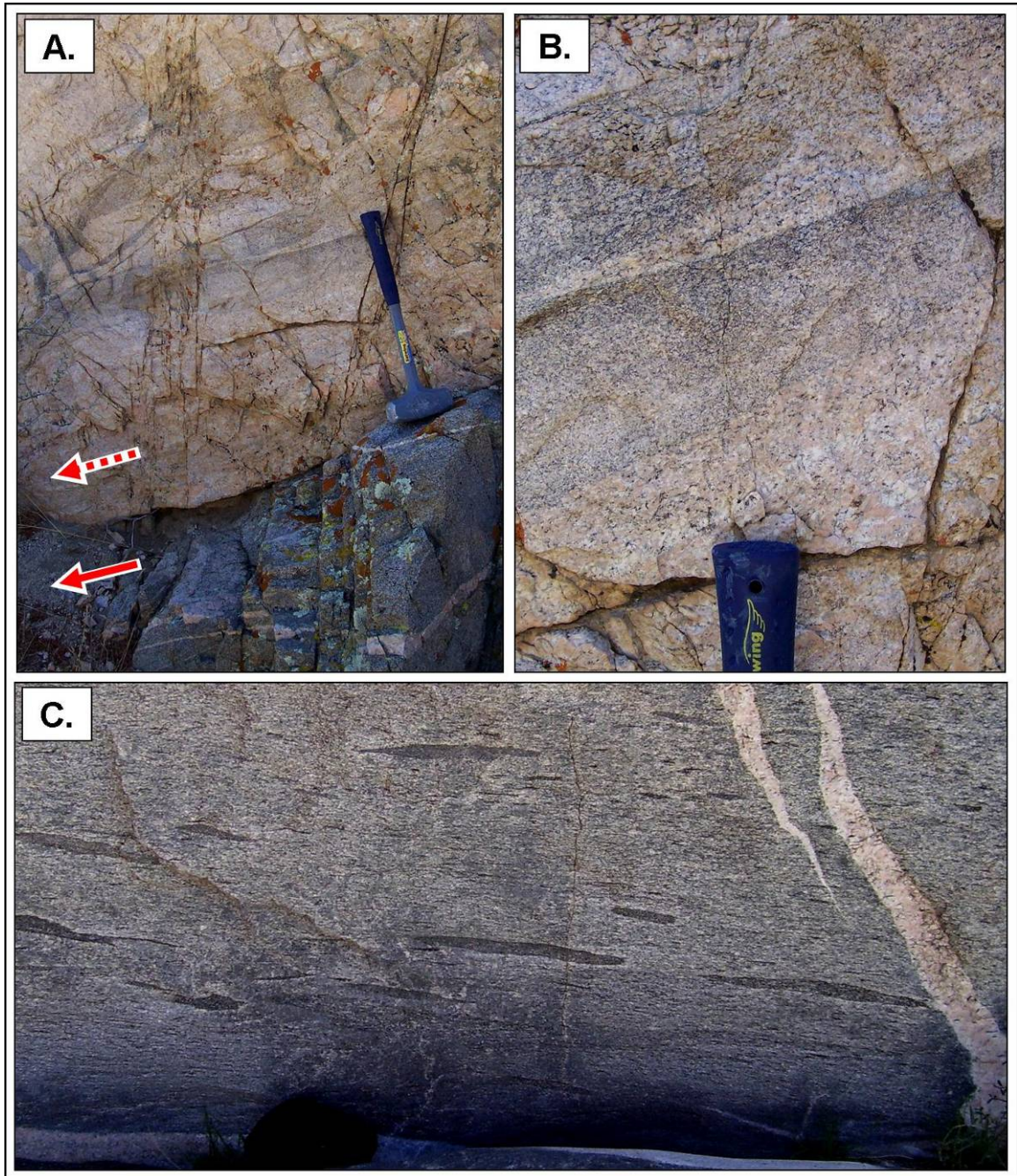


Figure 11. Outcrop photographs of Bighorn sheeted complex (BSC) magmatic structures and fabrics. (A) Contact between fine-grained, biotite tonalite and coarse-grained granite sheet. Foliations in both sheets are parallel (dotted and solid arrows mark foliations). Magmatic foliation in granite is defined by schlieren. Magmatic foliation in tonalite is defined by a modal increase in biotite. Hammer length is 40 cm. (B) Close-up photograph of schlieren in granitic sheet. Handle width is 4 cm. (C) Photo of fine-grained, biotite-granodiorite showing strong magmatic foliation defined by an increase in modal biotite (forming clots or mats) and elongate mafic enclaves. Black camera case (bottom) is 14 cm long.

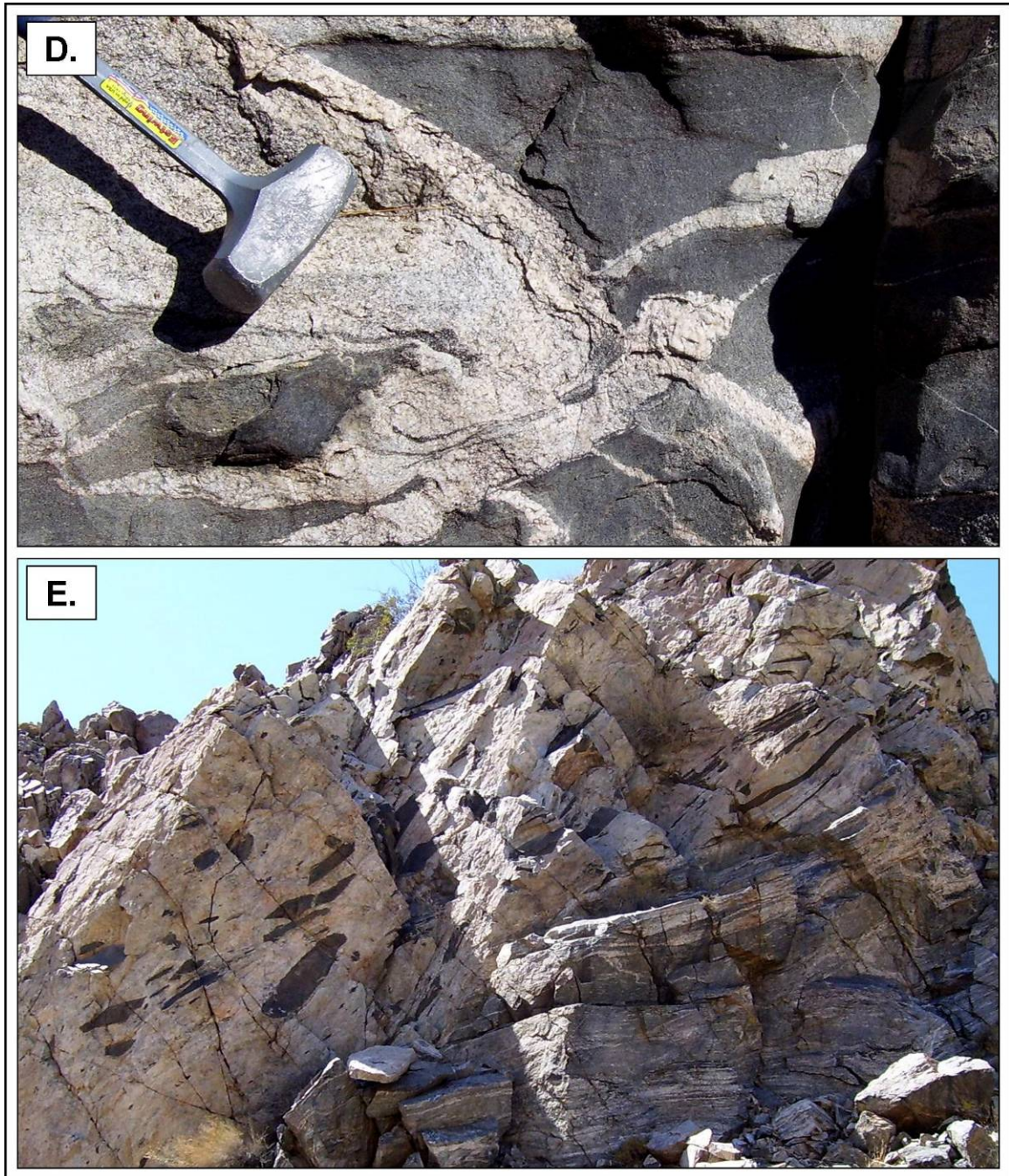


Figure 11. (continued) (D) Medium-grained, biotite granite host sheet with large inclusions (enclaves?) of fine-grained, mafic tonalite. Tonalite inclusions contain strong foliation subparallel to the magmatic host foliation. Also, some inclusions become wispy along their terminations, suggestive of magma mingling and flow. Hammer (shown) is about 25 cm. (E) Outcrop of strongly foliated granodiorite sheet (bottom right) with overlying coarse-grained, granite sheet containing swarms of elongate mafic inclusions. The orientations of mafic inclusions are subparallel to magmatic foliation of underlying granodiorite sheet. Field of view (width) is approximately 8 m.

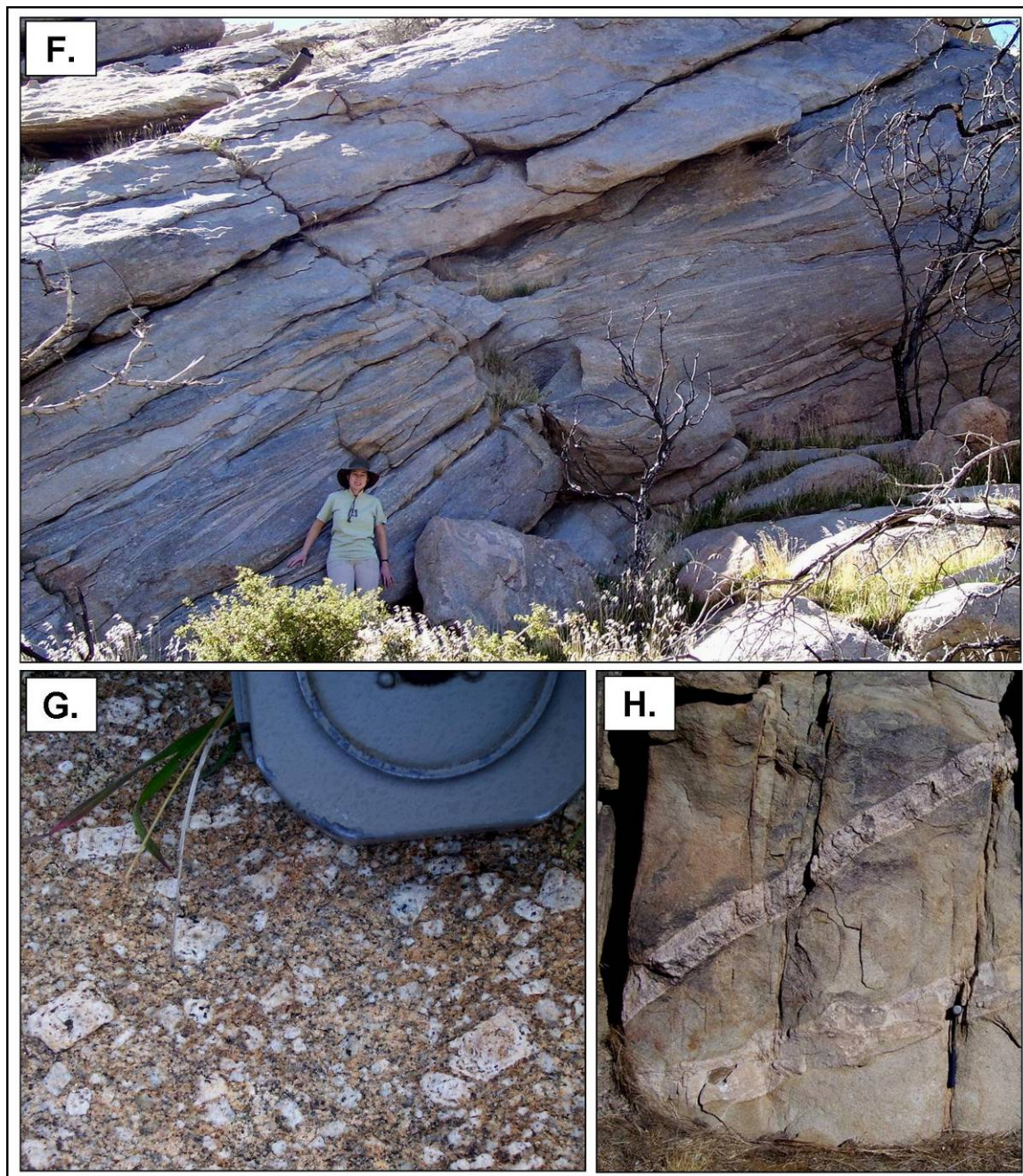


Figure 11. (continued) (F) Outcrop of coarse-grained, granite sheet with a strong magmatic fabric defined by aligned potassium feldspars (see G below), an increase in modal biotite, and compositional layering. Field assistant (TMM) is an average-sized female human, standing a respectable ~163 cm (at least she claims this is average height). (G) Aligned, euhedral potassium feldspars that define strong magmatic fabric in above outcrop (upper right to lower left). Grains also show compositional zoning defined by biotite inclusions. Brunton compass is ~8 cm wide. (H) Outcrop of medium-grained granite with weak magmatic fabric cut by muscovite-garnet, pegmatite dikes. Hammer (stuck in cleavage plane- lower right) is 40 cm.

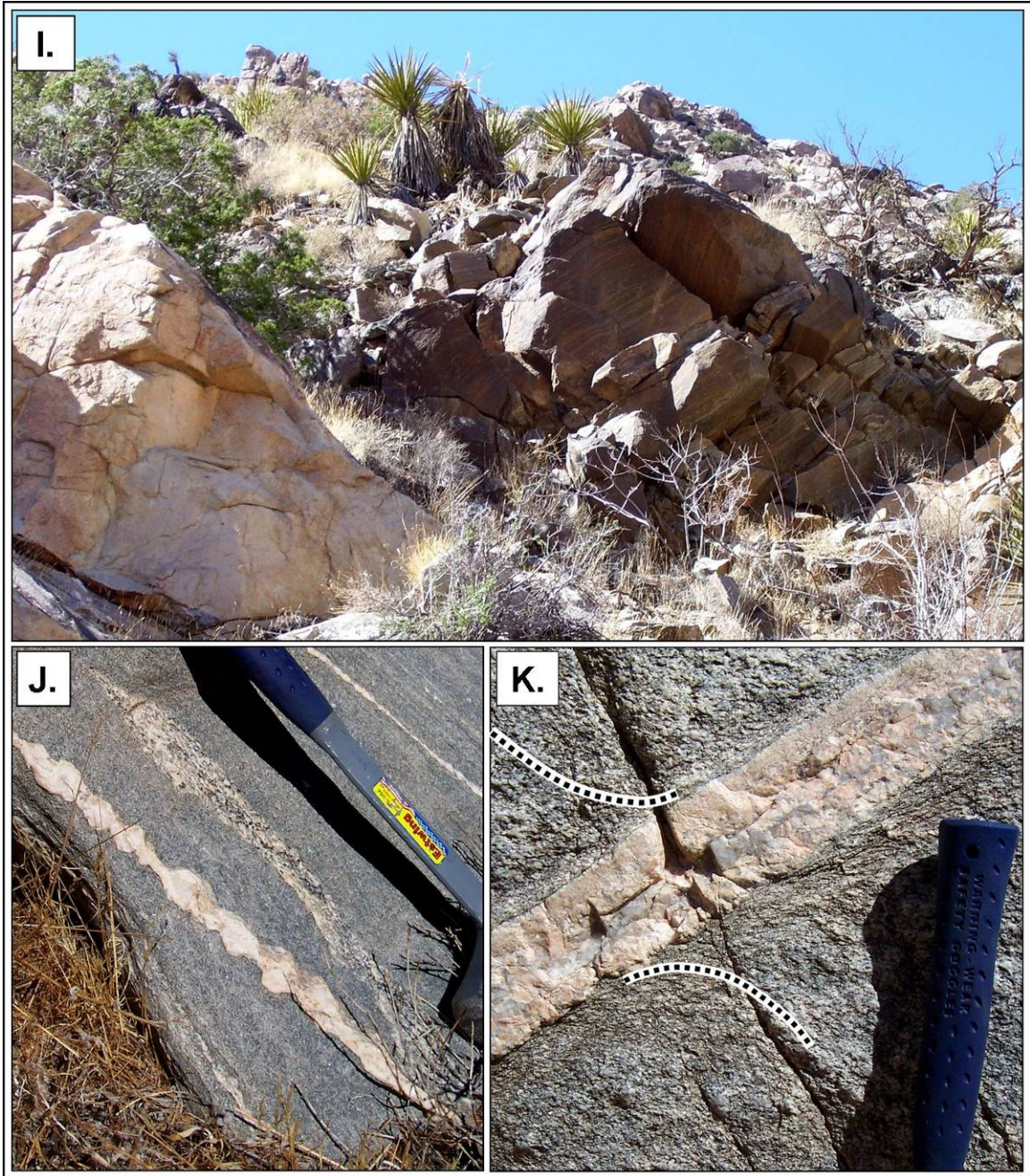


Figure 11. (continued) (I) Raft (non-rotated block) of paragneiss (dark-colored outcrop) within a fine-grained granite sheet (light-colored outcrop). Field of view (width) is approximately 6 m. (J) Outcrop of fine-grained tonalite with inclusion of coarse-grained, biotite-hornblende granodiorite and boudinaged aplitic dike. Note that the tonalite is filling the boudin necks and the aplitic dike is being thinned and thickened. Hammer (shown) is ~ 25 cm. (K) Pegmatitic dike cutting a medium-grained granodiorite sheet. Note the deflection of the host granodiorite foliation along the margin of the dike (dotted lines). Microstructures in both the pegmatite and the granodiorite are magmatic with weak solid-state overprinting. Handle width is 4 cm.

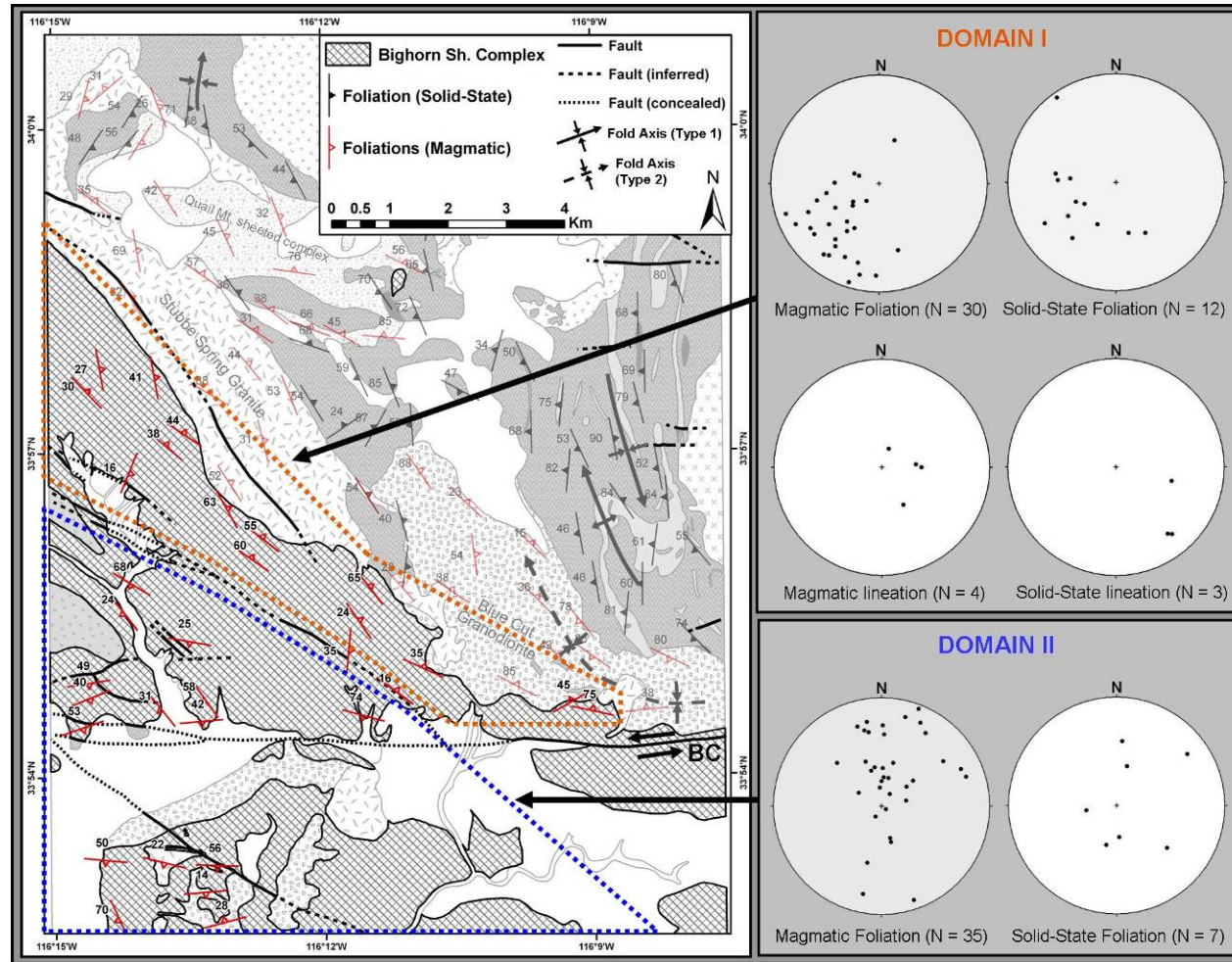


Figure 12. Summary of BSC fabrics. Red symbols are defined as follows: bold red symbols are foliations within the BSC; faint red symbols are foliations in juxtaposed igneous bodies. All symbols show dip angles. Label 'BC' = Blue Cut fault. Fold Axis (type 1) = metamorphic fold, Fold Axis (type 2) = igneous fold. Foliations plotted as poles to planes on equal area stereonets. Outcrop measurements from Paterson (unpublished data), Barth (unpublished data), and this study.

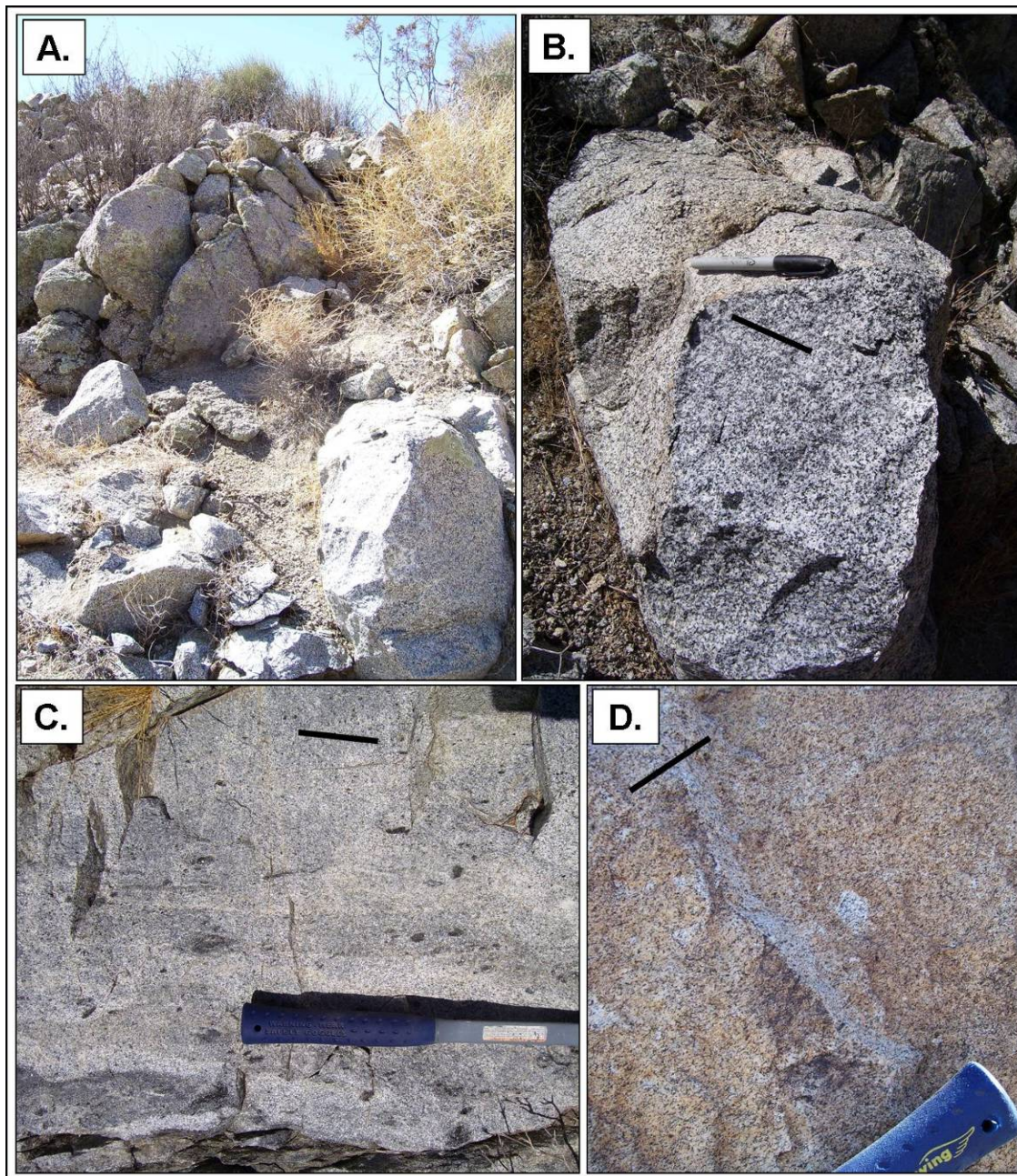


Figure 13. Field and outcrop photographs of Blue Cut granodiorite pluton. (A) Typical outcrop showing large weathered boulders. Field of view (width) is approximately 2 m. (B) Large boulder of medium-grained granodiorite showing a typical weak magmatic foliation. Foliation is defined by aligned hornblende and biotite (foliation is parallel to black line). Pen is 14 cm long. (C) Outcrop of medium-grained granodiorite showing strong magmatic foliation defined by biotite clots and a modal increase in biotite and hornblende (foliation is parallel to black line and hammer handle). Hammer (shown) is approximately 30 cm. (D) Outcrop of finer-grained granodiorite showing strong alignment of biotite (and some hornblende) grains (foliation is parallel to black line). Hammer handle width is 4 cm.

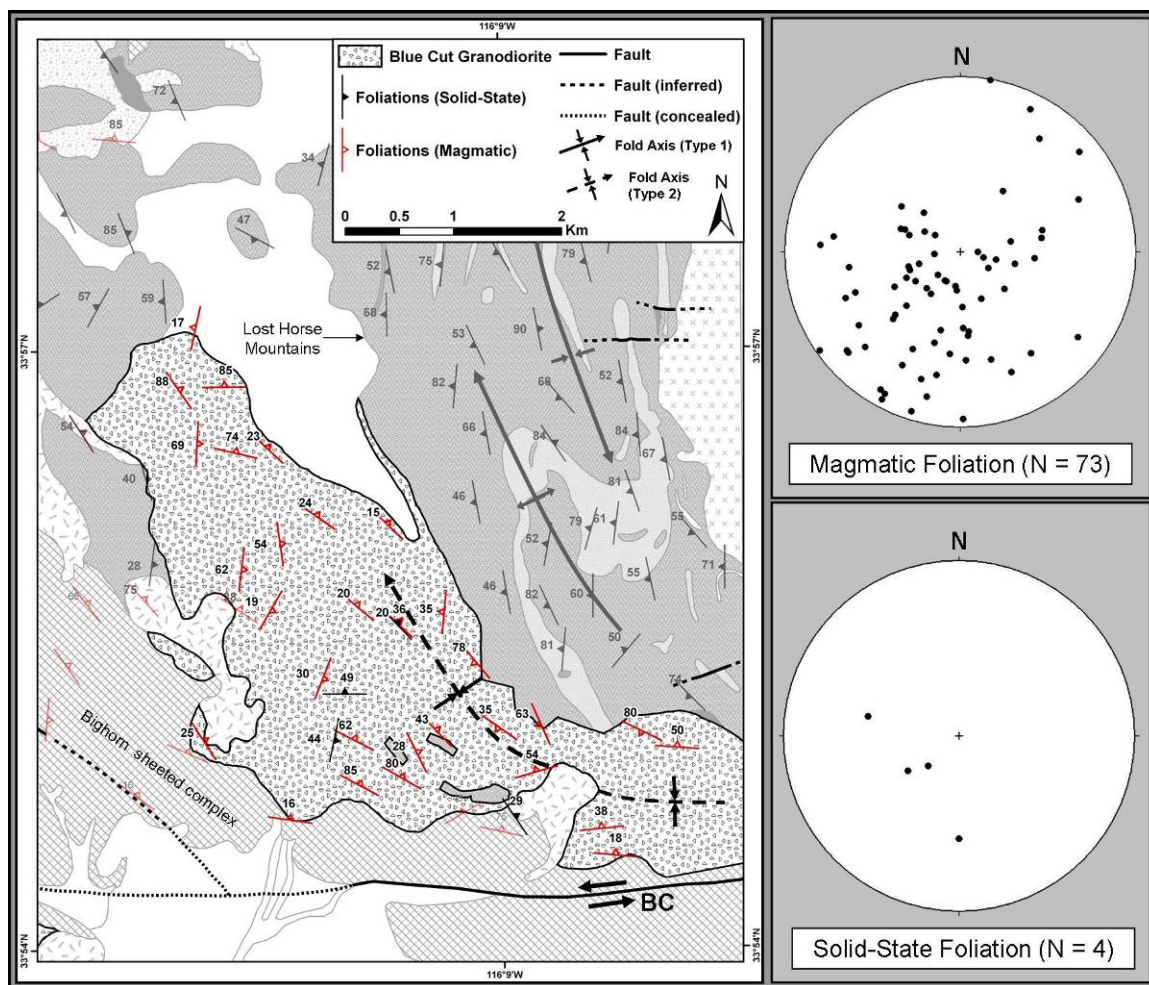


Figure 14. Map of Blue Cut granodiorite foliations. Red symbols are defined as follows: bold red symbols are foliations within the Blue Cut granodiorite; faint red symbols are foliations in juxtaposed igneous bodies. Black symbols are defined as follows: bold black symbols are solid-state foliations within the Blue Cut granodiorite; faint black symbols solid-state lineations in juxtaposed metamorphic framework rocks. All symbols show dip angles. Label ‘BC’ = Blue Cut fault. Fold Axis (type 1) = metamorphic fold, Fold Axis (type 2) = igneous fold. Foliations plotted as poles to planes on equal area stereonets. Outcrop measurements from Paterson (unpublished data), Barth (unpublished data), and this study.

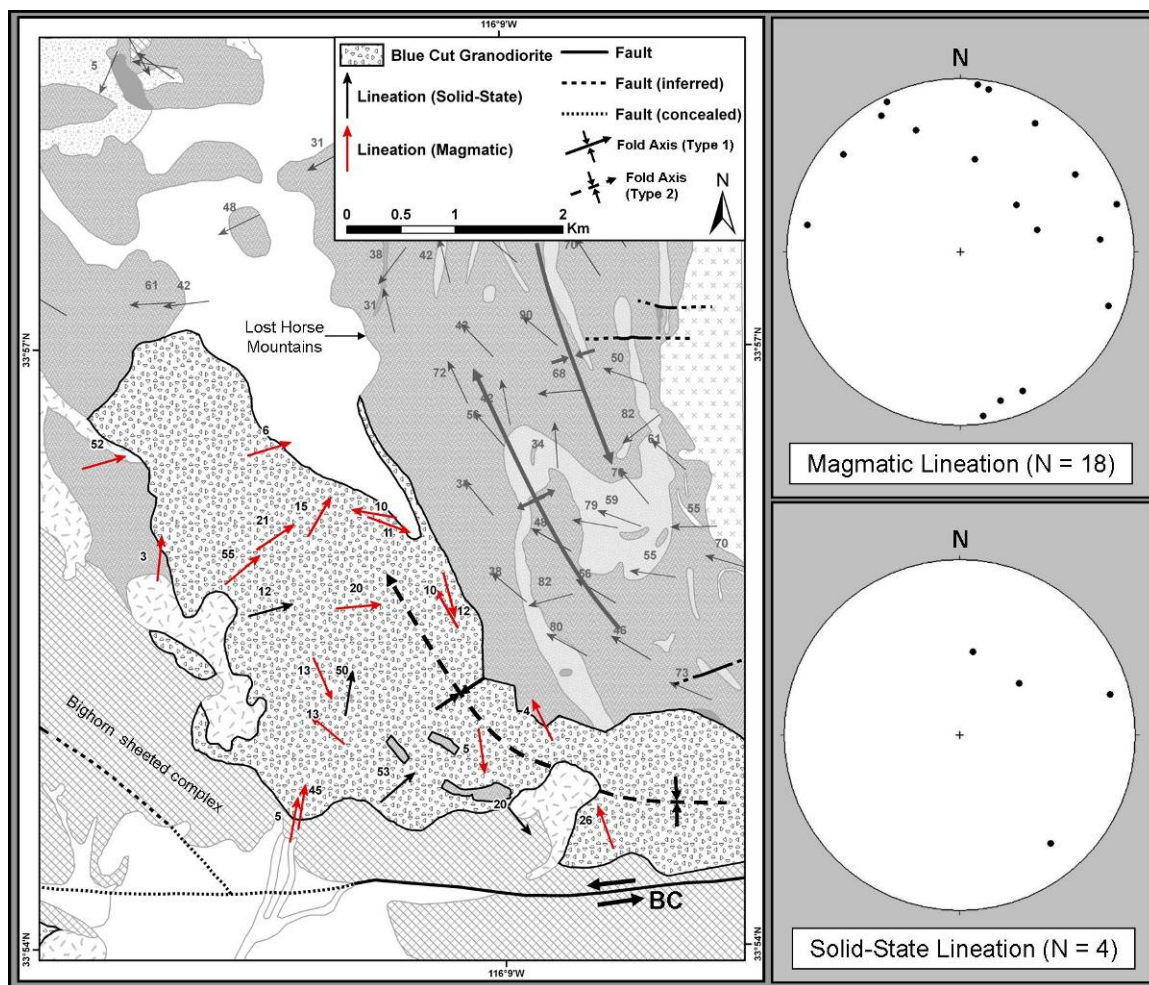


Figure 15. Map of Blue Cut granodiorite lineations. Black symbols are defined as follows: bold black symbols are solid-state lineations within the Blue Cut granodiorite; faint black symbols are solid-state lineations in juxtaposed metamorphic framework rocks. All symbols show plunge angles. Label 'BC' = Blue Cut fault. Fold Axis (type 1) = metamorphic fold, Fold Axis (type 2) = igneous fold. Lineations plotted on equal area stereonets. Outcrop measurements from Paterson (unpublished data), Barth (unpublished data), and this study.

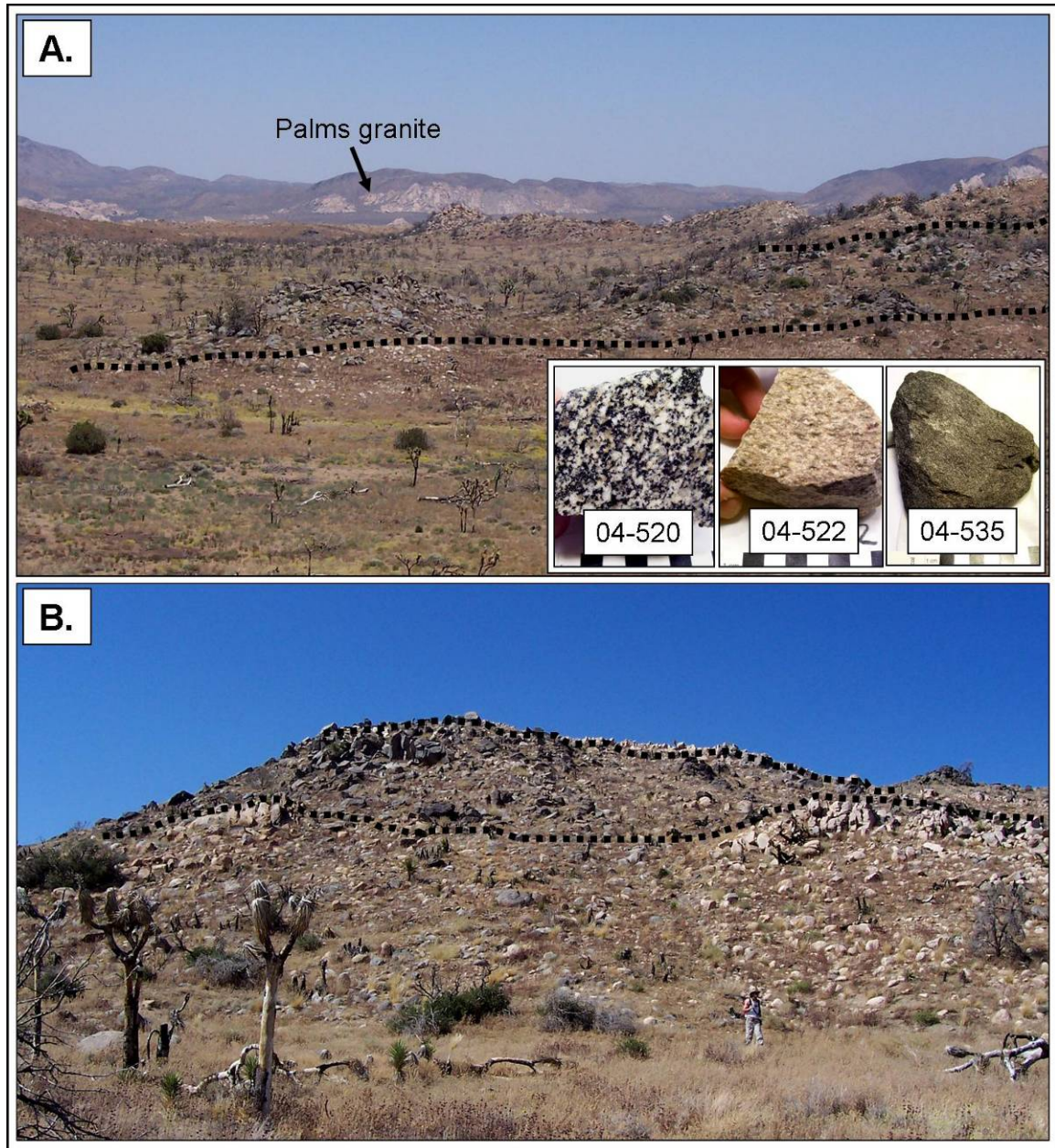


Figure 16. Field and outcrop photographs of Quail Mountain sheeted complex (QMSC). (A) View looking approximately northeast showing well-exposed magmatic sheets (dotted lines) and the discordant Palms granite (Ryan Mountain area). Field of view (width) is approximately 50 m. Sample inserts are 04-520 (medium to coarse-grained granodiorite), 04-522 (two-mica, garnet granite), and 04-535 (fine-grained tonalite) (scale in inserts is centimeter scale). (B) Same outcrop as seen in A, but taken from the south. View is facing roughly north. Outcrop contains two-mica, garnet granite sheet (bottom), granodiorite sheet (middle), and overlying two-mica, garnet granite sheet (top). Dr. Andrew Barth for scale (lower right).

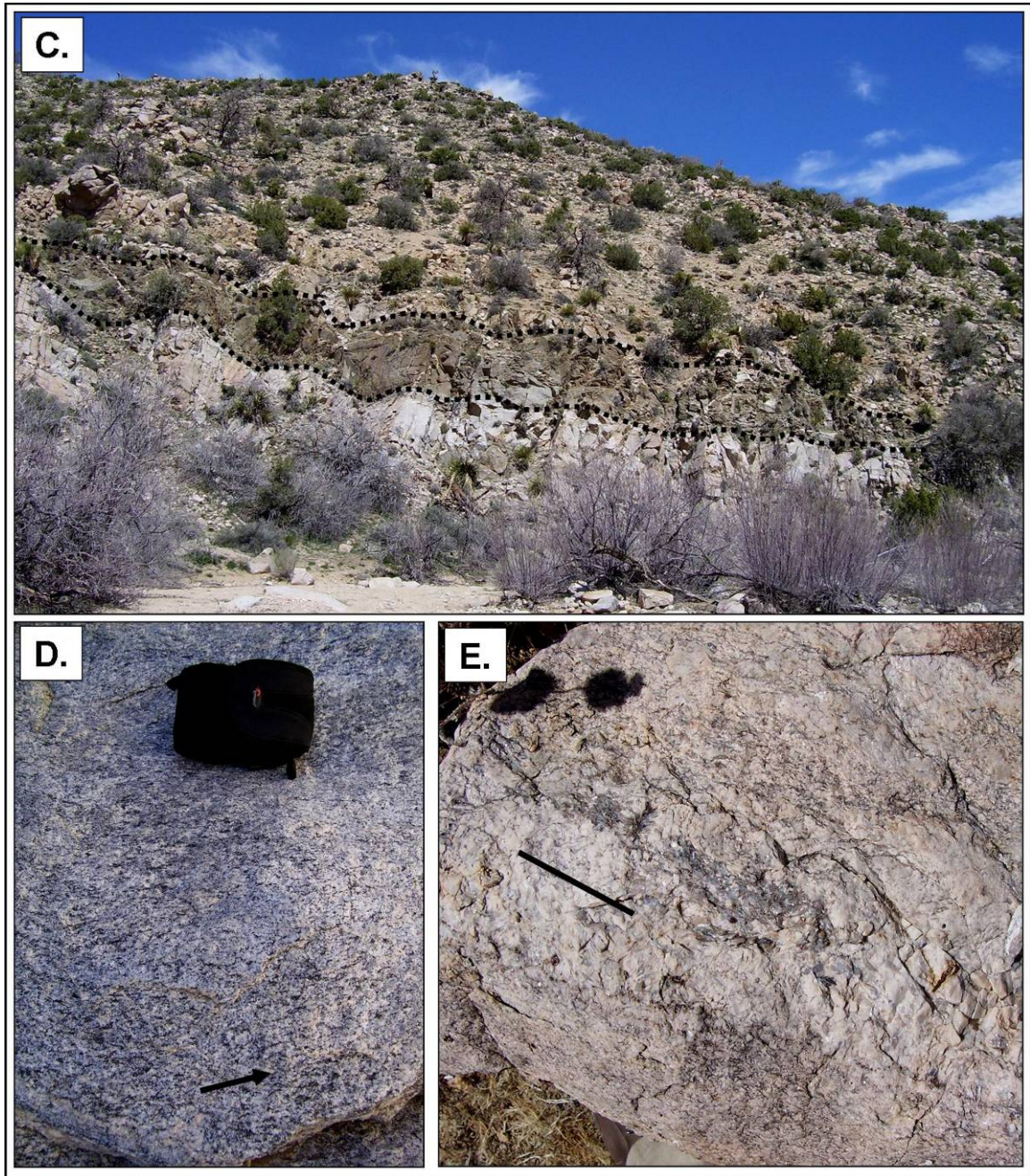


Figure 16. (continued) (C) View facing approximately north showing well-exposed magmatic sheets. Outcrop contains medium-grained, biotite granodiorite sheet (bottom), fine-grained tonalite sheet (middle), and overlying fine-grained, biotite granite sheet (top). Field of view (width) is approximately 15 m. (D) Outcrop of coarse-grained granodiorite showing weak magmatic foliation defined by biotite clots and the alignment of feldspars (fabric is parallel to black arrow). Camera case is 14 cm long. (E) Outcrop of coarse-grained, two-mica, garnet granite similar to that observed in photos A and B. Weak foliation (upper left to lower right) is defined by clots of primary muscovite grains (black line). Field of view is approximately 0.5 m.



Figure 16. (continued) (F) Outcrop of medium-grained granodiorite showing a strong magmatic fabric primarily defined by flattened enclaves (photo courtesy of Dr. Andrew Barth). Hammer is 40 cm. (G) Outcrop of fine-grained tonalite showing a strong magmatic fabric defined by a modal increase in biotite and hornblende and flattened enclaves. Hammer (shown) is approximately 30 cm. (H) Outcrop of medium-grained granodiorite showing strong magmatic lineation defined by the alignment of euhedral hornblende (some >1 cm long) (black arrow is parallel to lineation). Hammer (length) is approximately 18 cm long.

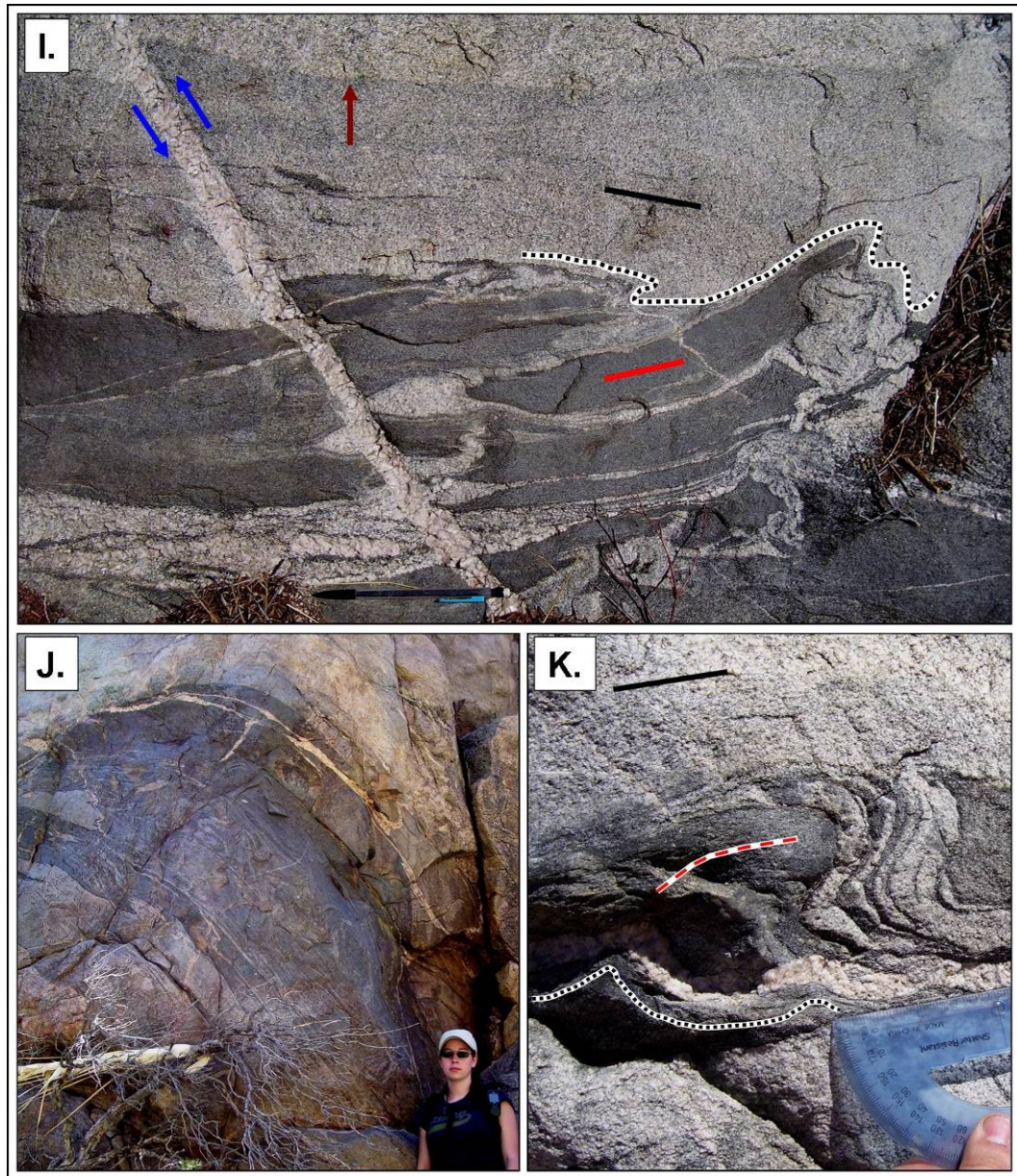


Figure 16. (continued) (I) Outcrop of biotite granodiorite containing elongate, mafic inclusions and pegmatitic dike. Host granodiorite contains weak magmatic fabric (black line) defined by the increase of biotite. Inclusion foliation (red line) is subparallel to the host foliation. Dark red arrow (top) shows location of compositional boundary in host granodiorite. Blue arrows (top-left) indicate pegmatitic dike offset. The dotted line (center-right) is parallel to folds observed within the host granodiorite; fold hinges are subparallel to host rock fabric. Pencil (bottom-center) is 14 cm. (J) Outcrop of biotite granodiorite with large mafic inclusion showing complex folding and mingling. Field assistant is ~ 163 cm tall. (K) Outcrop of biotite granodiorite showing folding of mafic enclave, granitic dike, and host rock (dotted black line defines fold in granitic dike). Note the similarities in axial planes (dotted red line). Black line defines weak magmatic foliation in host granodiorite defined by biotite clots. Protractor is ~8 cm wide.

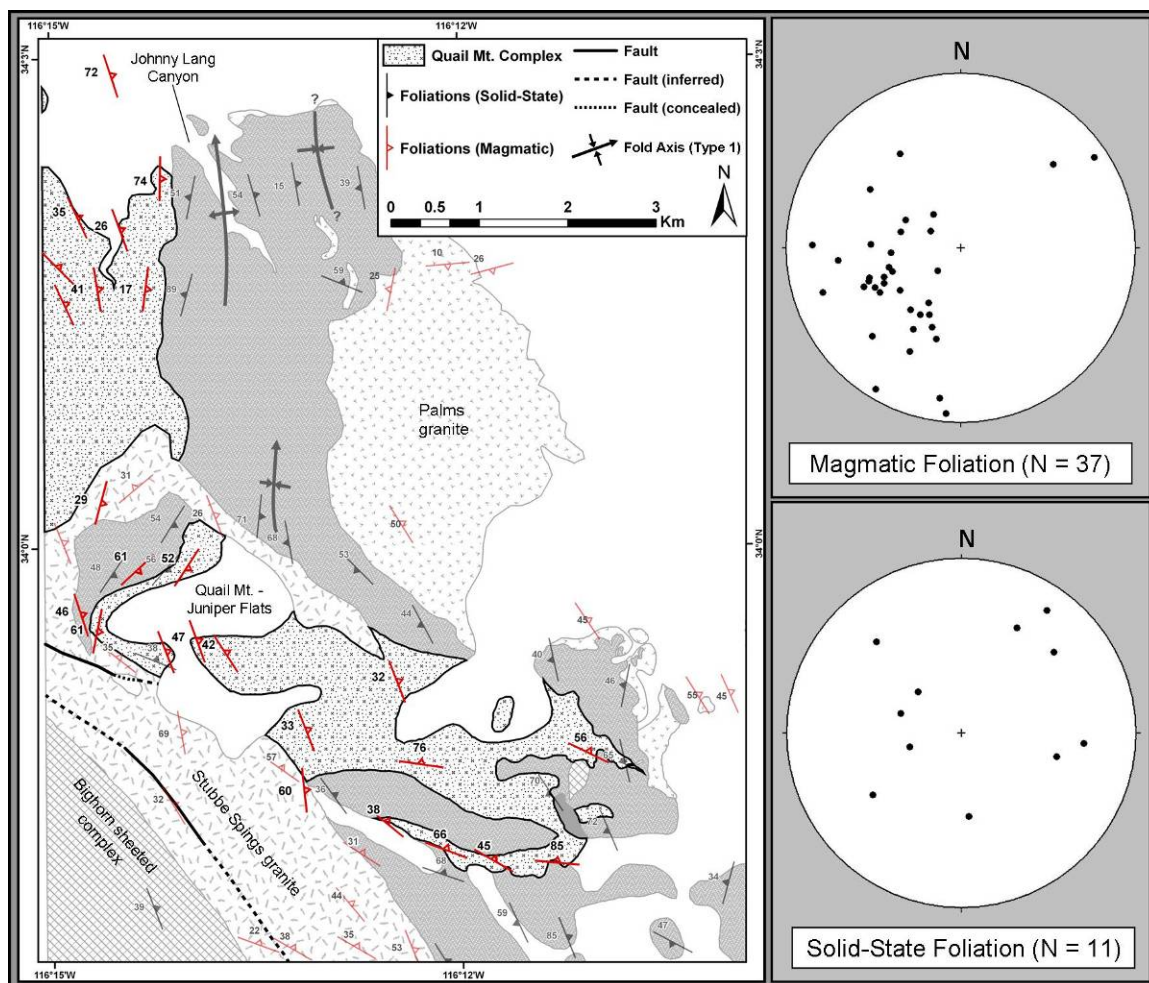


Figure 17. Map of Quail Mountain sheeted complex (QMSC) foliations. Red symbols are defined as follows: bold red symbols are foliations within the QMSC; faint red symbols are foliations in juxtaposed igneous bodies. All symbols show dip angles. Fold Axis (type 1) = metamorphic fold. Foliations plotted as poles to planes on equal area stereonets. Outcrop measurements from Paterson (unpublished data), Barth (unpublished data), and this study.

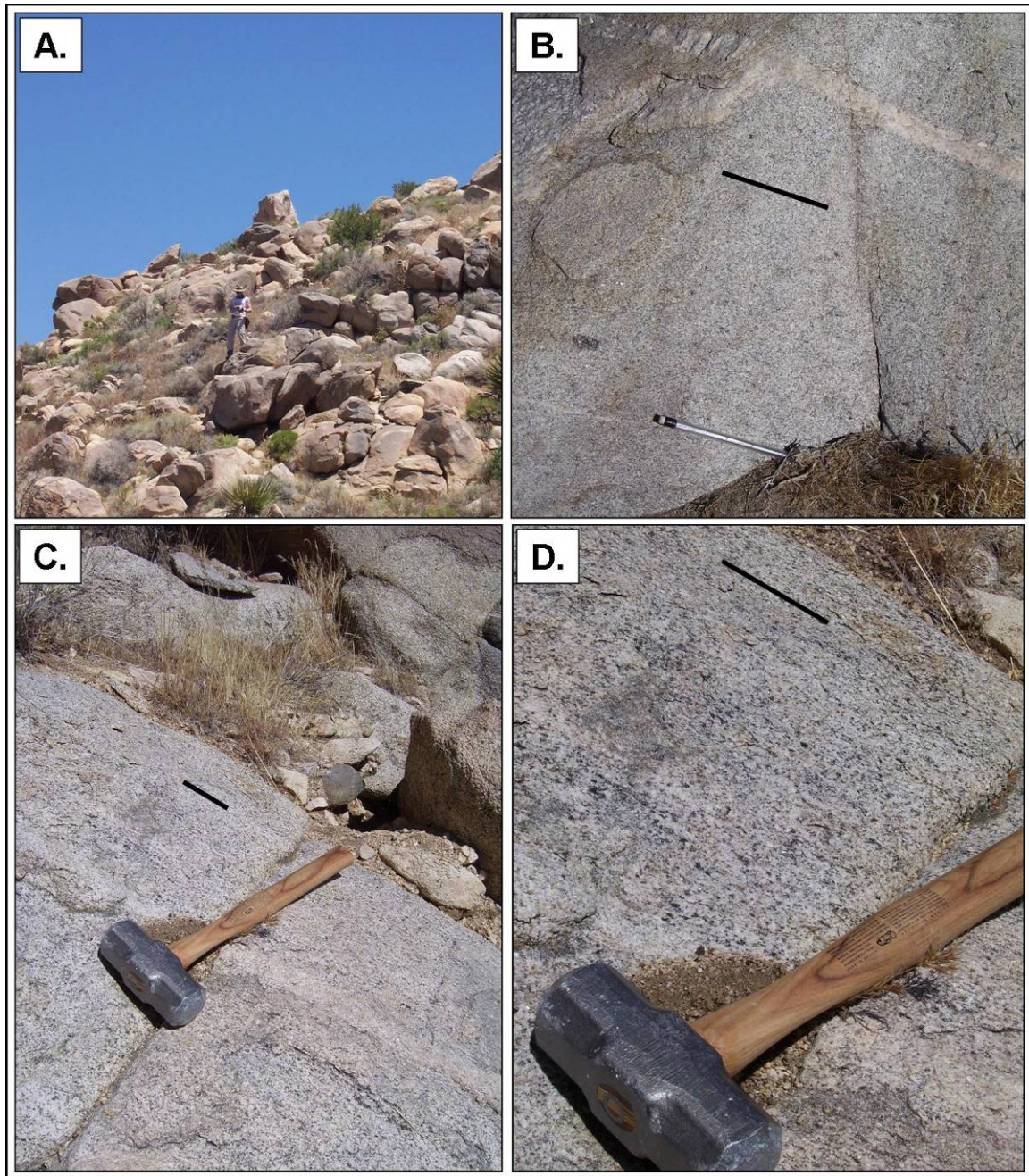


Figure 18. Field and outcrop photographs of Stubbe Spring granite pluton (SS). (A) Typical outcrop showing large weathered boulders of biotite granite. Field of view (width) is approximately 8 meters. Dr. Andrew Barth for scale (center). (B) Outcrop of fine-grained granite with very weak magmatic foliation defined by biotite (black line). Pencil is 14 cm long. (C) Outcrop of medium-grained, biotite granite with weak magmatic foliation defined by clots/mats of biotite (black line) and weakly-defined compositional layers (cutting hammer handle). Hammer is 40 cm long. (D) Close-up photograph showing elements of the weak magmatic foliation described in C. Hammer (shown) is approximately 30 cm.

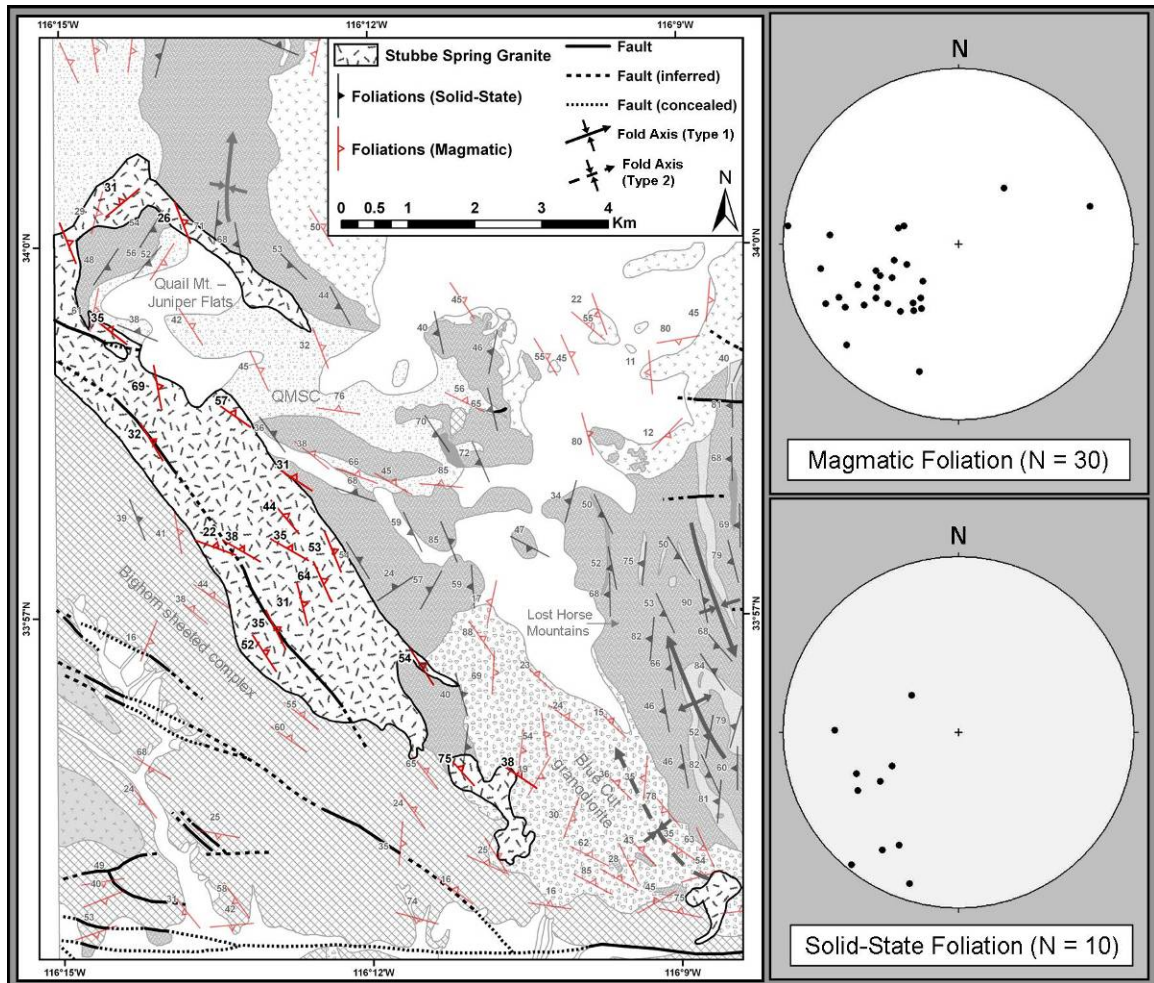


Figure 19. Map of Stubbe Spring granite foliations. Red symbols are defined as follows: bold red symbols are foliations within the Stubbe Spring granite; faint red symbols are foliations in juxtaposed igneous bodies. All symbols show dip angles. Fold Axis (type 1) = metamorphic fold, Fold Axis (type 2) = igneous fold. Foliations plotted as poles to planes on equal area stereonets. Outcrop measurements from Paterson (unpublished data) and Barth (unpublished data).

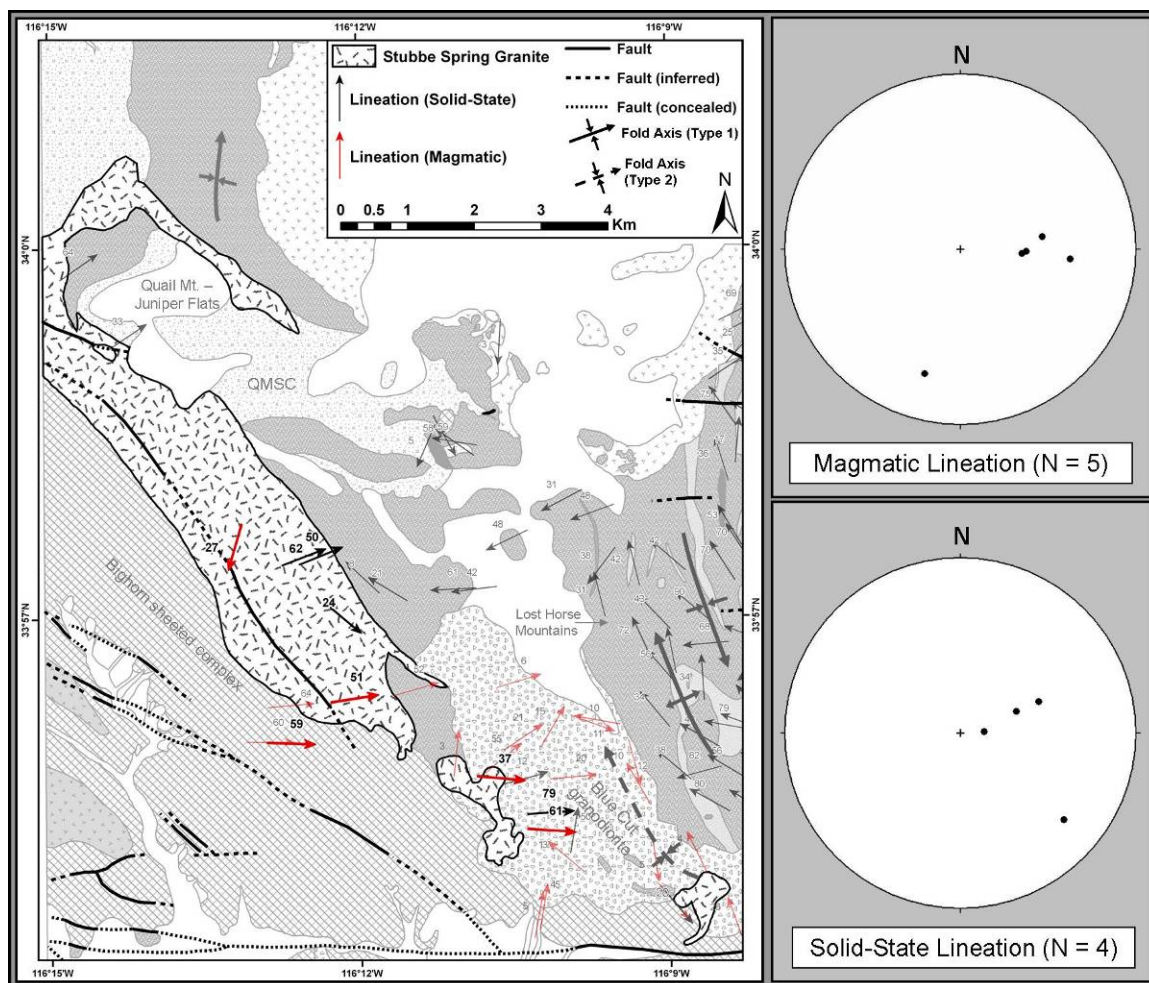


Figure 20. Map of Stubbe Spring granite lineations. Red symbols are defined as follows: bold red symbols are lineations within the Stubbe Spring granite; faint red symbols are lineations in juxtaposed igneous bodies. Black symbols are defined as follows: bold black symbols are solid-state lineations within the Stubbe Spring granite; faint black symbols are solid-state lineations in juxtaposed metamorphic framework rocks. All symbols show plunge angles. Fold Axis (type 1) = metamorphic fold, Fold Axis (type 2) = igneous fold. Lineations plotted on equal area stereonets. Outcrop measurements from Paterson (unpublished data) and Barth (unpublished data).

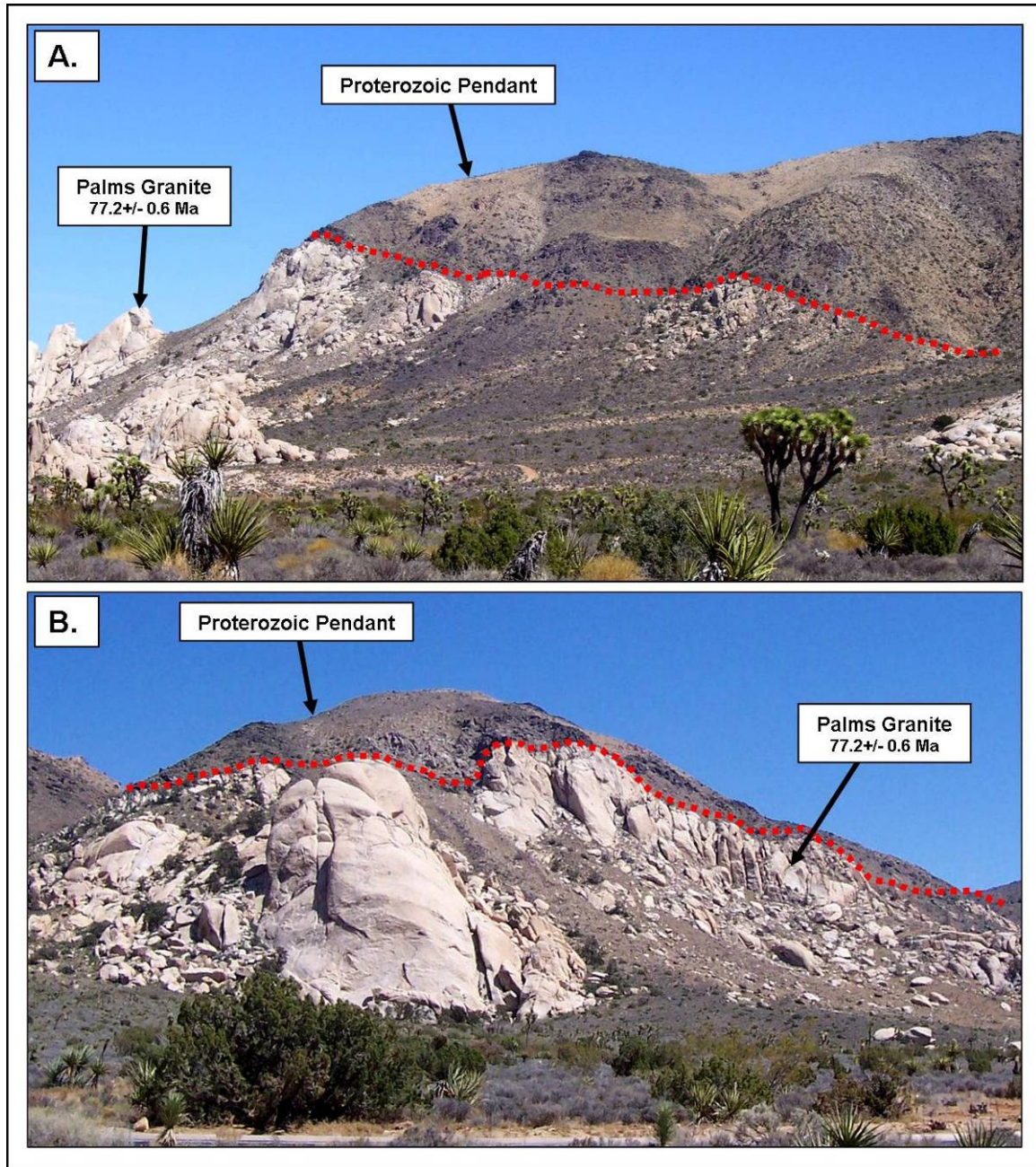


Figure 21. Field photographs of Palms granite pluton. (A) View looking approximately north showing well-exposed northeast to east-dipping contact between Palms granite and overlying metamorphic pendant (dotted red line) (image of Ryan Mountain). Sample 04-561 was collected at the base of this outcrop (marked by arrow), yielding a U-Pb zircon age of 77.2 ± 0.6 Ma (Barth et al., 2004). (B) View facing approximately east towards outcrop in photo A showing same contact.

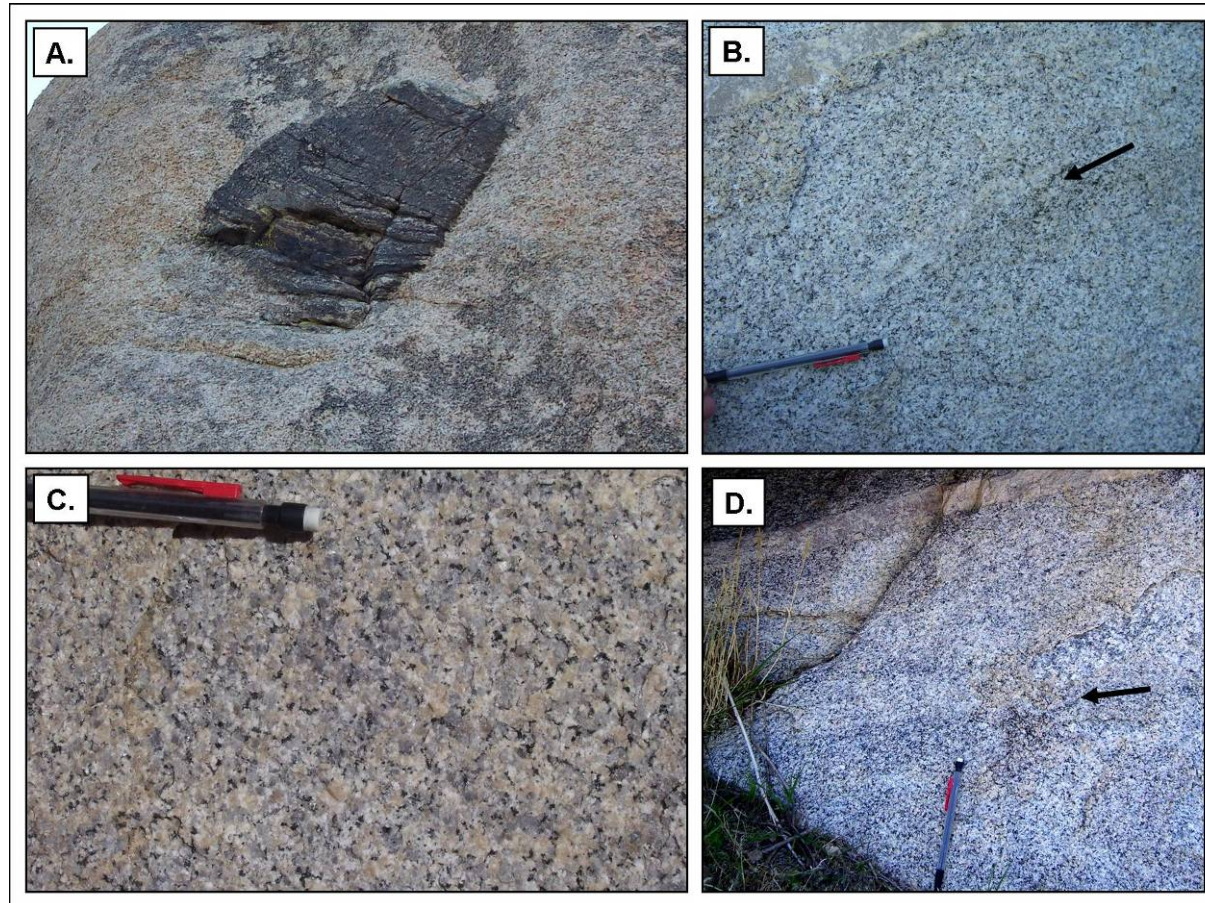


Figure 22. Outcrop photographs of the Palms granite. (A) Xenolith (rotated host rock) of Proterozoic biotite gneiss within outcrop of Palms pluton. Field of view is ~1.50 m. (B) Formation of weak foliation defined by an increase in modal biotite. Pencil is 14 cm long. (C) Typical outcrop of Palms granite, showing typical modal mineralogy discussed in text. Pencil (shown) is approximately 8 cm long. (D) Formation of weak foliation defined by the increase in modal biotite. The intensity of this foliation is slightly stronger than foliation observed in photograph B. An increase in grain size was also observed at this outcrop. Outcrop is cut by an aplite dike (upper left). Pencil is 14 cm long.

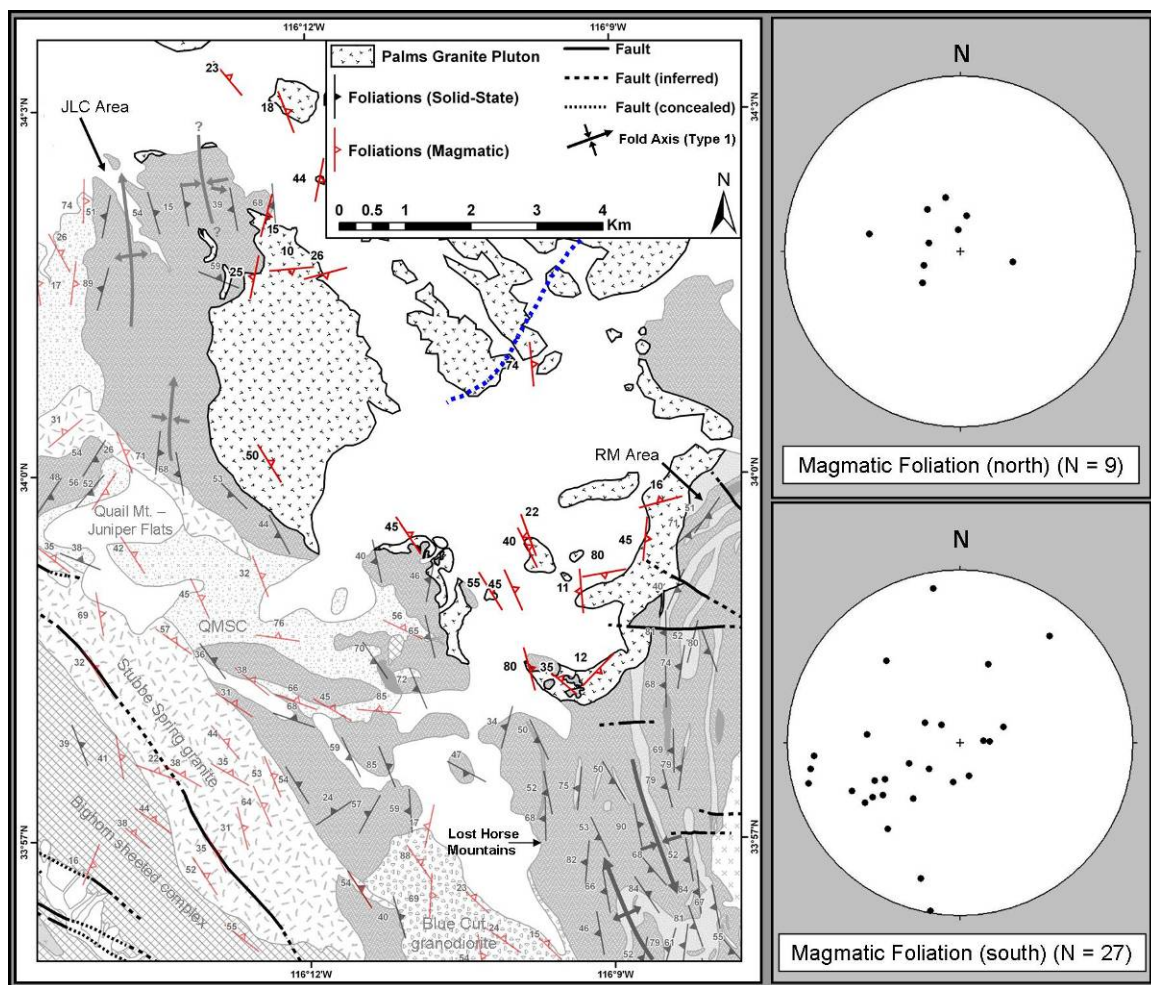


Figure 23A. Map of Palms granite fabric. Red symbols are defined as follows: bold red symbols are foliations within the Palms granite; faint red symbols are foliations in juxtaposed igneous bodies. All symbols show dip angles. Fold Axis (type 1) = metamorphic fold. Foliations plotted as poles to planes on equal area stereonets. JLC = Johnny Lang Canyon Area; QMSC = Quail Mt. sheeted complex; RM = Ryan Mountain area. Dotted blue line is boundary visible in satellite image (see Figure 23B). Within the stereonet plots, north corresponds to measurements northwest of the boundary; south corresponds to measurements southeast of the boundary. Outcrop measurements from Paterson (unpublished data), Barth (unpublished data), and this study.

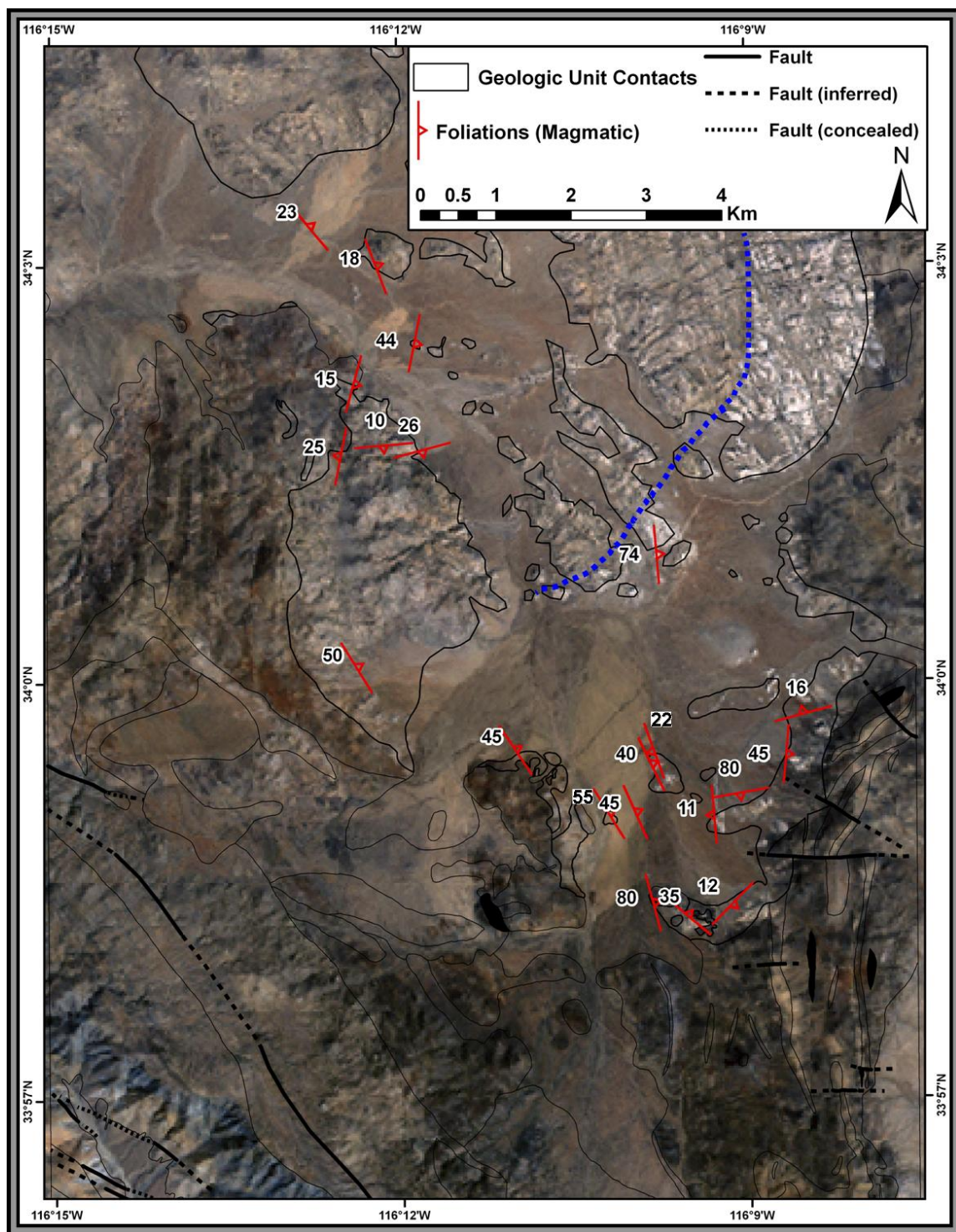


Figure 23B. True-color satellite image of Palms granite pluton. Note the visible boundary outlined by the blue dotted line. Contacts of major rock units are outlined in thin black lines. All symbols show dip angles. Outcrop measurements from Paterson (unpublished data), Barth (unpublished data), and this study.

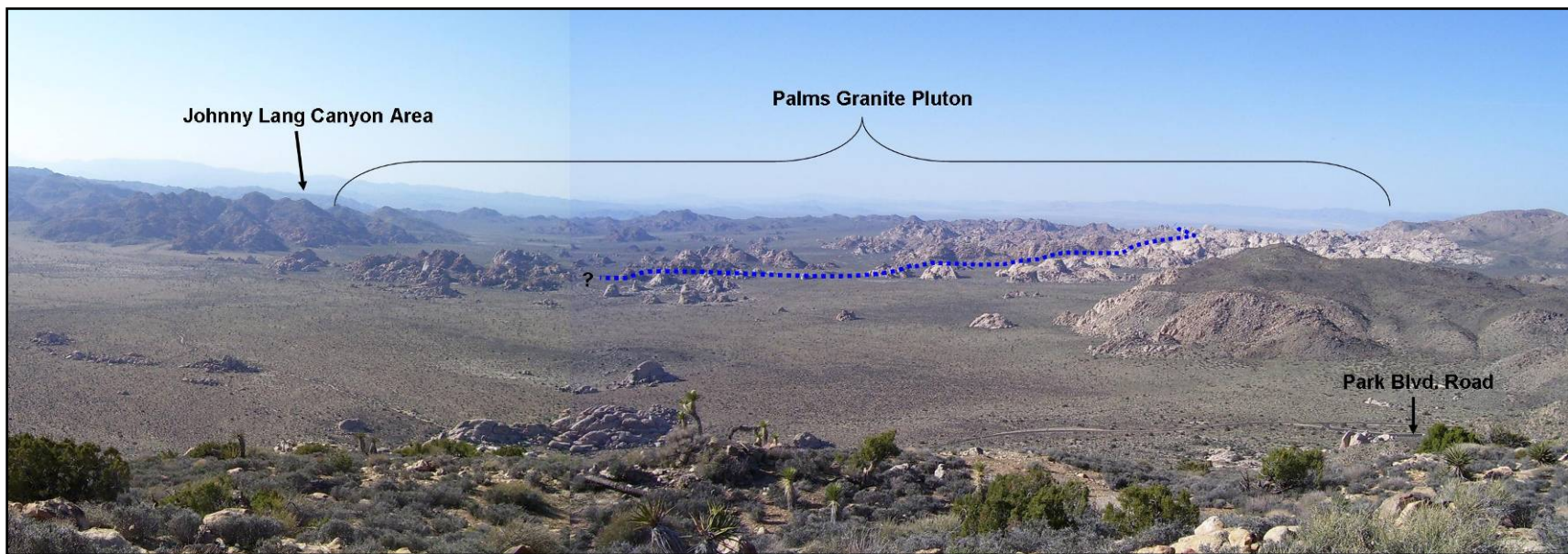


Figure 23C. Composite field photograph of Palms granite pluton. Note the color difference across the blue dotted line. Dotted blue line corresponds to the blue lines in Figure 23A and B. Image was taken from Ryan Mountain area (see Figure 23A for location), facing approximately northwest. Park Blvd. Road for scale (lower right corner).

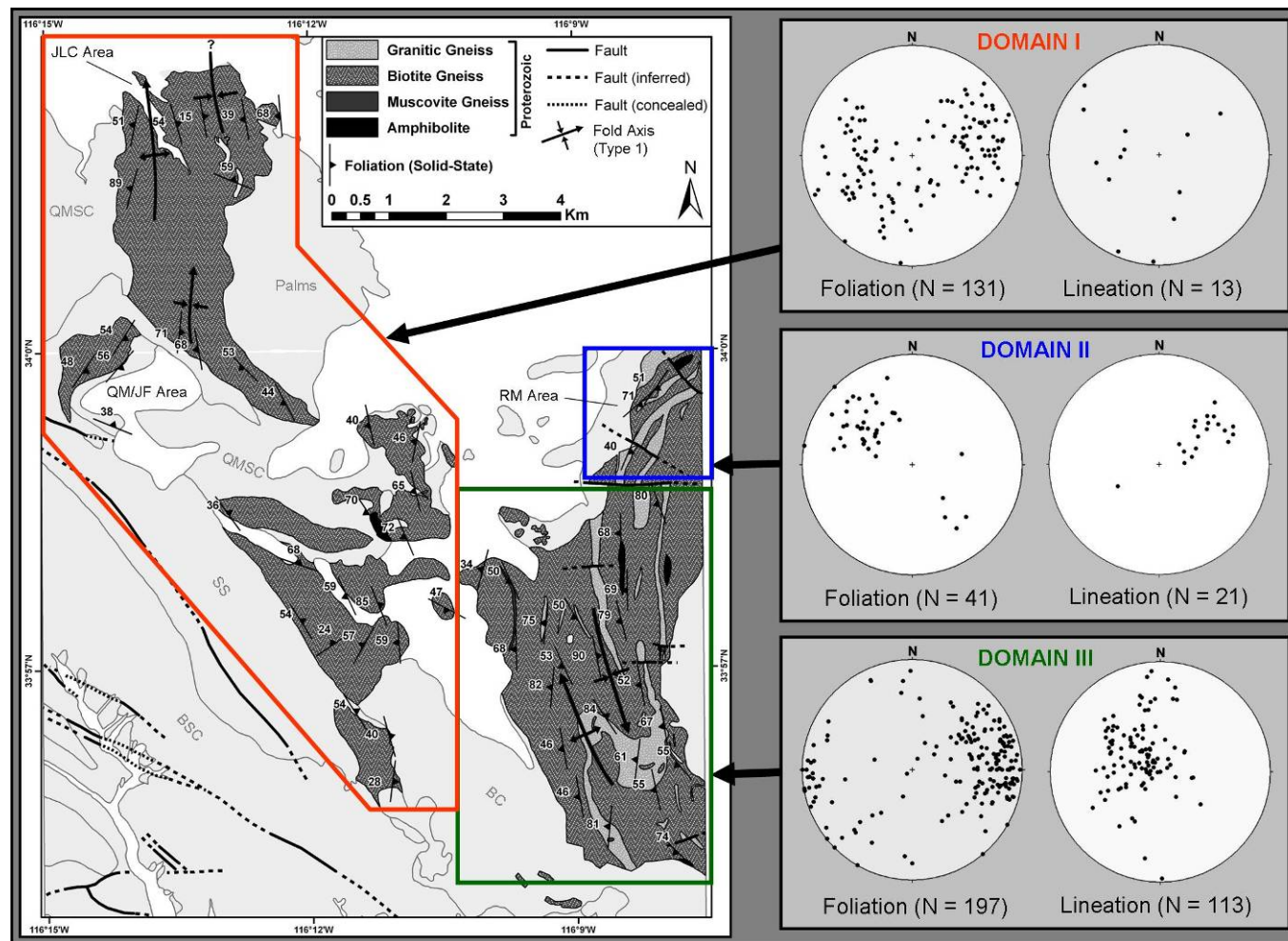


Figure 24. Summary of framework rock fabrics. Fold Axis (type 1) = metamorphic fold. Foliations plotted as poles to planes. BC = Blue Cut granodiotite; BSC = Bighorn sheeted complex; JLC = Johnny Lang Canyon; QM/JF = Quail Mt./ Juniper Flats; QMSC = Quail Mt. sheeted complex; RM = Ryan Mountain; SS = Stubbe Spring granite. Outcrop measurements from Paterson (unpublished data) and Barth (unpublished data).

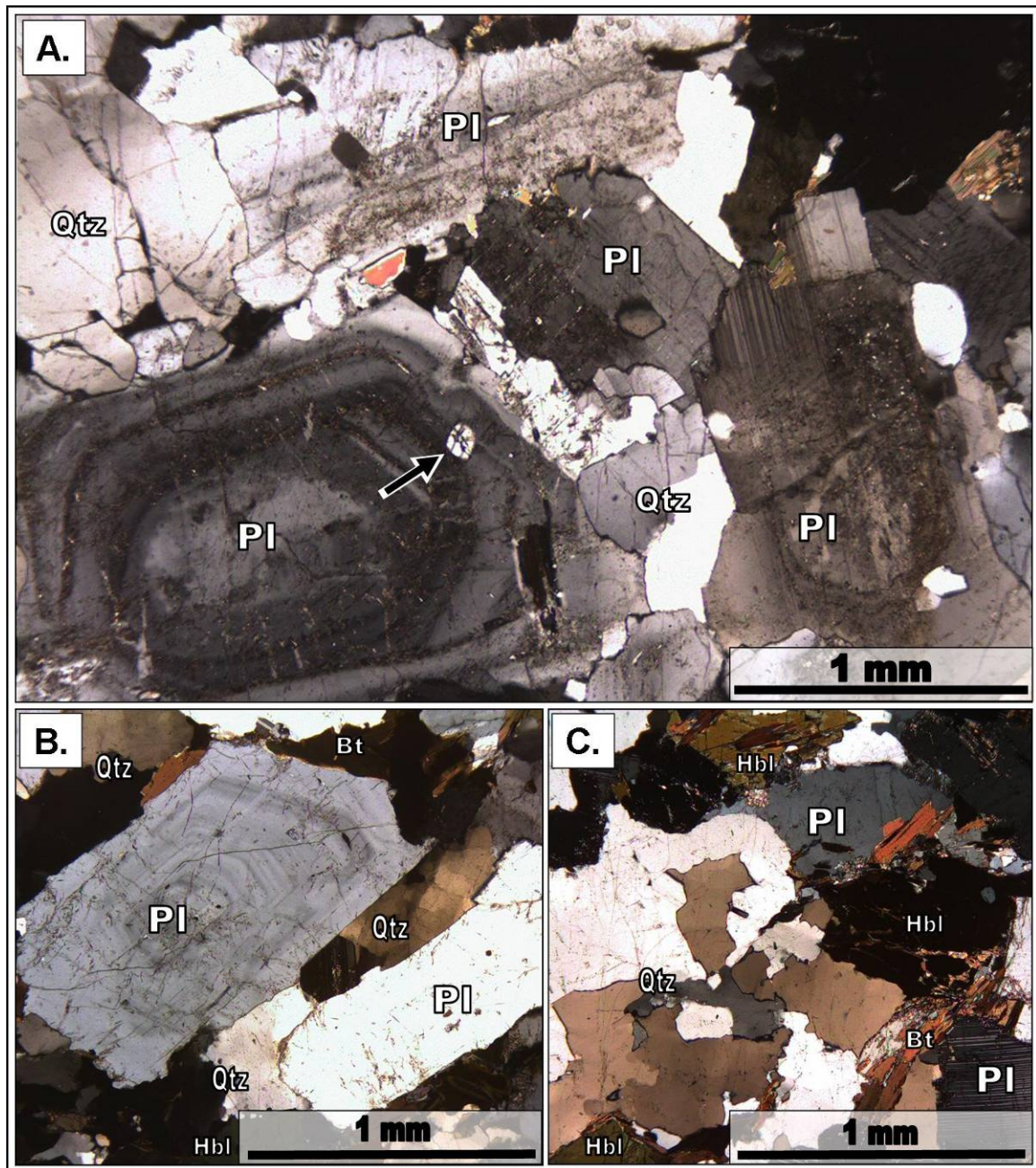


Figure 25. Photomicrographs of quartz microstructures. (A) Coarse-grained, hornblende-biotite granodiorite (077KB) showing weakly deformed quartz grains defined by minor undulose extinction. Arrow points to strain-free quartz inclusion within plagioclase lath. (B) Medium-grained, hornblende-biotite tonalite (0710KB) showing interstitial quartz grains with chessboard extinction. (C) Fine-grained, hornblende-biotite tonalite (JW95-256) showing grain-boundary migration recrystallization (lobate, amoeboid grain-shapes). Internally, grains show only weak undulose extinction. All images are shown with crossed polars. Biotite = Bt; Hornblende = Hbl; Plagioclase = Pl; Quartz = Qtz.

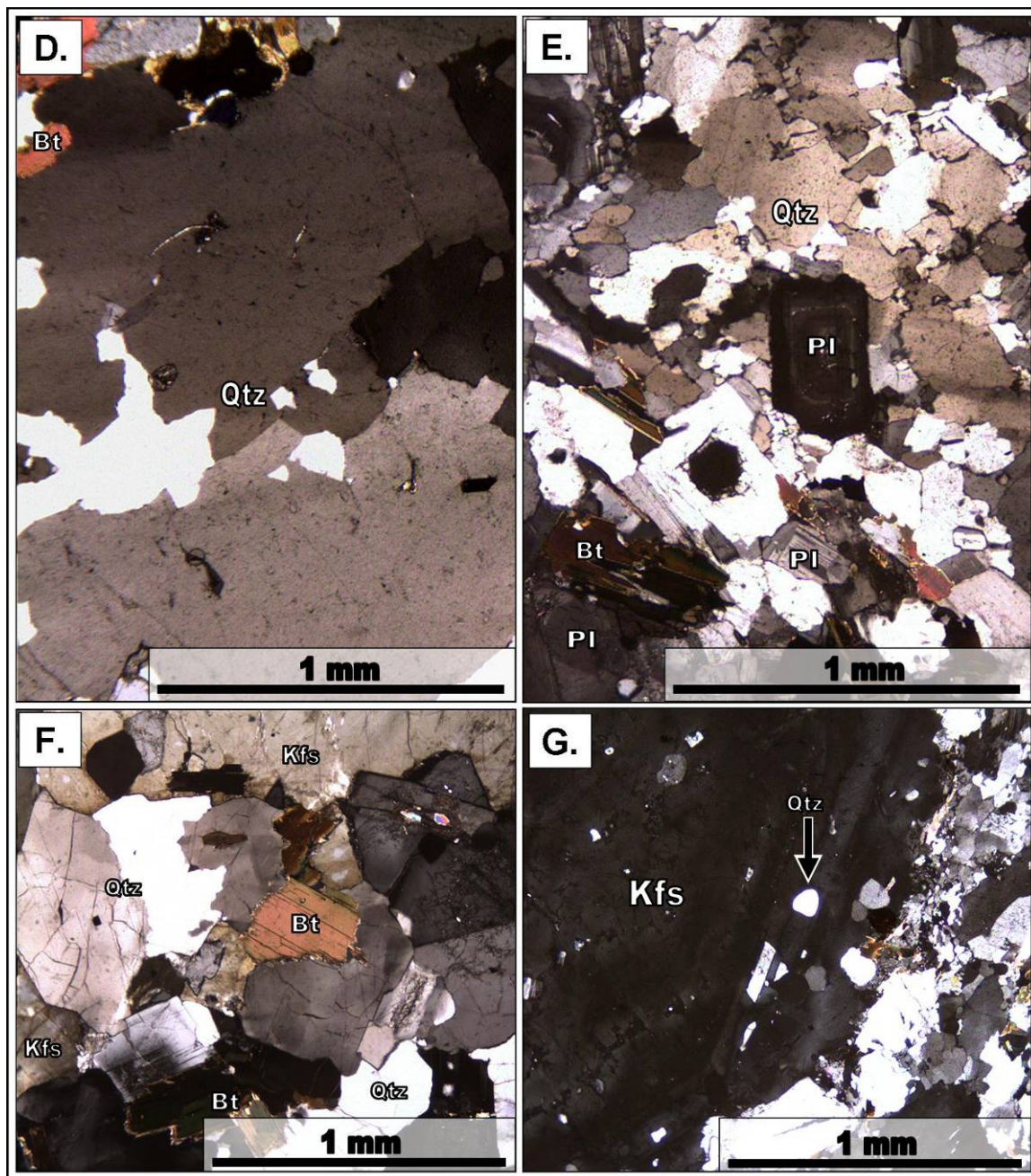


Figure 25. (continued) (D) Medium-grained, hornblende-biotite granodiorite (04-520) showing grain-boundary migration in quartz. (E) Medium-grained, biotite granite (071KB) showing subhedral plagioclase lath with compositional zoning surrounded by quartz that displays grain-boundary migration and minor subgrain formation. (F) Coarse-grained, biotite granite (04-561) showing weakly deformed quartz defined by weak undulose extinction and minor grain-boundary migration. (G) Fine-grained, biotite granodiorite (04-530) showing large, compositionally zoned potassium feldspar with inclusions of strain-free quartz. All images are shown with crossed polars. Biotite = Bt; Plagioclase = Pl; Potassium feldspar = Kfs; Quartz = Qtz.

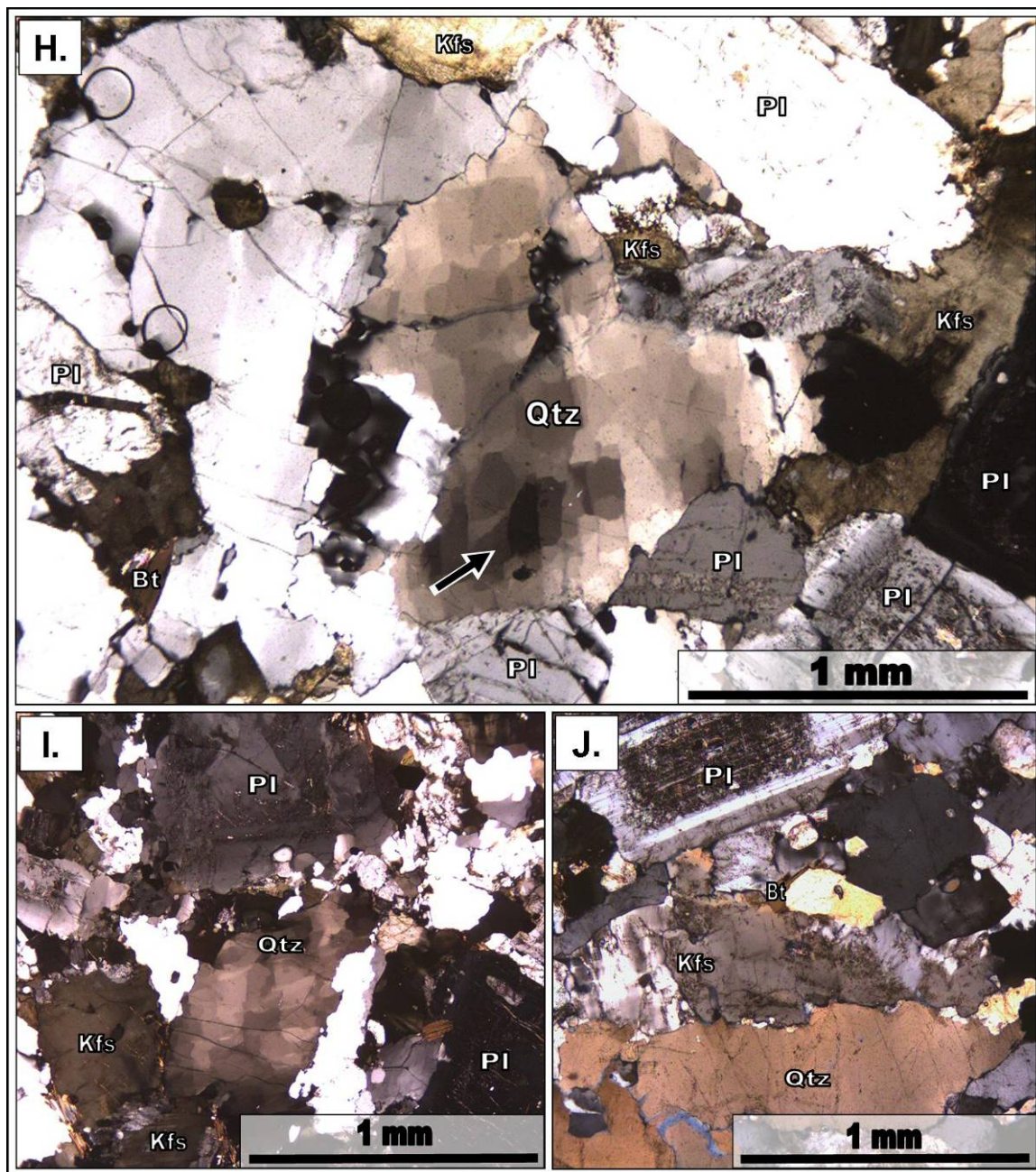


Figure 25. (continued) (H) Fine-grained, biotite granite (04-550) showing grain-boundary migration in quartz and chessboard extinction (arrow). (I) Medium-grained, biotite granodiorite (04-568) showing quartz with grain-boundary migration and chessboard extinction (crossed polars). (J) Fine-grained, biotite granite dike (JW95-263) showing slightly elongate quartz ribbon. Also note the compositional zoning within the plagioclase grain (top). Calcium-rich core is replaced by sericite. All images are shown with crossed polars. Biotite = Bt; Plagioclase = Pl; Potassium feldspar = Kfs; Quartz = Qtz.

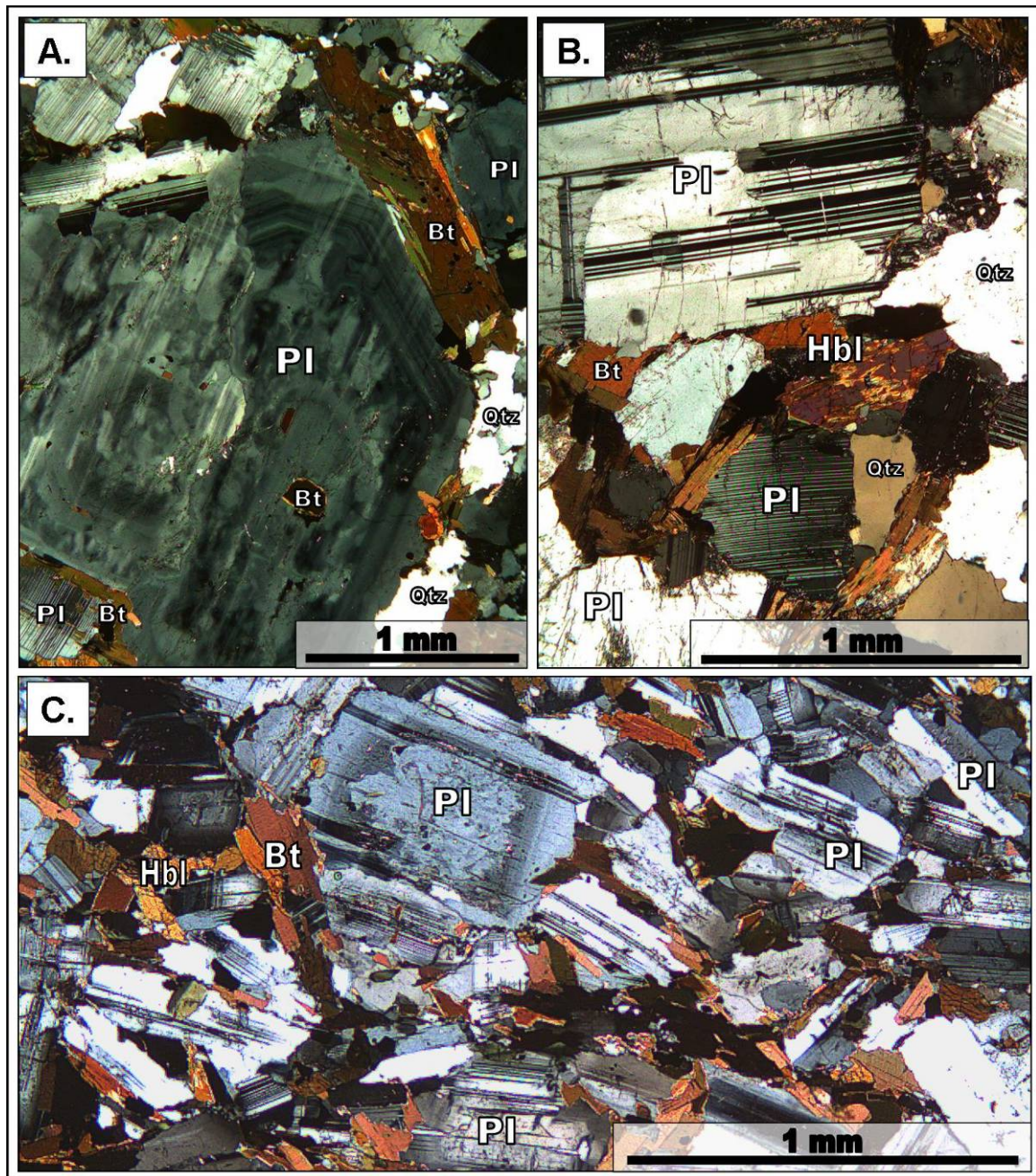


Figure 26. Photomicrographs of plagioclase microstructures. (A) Medium-grained, hornblende-biotite granodiorite (04-537) showing subhedral plagioclase grain with compositional zoning and biotite inclusions. (B) Fine-grained, hornblende-biotite tonalite (JW95-256) showing growth twins (top) and deformation twins (center-bottom) in plagioclase. (C) Fine-grained, hornblende-biotite tonalite (072KB) showing multiple, aligned plagioclase laths that do not show significant deformation. Plagioclase grains show evidence of zoning and inclusions of other primary, igneous minerals. All images are shown with crossed polars. Biotite = Bt; Hornblende = Hbl; Plagioclase = Pl; Quartz = Qtz.

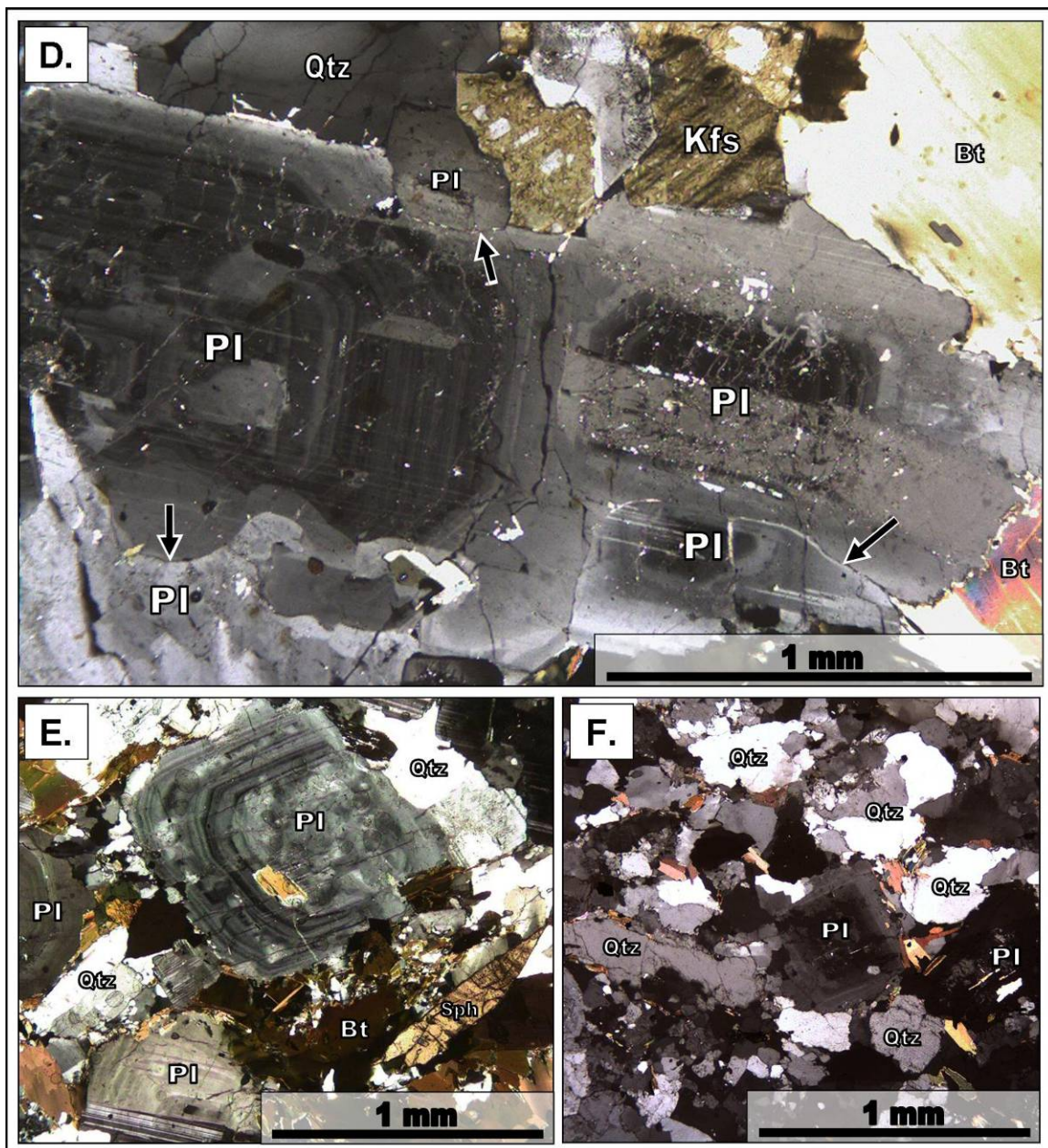


Figure 26. (continued) (D) Coarse-grained, biotite granite (04-528) showing subhedral plagioclase grain with compositional zoning and synneusis. Also shown is an example of contact melting between impinging plagioclase grains (arrows). (E) Medium-grained, hornblende-biotite granodiorite (04-520) showing compositional zoning and biotite inclusions. (F) Fine-grained, biotite granite (04-544) showing weak zoning and grain-boundary migration defined by amoeboid grain-boundaries within plagioclase (center). Note that quartz also displays grain-boundary migration. Quartz also displays both ribbon and pooled crystal shapes. All images are shown with crossed polars. Biotite = Bt; Plagioclase = Pl; Potassium feldspar = Kfs; Quartz = Qtz; Sphene = Sph.

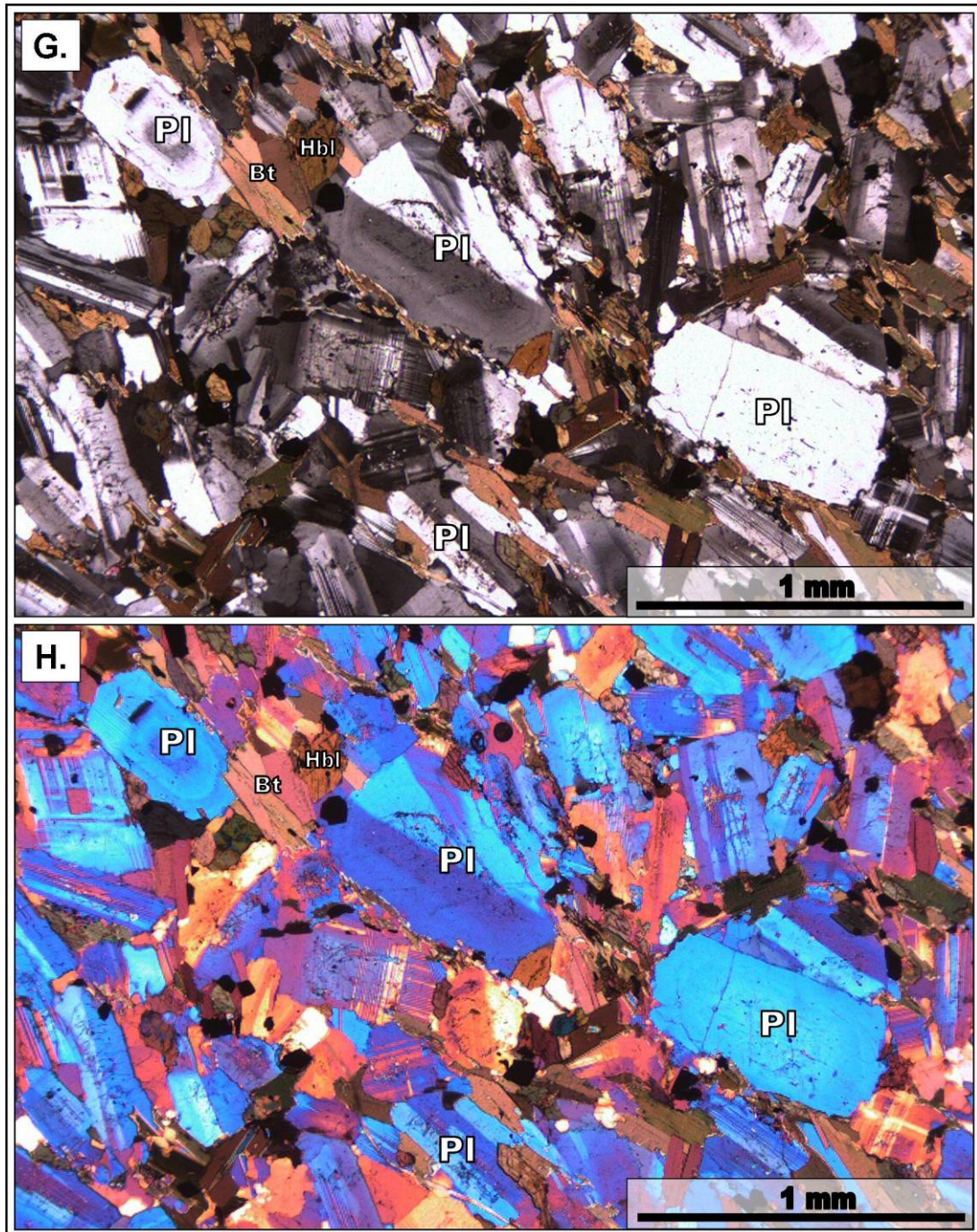


Figure 26. (continued) (G) Fine-grained, hornblende-biotite tonalite (04-535) showing alignment of euhedral to subhedral plagioclase laths with deformation twinning (crossed polars). (H) Same image as G, but taken with accessory plate (gypsum plate). Cool colors indicate that the grain's high index of refraction (slow ray) is parallel to the NE-SW slow ray in the gypsum plate. Note that nearly all plagioclase grains have the same orientation as observed with the gypsum plate. Biotite = Bt; Hornblende = Hbl; Plagioclase = Pl.

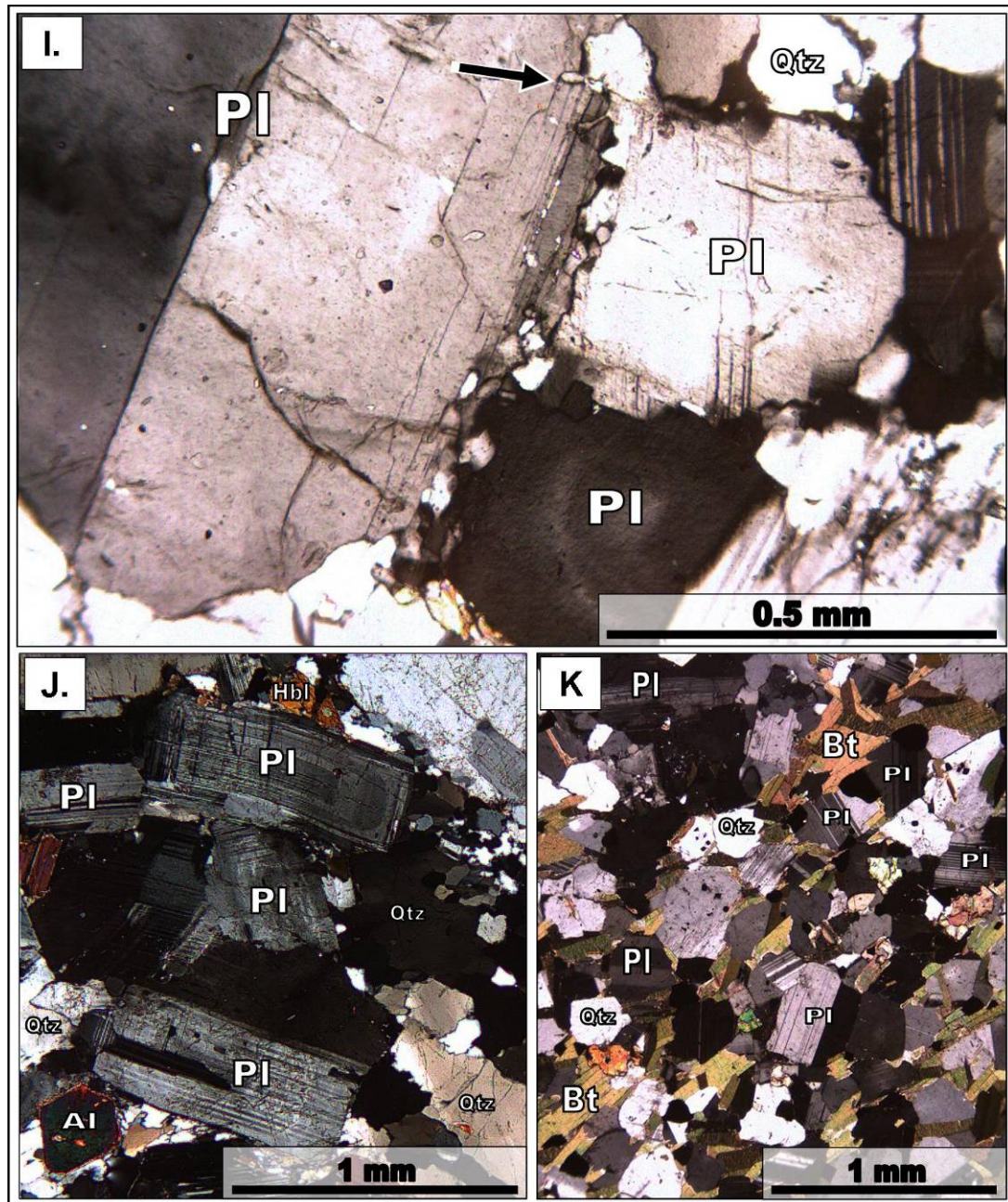


Figure 26. (continued) (I) Fine-grained, biotite granite (JW95-262) showing anhedral plagioclase grains with simple twins and grain-boundary migration (GBM) (arrow). GBM is defined by more amoeboid grain shapes. Also, note the small recrystallized plagioclase grains along the boundary. (J) Medium-grained, hornblende-biotite granodiorite (04-518) showing euhedral to subhedral plagioclase laths with deformation twins and ductile bending. (K) Medium-grained, hornblende-biotite tonalite (04-548) showing significant grain-boundary migration in plagioclase. Grains retain simple twins and deformation twins, but are extensively recrystallized into more amoeboid shapes. All images are shown with crossed polars. Allanite = Al; Biotite = Bt; Hornblende = Hbl; Plagioclase = Pl; Quartz = Qtz.

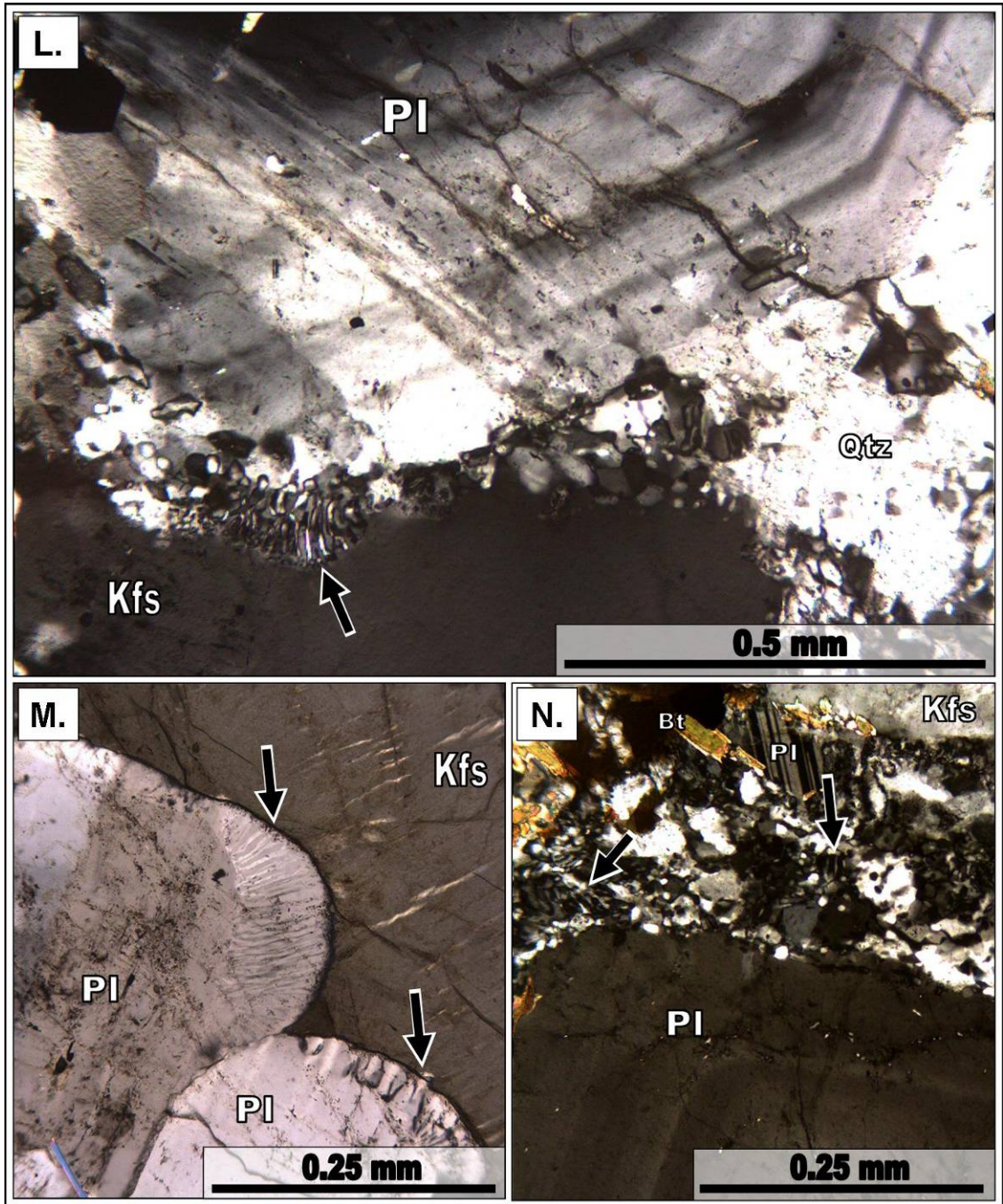


Figure 26. (continued) (L) Medium-grained, hornblende-biotite granodiorite (04-520) showing euhedral plagioclase grains with compositional zoning and myrmekite (arrow). Recrystallization of myrmekite, quartz, potassium feldspar, and plagioclase are observed along the boundary. (M) Coarse-grained, biotite granite (JW93-217) showing delicate myrmekite along plagioclase boundaries (arrows). (N) Medium-grained, hornblende-biotite granodiorite (04-546) showing intergranular recrystallization of myrmekite (left arrow) and plagioclase (right arrow). All images are shown with crossed polars. Biotite = Bt; Plagioclase = Pl; Potassium feldspar = Kfs; Quartz = Qtz.

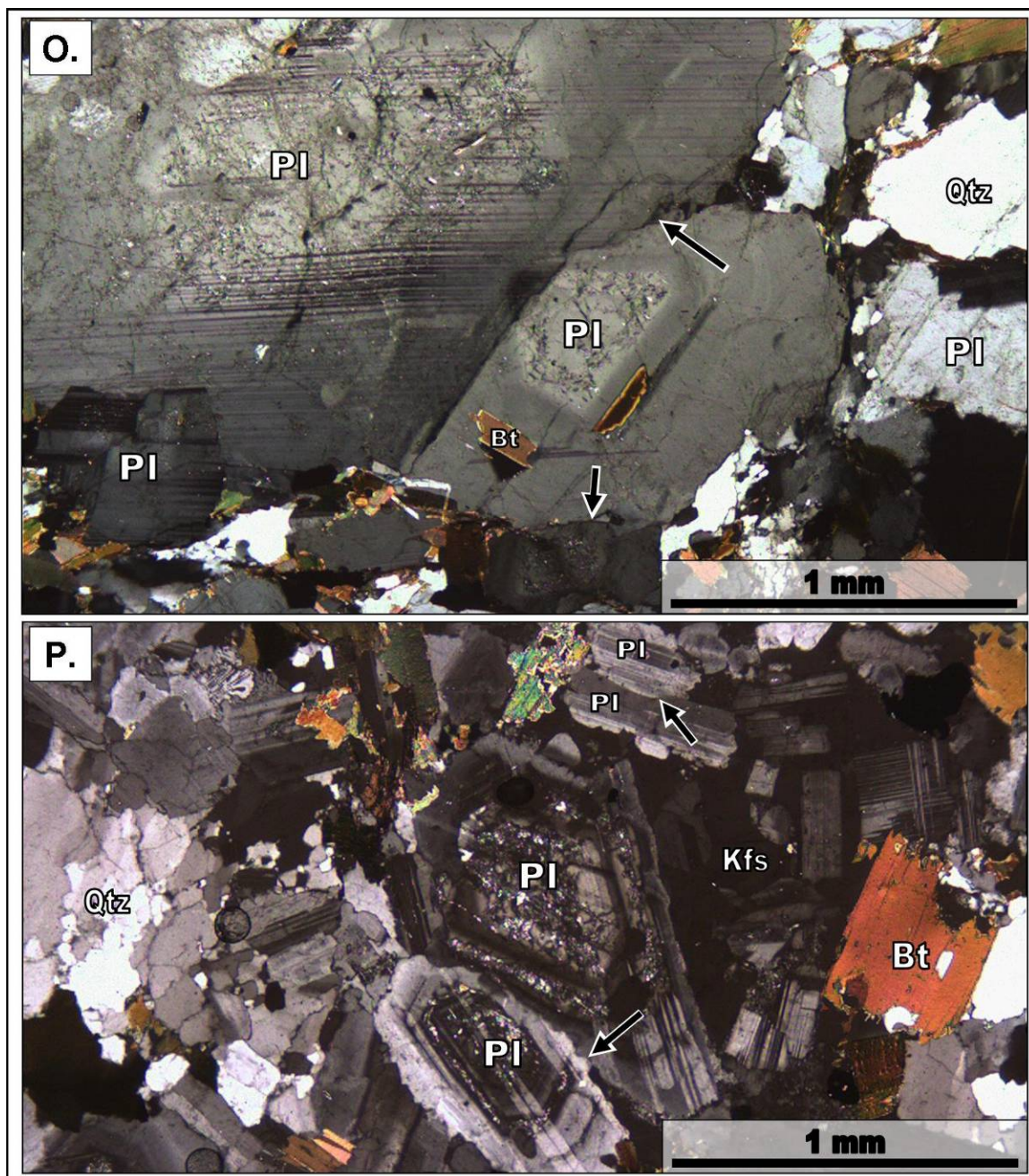


Figure 26. (continued) (O) Medium-grained, biotite granite (071KB) with impinging plagioclase grains that truncate compositional zoning (arrows). Both grains contain well-separated cores that are nearly surrounded by compositional zoning. Also, note that the lower plagioclase grain (center) contains euhedral, strain-free biotite grains that are parallel to the compositional zoning. (P) Fine-grained, biotite granodiorite (04-526) with impinging plagioclase grains that truncate compositional zoning (arrows). Also, note that potassium feldspar is found molding both sets of impinging grains. All images are shown with crossed polars. Biotite = Bt; Plagioclase = Pl; Potassium feldspar = Kfs; Quartz = Qtz.

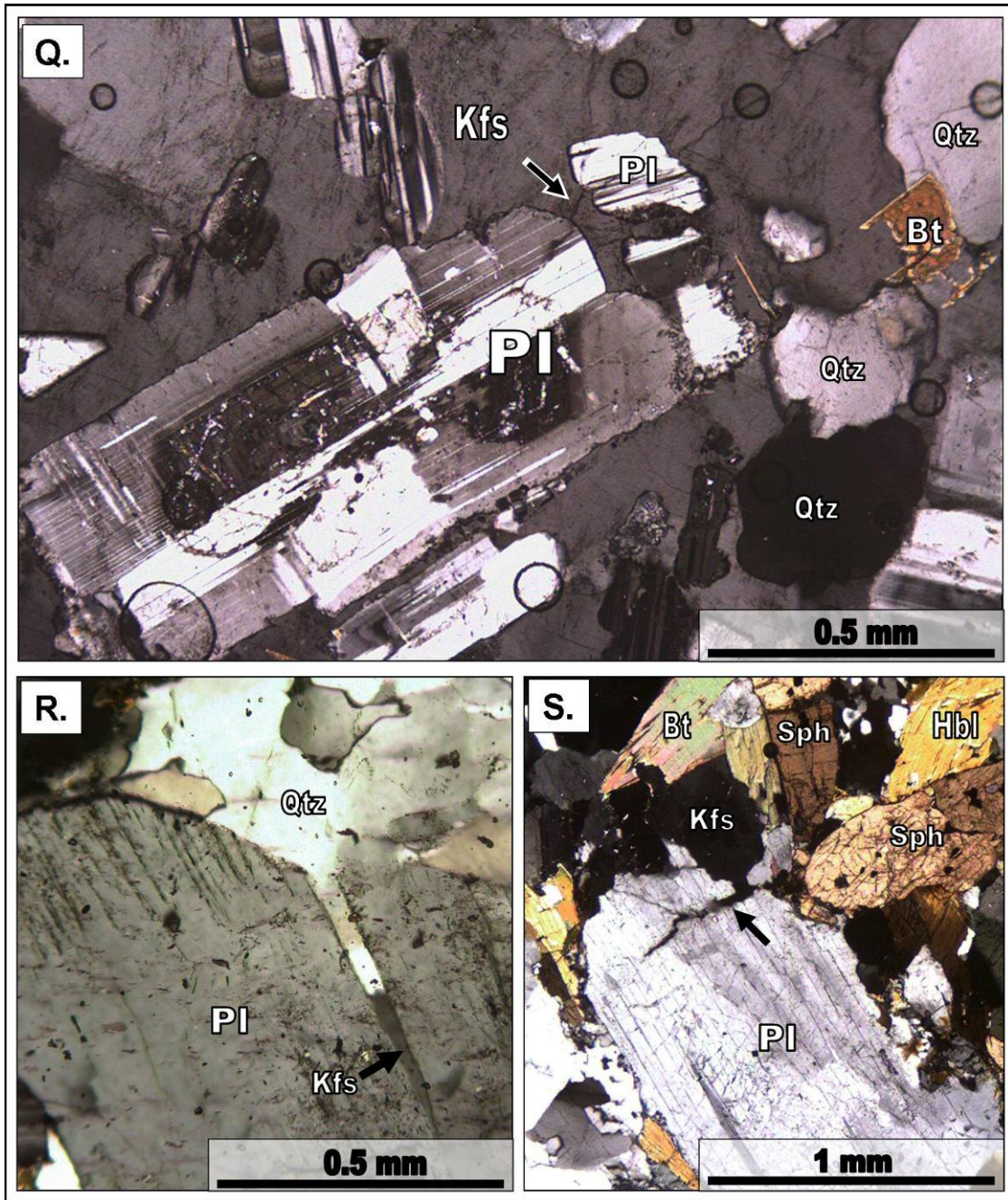


Figure 26. (continued) (Q) Fine-grained, biotite granodiorite (04-527) showing intragranular fracture of plagioclase grain (arrow). Plagioclase grain is found within large, potassium feldspar host. Mineral filling the fracture is potassium feldspar. (R) Medium-grained, hornblende-biotite granodiorite (04-531) showing intragranular fracture of plagioclase filled with potassium feldspar and quartz. (S) Medium-grained, hornblende-biotite granodiorite (04-518) showing intragranular fracture of plagioclase filled with potassium feldspar. All images are shown with crossed polars. Biotite = Bt; Hornblende = Hbl; Plagioclase = Pl; Potassium feldspar = Kfs; Quartz = Qtz; Sphene = Sph.

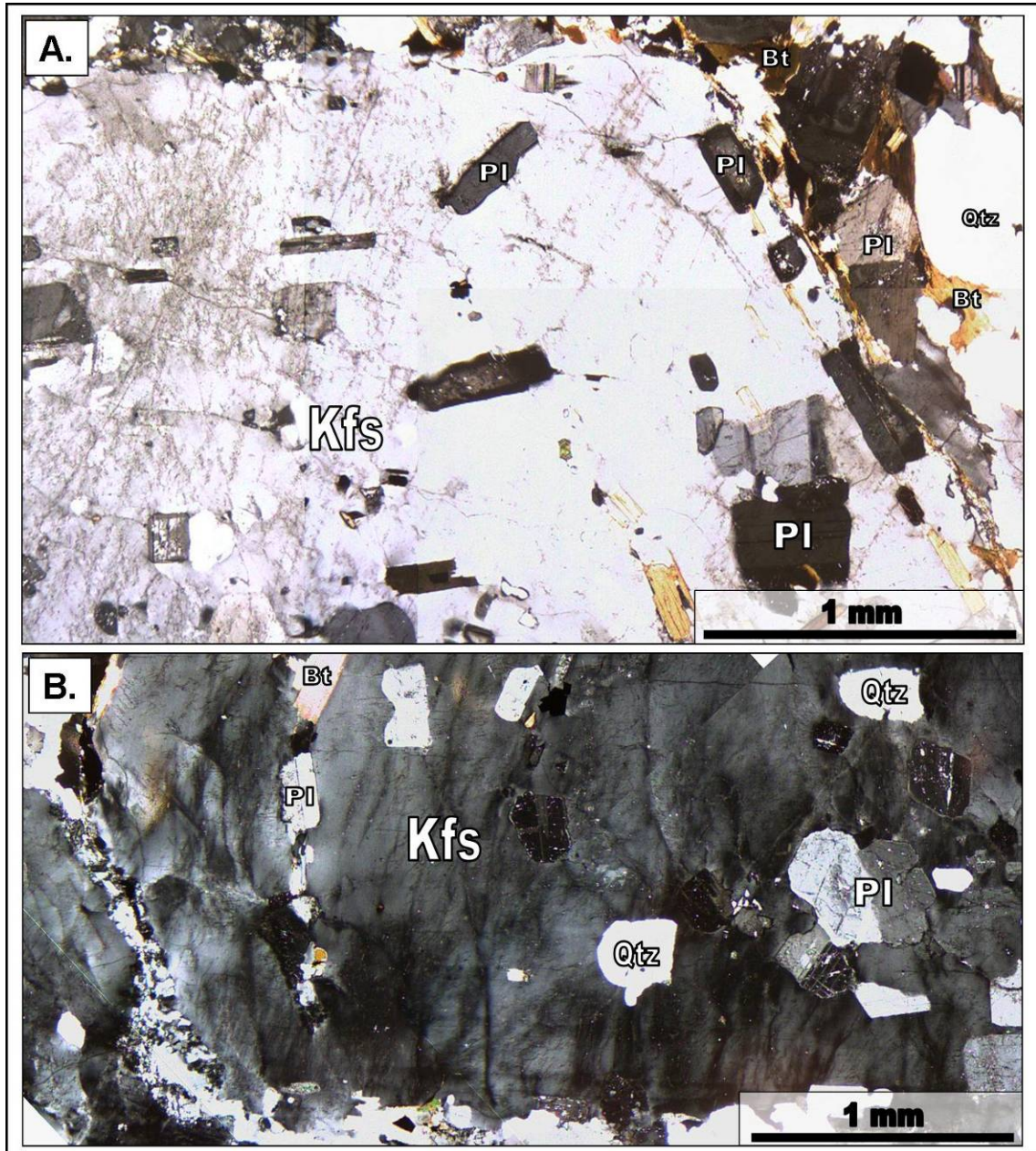


Figure 27. Photomicrographs of potassium feldspar microstructures. (A) Medium-grained, biotite granite (071KB) showing euhedral to subhedral potassium feldspar phenocrysts with compositional zoning defined by inclusions of primary, igneous minerals (biotite, plagioclase, and quartz). (B) Coarse-grained, hornblende-biotite granodiorite (077KB) showing euhedral to subhedral potassium feldspar phenocrysts with compositional zoning defined by inclusions of primary, igneous minerals (biotite, plagioclase, and quartz). All images are shown with crossed polars. Biotite = Bt; Plagioclase = Pl; Potassium feldspar = Kfs; Quartz = Qtz.

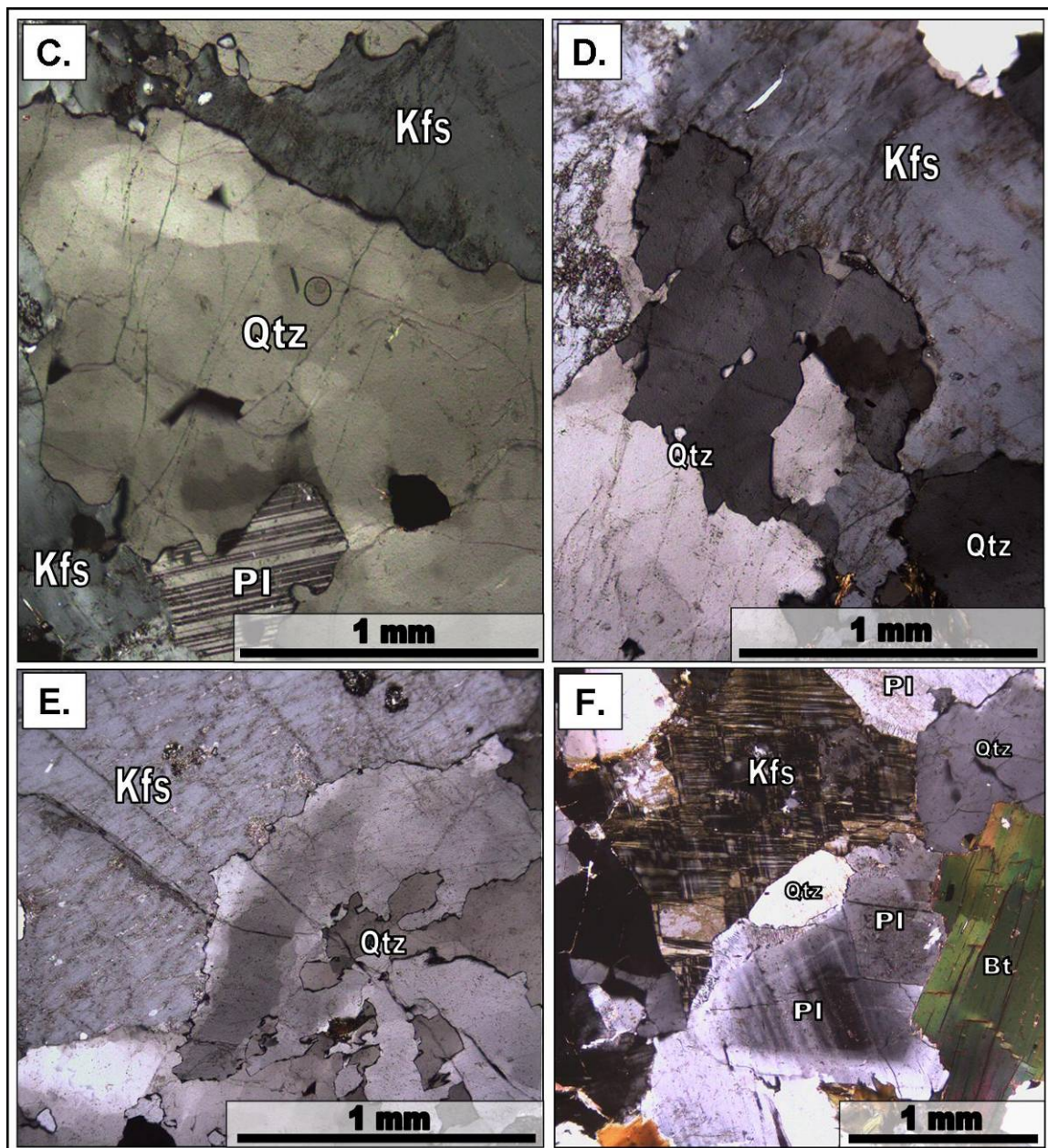


Figure 27. (continued) (C) Fine-grained, biotite granite (JW95-262) showing grain-boundary migration in potassium feldspar, plagioclase, and quartz. Also, note that quartz shows evidence of chessboard extinction. (D) Coarse-grained, biotite granite (JW93-217) showing grain-boundary migration in potassium feldspar and quartz. Potassium feldspar also shows evidence of flame perthite (upper right to lower left). (E) Coarse-grained, biotite granodiorite (04-566) showing grain-boundary migration in potassium feldspar and quartz. (F) Coarse-grained, biotite granite (04-528) showing interstitial potassium feldspar with microcline twinning. Also, note the formation of myrmekite along the plagioclase/potassium feldspar boundaries. All images are shown with crossed polars. Biotite = Bt; Plagioclase = Pl; Potassium feldspar = Kfs; Quartz = Qtz.

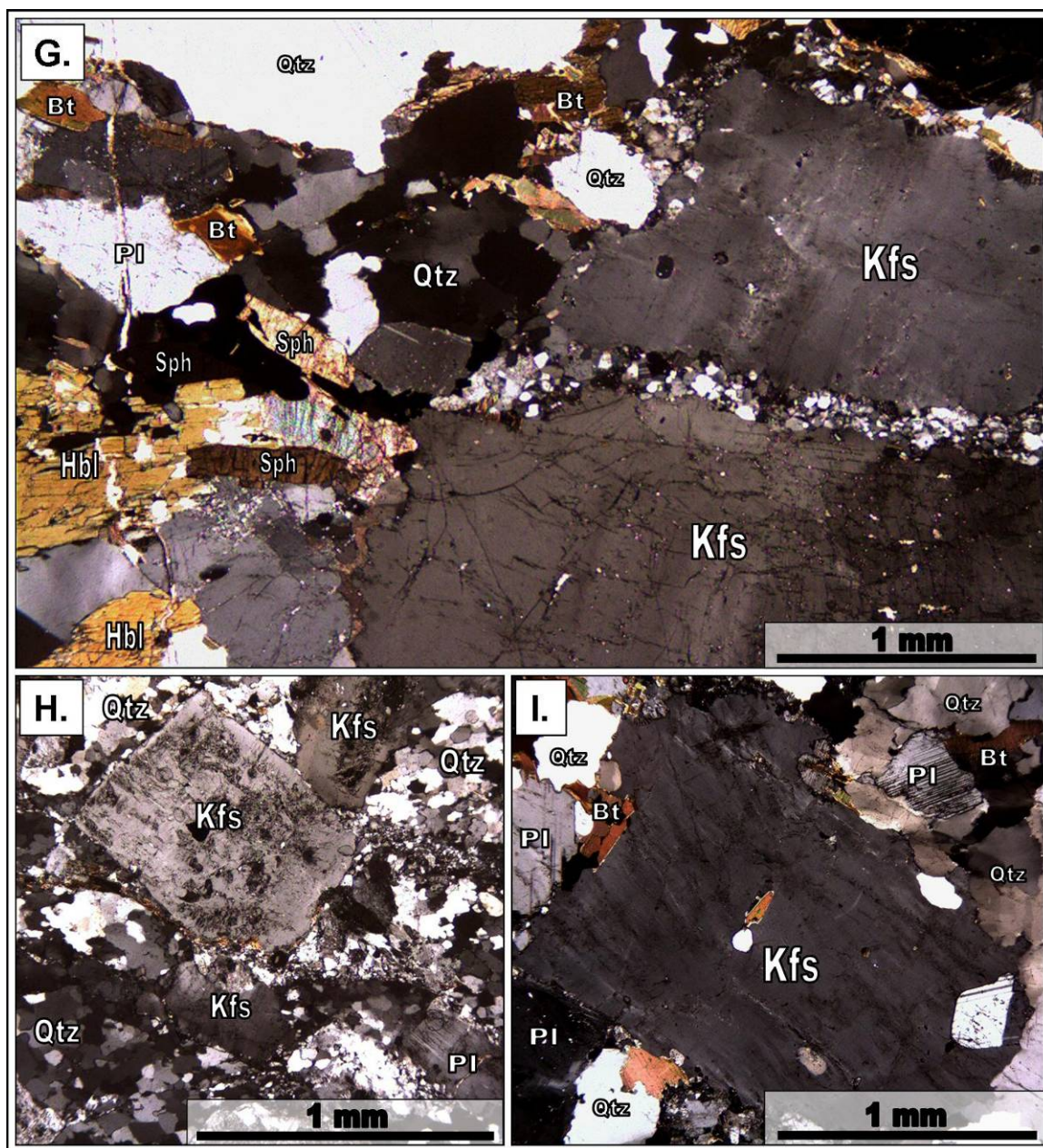


Figure 27. (continued) (G) Medium-grained, hornblende-biotite granodiorite (JW92-199) showing potassium feldspar phenocrysts (right) with intergranular aggregates of recrystallized quartz, plagioclase, and potassium feldspar. Also, note that intergranular aggregates are localized along potassium feldspar grain-boundaries. (H) Fine-grained, muscovite granite (04-522) showing large, isolated phenocrysts of potassium feldspar surrounded by recrystallized quartz, potassium feldspar, and plagioclase. (I) Medium-grained, hornblende biotite granodiorite (04-565) showing grain-boundary migration in potassium feldspar, plagioclase, and quartz. All images are shown with crossed polars. Biotite = Bt; Plagioclase = Pl; Potassium feldspar = Kfs; Quartz = Qtz.

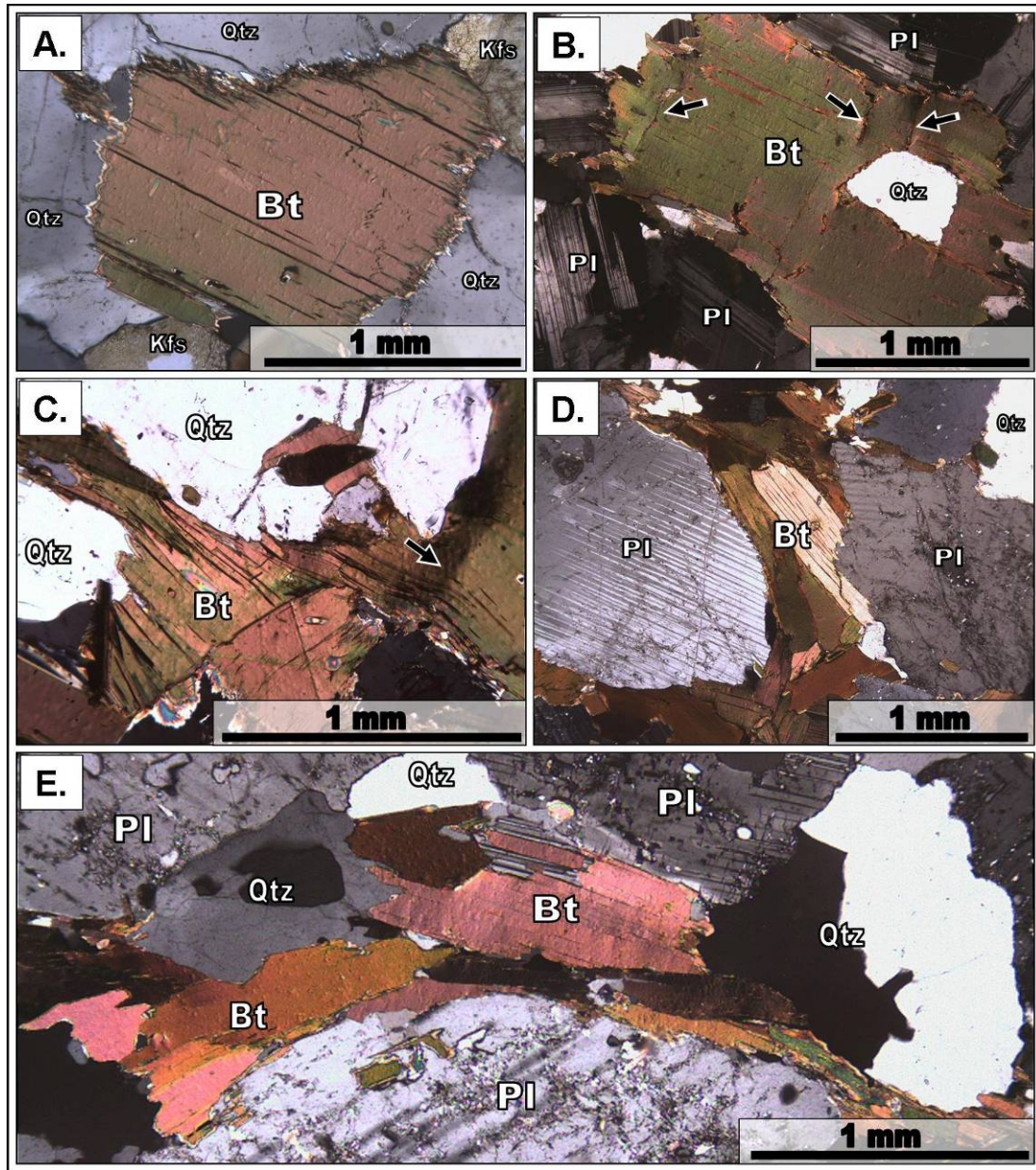


Figure 28. Photomicrographs of biotite microstructures. (A) Coarse-grained, biotite granite (04-561) showing primary biotite grain with slightly ragged margins. (B) Coarse-grained, hornblende-biotite granodiorite (JW92-199) showing primary biotite grains with ragged margins and incipient intragranular fractures (arrows). (C) Medium-grained, biotite granite (04-562) showing primary biotite grains with slight kinking (arrow) and ragged margins. (D) Medium-grained, biotite granodiorite (JW93-215) showing cluster of primary biotite grains that contain ragged margins and incipient intragranular fractures. (E) Medium-grained, biotite granodiorite (JW93-216) showing cluster of primary biotite grains wrapping plagioclase laths that define folia (left to right). All images are shown with crossed polars. Biotite = Bt; Plagioclase = Pl; Potassium feldspar = Kfs; Quartz = Qtz.

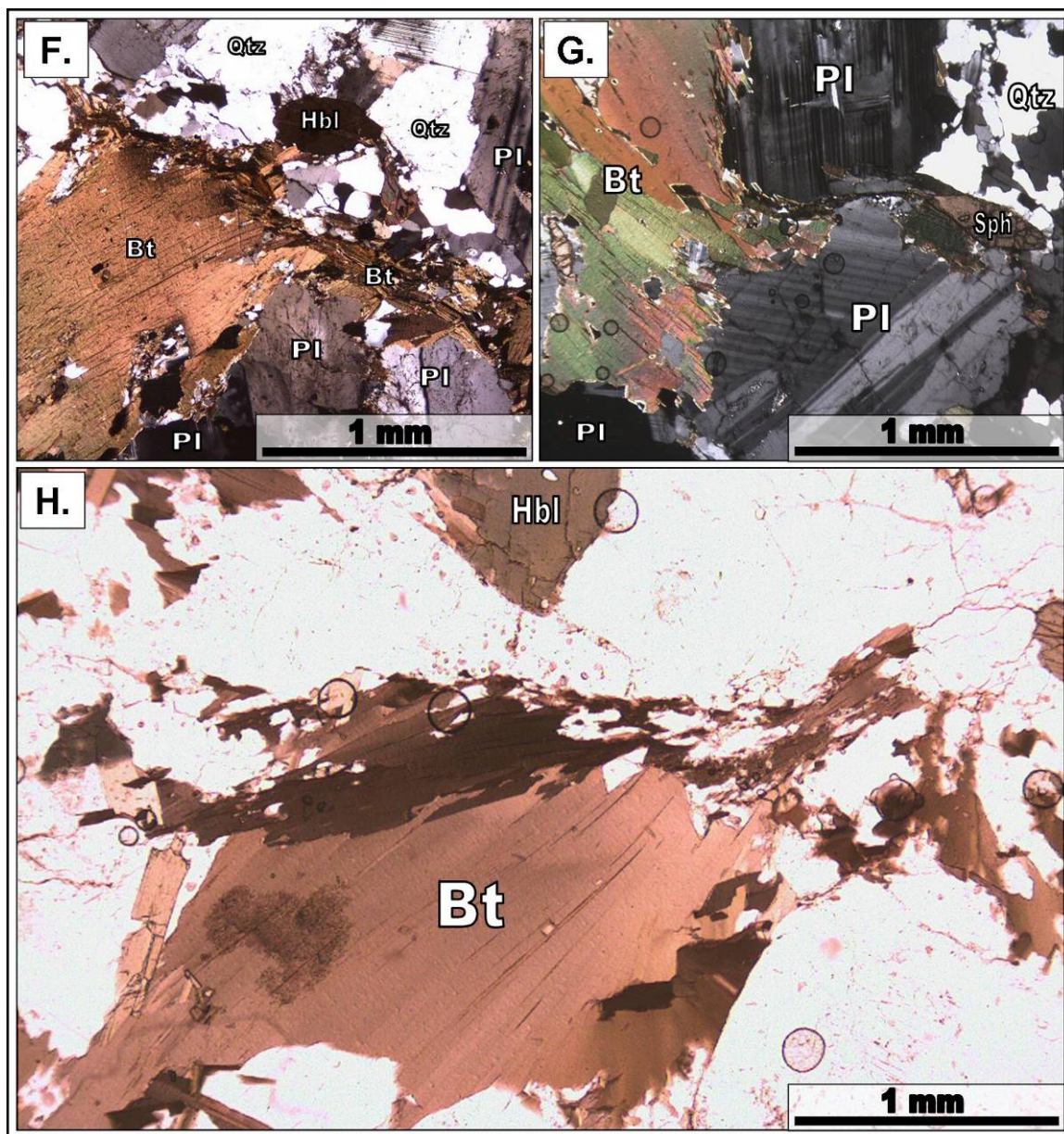


Figure 28. (continued) (F) Medium-grained, hornblende-biotite granodiorite (04-534) with primary biotite grains forming the incipient stages of folia development. Grains are cleaved and squeezed between plagioclase, hornblende, and quartz grains. Many of the grains that form the fine-grained folia show evidence of recrystallization. (G) Medium-grained, hornblende-biotite granodiorite (JW92-199) with primary biotite grains that are cleaved and squeezed between impinging plagioclase grains, forming the incipient stages of folia development. (H) Medium-grained, hornblende-biotite tonalite (0710KB) with primary biotite grains that are squeezed into a fine-grained folia. Finer-grained biotite aggregate shows evidence of recrystallization. Image F and G are shown with crossed polars. Image H shown in plain polar light. Biotite = Bt; Hornblende = Hbl; Plagioclase = Pl; Quartz = Qtz; Sphene = Sph.

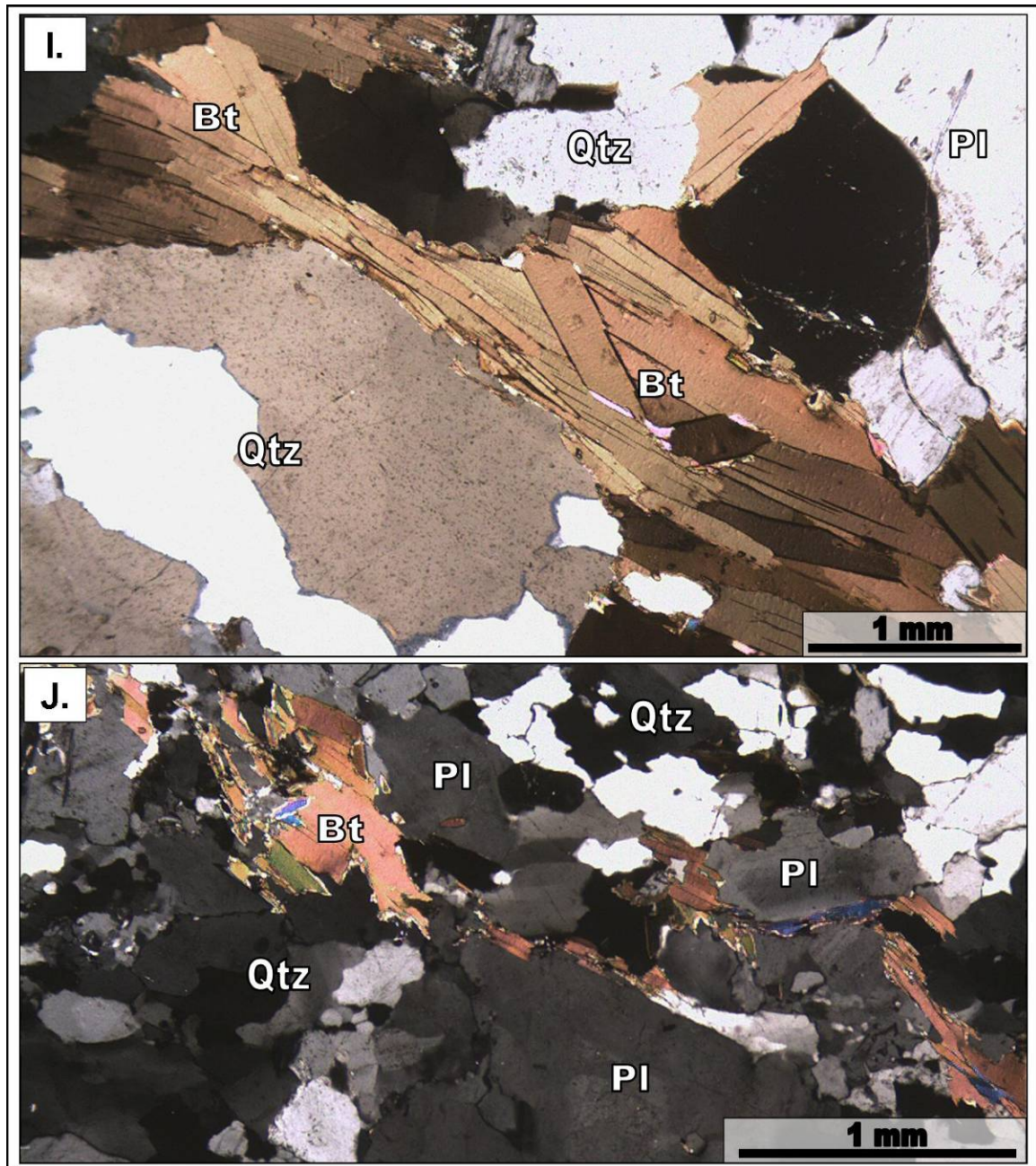


Figure 28. (continued) (I) Coarse-grained, biotite granodiorite (04-564) showing cluster of primary biotite grains squeezed between quartz grains. Biotite grains show evidence of minor subsolidus deformation defined by ragged margins and local kinking (left). (J) Fine-grained, biotite granite (04-551) showing primary biotite grains with minor subsolidus deformation defined by ragged margins and local kinking. Some grains show evidence of recrystallization, forming fine-grained aggregates along grain boundaries. These grains define a biotite folia (upper left to lower right). All images show with crossed polars. Biotite = Bt; Plagioclase = Pl; Quartz = Qtz.

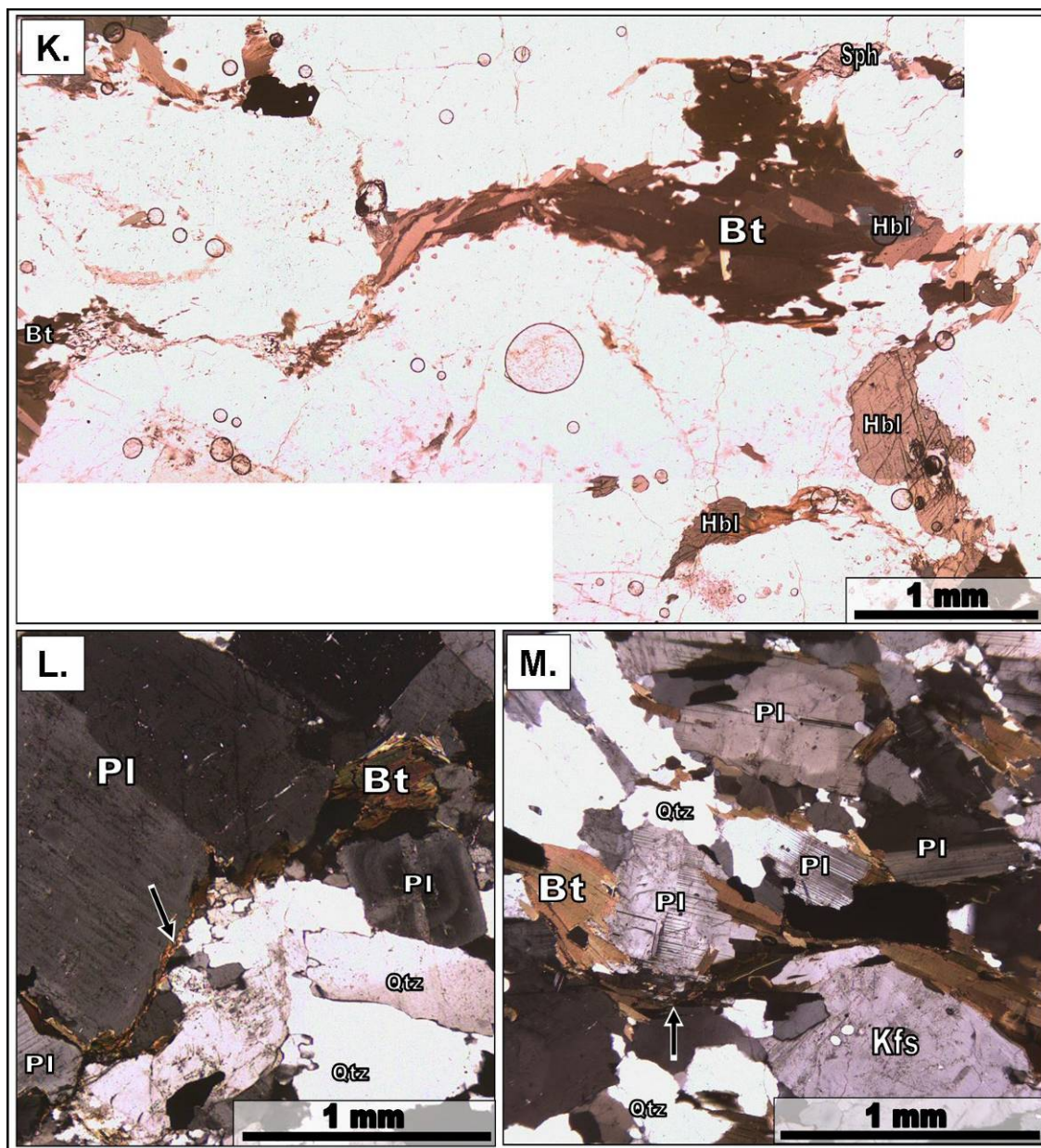


Figure 28. (continued) (K) Medium-grained, hornblende-biotite granodiorite (04-520) showing primary biotite and hornblende grains that define hand-specimen foliation (left to right). (L) Fine-grained, biotite granite (04-544) showing strongly deformed biotite grains. Recrystallized grains (arrow – left) anastomose strong plagioclase and quartz grains. Also, note that plagioclase retains compositional zoning (center-right) (M) Fine-grained, hornblende-biotite granodiorite (04-553) showing biotite grains that are locally recrystallized. Recrystallization of biotite occurs preferentially between zones of high stress (impinging plagioclase and quartz grains). Grain-boundary migration is present in all phases. Image K shown in plain polar light. Images L and M are shown with crossed polars. Biotite = Bt; Hornblende = Hbl; Plagioclase = Pl; Potassium feldspar = Kfs; Quartz = Qtz; Sphene = Sph.

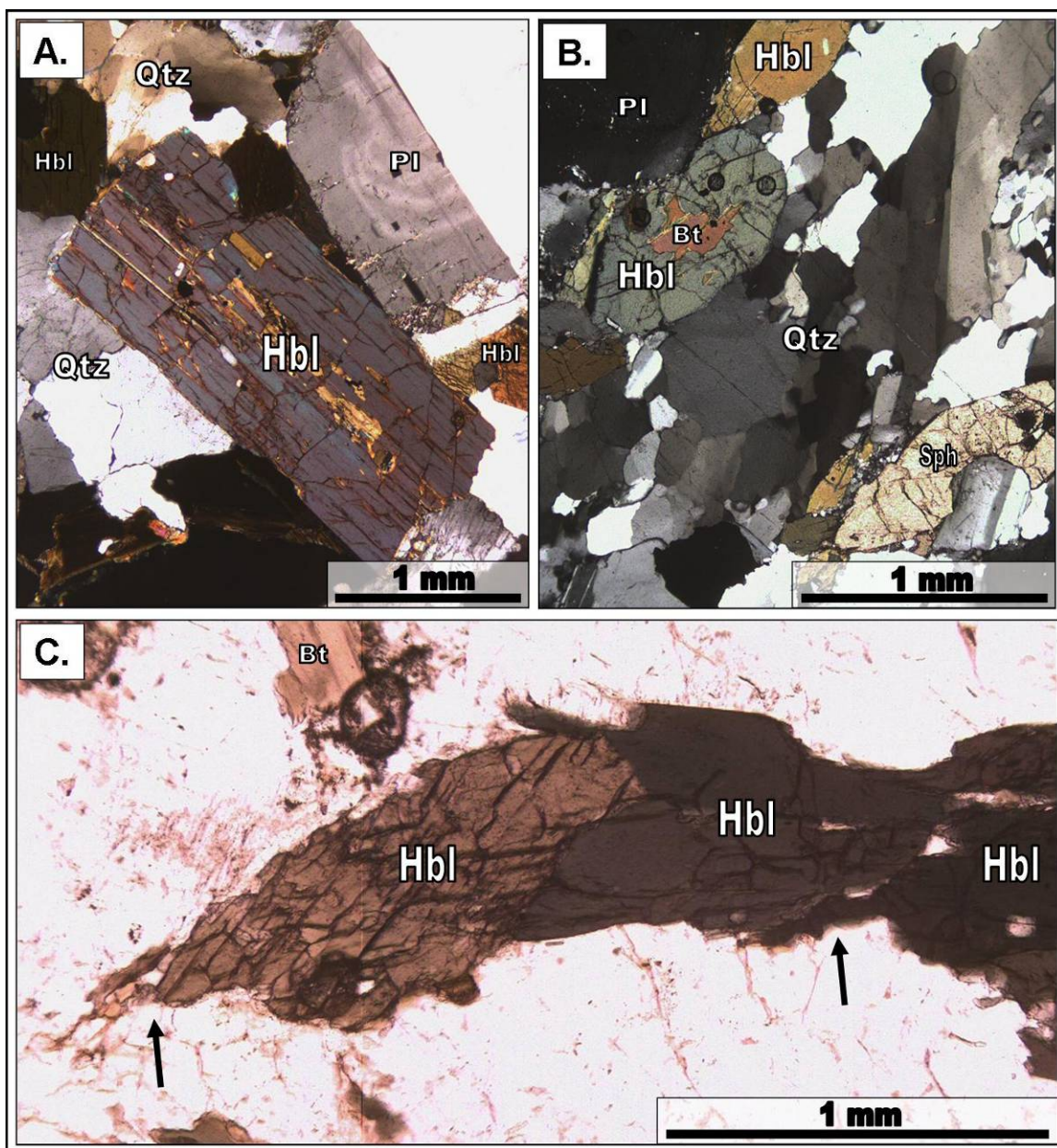


Figure 29. Photomicrographs of hornblende microstructures. (A) Medium-grained, hornblende-biotite tonalite (0710KB) showing euhedral hornblende lath with biotite inclusions. (B) Medium-grained, hornblende-biotite granodiorite (04-520) showing euhedral hornblende grain with biotite inclusions. (C) Medium-grained, hornblende-biotite granodiorite (04-520) showing cleavage-controlled fractures and misoriented grain fragments (arrows). Images A and B are shown with crossed polars; C in plain polar light. Biotite = Bt; Hornblende = Hbl; Plagioclase = Pl; Quartz = Qtz; Sphene = Sph.

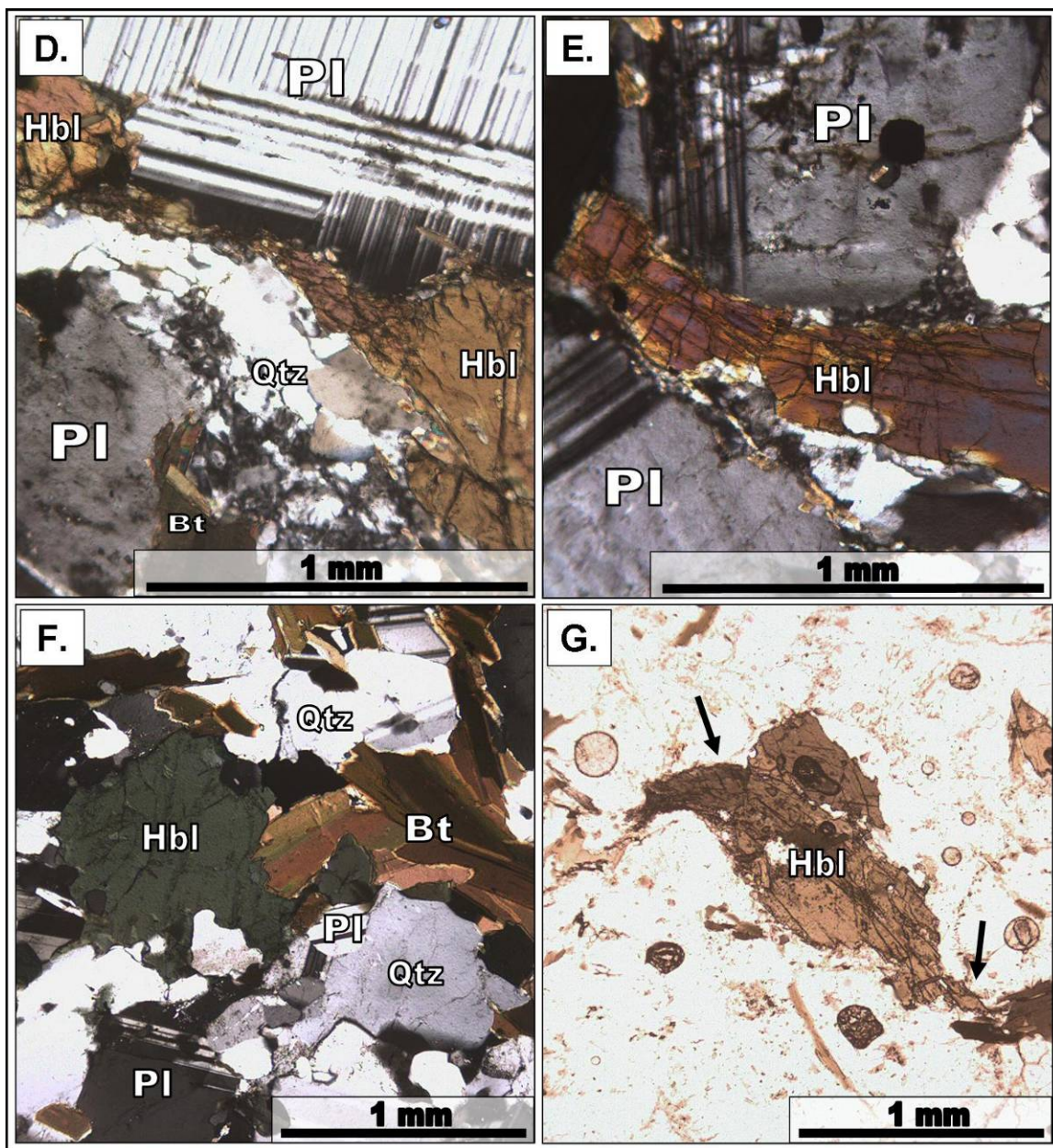


Figure 29. (D) Medium-grained, hornblende-biotite granodiorite (04-520) showing lozenge-shaped grain with tails of cleavage-controlled fragments. (E) Fine-grained, hornblende-biotite tonalite (JW95-256) showing hornblende lath between impinging plagioclase laths. Hornblende grain is fractured and misoriented. (F) Medium-grained, hornblende-biotite tonalite (04-548) showing sutured, amoeboid crystal (G) Medium-grained, hornblende-biotite granodiorite (04-537) showing subhedral hornblende grain with evidence of ductile bending (arrows) into parallelism with foliation. Images D, E, and F are shown with crossed polars; G in plain polar light. Biotite = Bt; Hornblende = Hbl; Plagioclase = Pl; Quartz = Qtz.

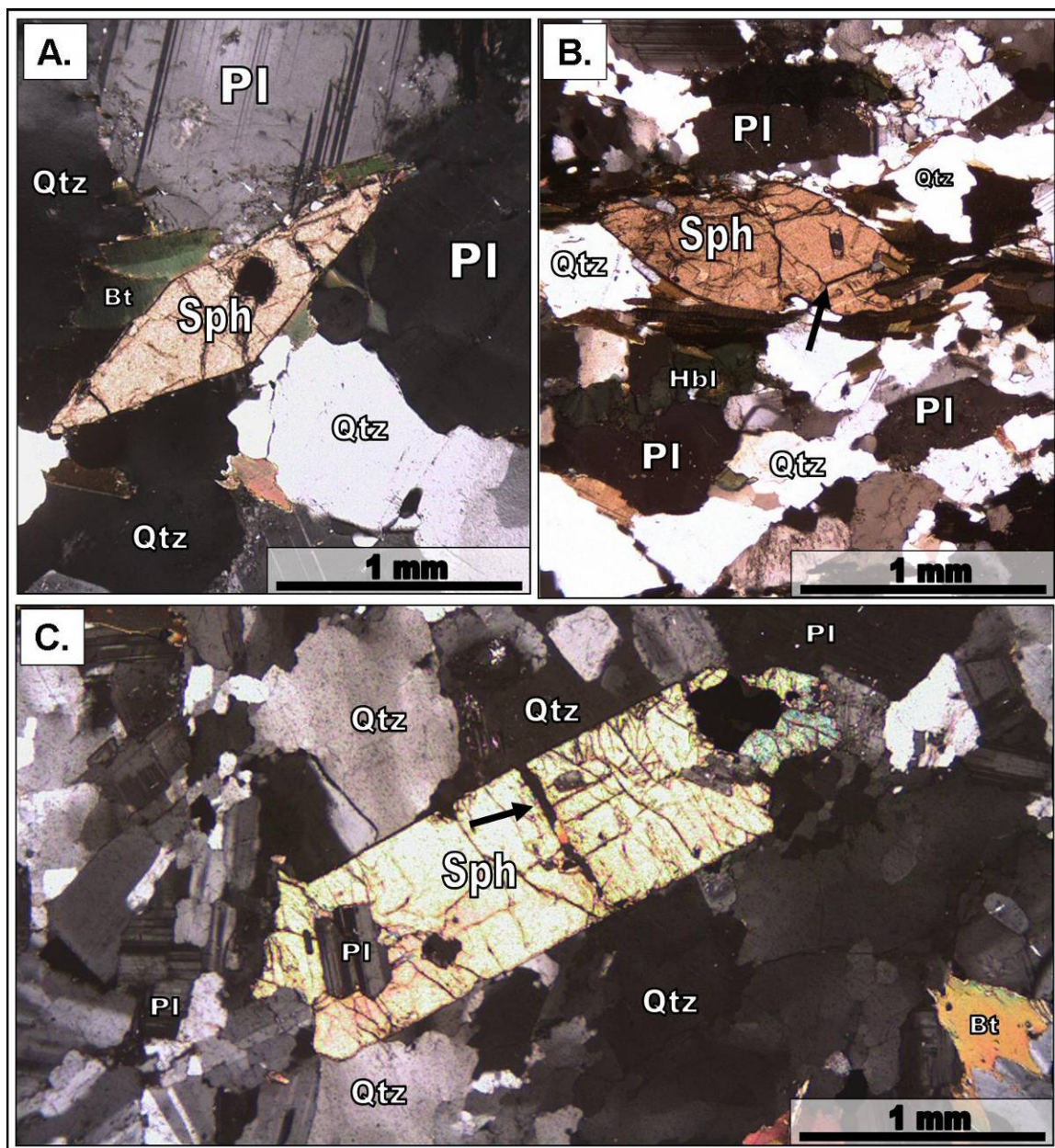


Figure 30. Photomicrographs of sphenes microstructures. (A) Medium-grained, hornblende-biotite granodiorite (04-518) showing euhedral sphenes grain with opaque mineral inclusion. (B) Fine-grained, hornblende-biotite granodiorite (04-553) showing euhedral sphenes grain that is parallel to the main foliation. Deformation twinning is subparallel to foliation (arrow). (C) Fine-grained, biotite granodiorite (04-527) showing euhedral sphenes grain with intragranular fracture filled with quartz (arrow). Images A, B, and C are shown with crossed polars. Biotite = Bt; Hornblende = Hbl; Plagioclase = Pl; Quartz = Qtz; Sphenes = Sph.

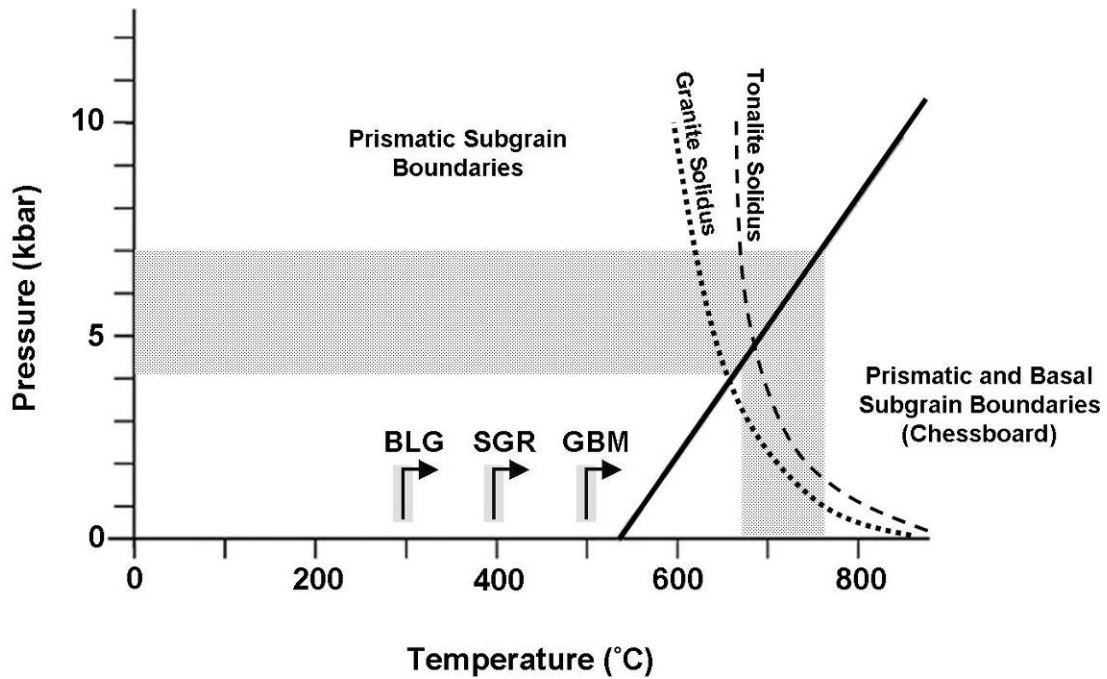


Figure 31. Thermal constraints using chessboard extinction. The presence of chessboard extinction in quartz can be used to constrain temperature of deformation (Passchier and Trouw, 2006). The bold diagonal line represents the boundary between slip regimes in quartz (Passchier and Trouw, 2006). The right side of the diagonal line corresponds to two active slip systems (C slip and A slip) and the formation of chessboard extinction. The left side corresponds to one slip system. Based on pressures determined by Needy et al., (2006) (4-6Kb), we observe that chessboard extinction formation must have occurred at or above the granite and tonalite solidus. Granite and tonalite solidus curves from Whitney (1975). BLG = bulging recrystallization; GBM = grain boundary migration recrystallization; SGR = subgrain rotation recrystallization.

Appendix A. Bighorn Sheeted Complex Structural Data

Station	Easting	Northing	Domain	Fol. Strike	Fol. Dip	Fol. Type	Intensity	Lin. Trend	Lin. Plunge	Lin. Type
1631	-	-	-	-	-	-	-	-	-	-
1643	-	-	-	-	-	-	-	-	-	-
1644	-	-	-	-	-	-	-	-	-	-
1645	-	-	-	-	-	-	-	-	-	-
1646	-	-	-	-	-	-	-	-	-	-
04-548*	-	-	-	-	-	M	3	-	-	-
04-549*	-	-	-	-	-	MS	1	-	-	-
04-550*	-	-	-	-	-	M	3	-	-	-
04-552*	-	-	-	-	-	M	2	-	-	-
04-553*	-	-	-	-	-	M	3	-	-	-
04-554*	-	-	-	-	-	M	3	-	-	-
04-568*	-	-	-	-	-	M	1	-	-	-
SRP 199	573082	3755405	BSC I	327	65	MS	3	85	64	M
SRP 200	572970	3755196	BSC I	308	55	M	2	-	-	-
SRP 200	572970	3755196	BSC I	308	55	S	-	-	-	-
SRP 201	572873	3755012	BSC I	295	64	MS	2	-	-	-
SRP 202	572784	3754846	BSC I	305	60	M	2	90	60	M
SRP 235	578304	3752448	BSC I	110	35	M	2	-	-	-
SRP 235	578304	3752448	BSC I	240	45	S	-	-	-	-
SRP 302	578977	3752824	BSC I	254	54	M	3	-	-	-
SRP 303	578847	3752601	BSC I	285	65	M	2	-	-	-
SRP 304	578811	3752414	BSC I	287	85	M	2	-	-	-
SRP 305	578763	3752389	BSC I	338	60	M	2	-	-	-
SRP 305	578763	3752389	BSC I	326	29	S	2	140	20	S
SRP 306	578649	3752265	BSC I	282	75	M	2	-	-	-
SRP 307	578524	3752273	BSC I	272	74	M	2	-	-	-
SRP 307	578524	3752273	BSC I	256	40	S	-	-	-	-
SRP 320	574883	3754719	BSC I	345	50	M	2	-	-	-
SRP 320	574883	3754719	BSC I	342	80	MS	3	-	-	-
SRP 320	574883	3754719	BSC I	334	34	S	3	142	23	S
SRP 321	574845	3754534	BSC I	8	47	S	3	104	46	S
SRP 321	574845	3754534	BSC I	330	65	S	3	-	-	-
SRP 322	574815	3754460	BSC I	1	34	M	2	-	-	-
SRP 322	574815	3754460	BSC I	2	45	S	3	-	-	-
SRP 323	574805	3754357	BSC I	322	65	M	3	-	-	-
SRP 324	574809	3754168	BSC I	321	50	M	2	-	-	-
SRP 325	574620	3753777	BSC I	325	24	M	2	-	-	-
SRP 325	574620	3753777	BSC I	325	45	S	3	-	-	-
SRP 326	574459	3753480	BSC I	334	75	M	2	-	-	-
SRP 327	574431	3753285	BSC I	5	35	SM	3	-	-	-
SRP 333	575271	3752578	BSC I	306	16	M	2	-	-	-
SRP 334	575309	3752662	BSC I	22	20	M	2	-	-	-
SRP 335	575490	3752716	BSC I	280	26	-	-	-	-	-
SRP 337	575749	3752980	BSC I	294	35	S	3	-	-	-
SRP 045	582028	3752381	BSC I	331	38	M	3	-	-	-
SRP 047	581253	3751922	BSC I	308	72	M	2	150	57	M
SRP 047	581253	3751922	BSC I	305	70	M	2	-	-	-
SRP 048	581306	3751948	BSC I	55	85	S	1	20	75	M

SPR = Scott R. Paterson; others from Barth (unpublished) - Data can be obtained from Barth; * = sample

Appendix A. (continued) Bighorn Sheeted Complex Structural Data

Station	Easting	Northing	Domain	Fol. Strike	Fol. Dip	Fol. Type	Intensity
1693	-	-	-	-	-	-	-
1694	-	-	-	-	-	-	-
1695	-	-	-	-	-	-	-
1696	-	-	-	-	-	-	-
1697	-	-	-	-	-	-	-
1700	-	-	-	-	-	-	-
1702	-	-	-	-	-	-	-
1708	-	-	-	-	-	-	-
1710	-	-	-	-	-	-	-
1712	-	-	-	-	-	-	-
1714	-	-	-	-	-	-	-
1718	-	-	-	-	-	-	-
1719	-	-	-	-	-	-	-
1722	-	-	-	-	-	-	-
1724	-	-	-	-	-	-	-
1729	-	-	-	-	-	-	-
1730	-	-	-	-	-	-	-
1731	-	-	-	-	-	-	-
1732	-	-	-	-	-	-	-
1735	-	-	-	-	-	-	-
1736	-	-	-	-	-	-	-
1740	-	-	-	-	-	-	-
04-562*	-	-	-	-	-	M	2
04-563*	-	-	-	-	-	M	2
04-564*	-	-	-	-	-	M	3
04-565*	-	-	-	-	-	M	2
04-566*	-	-	-	-	-	M	1
04-567*	-	-	-	-	-	M	2
SRP 191	575160	3736089	BSC II	111	86	M	2
SRP 232	577254	3751737	BSC II	124	11	M	2
SRP 255	569854	3751976	BSC II	105	31	S	3
SRP 257	569929	3752317	BSC II	251	81	M	2
SRP 257	569929	3752317	BSC II	220	51	S	2
SRP 258	569702	3752636	BSC II	91	64	M	2
SRP 262	569428	3753837	BSC II	282	72	M	2
SRP 263	569508	3753976	BSC II	161	72	M	2
SRP 264	569603	3754056	BSC II	115	74	M	2
SRP 265	569810	3753880	BSC II	285	31	SM	2
SRP 268	570398	3753139	BSC II	80	68	M	2
SRP 269	570467	3752999	BSC II	44	48	M	2
SRP 273	571042	3752263	BSC II	73	66	M	2
SRP 275	570785	3751904	BSC II	77	61	M	2
SRP 310	578735	3751744	BSC II	284	45	M	2
SRP 311	578519	3751579	BSC II	167	19	M	3
SRP 328	574120	3753080	BSC II	144	60	M	2
SRP 328	574120	3753080	BSC II	265	24	S	4
SRP 330	574664	3752215	BSC II	105	74	M	2
SRP 331	574898	3752114	BSC II	70	36	MS	3
SRP 332	575102	3752183	BSC II	80	59	M	2
SRP 341	570513	3748740	BSC II	155	70	M	2
SRP 341	570513	3748740	BSC II	144	70	S	4
SRP 348	572358	3748653	BSC II	255	28	M	3
SRP 349	572383	3748900	BSC II	255	25	M	3
SRP 362	574186	3750167	BSC II	351	23	S	4
SRP 368	570243	3749727	BSC II	95	50	SM	3
SRP 373	571251	3749697	BSC II	104	22	M	3
SRP 374	571387	3749751	BSC II	92	29	M	2
SRP 380	571741	3749102	BSC II	30	20	M	3
SRP 381	571956	3749177	BSC II	85	14	M	3
SRP 383	572160	3749640	BSC II	92	56	M	2
SRP 384	572304	3749837	BSC II	80	30	M	2
SRP 384	572304	3749837	BSC II	90	19	MS	3
SRP 389	572865	3750389	BSC II	214	4	M	3
SRP 395	572787	3749267	BSC II	94	22	M	3

SPR = Scott R. Paterson; others from Barth (unpublished); * = sample

Appendix B. Blue Cut Granodiorite Structural Data

Station	Easting	Northing	Domain	Fol. Strike	Fol. Dip	Fol. Type	Intensity	Lin. Trend	Lin. Plunge	Lin. Type
GP04	577078	3753100	BC	12	44	S	2	-	-	-
SRP 239	577208	3753538	BC	270	49	S	3	9	50	S
SRP 305	578763	3752389	BC	326	29	S	-	140	20	S
SRP013	577672	3754177	BC	316	20	S	-	-	-	-
SRP014	577302	3754342	BC	310	20	-	-	85	20	M
SRP098	580277	3753050	BC	274	50	-	-	-	-	-
04-523*	-	-	-	-	-	M	2	-	-	-
04-524*	-	-	-	-	-	M	2	-	-	-
04-525*	-	-	-	-	-	M	2	-	-	-
04-526*	-	-	-	-	-	M	2	-	-	-
04-527*	-	-	-	-	-	M	1	-	-	-
JW00-340*	-	-	-	-	-	M	2	-	-	-
GP01	577025	3753125	BC	296	52	M	3	-	-	-
GP010	577336	3752687	BC	298	85	M	2	-	-	-
GP011	577389	3752641	BC	220	27	M	2	-	-	-
GP013	577341	3752330	BC	356	12	M	2	-	-	-
GP014	577257	3752302	BC	22	28	M	2	-	-	-
GP015	577133	3752254	BC	267	52	M	2	-	-	-
GP017	577430	3752410	BC	235	60	M	2	-	-	-
GP018	577506	3752507	BC	295	15	M	2	-	-	-
GP019	577603	3752627	BC	268	26	M	2	-	-	-
GP020	577664	3752671	BC	281	61	M	2	49	53	S
GP021	577726	3752753	BC	300	80	M	2	-	-	-
GP022	577802	3752837	BC	284	38	M	2	-	-	-
GP023	577810	3752913	BC	319	75	M	3	-	-	-
GP024	577855	3752984	BC	334	28	M	2	-	-	-
GP025	577925	3753073	BC	315	45	M	2	-	-	-
GP027	578041	3753188	BC	316	43	M	2	-	-	-
GP028	578172	3753266	BC	47	25	M	2	-	-	-
GP029	578311	3753421	BC	210	15	M	2	-	-	-
GP030	578581	3753448	BC	125	68	M	2	-	-	-
GP031	578651	3753566	BC	315	66	M	2	-	-	-
GP05	577137	3753126	BC	286	45	M	2	-	-	-
GP06	577286	3753104	BC	297	62	M	2	-	-	-
GP08	577278	3752910	BC	100	90	M	2	-	-	-
KBBC-1*	576531	3754984	BC	340	25	M	2	56	21	M
KBBC-2	576857	3755096	BC	332	35	M	2	-	-	-
SRP 168	575818	3756949	BC	192	17	M	2	-	-	-
SRP 184	576092	3756379	BC	269	85	M	2	-	-	-
SRP 185	575985	3756243	BC	247	64	M	2	-	-	-
SRP 186	575817	3755844	BC	3	69	M	2	-	-	-
SRP 187	576194	3755762	BC	216	72	M	2	-	-	-
SRP 187	576194	3755762	BC	283	74	M	2	-	-	-
SRP 188	576476	3755800	BC	313	23	M	2	73	6	M
SRP 190	575656	3756334	BC	325	88	M	2	-	-	-
SRP 211	575332	3754394	BC	318	75	M	2	-	-	-
SRP 211	575332	3754394	BC	287	65	M	2	-	-	-
SRP 213	575458	3754787	BC	344	20	M	2	6	3	M
SRP 219	574946	3755672	BC	339	54	M	2	74	52	M
SRP 224	576970	3753672	BC	21	30	M	2	156	13	M
SRP 226	577007	3753202	BC	298	15	M	2	310	13	M
SRP 227	576938	3752937	BC	18	25	M	3	-	-	-
SRP 229	576772	3752487	BC	38	35	M	2	9	45	M
SRP 230	576701	3752369	BC	278	16	M	2	10	5	M
SRP 231	576521	3752140	BC	246	24	M	2	-	-	-
SRP 238	578442	3753001	BC	34	14	M	3	172	5	M
SRP 251	580434	3753304	BC	192	26	M	2	-	-	-
SRP 298	578046	3753183	BC	168	24	M	2	-	-	-
SRP 299	578364	3753119	BC	268	36	M	2	-	-	-
SRP 300	578599	3753257	BC	125	35	M	2	-	-	-
SRP 301	578620	3753038	BC	180	8	M	2	-	-	-
SRP 302	578977	3752824	BC	254	54	M	3	-	-	-
SRP 304	578811	3752414	BC	287	85	M	2	-	-	-
SRP 305	578763	3752389	BC	338	60	M	2	-	-	-
SRP 317	579710	3752050	BC	275	18	M	2	-	-	-
SRP 318	579580	3752299	BC	264	38	M	2	340	26	M
SRP 338	575888	3753089	BC	327	25	M	2	-	-	-

SPR = Scott R. Paterson; GP = Geoffrey Pignotta; KB = Kenneth Brown; others from Barth (unpublished); * = sample

Appendix B. (continued) Blue Cut Granodiorite Structural Data

Station	Easting	Northing	Domain	Fol. Strike	Fol. Dip	Fol. Type	Intensity	Lin. Trend	Lin. Plunge	Lin. Type
SRP001	576225	3754681	BC	7	62	M	2	50	55	M
SRP002	576584	3754913	BC	352	54	M	2	-	-	-
SRP003	576936	3755171	BC	305	24	M	2	30	15	M
SRP005	577440	3755197	BC	194	11	M	2	280	11	M
SRP006	577585	3755098	BC	314	15	M	2	110	10	M
SRP012	577967	3754129	BC	344	25	M	1	-	-	-
SRP013	577672	3754177	BC	315	36	M	2	-	-	-
SRP015	576490	3754310	BC	30	19	M	2	75	12	S
SRP033	578111	3754323	BC	185	35	M	2	330	10	M
SRP034	578141	3754445	BC	170	39	M	2	165	12	M
SRP085	578332	3754169	BC	298	81	M	3	-	-	-
SRP088	578390	3753862	BC	140	78	M	2	-	-	-
SRP089	578732	3753497	BC	165	40	M	2	-	-	-
SRP091	578996	3753290	BC	156	63	M	2	334	4	M
SRP095	579616	3753155	BC	324	61	M	3	-	-	-
SRP096	579917	3753220	BC	116	80	M	2	-	-	-
SRP097	580103	3753140	BC	265	40	M	2	-	-	-
SRP099	580410	3753180	BC	276	49	M	2	-	-	-
SPR = Scott R. Paterson										

Appendix C. Quail Mountain Sheeted Complex Structural Data

Station	Easting	Northing	Domain	Fol. Strike	Fol. Dip	Fol. Type	Intensity	Lin. Trend	Lin. Plunge	Lin. Type
598	-	-	-	-	-	MS	2	-	-	-
608	-	-	-	-	-	M	3	-	-	-
612	-	-	-	-	-	MS	3	-	-	-
615	-	-	-	-	-	M	3	-	-	-
616	-	-	-	-	-	M	3	-	-	-
617	-	-	-	-	-	M	3	-	-	-
1539	-	-	-	-	-	-	-	-	-	-
1557	-	-	-	-	-	-	-	-	-	-
1558	-	-	-	-	-	-	-	-	-	-
1562	-	-	-	-	-	-	-	-	-	-
1565	-	-	-	-	-	-	-	-	-	-
1590	-	-	-	-	-	-	-	-	-	-
1593	-	-	-	-	-	-	-	-	-	-
1624	-	-	-	-	-	-	-	-	-	-
1625	-	-	-	-	-	-	-	-	-	-
1810	-	-	-	-	-	-	-	-	-	-
1811	-	-	-	-	-	-	-	-	-	-
1812	-	-	-	-	-	-	-	-	-	-
1814	-	-	-	-	-	-	-	-	-	-
1824	-	-	-	-	-	-	-	-	-	-
1825	-	-	-	-	-	-	-	-	-	-
1832	-	-	-	-	-	-	-	-	-	-
1834	-	-	-	-	-	-	-	-	-	-
1836	-	-	-	-	-	-	-	-	-	-
1838	-	-	-	-	-	-	-	-	-	-
1839	-	-	-	-	-	-	-	-	-	-
1840	-	-	-	-	-	-	-	-	-	-
1841	-	-	-	-	-	-	-	-	-	-
04-518*	-	-	-	-	-	M	3	-	-	-
04-520*	-	-	-	-	-	M	3	-	-	-
04-522*	-	-	-	-	-	MS	1	-	-	-
04-530*	-	-	-	-	-	M	3	-	-	-
04-532*	-	-	-	-	-	MS	2	-	-	-
04-534*	-	-	-	-	-	M	3	-	-	-
04-535*	-	-	-	-	-	M	3	-	-	-
04-536*	-	-	-	-	-	MS	1	-	-	-
04-537*	-	-	-	-	-	M	3	-	-	-
04-546*	-	-	-	-	-	M	3	-	-	-
QMSC-1*	569479	3764954	QMSC	335	40	M	2	-	-	-
QMSC-2*	568935	3765258	QMSC	345	35	MS	2	-	-	-
QMSC-2a*	569412	3765372	QMSC	315	15	M	3	-	-	-
QMSC-3*	569188	3767177	QMSC	295	35	M	2	-	-	-
QMSC-4*	567113	3765908	QMSC	345	25	SM	3	-	-	-
QMSC-5*	567242	3766193	QMSC	338	50	M	3	-	-	-
QMSC-6*	567220	3766281	QMSC	290	40	M	2	-	-	-
QMSC-7*	567220	3766281	QMSC	285	45	M	3	-	-	-
SRP 119	575425	3759890	QMSC	296	56	M	2	-	-	-
SRP 120	575291	3759740	QMSC	194	47	S	-	36	32	S
SRP 120	575291	3759740	QMSC	185	60	S	-	36	45	S
SRP 155	574348	3758668	QMSC	300	45	M	3	-	-	-
SRP 156	574148	3758713	QMSC	325	52	SM	3	91	11	S
SRP 157	573124	3759100	QMSC	44	28	SM	3	-	-	-
SRP 157	573124	3759100	QMSC	325	35	MS	3	-	-	-
SRP 236	578466	3752605	QMSC	29	16	M	2	-	-	-
SRP 276	575075	3758656	QMSC	139	60	S	-	-	-	-
SRP 276	575075	3758656	QMSC	275	85	M	2	-	-	-
SRP 277	574703	3758634	QMSC	118	58	S	-	-	-	-
SRP 277	574703	3758634	QMSC	301	84	M	2	-	-	-
SRP 278	574620	3758629	QMSC	138	61	M	2	-	-	-

SPR = Scott R. Paterson; others from Barth (unpublished) - Data can be obtained from Barth; * = sample

Appendix C. (continued) Quail Mountain Sheeted Complex Structural Data

Station	Easting	Northing	Domain	Fol. Strike	Fol. Dip	Fol. Type	Intensity	Lin. Trend	Lin. Plunge	Lin. Type
SRP 293	569666	3761442	QMSC	342	46	M	2	-	-	-
SRP 295	570292	3761018	QMSC	339	39	M	2	130	32	M
SRP 278	574620	3758629	QMSC	125	75	S	-	-	-	-
SRP 281	573733	3759051	QMSC	146	82	M	2	-	-	-
SRP 281	573733	3759051	QMSC	18	30	S	3	-	-	-
SRP 282	573537	3759767	QMSC	278	76	M	2	-	-	-
SRP 286	570285	3761970	QMSC	57	54	M	2	60	50	M
SRP 286	570285	3761970	QMSC	47	61	S	3	64	58	S
SRP 293	569666	3761442	QMSC	265	40	S	3	-	-	-
SRP 293	569666	3761442	QMSC	51	20	M	2	-	-	-
SRP 293	569666	3761442	QMSC	51	20	M	2	-	-	-

SPR = Scott R. Paterson

Appendix D. Stubbe Spring Granite Structural Data

Station	Easting	Northing	Domain	Fol. Strike	Fol. Dip	Fol. Type	Intensity	Lin. Trend	Lin. Plunge	Lin. Type
SRP 290	569462	3762251	SS	338	40	M	2	-	-	-
SRP 291	569277	3762040	SS	38	28	S	3	-	-	-
SRP 294	570100	3760949	SS	308	35	M	2	-	-	-
SRP 160	572835	3758389	SS	331	63	M	2	-	-	-
SRP 161	572476	3758160	SS	309	87	SM	3	-	-	-
SRP 162	572110	3757667	SS	129	34	M	2	196	27	M
SRP 163	572799	3757682	SS	300	35	MS	3	-	-	-
SRP 164	573178	3757624	SS	303	69	S	3	69	62	S
SRP 165	573429	3757640	SS	338	53	SM	3	68	50	S
SRP 204	572576	3756480	SS	333	35	S	1	-	-	-
SRP 204	572576	3756480	SS	333	35	M	2	-	-	-
SRP 205	572962	3756859	SS	346	31	MS	3	-	-	-
SRP 206	573270	3757199	SS	336	64	M	2	-	-	-
SRP 179	573832	3756996	SS	4	63	M	2	-	-	-
SRP 179	573832	3756996	SS	18	27	M	1	-	-	-
SRP 180	573766	3756696	SS	330	56	S	1	130	24	S
SRP 180	573766	3756696	SS	327	47	M	2	-	-	-
SRP 180	573766	3756696	SS	314	24	M	2	-	-	-
SRP 181	574020	3756575	SS	164	67	M	2	-	-	-
SRP 198	573192	3755410	SS	332	44	M	2	-	-	-
SRP 203	573084	3754824	SS	6	88	MS	3	-	-	-
SRP 203	573084	3754824	SS	1	60	S	1	92	59	M
SRP 195	574207	3755718	SS	336	72	M	2	-	-	-
SRP 196	574029	3755518	SS	338	52	MS	2	81	51	M
SRP 197	573695	3755479	SS	342	41	M	3	-	-	-
SRP 197	573695	3755479	SS	328	44	S	1	-	-	-
SRP 193	574760	3755929	SS	327	54	M	2	-	-	-
SRP 163	572799	3757682	SS	300	35	MS	3	-	-	-
SRP 193	574760	3755929	SS	327	54	M	2	-	-	-
SRP 211	575332	3754394	SS	318	75	M	2	-	-	-
SRP 211	575332	3754394	SS	287	65	M	2	-	-	-
SRP 222	576222	3754299	SS	304	38	M	3	95	37	M
SRP 223	576869	3753797	SS	288	80	S	3	86	79	S
SRP 225	576977	3753521	SS	298	62	S	3	94	61	M
1587	-	-	-	-	-	-	-	-	-	-
1599	-	-	-	-	-	-	-	-	-	-
1607	-	-	-	-	-	-	-	-	-	-
1608	-	-	-	-	-	-	-	-	-	-
1609	-	-	-	-	-	-	-	-	-	-
1612	-	-	-	-	-	-	-	-	-	-
1613	-	-	-	-	-	-	-	-	-	-
1626	-	-	-	-	-	-	-	-	-	-
1632	-	-	-	-	-	-	-	-	-	-
1633	-	-	-	-	-	-	-	-	-	-
1649	-	-	-	-	-	-	-	-	-	-
04-533*	-	-	-	-	-	MS	2	-	-	-
04-541*	-	-	-	-	-	MS	2	-	-	-
04-544*	-	-	-	-	-	M	2	-	-	-
04-545*	-	-	-	-	-	M	1	-	-	-
04-546*	-	-	-	-	-	M	3	-	-	-
04-551*	-	-	-	-	-	M	2	-	-	-
04-556*	-	-	-	-	-	MS	1	-	-	-
04-557*	-	-	-	-	-	MS	1	-	-	-
04-558*	-	-	-	-	-	M	1	-	-	-
1627	-	-	-	-	-	-	-	-	-	-
1628	-	-	-	-	-	-	-	-	-	-
1630	-	-	-	-	-	-	-	-	-	-
1639	-	-	-	-	-	-	-	-	-	-
1620	-	-	-	-	-	-	-	-	-	-
1638	-	-	-	-	-	-	-	-	-	-

SPR = Scott R. Paterson; others from Barth (unpublished) - Data can be obtained from Barth; * = sample

Appendix E. Discordant Palms Granite Structural Data

Station	Easting	Northing	Domain	Fol. Strike	Fol. Dip	Fol. Type	Intensity
KB7	578023	3759332	Kp	178	14	M	1
KB8	577779	3759309	Kp	286	71	M	1
1245	-	-	-	-	-	M	1
1266	-	-	-	-	-	M	1
1267	-	-	-	-	-	M	1
1281	-	-	-	-	-	M	1
1303	-	-	-	-	-	M	1
1317	-	-	-	-	-	M	1
1318	-	-	-	-	-	M	1
1334	-	-	-	-	-	M	1
1335	-	-	-	-	-	M	1
1336	-	-	-	-	-	M	1
1527	-	-	-	-	-	M	1
1549	-	-	-	-	-	M	1
1775	-	-	-	-	-	M	1
1788	-	-	-	-	-	M	1
1792	-	-	-	-	-	M	1
1795	-	-	-	-	-	M	1
1796	-	-	-	-	-	M	1
1798	-	-	-	-	-	M	1
1800	-	-	-	-	-	M	1
1801	-	-	-	-	-	M	1
1820	-	-	-	-	-	M	1
KB1	576739	3760464	Kp	328	55	M	2
KB2	577082	3760481	Kp	336	45	M	2
KB3	577674	3758972	Kp	336	58	M	1
KB4	577410	3760972	Kp	310	55	M	2
KB5	577298	3761124	Kp	334	40	M	2
KB6	579071	3761260	Kp	5	45	M	1
SRP 130	575494	3761310	Kp	326	45	M	1
SRP 151	577320	3759280	Kp	345	80	M	1
SRP 152	577797	3759118	Kp	310	35	M	1
SRP109	577353	3763908	Kp	130	70	M	1
SRP109	577353	3763908	Kp	355	74	M	1
SRP109	577353	3763908	Kp	350	77	M	1
SRP110	577642	3763910	Kp	280	89	M	1
03-501*	-	-	-	-	-	M	2
03-515*	-	-	-	-	-	M	1
03-516*	-	-	-	-	-	M	1
05-599*	-	-	-	-	-	M	1
05-618*	-	-	-	-	-	M	1
04-561*	-	-	-	-	-	M	1

SPR = Scott R. Paterson; KB= Kenneth Brown; others from Barth (unpub.); * = sample

Appendix F. Framework Rock Structural data (Domain I - Lost Horse Mountains)

Station	Easting	Northing	Domain	Fol. Strike	Fol. Dip	Lin. Trend	Lin. Plunge
1254	-	-	-	-	-	-	-
1255	-	-	-	-	-	-	-
1279	-	-	-	-	-	-	-
1246	-	-	-	-	-	-	-
1247	-	-	-	-	-	-	-
1248	-	-	-	-	-	-	-
1249	-	-	-	-	-	-	-
1250	-	-	-	-	-	-	-
1251	-	-	-	-	-	-	-
1252	-	-	-	-	-	-	-
1253	-	-	-	-	-	-	-
1256	-	-	-	-	-	-	-
1257	-	-	-	-	-	-	-
1258	-	-	-	-	-	-	-
1259	-	-	-	-	-	-	-
1260	-	-	-	-	-	-	-
1268	-	-	-	-	-	-	-
1269	-	-	-	-	-	-	-
1270	-	-	-	-	-	-	-
1271	-	-	-	-	-	-	-
1272	-	-	-	-	-	-	-
1273	-	-	-	-	-	-	-
1274	-	-	-	-	-	-	-
1275	-	-	-	-	-	-	-
1276	-	-	-	-	-	-	-
1277	-	-	-	-	-	-	-
1278	-	-	-	-	-	-	-
1280	-	-	-	-	-	-	-
1304	-	-	-	-	-	-	-
1305	-	-	-	-	-	-	-
1306	-	-	-	-	-	-	-
1307	-	-	-	-	-	-	-
1308	-	-	-	-	-	-	-
1309	-	-	-	-	-	-	-
1310	-	-	-	-	-	-	-
1311	-	-	-	-	-	-	-
1312	-	-	-	-	-	-	-
1313	-	-	-	-	-	-	-
1314	-	-	-	-	-	-	-
1315	-	-	-	-	-	-	-
1316	-	-	-	-	-	-	-
Data from Barth (unpublished) - Data can be obtained from Barth							

Appendix F. (continued) Framework Rock Structural data (Domain II)

Station	Easting	Northing	Domain	Fol. Strike	Fol. Dip	Lin. Trend	Lin. Plunge
SRP 143	575070	3759399	Xam	157	85	-	-
SRP118	575691	3760135	Xbg	170	73	-	-
SRP 121	575292	3759617	Xbg	180	60	-	-
SRP 127	574804	3760844	Xbg	155	60	-	-
SRP 131	575700	3761148	Xbg	160	41	-	-
SRP 134	576084	3760825	Xbg	160	44	183	3
SRP 135	576059	3759642	Xbg	207	69	-	-
SRP 135	576059	3759642	Xbg	276	88	-	-
SRP 136	576000	3759558	Xbg	198	56	-	-
SRP 141	575409	3759347	Xbg	132	64	279	64
SRP 141	575409	3759347	Xbg	132	64	305	59
SRP 142	575272	3759427	Xbg	139	73	151	58
SRP 146	574984	3759270	Xbg	113	13	203	5
SRP 147	575101	3758514	Xbg	165	38	-	-
SRP 149	576333	3757784	Xbg	118	47	-	-
SRP 150	576187	3757868	Xbg	127	51	244	48
SRP 154	574873	3758789	Xbg	135	82	-	-
SRP 167	576136	3757450	Xbg	27	63	-	-
SRP 167	576136	3757450	Xbg	27	63	-	-
SRP 169	575697	3757136	Xbg	174	42	263	42
SRP 170	575625	3757271	Xbg	148	75	167	40
SRP 171	575523	3757206	Xbg	176	59	-	-
SRP 172	575386	3757139	Xbg	158	61	267	61
SRP 173	574929	3757141	Xbg	209	57	-	-
SRP 174	574683	3757185	Xbg	242	34	-	-
SRP 175	574408	3757146	Xbg	236	24	301	21
SRP 176	574209	3757288	Xbg	193	43	-	-
SRP 177	574034	3757324	Xbg	244	11	313	8
SRP 182	574449	3756622	Xbg	260	38	-	-
SRP 183	574946	3756742	Xbg	232	23	-	-
SRP 193	574760	3755929	Xbg	327	54	-	-
SRP 207	573816	3757501	Xbg	324	55	-	-
SRP 207	573816	3757501	Xbg	328	54	-	-
SRP 208	574099	3757841	Xbg	154	49	-	-
SRP 209	574607	3758022	Xbg	155	59	-	-
SRP 210	575172	3757775	Xbg	338	85	-	-
SRP 212	575397	3754717	Xbg	7	28	-	-
SRP 215	575332	3755248	Xbg	38	15	-	-
SRP 215	575332	3755248	Xbg	340	80	-	-
SRP 216	575351	3755493	Xbg	344	40	-	-
SRP 220	574862	3755745	Xbg	335	45	-	-
SRP 220	574862	3755745	Xbg	295	54	-	-
SRP 221	574698	3755712	Xbg	260	24	-	-
SRP 279	574065	3758333	Xbg	156	65	-	-
SRP 280	573795	3758507	Xbg	289	68	-	-
SRP 128	575011	3761000	Xbg	168	40	-	-
SRP 129	575189	3761060	Xbg	180	65	-	-
SRP 297	573817	3758793	Xbg	293	64	-	-
1528	-	-	-	-	-	-	-
1529	-	-	-	-	-	-	-
1530	-	-	-	-	-	-	-
1531	-	-	-	-	-	-	-
1534	-	-	-	-	-	-	-
1535	-	-	-	-	-	-	-
1536	-	-	-	-	-	-	-
1537	-	-	-	-	-	-	-
1538	-	-	-	-	-	-	-
1540	-	-	-	-	-	-	-
1541	-	-	-	-	-	-	-
1542	-	-	-	-	-	-	-
1543	-	-	-	-	-	-	-

SRP = Scott R. Paterson; other from Barth (unpublished) - Data can be obtained from Barth

Appendix F. (continued) Framework Rock Structural data (Domain II)

Station	Easting	Northing	Domain	Fol. Strike	Fol. Dip	Lin. Trend	Lin. Plunge
1544	-	-	-	-	-	-	-
1553	-	-	-	-	-	-	-
1554	-	-	-	-	-	-	-
1556	-	-	-	-	-	-	-
1561	-	-	-	-	-	-	-
1584	-	-	-	-	-	-	-
1647	-	-	-	-	-	-	-
KB-120	572604	3759236	Xbg	300	35	-	-
KB-121	570505	3758102	Xbg	339	39	-	-
SRP 283	570608	3761975	Xbg	41	56	-	-
SRP 284	570515	3762023	Xbg	37	45	-	-
SRP 285	570370	3762148	Xbg	301	45	-	-
SRP 287	569996	3761903	Xbg	34	48	-	-
SRP 288	569808	3761962	Xbg	40	68	55	64
SRP 292	569397	3761874	Xbg	271	57	-	-
SRP 296	570542	3760918	Xbg	308	89	-	-
SRP 296	570542	3760918	Xbg	292	38	56	33
1776	-	-	-	-	-	-	-
1777	-	-	-	-	-	-	-
1778	-	-	-	-	-	-	-
1779	-	-	-	-	-	-	-
1780	-	-	-	-	-	-	-
1781	-	-	-	-	-	-	-
1782	-	-	-	-	-	-	-
1783	-	-	-	-	-	-	-
1784	-	-	-	-	-	-	-
1785	-	-	-	-	-	-	-
1786	-	-	-	-	-	-	-
1789	-	-	-	-	-	-	-
1790	-	-	-	-	-	-	-
1791	-	-	-	-	-	-	-
1802	-	-	-	-	-	-	-
1803	-	-	-	-	-	-	-
1804	-	-	-	-	-	-	-
1805	-	-	-	-	-	-	-
1806	-	-	-	-	-	-	-
1807	-	-	-	-	-	-	-
1808	-	-	-	-	-	-	-
1815	-	-	-	-	-	-	-
1816	-	-	-	-	-	-	-
1817	-	-	-	-	-	-	-
1821	-	-	-	-	-	-	-
1822	-	-	-	-	-	-	-
KB-122	571097	3762348	Xbg	339	33	-	-
KB-123	572351	3762109	Xbg	150	74	-	-
KB-124	570128	3762859	Xbg	11	27	-	-
1546	-	-	-	-	-	-	-
1547	-	-	-	-	-	-	-
1548	-	-	-	-	-	-	-
1566	-	-	-	-	-	-	-
1567	-	-	-	-	-	-	-
1595	-	-	-	-	-	-	-
1600	-	-	-	-	-	-	-
1601	-	-	-	-	-	-	-

SRP = Scott R. Paterson; KB = Kenneth Brown; other from Barth (unpublished) - Data can be obtained from Barth

Appendix F. (continued) Framework Rock Structural data (Domain II)

Station	Easting	Northing	Domain	Fol. Strike	Fol. Dip	Lin. Trend	Lin. Plunge
1602	-	-	-	-	-	-	-
1603	-	-	-	-	-	-	-
1606	-	-	-	-	-	-	-
1614	-	-	-	-	-	-	-
1615	-	-	-	-	-	-	-
1616	-	-	-	-	-	-	-
1617	-	-	-	-	-	-	-
1621	-	-	-	-	-	-	-
1622	-	-	-	-	-	-	-
1623	-	-	-	-	-	-	-
KB-125	571097	3762348	Xbg	339	33	-	-
SRP 122	575156	3759714	Xbg	262	26	-	-
SRP 122	575156	3759714	Xbg	348	67	-	-
SRP 139	575594	3759573	Xbg	154	58	-	-
SRP 158	572965	3758735	Xbg	289	45	-	-
SRP 159	572941	3758619	Xbg	329	46	-	-

SRP = Scott R. Paterson; KB = Kenneth Brown; other from Barth (unpublished) - Data can be obtained from Barth

Appendix F. (continued) Framework Rock Structural data (Domain III)

Station	Easting	Northing	Domain	Fol. Strike	Fol. Dip	Lin. Trend	Lin. Plunge
1282	-	-	-	-	-	-	-
1283	-	-	-	-	-	-	-
1284	-	-	-	-	-	-	-
1285	-	-	-	-	-	-	-
1286	-	-	-	-	-	-	-
1287	-	-	-	-	-	-	-
1290	-	-	-	-	-	-	-
1291	-	-	-	-	-	-	-
1292	-	-	-	-	-	-	-
1293	-	-	-	-	-	-	-
1294	-	-	-	-	-	-	-
1295	-	-	-	-	-	-	-
1296	-	-	-	-	-	-	-
1297	-	-	-	-	-	-	-
1298	-	-	-	-	-	-	-
1299	-	-	-	-	-	-	-
1300	-	-	-	-	-	-	-
1301	-	-	-	-	-	-	-
1302	-	-	-	-	-	-	-
1319	-	-	-	-	-	-	-
1320	-	-	-	-	-	-	-
1322	-	-	-	-	-	-	-
1323	-	-	-	-	-	-	-
1324	-	-	-	-	-	-	-
1325	-	-	-	-	-	-	-
1326	-	-	-	-	-	-	-
1327	-	-	-	-	-	-	-
1328	-	-	-	-	-	-	-
1329	-	-	-	-	-	-	-
1330	-	-	-	-	-	-	-
1331	-	-	-	-	-	-	-
1332	-	-	-	-	-	-	-
1333	-	-	-	-	-	-	-
1337	-	-	-	-	-	-	-
1338	-	-	-	-	-	-	-
1339	-	-	-	-	-	-	-
1340	-	-	-	-	-	-	-
1341	-	-	-	-	-	-	-
1342	-	-	-	-	-	-	-
1343	-	-	-	-	-	-	-
1344	-	-	-	-	-	-	-
1345	-	-	-	-	-	-	-
1346	-	-	-	-	-	-	-
1347	-	-	-	-	-	-	-
1348	-	-	-	-	-	-	-
1349	-	-	-	-	-	-	-
1350	-	-	-	-	-	-	-
1351	-	-	-	-	-	-	-
1352	-	-	-	-	-	-	-
1353	-	-	-	-	-	-	-
1355	-	-	-	-	-	-	-
1356	-	-	-	-	-	-	-
1357	-	-	-	-	-	-	-
1358	-	-	-	-	-	-	-
1359	-	-	-	-	-	-	-
1360	-	-	-	-	-	-	-
1361	-	-	-	-	-	-	-
1362	-	-	-	-	-	-	-
1363	-	-	-	-	-	-	-
1364	-	-	-	-	-	-	-
1365	-	-	-	-	-	-	-
1366	-	-	-	-	-	-	-
# unknown	-	-	-	-	-	-	-
1367	-	-	-	-	-	-	-

Data from Barth (unpublished) - Data can be obtained from Barth

Appendix F. (continued) Framework Rock Structural data (Domain III)

Station	Easting	Northing	Domain	Fol. Strike	Fol. Dip	Lin. Trend	Lin. Plunge
1368	-	-	-	-	-	-	-
1369	-	-	-	-	-	-	-
1370	-	-	-	-	-	-	-
1371	-	-	-	-	-	-	-
1372	-	-	-	-	-	-	-
1373	-	-	-	-	-	-	-
# unknown	-	-	-	-	-	-	-
1374	-	-	-	-	-	-	-
1375	-	-	-	-	-	-	-
1376	-	-	-	-	-	-	-
1377	-	-	-	-	-	-	-
1378	-	-	-	-	-	-	-
1379	-	-	-	-	-	-	-
1380	-	-	-	-	-	-	-
1381	-	-	-	-	-	-	-
1382	-	-	-	-	-	-	-
1383	-	-	-	-	-	-	-
1384	-	-	-	-	-	-	-
1385	-	-	-	-	-	-	-
1386	-	-	-	-	-	-	-
1387	-	-	-	-	-	-	-
1388	-	-	-	-	-	-	-
1389	-	-	-	-	-	-	-
1390	-	-	-	-	-	-	-
1391	-	-	-	-	-	-	-
1392	-	-	-	-	-	-	-
1393	-	-	-	-	-	-	-
1394	-	-	-	-	-	-	-
1395	-	-	-	-	-	-	-
1396	-	-	-	-	-	-	-
1397	-	-	-	-	-	-	-
1398	-	-	-	-	-	-	-
1399	-	-	-	-	-	-	-
1400	-	-	-	-	-	-	-
1401	-	-	-	-	-	-	-
1402	-	-	-	-	-	-	-
1403	-	-	-	-	-	-	-
1404	-	-	-	-	-	-	-
1406	-	-	-	-	-	-	-
1407	-	-	-	-	-	-	-
1408	-	-	-	-	-	-	-
1409	-	-	-	-	-	-	-
1410	-	-	-	-	-	-	-
1415	-	-	-	-	-	-	-
1416	-	-	-	-	-	-	-
1417	-	-	-	-	-	-	-
1418	-	-	-	-	-	-	-
1419	-	-	-	-	-	-	-
1420	-	-	-	-	-	-	-
1421	-	-	-	-	-	-	-
1422	-	-	-	-	-	-	-
1423	-	-	-	-	-	-	-
1424	-	-	-	-	-	-	-
1425	-	-	-	-	-	-	-
1426	-	-	-	-	-	-	-
1427	-	-	-	-	-	-	-
1428	-	-	-	-	-	-	-
1429	-	-	-	-	-	-	-
1430	-	-	-	-	-	-	-
1431	-	-	-	-	-	-	-
1432	-	-	-	-	-	-	-
1433	-	-	-	-	-	-	-
1435	-	-	-	-	-	-	-
1436	-	-	-	-	-	-	-

Data from Barth (unpublished) - Data can be obtained from Barth

Appendix F. (continued) Framework Rock Structural data (Domain III)

Station	Easting	Northing	Domain	Fol. Strike	Fol. Dip	Lin. Trend	Lin. Plunge
1437	-	-	-	-	-	-	-
1438	-	-	-	-	-	-	-
1439	-	-	-	-	-	-	-
1440	-	-	-	-	-	-	-
1441	-	-	-	-	-	-	-
1442	-	-	-	-	-	-	-
1443	-	-	-	-	-	-	-
1444	-	-	-	-	-	-	-
1445	-	-	-	-	-	-	-
SRP016	579842	3756167	Xbg	191	70	-	-
SRP018	580088	3756224	Xbg	140	80	-	-
SRP023	578309	3755386	Xbg	140	38	-	-
SRP024	578467	3754869	Xbg	190	68	10	23
SRP025	578581	3754938	Xbg	145	20	-	-
SRP028	578692	3754633	Xbg	161	74	-	-
SRP029	578683	3754522	Xbg	170	46	310	38
SRP030	578567	3754520	Xbg	155	56	-	-
SRP031	578386	3754490	Xbg	350	85	-	-
SRP035	578059	3755003	Xbg	190	25	-	-
SRP070	578933	3757219	Xbg	191	55	-	-
SRP073	578699	3757459	Xbg	135	54	-	-
SRP086	578454	3754153	Xbg	136	25	-	-
SRP087	578457	3753992	Xbg	324	5	-	-
SRP107	578917	3754070	Xbg	148	45	-	-
SRP108	578685	3754236	Xbg	152	50	-	-
SRP 189	576907	3757751	Xbg	144	50	-	-
SRP 189	576907	3757751	Xbg	143	74	179	3
SRP 240	580257	3755388	Xbg	358	80	-	-
SRP 241	580333	3755219	Xbg	144	44	-	-
SRP 243	578622	3754855	Xbg	165	45	-	-
SRP 244	580780	3754550	Xbg	65	79	-	-
SRP 244	580780	3754550	Xbg	214	65	-	-
SRP 245	580811	3754309	Xbg	151	80	-	-
SRP 246	580788	3754046	Xbg	306	40	-	-
SRP 247	580802	3753858	Xbg	315	57	-	-
SRP 248	580766	3753772	Xbg	151	50	-	-
SRP 249	580690	3753897	Xbg	96	55	-	-
SRP 250	580713	3753355	Xbg	134	55	-	-
SRP017	579982	3756195	Xgg	150	55	-	-
SRP026	578753	3754891	Xgg	162	56	-	-
SRP027	578767	3754646	Xgg	162	73	-	-
SRP071	579153	3757261	Xgg	350	75	-	-
SRP072	579022	3757467	Xgg	84	70	-	-
SRP106	579216	3753992	Xgg	185	81	299	80
SRP101	580362	3753561	Xgn	135	74	293	73
SRP103	580008	3753924	Xgn	344	81	-	-
SRP104	579811	3753962	Xgn	220	50	301	46
SRP105	579510	3753981	Xgn	152	64	-	-
GJT001	573588	3751754	Xgn	115	22	-	-
GP026	577971	3753118	Xgn	0	90	-	-
GP033	578669	3753647	Xgn	189	75	-	-
GP033	578643	3753935	Xgn	140	80	-	-
GP034	578711	3753905	Xgn	155	77	-	-
GP035	578736	3753821	Xgn	160	78	-	-
GP036	578723	3753760	Xgn	4	82	-	-
GP036	578723	3753760	Xgn	115	9	-	-
GP037	578669	3753683	Xgn	197	80	-	-
GP038	578506	3753693	Xgn	289	21	-	-
SRP007	577776	3755102	Xgn	165	30	-	-
SRP008	577964	3755188	Xgn	169	65	-	-
SRP009	578067	3754936	Xgn	194	37	-	-
SRP010	578132	3754802	Xgn	120	60	-	-
SRP011	578262	3754575	Xgn	195	70	-	-
SRP090	578796	3753439	Xgn	15	29	-	-

SRP = Scott R. Paterson; GP = Geoffrey Pignotta; others from Barth (unpublished) - Data can be obtained from Barth

Appendix F. (continued) Framework Rock Structural data (Domain III)

Station	Easting	Northing	Domain	Fol. Strike	Fol. Dip	Lin. Trend	Lin. Plunge
SRP092	Xgn	579036	3753276	275	68	-	-
SRP094	Xgn	579549	3753232	270	74	-	-
SRP095	Xgn	579616	3753155	314	65	-	-
SRP100	Xgn	580417	3753395	82	60	221	49
SRP032	Xgn	578331	3754417	151	65	-	-
SRP = Scott R. Paterson							

REFERENCES

- Albertz, M., Paterson, S. R., and Okaya, D., 2005, Fast strain rates during pluton emplacement: Magmatically folded leucocratic dikes in aureoles of the Mount Stuart Batholith, Washington, and the Tuolumne Intrusive Suite, California: Geological Society of America Bulletin, v. 117, p. 450-465.
- Anderson, J. L., 1990, Preface to the nature and origin of Cordilleran magmatism, *in* Anderson, J. L., ed, 1990, The Nature and Origin of Cordilleran Magmatism: Geological Society of America Memoir 174, p. vii-x.
- Armstrong, R. L., 1968, Sevier Orogenic Belt in Nevada and Utah: Geological Society of America Bulletin, v. 79, p. 429-458.
- Barazangi, M. and Isacks, B. L., 1976, Spatial distribution of earthquakes and subduction of the Nazca plate beneath South America, *Geology*, v. 4, p. 686-692.
- Barth, A. P. and Schneiderman, J. S., 1996, A comparison of structures in the Andean Orogen of northern Chile and exhumed mid-crustal structures in southern California, U.S.A.: An analogy in tectonic style?: *International Geology Review*, v. 38, p. 1075-1085.
- Barth, A. P., Coleman, D. S., Fleck, R. J., Paterson, S. R., and Wilson, J., 2004, Geology of Joshua Tree National Park: Geological Society of America Abstracts with Programs, v. 36, p 251.
- Best, M. G., 1993, *Igneous and Metamorphic Petrology*: New York, N.Y., W.H. Freeman and Company, 630 p.
- Bouchez, J. L., Delas, C., Gleizes, G., Nedelec, A., and Cuney, M., 1992, Submagmatic fractures in granites: *Geology*, v. 20, p. 35-38.
- Brown, K. L., Paterson, S. R., and Barth, A. P., 2006, Changing melt-migration geometries with crustal depth: An example from the eastern Transverse Ranges: *EOS Trans. AGU*, 87, v. 52, Fall Meeting Supplemental Abstract V23D-0661.
- Brown, K. L. and Barth, A. P., 2007, Magmatic and solid-state fabric development in mid-crustal sheeted plutons, eastern Transverse Ranges, southern California: Geological Society of America Abstracts with Programs, v. 39, p. 224.

- Carter, C. N., Luyendyk, B. P., and Terres, R. R., 1987, Neogene clockwise tectonic rotation of the eastern Transverse Ranges, California suggested by paleomagnetic vectors: *Geological Society of America Bulletin*, v. 98, p. 199-206.
- Crowell, J. C., 1992, Cenozoic faulting in the Little San Bernardino-Orocopia Mountains region, southern California, *in* Richards, S. M., ed., 1992, *Deformation Associated with the Neogene Eastern California Shear Zone, Southwestern Arizona and Southeastern California*: Redlands, CA: San Bernardino County Museum Special Publication, p. 16-19.
- Dickinson, W. R. and Snyder, W.S, 1978, Plate tectonics of the Laramide Orogeny., *in* Matthews III, V., ed., 1978, *Laramide Folding Associated with Basement Block Faulting in the Western U.S.*: Geological Society of America Memoir 151, p. 355-366.
- Dickinson, W. R., 1981, Plate tectonics and the continental margin of California, *in* Ernst, W.G., ed., 1981, *The Geotectonic Development of California*: Prentice-Hall, Englewood Cliffs, p. 2-28.
- Dickinson, W. R., 2004, Evolution of the North American Cordillera: *Annual Review of Earth and Planetary Science*, v. 32, p. 13-45.
- Dumitru, T. A., Gans, P. B., Foster, D. A., and Miller, E. L., 1991, Refrigeration of the western Cordilleran lithosphere during Laramide shallow-angle subduction: *Geology*, v. 19, p. 1145-1148.
- Gapais, D., 1989, Shear structures within deformed granites: Mechanical and thermal indicators: *Geology*, v. 17, p. 1144-1147.
- Glazner, A. F., Bartley, J. M., Coleman, D. S., Gray, W., and Taylor, R. Z., 2004, Are plutons assembled over millions of years by amalgamation from small magma chambers?: *GSA Today*, v. 14, p. 4-11.
- Grove, M., Jacobson, C. E., Barth, A. P., and Vucic, A., 2003, Temporal and spatial trends of Late Cretaceous – Early Tertiary underplating of Pelona and related schist beneath southern California and southwestern Arizona: *Geological Society of America Special Paper* 374, 381-406.

- Heller, P. L., Bowdler, S. S., Chambers, H. P., Coogan, J. C., Hagen, E. S., Shuster, M. W., and Winslow, N. S., 1986, Time of initial thrusting in the Sevier Orogenic Belt, Idaho-Wyoming and Utah: *Geology*, v. 14, p. 388-391.
- Hibbard, M. J., 1987, Deformation of incompletely crystallized magma systems: Granitic gneisses and their tectonic implications: *Journal of Geology*, v. 95, p. 543-561.
- Ingersoll, R. V., 1997, Phanerozoic tectonic evolution of central California and environs: *International Geology Review*, v. 39, p. 957-992.
- Ingram, G. M. and Hutton, D. H. W., 1994, The Great Tonalite Sill: Emplacement into a contractional shear zone and implications for Late Cretaceous to Early Eocene tectonics in southeastern Alaska and British Columbia: *Geological Society of America Bulletin*, v. 106, p. 715-728.
- Kistler, R. W., 1990, Two different lithosphere types in the Sierra Nevada, California, *in* Anderson, J. L., ed, 1990, *The Nature and Origin of Cordilleran Magmatism*: Geological Society of America Memoir 174, p. 271-281.
- Law, R. D., Eriksson, K., and Davisson, C., 2001, Formation evolution, and inversion of the Middle Tertiary Diligencia Basin, Orocochia Mountains, southern California: *Geological Society of America Bulletin*, v. 113, p. 196-221.
- Livaccari, R. F., 1991, Role of crustal thickening and extensional collapse in the tectonic evolution of the Sevier-Laramide Orogeny, western United States: *Geology*, v. 19, p. 1104-1107.
- Manduca, C. A., Kuntz, M. A., and Silver, L. T., 1993, Emplacement and deformation history of the western margin of the Idaho Batholith near McCall, Idaho: Influence of a major terrane boundary: *Geological Society of America Bulletin*, v. 105, p. 749-765.
- Maxson, J. and Tikoff, B., 1996, Hit-and-run collision model for the Laramide Orogeny, western United States: *Geology*, v. 24, p. 968-972.
- Means, W. D. and Park, Y., 1994, New Experimental approach to understanding igneous textures: *Geology*, v. 22, p. 323-326.

- Miller, C. F., Wooden, J. L., Bennett, V. C., Wright, J. E., Solomon, G. C., and Hurst, R. W., 1990, Petrogenesis of the composite peraluminous-metaluminous Old Woman-Puite Range Batholith, southeastern California: Isotopic constraints, *in* Anderson, J. L., ed., 1990, The Nature and Origin of Cordilleran Magmatism, Geological Society of America Memoir 174, p. 99-110.
- Miller, R. B. and Paterson, S. R., 1994, The transition from magmatic to high-temperature solid-state deformation: implications from the Mount Stuart Batholith, Washington: *Journal of Structural Geology*, v. 16, p. 853-865.
- Miller, R. B. and Paterson, S. R., 2001, Construction of mid-crustal sheeted plutons: Examples from the North Cascades, Washington: *Geological Society of America Bulletin*, v. 113, p. 1423-1442.
- Needy, S. K., Barth, A. P., Anderson, J. L., and Wooden, J. L., 2006, Geothermobarometry of the eastern Transverse Ranges, southern California: *Geological Society of America Abstracts with Programs*, v. 38, p. 416.
- Palmer, E. F., Brown, K. L., Wiegand, B., Wooden, J. L., and Barth, A. P., 2006, A geochemical comparison plutonic granitoids to deeper sheeted plutonic rocks: Eastern Transverse Ranges, southern California: *Geological Society of America Abstracts with Programs*, v. 38, p. 560.
- Park, Y. and Means W.D., 1996, Direct observations of deformation processes in crystal mushes: *Journal of Structural Geology*, v. 18, p. 847-858.
- Passchier, C. W., and Trouw, R. A., J, 2006, *Microtectonics*, (2nd ed.): New York, N.Y., Springer, 365 p.
- Paterson, S. R. and Tobisch, O. T., 1988, Using pluton ages to date regional deformation: Problems with commonly used criteria: *Geology*, v. 16, p. 1108-1111.
- Paterson, S. R., Vernon, R. H., and Tobisch, O. T., 1989, A review of criteria for the identification of magmatic and tectonic foliations in granitoids: *Journal of Structural Geology*, v. 11, p. 349-363.
- Paterson, S. R. and Tobisch, O. T., 1992, Rates of processes in magmatic arcs: Implications for the timing and nature of pluton emplacement and wall rock deformation: *Journal of Structural Geology*, v. 14, p. 291-300.

- Paterson, S. R., Fowler, T. K., Schmidt, K. L., Yoshinobu, A. S., Yuan, E. S., and Miller, R. B., 1998, Interpreting magmatic fabric patterns in plutons: *Lithos*, v. 44, p. 53-82.
- Paterson, S. R., and Miller, R. B., 1998, Mid-crustal magmatic sheets in the Cascades Mountains, Washington: Implications for magma ascent: *Journal of Structural Geology*, v. 20, p. 1345-1363.
- Paterson, S. R., Barth, A. P., Wooden, J. L., Pignotta, G. S., and Memeti, V., 2006, Bedrock geologic map of the Keys View 7.5 minute quadrangle, Riverside County, California, unpublished, scale 1:24,000.
- Powell, R. E., 1981, Geology of the crystalline basement complex, eastern Transverse Ranges, southern California: Pasadena, California Institute of Technology, Ph.D dissertation, 441 p.
- Powell, R. E., 1993, Balanced palinspastic reconstruction of pre-Late Cenozoic paleogeology, southern California: Geologic and kinematic constraints on evolution of the San Andreas fault system, *in* Powell, R. E., Weldon, R. J., and Matti, J. C., eds., 1993, *The San Andreas Fault System: Geological Society of America Memoir 178*, p. 1-106.
- Rosenberg, C. L., 2001, Deformation of partially molten granite: A review and comparison of experimental and natural case studies: *International Journal of Earth Sciences*, v. 90, p. 60-76.
- Rushmer, T., 1995, An experimental deformation study of partially molten amphibolite: applications to low-melt fraction segregation: *Journal of Geophysical Research*, v. 100, p. 15681-15695.
- Schofield, D. I. and D'Lemos, R. S., 1998, Relationships between syn-tectonic granite fabrics and regional PTtd paths: An example from the Gander-Avalon boundary of NE Newfoundland: *Journal of Structural Geology*, v. 20, p. 459-471.
- Schmidt, K. L., Wetmore, P. H., Johnson, S. E., and Paterson, S. R., 2002, Controls on orogenesis along an ocean-continent margin transition in the Jura-Cretaceous Peninsular Ranges Batholith, *in* Barth, A. P., ed., 2002, *Contributions to Crustal Evolution of the Southwestern United States: Geological Society of America Special Paper*, v. 365, p. 49-71.

- Simpson, C., 1985, Deformation of granitic rocks across the brittle-ductile transition: *Journal of Structural Geology*, v. 7, p. 503-511.
- Simpson, C. and Wintsch, R. P., 1989, Evidence for deformation-induced K-feldspar replacement by myrmekite: *Journal of Metamorphic Petrology*, v. 7, p. 261-275.
- Tribe, I. R. and D'Lemos, R. S., 1996, Significance of a hiatus in down-temperature fabric development within syntectonic quartz diorite complexes, Channel Islands, UK: *Journal of the Geological Society, London*, v. 153, p. 127-138.
- Tullis, J., 2002, Deformation of granitic rocks: experimental studies and natural examples, *in* Karato, S., and Wenk, H., (eds.), 2002, *Plastic Deformation of Minerals and Rocks: Reviews in mineralogy and geochemistry*, v. 51, p. 51-95.
- Vernon, R. H., 2004, *A Practical Guide to Rock Microstructure*: New York, N.Y., Cambridge University Press, 594 p.
- Vernon, R. H., Johnson, S. E., and Melis, E. A., 2004, Emplacement-related microstructures in the margin of a deformed pluton: The San Jose Tonalite, Baja California, Mexico: *Journal of Structural Geology*, v. 26, p. 1867-1884.
- Whitney, J. A., 1975, The effects of pressure, temperature, and XH_2O on phase assemblage in four synthetic rock compositions: *Journal of Geology*, v. 83, p. 1-30.
- Wooden, J. L., Tosdal, R. M., Howard, K. A., Powell, R. E., Matti, J. C., and Barth, A. P., 1994, Mesozoic intrusive history of parts of the eastern Transverse Ranges, California: Preliminary U-Pb zircon results: *Geological Society of America Abstracts with Programs*, v. 26, p. 104.
- Wooden, J. L., Fleck, R. J., Matti, J. C., Powell, R. E., and Barth, A. P., 2001, Late Cretaceous intrusive migmatites of the Little San Bernardino Mountains, California: *Geological Society of America Abstracts with Programs*, v. 33, p. A65.

CURRICULUM VITAE

Kenneth Lee Brown

Education

Ph.D., Geology, in progress, Miami University of Ohio
M.S., Geology, Nov. 2008, Indiana University
B.A., Geology (with distinction), Aug. 2005, Indiana University-Purdue
University, Indianapolis

Awards and Honors

GSA Graduate Student Research Grant (2007)
IUPUI Graduate Student Teaching Assistantship (TA) (2006-07)
IUPUI Graduate Student Research Investment Fellowship (RIF) (2005-06)
Indiana University Crossroads Geology Conference Best Student Poster (2008)
Indiana University Department of Geological Sciences (DOGS) Research Day –
Best Student Poster Presentation (2007)
IUPUI Andrew Cebula memorial scholarship (2007)
IUPUI School of Science Travel Fellowship (2006)
IUPUI School of Science Graduate Student Organization Travel Grant (2006)
IUPUI Geology Department Academic Achievement Award (2005)
IUPUI Geology Department Geology Alumni Scholarship (2005)
Undergraduate Research Opportunity Program (UROP) research grant (2003-05)
IUPUC Exceptional Chemistry Student Award (2003)
Golden Key International Honor Society (2003- present)

Research/ Training Experiences

Graduate Instructor/Lecturer (August 2006-08)
IUPUI Department of Earth Sciences, Indianapolis, IN
Research Assistant in GIS (March 2006 - May 2006)
Digitize Geologic Maps for NPS and USGS Publications
Laboratory Researcher (August 2004 - 2007)
IUPUI Petrology Laboratory, Indianapolis, IN
Field and Laboratory Research Intern (Jan. 2004 - Aug. 2004)
Center for Earth and Environmental Sciences, IUPUI, Indianapolis, IN
Laboratory Assistant (August 2003 – August 2004)
IUPUI Biogeochemistry Laboratory, Indianapolis, IN

Publications

- Brown, K. L. and Barth, A. P., 2007, Magmatic and solid-state fabric development in mid-crustal sheeted plutons, eastern Transverse Ranges, southern California, GSA Abstracts with Programs v. 39, p. 224.
- Brown, K. L. and Barth, A. P., 2007, Depth- dependent geochemical changes in Late Cretaceous granitic rocks, Transverse Ranges, southern California, GSA Abstracts with Programs v. 39, p. 388.
- Wiegand, B. A., Barth, A. P., Wooden, J. L., Brown, K. L., and Palmer, E. F., 2007, Sr and Nd isotopic evolution in Late Cretaceous lower to upper crustal granitic rocks from the Transverse Ranges, southern California, GSA Abstracts with Programs v. 39, p. 407.
- Barnes, J. L., Brown, K. L., Barth, A. P., 2007, Geothermometry of Pelitic gneiss in the Little San Bernardino Mts, southern California, GSA Abstracts with Programs v. 39, p. 318.
- Barth, A. P., Wooden, J. L., Brown, K. B., Forbes, C. C., Hellem-Hughes, K. L., Needy, S. K., Palmer, E. P., Probst, K. P., 2007, Observations of crust and mantle composition and structural evolution along the eastern margin of the Salton Trough, MARGINS Integrated Collaborations in the Cascadia and Walker Lane/Salton Trough.
- Brown, K. L., Paterson, S. R., and Barth, A. P., 2006, Changing melt-migration geometries with crustal depth: An example from the Eastern Transverse Ranges, southern California: EOS.
- Palmer, E. F., Brown, K. L., Wiegand, B., Wooden, J. L., Needy, S. K., and Barth, A. P., 2006, A geochemical comparison of plutonic granitoids to deeper sheeted plutonic rocks: Eastern Transverse Ranges, southern California: GSA Abstracts with Programs v. 38, p. 560.
- Brown, K. L. and Barth, A.P., 2006, The Rheology of Mid-Crustal Sheeted Granitoids: An example from the eastern Transverse Ranges, southern California: Integrated Solid Earth Sciences (ISES): Summer Program on the Rheology of Earth Materials.
- Brown, K. L. and Barth, A. P., 2006, Deformation of Mid-Crustal Sheeted Granitoids: An example from the eastern Transverse Ranges, southern California: GSA Field Forum on the Tectonic Significance of Vertical Boundaries in the Cordillera.
- Brown, K. L., Carter, C. A., Fohey, N. K., Wooden, J. L., Yi, K., and Barth, A. P., 2004, A study of the origin of rhyolite at mid-ocean ridges; geochronology and petrology of trachydacite and rhyolite from Salton Sea, California, and Torfajokull, Iceland: GSA Abstracts with Programs v. 36, pp.79
- Brown, K. L. and Barth A. P., 2003, A study of the origin of rhyolite: Torfajokull, Iceland: 18th Annual National Conference of Undergraduate Research (NCUR).
- Brown, K. L. and Barth A. P., 2003, A study of the origin of rhyolite: Torfajokull, Iceland: Indiana University Undergraduate Research Conference (IUURC)